Summer 8-15-2021

Human iPSC Tissue-Engineered Cartilage for Disease Modeling of Skeletal Dysplasia-Causing TRPV4 Mutations

Amanda R. Dicks
Washington University in St. Louis

WASHINGTON UNIVERSITY IN ST. LOUIS

McKelvey School of Engineering and Applied Science
Department of Biomedical Engineering

Dissertation Examination Committee:
Farshid Guilak, Chair
Nathaniel Huebsch
Spencer Lake
Ingrid Meulenbelt
Simon Tang

Human iPSC Tissue-Engineered Cartilage for
Disease Modeling of Skeletal Dysplasia-Causing TRPV4 Mutations

by

Amanda Dicks

A dissertation presented to
The Graduate School
of Washington University in
partial fulfillment of the
requirements for the degree
of Doctor of Philosophy

August 2021
St. Louis, Missouri

Table of Contents

List of Figures

List of Tables

Acknowledgements

Thank you to my mentor, Farshid Guilak, for his continued support and guidance. Thank you for accepting me into your laboratory and believing in me and my projects. Thank you for always having an optimistic view and an alternative perspective on my data. Beyond doing the science, thank you for teaching me how to communicate my science and inspiring my love of storytelling science and visualizing data by continuously motivating me with your presentations. Furthermore, thank you for supporting my professional development at and away from the bench. You have set a high bar and an excellent example for all of us to strive for throughout our careers.

Thank you to my second mentor and co-author, Chia-Lung Wu, for your never-ending encouragement and support. Thank you for sending me home with conical tubes to practice with on my first day and teaching me everything I know from basic laboratory techniques to hiPSC culture to experimental design to RNA sequencing analysis. Thank you for the rides home late at night and on weekends, the conversations about science and life, the Tai Ke dinners, and trimming Evie's nails. Thank you for your friendship. Thank you to the other hiPSC team members Nancy Steward and Zainab Harissa. Thanks for the long chats in the tissue culture hoods and all the help with experiments. Thank you to the hiPSC team for always being there for whatever I needed; you have all been an incredible help to this thesis. Thank you to Bob Nims and Alireza Savadipour for their never-ending mechanics assistance. Thank you to the rest of the Guilak lab. You have all taught me so much and inspired me to do great science. It has been an honor to work with and be a part of the Guilak lab family. Special thanks to the people who keep the lab running no matter what, even a pandemic, Nick Thompson, Jim Maus, and Sara Oswald.

Thank you to the Washington University research community for their assistance and

Thank you to my friends and family for all their love and support throughout graduate school; it's been a wild ride. Thank you to my undergraduate professors Jack Phlipot and Amy Shank who gave me the educational foundation to get to where I am. Thanks to my late grandmother for always supporting my academic ventures; she would be so proud. Thanks to my mother, Joyce Dicks, for encouraging me to pursue my PhD despite my doubts, never settling for anything less than my best, and always being there to cheer me on, listen to me vent, or cook some good food. Thanks to my best friend, Katelyn Schoenike, for always being there for some Handle's or a wine night, even from 6000 miles away. Special thanks to my partner, Andy Daniel. I cannot imagine doing this PhD without you by my side, especially through a pandemic. And thanks to our mascot, Evie.

Amanda Dicks

Washington University in St. Louis
August 2021

Dedicated to my supportive mother and grandmother and loving partner.

ABSTRACT OF THE DISSERTATION

Human iPSC Tissue-Engineered Cartilage for

Disease Modeling of Skeletal Dysplasia-Causing TRPV4 Mutations

by

Amanda Dicks

Doctor of Philosophy in Biomedical Engineering

Washington University in St. Louis, 2021

Professor Farshid Guilak, Chair

Cartilage is essential to joint development and function. However, there is a variety of cartilage diseases, ranging from developmental (e.g., skeletal dysplasias) to degenerative (e.g., arthritis), in which treatments and therapeutics are lacking. For example, specific point mutations in the ion channel transient receptor potential vanilloid 4 (TRPV4) prevent proper joint development, leading to mild brachyolmia and severe, neonatally lethal metatropic dysplasia. Tissue-engineered cartilage offers an opportunity to elucidate the underlying mechanisms of these cartilage diseases for the development of treatments.

Human induced pluripotent stem cells (hiPSCs) are an improved cell source option for cartilage tissue engineering given their minimal donor site morbidity, absence of ethical concerns, and extensive proliferation, differentiation, and gene editing capacities. Unfortunately, previously published hiPSC chondrogenesis protocols were time consuming, difficult to reproduce, and resulted in off-target differentiation. Here, we used two methods to enhance hiPSC chondrogenesis using our previously published stepwise chondrogenic differentiation protocol. Next, we used the improved protocol to perform *in vitro* disease modeling of

brachyolmia and metatropic dysplasia resulting from mutations in mechanosensor TRPV4.

To enhance chondrogenesis, we used a CRISPR-Cas9-edited hiPSC cell line with a GFP reporter to determine surface markers co-expressed with early chondrogenic marker and cartilage matrix protein *COL2A1*. We found that chondroprogenitors that were positive for PDGFRβ, CD146, and CD166 and negative for CD45 had enhanced chondrogenic potential. In fact, sorted chondroprogenitors from the reporter line and an unedited line had significantly improved homogeneity compared to unsorted as determined by single-cell RNA sequencing. Furthermore, the derived chondrocytes synthesized more homogenous and robust matrix proteins and had higher chondrogenic gene expression.

In a continued effort to improve the chondrogenesis protocol, we used bulk and single-cell RNA sequencing to determine where the off-target differentiation occurred. We found that Wnt and melanocyte inducing transcription factor (MITF) signaling were driving the two primary off-target populations: neurogenic and melanogenic, respectively. Single-cell RNA sequencing, histology, and quantification of matrix production confirmed pan-Wnt and MITF inhibition during chondrogenesis improved homogeneity of the cells throughout differentiation and increased chondrogenic potential.

Using the findings from these studies, we created an hiPSC chondrogenesis protocol that follows the developmental mesodermal lineage and uses chemically defined medium. We also provide instructions for digesting the chondrogenic tissue to isolate hiPSC-derived chondrocytes at the single cell level. This protocol has applications for a variety of tissue engineering uses including regenerative therapies, gene editing, drug screening, and disease modeling.

In fact, we applied this protocol for disease modeling of TRPV4 mutations that result in skeletal dysplasias. Using CRISPR-Cas9 gene editing technology, we created two hiPSC lines

harboring either the brachyolmia-causing V620I substitution or the metatropic dysplasia-causing T89I substitution. The hiPSCs were chondrogenically differentiated and then were treated with BMP4 to stimulate hypertrophic differentiation. We determined that TRPV4 mutations increased basal signaling but decreased sensitivity to chemical agonist GSK1016790A using electrophysiology techniques and confocal imaging. Furthermore, using bulk RNA sequencing, we found the mutations suppressed chondrocyte maturation and hypertrophy, likely preventing endochondral ossification and long bone formation leading to the disease phenotype.

We also used these cell lines to study the effects of the mutations on mechanotransduction. The hiPSC-derived chondrocytes were physiologically loaded in agarose constructs for 3 hours and then sequenced to elucidate the temporal response to loading. We found the mutant TRPV4 increased gene expression in response to loading compared to wildtype. Gene expression patterns indicated increased proliferation in mutant cells, which could prevent chondrocyte hypertrophic differentiation and endochondral ossification.

Overall, we have developed an improved chondrogenic hiPSC protocol. The resulting tissue-engineered cartilage has many uses including *in vitro* disease modeling of genetic, developmental conditions, as shown here. Our findings provide target genes for future drug development to treat brachyolmia and metatropic dysplasia. Furthermore, we have increased the understanding of TRPV4 function in chondrocytes, which can be applied to cartilage tissue engineering and other cartilage disease studies.

Chapter 1

Introduction

1.1 Abstract

Cartilage is an avascular, aneural soft tissue composed only of chondrocytes and the extracellular matrix they produce. Cartilage serves two functions in the joint: as a template for endochondral ossification and long bone development and as a lining of long bones to provide a nearly frictionless surface. The transient receptor potential vanilloid 4 (TRPV4) ion channel serves as a regulator of both chondrogenic development and cartilage homeostasis through mechanotransduction. Physiologic loading mediated through TRPV4 promotes cartilage matrix synthesis. Moreover, gain-of-function mutations in the *TRPV4* gene cause mild to lethal skeletal dysplasias. While the underlying mechanisms of skeletal dysplasias is unclear, tissue-engineered cartilage offers the possibility to study these processes. Tissue-engineered cartilage, which can be derived from human induced pluripotent stem cells (hiPSCs) among other cell types, serves as an option to study cartilage development, homeostasis, function, and disease. In fact, *in vitro* disease modeling, drug screening, and genetic engineering with hiPSC-derived chondrocytes can aid in the development of regenerative therapeutics and treatments for cartilage diseases. In this thesis, we developed an hiPSC chondrogenic differentiation protocol and applied it to disease modeling of skeletal dysplasia-causing TRPV4 mutations.

1.2 Cartilage Development and Homeostasis

Following chondrogenesis, cartilage undergoes one of two fates: hypertrophy or homeostasis. In the first, chondrocytes differentiate into hypertrophic chondrocytes and undergo endochondral

ossification, or the formation of long bones. The second fate is homeostasis, during which the soft tissue lines diarthrodial joints throughout one's lifetime. Chondrocytes, the primary cell type of cartilage, are under strict regulation via transcription factors and biochemical and biomechanical cues that guide their differentiation, anabolic matrix synthesis, and catabolic matrix degradation occurring in both fates.

1.2.1 Chondrocyte differentiation

During embryogenesis, cartilage develops and forms the template for long bones (*1, 2*). Mesenchymal cells aggregate together before undergoing SOX9-driven chondrogenesis (*2-4*). Sry-related high-mobility-group box 9 (SOX9) and its downstream targets, SOX5 and SOX6, form a transcription factor axis responsible for driving chondrocyte differentiation and proliferation (*3*). Chondrocyte expression of *SOX9* is regulated by fibroblast growth factor (FGF), insulin-like growth factor I (IGF-I), transient receptor potential vanilloid 4 (TRPV4), and transcription factors Sp1 and CREB (*3*). SOX9 is required to upregulate expression of chondrogenic matrix proteins, such as collagen type II alpha chain I (*COL2A1*) and cartilage oligomeric matrix protein (*COMP*) (*3, 5*). Resting and proliferating chondrocytes secrete the cartilage extracellular matrix (ECM) primarily composed of sulfated glycosaminoglycans (sGAGs) and type II collagen (COL2) (*2, 6, 7*). Some of the chondrocytes will then stop proliferating, begin to hypertrophy, and undergo endochondral ossification.

Endochondral ossification is separate from membranous ossification, in which neural crest cells differentiate into osteoblasts and secrete cortical bone to form flat bones (e.g., skull, clavicle) (*2*). In contrast, endochondral ossification is responsible for formation of the long bones of the appendicular skeleton. Chondrocyte hypertrophy, which leads to endochondral ossification, is driven by transcription factors runt related transcription factor 2 (*RUNX2*) and

2

Indian hedgehog (*IHH*). Hypertrophic chondrocytes switch from COL2 to COL10 production, increase in size, and organize in columnar formations (*2, 6, 7*). Additionally, they begin secreting bone morphogenic proteins (BMPs), vascular endothelial growth factors (VEGFs), and parathyroid hormone-related peptide (PTHR) to recruit osteoblast progenitors (*2, 6, 7*). Hypertrophic chondrocytes the either undergo apoptosis or differentiate into osteoblasts (*2, 6, 7*). The newly differentiated osteoblasts express osteogenic factors (e.g., bone sialoprotein, osteopontin), begin to mineralize bone, and allow for vascular invasion (*2, 6, 7*). This process occurs in the center of the bone during embryogenesis and continues to occur in secondary ossification sites (i.e., growth plate), towards the ends of the bones, after birth and through adolescence (*2, 6, 7*).

1.2.2 Cartilage homeostasis

The remaining chondrocytes that did not undergo hypertrophy are the only cell type present in articular cartilage, the soft tissue lining the ends of the long bones (*8, 9*). In adults, chondrocytes compose 5% of cartilage's volume and maintain cartilage homeostasis in response to genetic and environmental signals, such as growth factors or physiologic loading, through a balanced regulation of anabolic and catabolic ECM synthesis and degradation (*10, 11*). The resulting ECM is avascular, aneural, and primarily composed of proteoglycans (e.g., glycosaminoglycans) and type II collagen, alongside several other collagens and non-collagenous proteins (e.g., hyaluronate, fibronectin) (*8, 9, 12*). Glycosaminoglycans (GAGs), largely comprising the large aggregating proteoglycan aggrecan (ACAN), make up 4-7% of cartilage (*8, 13, 14*). Due to their negative charge, GAGs retain water, which composes 65-80% of the tissue weight, contributing to the compressive properties of cartilage (*8, 13, 14*). Type II collagen, approximately 10-20% of cartilage matrix, primarily contributes to the shear and tensile properties of the tissue (*8, 13, 14*).

Cartilage has a highly hydrated, cross-linked composition that also has a unique structure: zonal organization. In the superficial zone, which experiences immediate strain and interacts with the opposing bone's cartilage, chondrocytes are flat, and the matrix proteins are aligned parallel with the surface, providing tensile strength. The deep zone provides compressive strength with rounded chondrocytes in a columnal alignment and matrix proteins in an alignment perpendicular to the surface. The chondrocytes and matrix proteins are randomly aligned and organized in the middle zone, providing a transition between the superficial and deep zones. The composition and structure of cartilage results in biphasic properties and viscoelastic behavior with a compressive Young's modulus of 240-850 kPa, an aggregate modulus of 100-2000 kPa, and a Poisson's ratio of 0.06-0.3 (*1, 8, 9, 15-21*). Due to these properties, articular cartilage can distribute stress while experiencing millions of cycles of compressive loading several times one's body weight (*1, 12, 16-18, 22, 23*).

Not only does cartilage withstand loading, but the mechanical forces from joint movements (e.g., walking, running, climbing stairs) are vital for tissue development and homeostasis (*17, 24-26*). Matrix synthesis, chondrogenic gene expression, and anti-inflammatory responses are stimulated by physiologic levels of compressive, shear, hydrostatic pressure, and osmotic forces (*9, 16, 17, 20, 23-25, 27-30*). Cartilage stress and strain during loading is filtered through the zonal organization to the pericellular matrix (PCM). The PCM, composed of collagen type VI (COL6), fibronectin 1, and proteoglycans perlecan and biglycan (*31-33*), integrates with the ECM and has approximately 35% of the ECM's mechanical properties (*34, 35*). The PCM surrounds the chondrocyte, forming the chondron, to serve as a biomechanical and biochemical filter (*31-33*). The chondrocyte senses load through mechanosensors such as integrins, primary cilium, and ion channels (e.g., TRPV4) and converts the signal into

4

downstream pathways (e.g., Indian hedgehog, Wnt, TGFβ, MAPK-ERK) resulting in transcriptomic changes (*27, 32*).

1.3 Transient Receptor Potential Vanilloid 4

Transient receptor potential vanilloid 4 (TRPV4) is a non-selective, calcium-permeable ion channel. The cell membrane protein is tetrameric with each component composed of six transmembrane alpha helices and a pore loop with an amino group on one end and a carboxyl group on the other (*36*). Recently, the crystalline cryo-EM structure has been identified, giving insights into gating mechanisms and therapeutics (*37*). It is well known that TRPV4 is an osmo-sensor (*38-41*) found in multiple osmotically-regulating cell types including the brain, liver, and kidneys (*36, 42, 43*). Furthermore, TRPV4 function has been found to play a role in bone (*44*), vasculature (*45*), adipose (*46*), and nociception (*47, 48*). The channel is activated by, but not limited to, heat (*49, 50*), hypo-osmolarity or cell swelling (*39, 41*), shear stress (*51, 52*), mechanical loading (*53*), and chemical agonists such as 4α-phorbol 12,13-didecanoate, ruthenium red, and GSK1016790A (*43, 54*). Mutations in TRPV4 lead to a variety of genetic disorders (*55, 56*) including hyponatremia (*57*), chronic obstructive pulmonary disorder (*58, 59*), and neuropathies (e.g., distal spinal muscular atrophy congenital non-progressive (*60-62*), Charcot–Marie–Tooth disease type 2C (CMT2C) (*63-68*), scapuloperoneal spinal muscular atrophy (SPSMA) (*63, 64, 68*)). TRPV4 mutations also lead to skeletal disorders including arthropathies, such as familial digital arthropathy-brachydactyly (*69*), and skeletal dysplasias, such as brachyolmia (*70*), metatropic dysplasia (*71-76*), spondyloepiphyseal dysplasia Maroteaux type (*77-80*), and parastremmatic dwarfism (*81*). Given the number of skeletal-related channelopathies associated with TRPV4 mutations, TRPV4 is critical for proper skeletal development.

In fact, TRPV4 plays a role in both chondrogenesis and cartilage homeostasis. TRPV4 activation was found to upregulate transcription factor *SOX9* in chondrogenic ATDC5 cells (*82*), while deletion of TRPV4 decreased chondrogenic potential of murine adipose-derived stem cells (*83*). Studies using compressive loading and chemical agonists to activate TRPV4 found that the resulting calcium signaling is coupled with transforming growth factor beta (TGFβ) signaling, an essential growth factor family in chondrogenesis and cartilage homeostasis (*84, 85*). Furthermore, TRPV4 activation also increased matrix production, elastic modulus, and anti-inflammatory gene expression in primary porcine chondrocytes (*53, 86-88*). Studies in mouse models found a TRPV4 global knockout increased the incidence of osteoarthritis (OA) (*89*) in male mice, especially on a high fat diet (*83*). However, a cartilage-specific knockout protected against age-related OA but not post-traumatic OA (*90*). In summary, TRPV4 is a critical component and regulator of chondrogenic development and homeostasis.

1.4 Cartilage Diseases

Cartilage diseases include, but are not limited to: aggrecanopathies, arthritis, arthropathies, cartilaginous tumors, chondrocalcinosis, chondrodysplasia, collagenopathies, osteochondritis dissecans, relapsing polychondritis, and skeletal dysplasias (*91*). Not only do these diseases range in severity, but they also range in onset – from developmental to degenerative disease. The large variety of cartilage diseases require research into their mechanisms, symptoms, treatment, and regenerative therapies. Here, we describe the most common cartilage disorder family, arthritis, and a family of developmental disorders, skeletal dysplasia.

1.4.1 Arthritis

Arthritis is a family of diseases that causes pain, swelling, and loss of motion of the diarthrodial joints (*92, 93*). It has been reported as one of the top three leading causes of pain and disability

across the United States (*94*). Arthritis currently affects at least 54 million adults in the United States (*95*), and the number is expected to rise with the aging, obese population (*12, 92*). Furthermore, it was estimated that by 2040 the number of adults affected by arthritis will increase to 78.4% in the US with 11.4% of the total population suffering from activity-limiting arthritis (*96*). As of 2007, arthritis cost the US $128 billion (direct medical and indirect losses combined) (*97*), and with incidence continuing to rise, so will the cost (*12, 92*). Beyond the costs and disability caused by arthritis, it is associated with many comorbidities including heart disease, respiratory disease, diabetes, and obesity (*92, 98*). Moreover, 31% of patients with arthritis also reported having anxiety (*99*), and 27% (compared to 12% without arthritis) reported fair to poor health-related quality of life (*100*).

Arthritis is typically diagnosed through repeated doctor's appointments using radiographs, looking for erosion and boney spurs, and self-reported joint pain, inflammation, and stiffness (*92, 101*). In fact, inflammation is the primary driver of disease onset, as the avascular and aneural environment leaves cartilage more susceptible to inflammatory degeneration without the ability to regenerate (*8, 92, 93, 102*). The degeneration, erosion, and cracking of articular cartilage occurs as collagen and proteoglycans are degraded by aggrecanases and matrix metalloproteinases (MMPs) stimulated by inflammatory cytokines interluekin-1 beta, -6, and -8 (IL-1β, IL-6, IL-8) and tumor necrosis factor alpha (TNFα) (*9, 16, 17, 19, 20, 30, 92, 97, 103*). Systemic, inflammatory flares occur in rheumatoid arthritis (RA), an autoimmune disease with a prevalence of 1% that affects women more often (*93, 104*). In osteoarthritis (OA), inflammation is caused by metabolic and biomechanical factors (*17, 22, 32, 102, 103, 105, 106*). Risk factors include age (*107*), female sex (*108*), genetics (*108*), obesity (*22*), and injury (*92, 103, 109, 110*). Despite the homeostatic benefits of physiologic loading (*17, 24, 25, 28*), injurious loading (i.e.,

greater than 35% strain) increases chondrocyte catabolism leading to post-traumatic OA (PTOA) (*17, 103*). In fact, prevalence of PTOA is higher in the younger population and risk increases to approximately 50% after traumatic injury that results in misalignment of the joint (e.g., ligament or meniscal tears) (*103, 109, 111*).

There is no cure for arthritis, and treatments are limited. Patients are encouraged to lose weight and exercise to reduce systemic inflammation. In mild cases, treatments include non-steroidal anti-inflammatories, which treat disease-induced pain short term (*17, 92, 97*). Disease-modifying antirheumatic drugs have been developed to treat RA; however, they are effective in only a fraction of individuals and have been associated with significant side effects (*93*). As the arthritis progresses, surgery and total joint arthroplasty becomes an option (*92, 101*), but the surgery has a dissatisfaction rate of up to 20% (*112*). Additionally, joint replacements have a limited lifespan, increasing the number of revisions and decreasing their effectiveness in younger populations (*113, 114*). Therefore, there is a critical need for treatment and therapeutics for arthritis.

1.4.2 Skeletal dysplasias

Skeletal dysplasias are a group of over 450 bone and cartilage diseases including achondroplasia, type 2 collagenopathies, osteogenesis imperfecta, brachyolmia, spondylometaphyseal dysplasia Kozlowski, and metatropic dysplasia (*115-118*). The diseases, which range in severity from moderate to neonatally lethal, are characterized by disproportionate stature and bones (*116*). With a birth incidence of 1 in 5000 (*119*), the dysplasias can be diagnosed prenatally with radiographic evidence of disproportion followed by skeletal surveying, histopathology, and molecular genetic testing (*115-118*). Early diagnosis, especially in severe or lethal incidences, is important for family counseling and immediate stabilization of the airway and respiratory status

upon birth to prevent death due to small chest size, pulmonary restriction, and cardiopulmonary compromise (*75, 116*). In non-lethal cases, the patient requires a multidisciplinary team to assess, diagnose, treat, and manage orthopedic, neurologic, auditory, visual, pulmonary, cardiac, renal, and psychological complications (*116, 120*). Skeletal dysplasia patients may require physical therapy and surgical intervention throughout their life (*121-123*). Additionally, a study showed that depression and anxiety, often associated with pain, is present in 34% and 31% of patients with skeletal dysplasia, respectively, representing the need for pain management and mental health counseling (*124*).

The heterogenous phenotypes of skeletal dysplasias is inherent to the cause of this family of diseases: genetic mutations. Skeletal dysplasia-causing mutations occur in ECM proteins, transcription factors, tumor suppressors, signal transducers, cellular transporters, and growth factor receptors (*116, 120*). A common location of these mutations is transient receptor vanilloid 4 (TRPV4), a non-selective cation channel. These mutations cause a spectrum of skeletal dysplasias, including autosomal-dominant brachyolmia and metatropic dysplasia, among other diseases (*55*). Autosomal-dominant brachyolmia is caused by a gain-of-function mutation in the transmembrane 5 pore region of TRPV4 caused by an exon 12 858G>A transition encoding a V620I substitution (*55, 70, 125*). The moderate dysplasia exhibits a phenotype of moderately short stature, mildly short limbs, mild brachydactyly, scoliosis, flattened and irregular vertebra, mild irregularities in metaphyses, and delayed epiphyseal and carpal ossification (*70, 125, 126*). In contrast, metatropic dysplasia is caused by a mutation in the cytoplasmic NH_2 end protein domain of TRPV4 caused by an exon 2 C366>T transition encoding a T89I substitution (*55, 75, 125*). Some studies have shown the T89I mutation to be gain-of-function (*126, 127*), while other reports have claimed it does not cause a change in conductivity (*55, 125*). This severe dysplasia

can be neonatally lethal and exhibits a phenotype of short extremities, dumbbell-shaped long bones with widened metaphyses, elongated and narrow trunk, scoliosis, flat vertebral bodies, joint contractures, prominent forehead, squared-off jaw, and brachydactyly with delayed carpal ossification (*75, 125*). Histological analysis of brachyolmia and metatropic dysplasia have shown disorganized, hypertrophic chondrocytes and cartilage islands among bone, indicating dysregulation of endochondral ossification and skeletal development to be an underlying cause of the diseases (*75, 116, 120*). It was hypothesized that increased TRPV4 signaling prevented proper endochondral ossification through an upregulated expression of follistatin, a potent BMP antagonist, a potential underlying cause of these conditions (*127-129*).

1.5 Tissue-Engineered Cartilage

Tissue-engineered cartilage provides opportunities for regenerative therapies, particularly for degenerative diseases such as arthritis. Furthermore, it can serve as an *in vitro* disease model for drug screening and as a tool for the elucidation of underlying mechanisms of cartilage diseases. To engineer cartilage, one needs a chondrocyte source, a 3D scaffold or environment, and chondrogenic medium. As the chondrocytes are cultured, they will synthesize the cartilaginous ECM, thus producing tissue-engineered cartilage. An advantage of using cartilage in the tissue engineering field is that it does not have any other cell types, such as vasculature. However, the unique composition and organization of the chondrocytes and ECM, which produces its impressive mechanical properties, poses much more of a challenge.

1.5.1 Cell sources

Studies have used a range of cell types for the chondrocyte cell source including primary chondrocytes and chondrocytes derived from adult multipotent stem cells and pluripotent stem cells (*14*). Primary chondrocytes eliminate *in vitro* chondrogenic differentiation as they are

already able to synthesize a cartilaginous matrix in 3D (*130*). However, their limited expansion potential paired with dedifferentiation during monolayer passaging limits their applicability (*130*). Furthermore, they are difficult to obtain due to donor site morbidity and limited cadaveric and surgical waste sources (*14*).

Therefore, most tissue engineering studies differentiate stem cells into chondrocytes. One of the most common sources are adult multipotent stem cells, such as mesenchymal stem cells (MSCs) and adipose-derived stem cells (ASCs). Chondrogenesis protocols for these cell types have been successfully optimized to produce robust cartilage-like tissue (*131-135*). While ASCs are isolated from adipose tissue, such as during liposuction (*131*), MSCs are typically isolated from adult bone marrow, an invasive process (*1, 135*). A drawback to this method, however, is it is well-recognized that adult stem cells are a heterogenous cell population with significant donor-to-donor variability and limited proliferation and differentiation potential after long-term expansion *in vitro* (*135-139*).

Pluripotent stem cells solve these problems with their high proliferation and differentiation capacities, which also provide the opportunity for gene editing (*140, 141*). Embryonic stem cells (ESCs) are derived from embryos prior to implantation, which may raise ethical concerns or be restricted in some places (*142*). However, adult somatic cells, such as fibroblasts, can be reprogrammed into a pluripotent state by defined transcriptional factors providing patient-specific cells with low to no donor morbidity (*140-143*). These reprogramed cells are known as induced pluripotent stem cells (iPSCs) and behave comparably to ESCs in terms of proliferation and differentiation (*136, 140-143*).

1.5.2 hiPSC chondrogenesis

Previously our lab developed a chondrogenic differentiation protocol for mouse iPSCs (*144*);

however, human cells have remained a larger challenge for the field. Using a variety of growth factor and morphogen combinations and chondrogenic medium solutions, several studies have reported protocols for differentiating human iPSCs (hiPSCs) into chondrocytes (*1, 136, 145-152*). Unfortunately, the methods are time consuming, have modest expression of chondrogenic genes, have irregular chondrocyte morphology, do not follow developmental pathways, or are difficult to reproduce. For example, many methods rely on the use of fetal bovine serum (FBS) in their medium to increase cell viability; however, FBS has extensive lot-to-lot variability preventing consistency and reproducibility.

Therefore, we aimed to develop a serum-free, chemically-defined chondrogenic differentiation protocol for hiPSCs. Using the newly elucidated temporal sequence of signaling cues required for stem cell differentiation across various lineages *in vivo* (*146*) and previous *in vitro* reports of stem cell chondrogenic differentiation (*144, 153, 154*), we developed a stepwise protocol for hiPSC differentiation following the paraxial mesodermal lineage (*155*). The protocol differentiates sclerotome cells into chondroprogenitors with bone morphogenic protein 4 (BMP4), similar to mesenchymal condensation during development (*155, 156*). Chondroprogenitors are then treated with transforming growth factor beta 3 (TGFβ3) to stimulate chondrogenesis (*144, 145, 148, 155, 157-159*). Given the chondrogenic requirement for a 3D environment, this protocol uses a conventional 3D pellet culture system (*9, 159*). With this culture system, chondroprogenitors are centrifuged in a tube to form a spherical construct, or "pellet," over multiple weeks growing in diameter as the cells differentiate and produce cartilaginous matrix. After 28 days in pellet culture, tissue-engineered cartilage matrix synthesized by hiPSC-derived chondrocytes has formed (*155*). Unfortunately, this protocol, among others has resulted in significant and unpredictable cellular and matrix heterogeneity

(*155, 160, 161*).

1.6 *In Vitro* Disease Modeling and Therapeutic Development

Tissue-engineered cartilage, particularly from hiPSCs, provides opportunities for *in vitro* disease modeling, genetic engineering, gene therapy, and drug development and validation (*162-172*). Genetic engineering tools such as clustered regularly interspaced short palindromic repeats (CRISPR) and the CRISPR-associated protein (Cas9) are valuable tools for disease modeling (*173*). For example, hiPSCs can be derived from adult patients with a genetic disorder, and the mutation can be corrected using CRISPR-Cas9 technology to create an isogenic control (*140, 141, 163, 173*). If patient samples are not available, CRISPR-Cas9 can be used to create the mutation in a control line (*140, 141, 163, 173*). After the development of mutant and isogenic lines, scientists can study the effects of the mutation on chondrogenesis and cartilage homeostasis. Additionally, diseased environments can be simulated using hiPSC-derived chondrocyte culture, such as the introduction of inflammatory cytokines to mimic arthritis (*162*). This system has pharmaceutical potential, as patient-specific, genetically engineered, or diseased hiPSC-derived chondrocytes can be used for drug development, and the large volumes produced provide the opportunity for high throughput screening.

Beyond disease modeling, hiPSC-derived chondrocytes are useful for elucidating the mechanisms driving or repressing chondrogenesis and regulating cartilage homeostasis (e.g., mechanical forces) (*26*). These findings will not only answer fundamental questions regarding chondrocyte biology, but they will provide insights into optimizing tissue engineering strategies for regenerative therapeutics. Moreover, our lab has developed stem cells modified for autonomous regenerative therapy (i.e., self-regulating "SMART" cells) harnessing synthetic biology to create cell-based therapies in murine iPSCs, which could be translated to human cells

in the future (*84, 174-176*).

1.7 Summary

Due to the importance of articular cartilage to skeletal development and joint loading, we developed an hiPSC chondrogenic differentiation protocol as a tool to study chondrogenesis and cartilage homeostasis. Unfortunately, there was cellular and matrix heterogeneity in the tissue-engineered cartilage. To address this, we applied two strategies: cell sorting and inhibition of off-target pathways. In the first method, CD146, CD166, and PDGFRβ were identified as pro-chondrogenic surface markers in hiPSC-derived chondroprogenitor cells as described in Chapter 2. In the second method, we used next-generation sequencing to identify wingless/integrated (Wnt) and melanocyte inducing transcription factor (MITF) signaling as the drivers of off-target differentiation. We found inhibition of these factors during chondrogenesis significantly improved the protocol and resulted in homogenous, robust tissue-engineered cartilage as described in Chapter 3 and 4. Next, we applied this protocol to a disease modeling application. We differentiated hiPSCs harboring skeletal dysplasia-causing TRPV4 mutations into chondrocytes to study the effects on TRPV4 function, chondrogenesis, and chondrocyte hypertrophy and on TRPV4 mechanotransduction, as described in Chapters 5 and 6, respectively. The findings from the disease modeling studies provide insights into therapeutic targets for mild brachyolmia and severe metatropic dysplasia. Furthermore, the hiPSC chondrogenesis protocol can be applied to other disease models, such as osteoarthritis risk mutations in type VI collagen, and tissue engineering studies. This thesis is summarized in Figure 1.1.
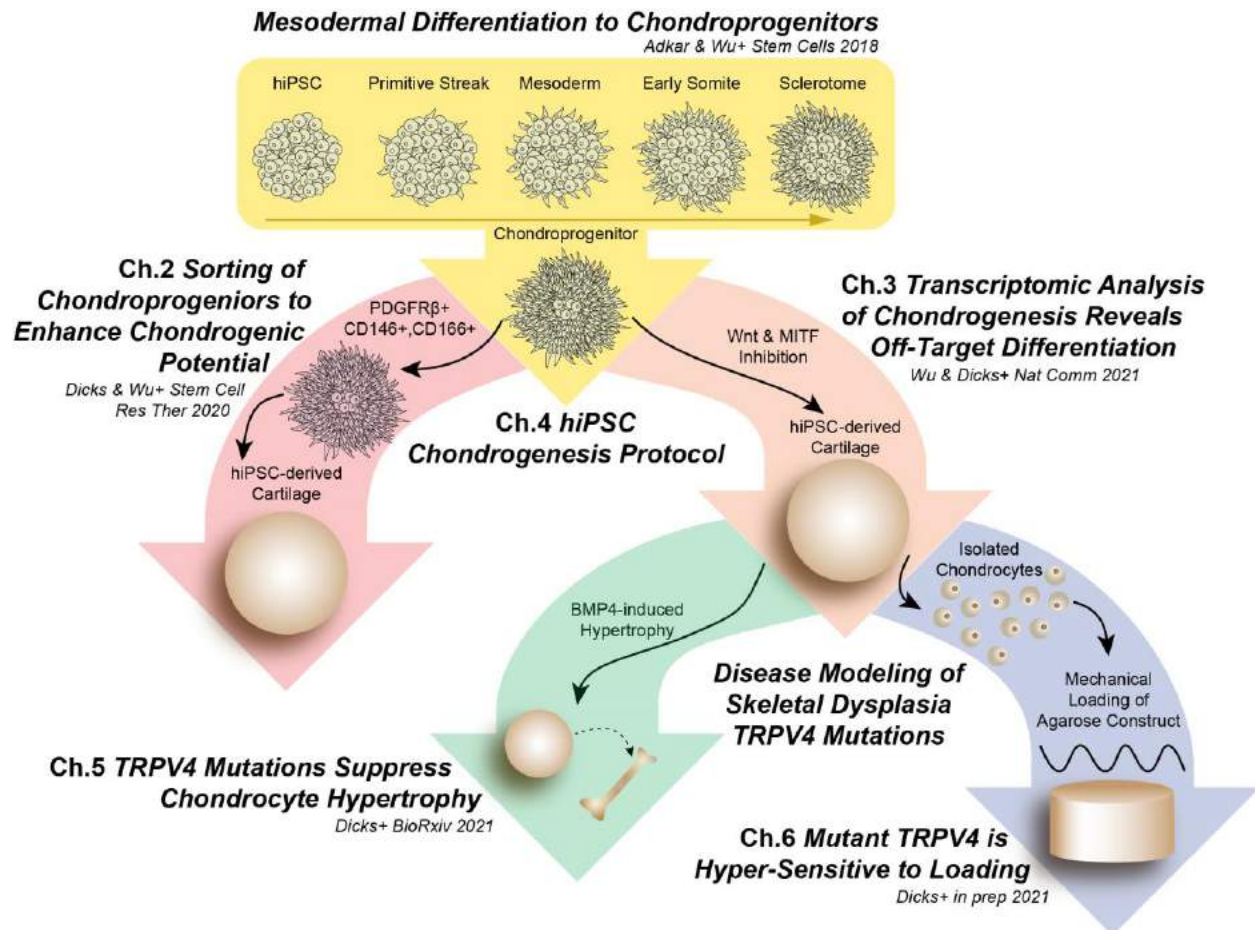
Figure 1.1 Representation of the thesis chapters and their integration. We developed a protocol to derive chondroprogenitors; however, they produced heterogenous hiPSC-derived cartilage. Therefore, we enhanced chondrogenesis through cell sorting or inhibition of off-target pathways. Then using the improved chondrogenesis protocol, we used hiPSC-derived cartilage for disease modeling of skeletal dysplasia-causing TRPV4 mutations. We found the mutations suppress chondrocyte hypertrophy but increase sensitivity to physiologic loading.

1.8 References

1. L. Wu *et al.*, Human developmental chondrogenesis as a basis for engineering chondrocytes from pluripotent stem cells. *Stem Cell Reports* **1**, 575-589 (2013).

2. G. Breeland, M. A. Sinkler, R. G. Menezes, *Embryology, Bone Ossification*. (Treasure Island (FL): StatPearls Publishing, SttatPearls (Internet), 2021).

3. H. Akiyama, Control of chondrogenesis by the transcription factor Sox9. *Mod Rheumatol* **18**, 213-219 (2008).

4. Y. Kamachi, M. Uchikawa, H. Kondoh, Pairing SOX off: with partners in the regulation of embryonic development. *Trends Genet* **16**, 182-187 (2000).

5. T. Furumatsu, T. Ozaki, Epigenetic regulation in chondrogenesis. *Acta Med Okayama* **64**,

155-161 (2010).

6. R. Nishimura *et al.*, Regulation of endochondral ossification by transcription factors. *Front Biosci (Landmark Ed)* **17**, 2657-2666 (2012).

7. C. Prein, F. Beier, ECM signaling in cartilage development and endochondral ossification. *Curr Top Dev Biol* **133**, 25-47 (2019).

8. A. J. Sophia Fox, A. Bedi, S. A. Rodeo, The basic science of articular cartilage: structure, composition, and function. *Sports Health* **1**, 461-468 (2009).

9. Z. Lin, C. Willers, J. Xu, M. H. Zheng, The chondrocyte: biology and clinical application. *Tissue Eng* **12**, 1971-1984 (2006).

10. F. Guilak, C. Hung, V. Mow, R. Huiskes, Basic orthopaedic biomechanics and mechano-biology. (2005).

11. A. C. Shieh, K. A. Athanasiou, Principles of cell mechanics for cartilage tissue engineering. *Ann Biomed Eng* **31**, 1-11 (2003).

12. J. M. Mansour, in *Kinesiology: The Mechanics and Pathomechanics of Human Movement*. (2003), vol. 2e, chap. 5, pp. 66-75.

13. Y. Xia *et al.*, in *Biophysics and Biochemistry of Cartilage by NMR and MRI*. (The Royal Society of Chemistry, 2017), pp. 1-43.

14. L. Zhang, J. Hu, K. A. Athanasiou, The role of tissue engineering in articular cartilage repair and regeneration. *Crit Rev Biomed Eng* **37**, 1-57 (2009).

15. C. J. Little, N. K. Bawolin, X. Chen, Mechanical properties of natural cartilage and tissue-engineered constructs. *Tissue Eng Part B Rev* **17**, 213-227 (2011).

16. J. Bleuel, F. Zaucke, G. P. Bruggemann, A. Niehoff, Effects of cyclic tensile strain on chondrocyte metabolism: a systematic review. *PLoS One* **10**, e0119816 (2015).

17. J. Sanchez-Adams, H. A. Leddy, A. L. McNulty, C. J. O'Conor, F. Guilak, The mechanobiology of articular cartilage: bearing the burden of osteoarthritis. *Curr Rheumatol Rep* **16**, 451 (2014).

18. N. J. Kuiper, A. Sharma, A detailed quantitative outcome measure of glycosaminoglycans in human articular cartilage for cell therapy and tissue engineering strategies. *Osteoarthritis Cartilage* **23**, 2233-2241 (2015).

19. S. Agarwal *et al.*, Role of NF-kappaB transcription factors in antiinflammatory and proinflammatory actions of mechanical signals. *Arthritis Rheum* **50**, 3541-3548 (2004).

20. C. Chen *et al.*, Cyclic Equibiaxial Tensile Strain Alters Gene Expression of Chondrocytes via Histone Deacetylase 4 Shuttling. *PLoS One* **11**, e0154951 (2016).

21. G. Ofek, R. M. Natoli, K. A. Athanasiou, In situ mechanical properties of the chondrocyte cytoplasm and nucleus. *J Biomech* **42**, 873-877 (2009).

22. F. Guilak, Biomechanical factors in osteoarthritis. *Best Pract Res Clin Rheumatol* **25**, 815-823 (2011).

23. F. Eckstein, M. Hudelmaier, R. Putz, The effects of exercise on human articular cartilage. *J Anat* **208**, 491-512 (2006).

24. C. Chen, D. T. Tambe, L. Deng, L. Yang, Biomechanical properties and mechanobiology of the articular chondrocyte. *Am J Physiol Cell Physiol* **305**, C1202-1208 (2013).

25. E. Kim, F. Guilak, M. A. Haider, The dynamic mechanical environment of the chondrocyte: a biphasic finite element model of cell-matrix interactions under cyclic compressive loading. *J Biomech Eng* **130**, 061009 (2008).

26. C. J. O'Conor, N. Case, F. Guilak, Mechanical regulation of chondrogenesis. *Stem Cell Res Ther* **4**, 61 (2013).

27. Z. Zhao *et al.*, Mechanotransduction pathways in the regulation of cartilage chondrocyte homoeostasis. *Journal of Cellular and Molecular Medicine* **24**, 5408-5419 (2020).

28. L. G. Alexopoulos, L. A. Setton, F. Guilak, The biomechanical role of the chondrocyte pericellular matrix in articular cartilage. *Acta Biomater* **1**, 317-325 (2005).

29. D. Ma *et al.*, Hydrostatic Compress Force Enhances the Viability and Decreases the Apoptosis of Condylar Chondrocytes through Integrin-FAK-ERK/PI3K Pathway. *Int J Mol Sci* **17**, (2016).

30. S. Madhavan *et al.*, Biomechanical signals exert sustained attenuation of proinflammatory gene induction in articular chondrocytes. *Osteoarthritis Cartilage* **14**, 1023-1032 (2006).

31. R. E. Wilusz, J. Sanchez-Adams, F. Guilak, The structure and function of the pericellular matrix of articular cartilage. *Matrix Biol* **39**, 25-32 (2014).

32. F. Guilak, R. J. Nims, A. Dicks, C. L. Wu, I. Meulenbelt, Osteoarthritis as a disease of the cartilage pericellular matrix. *Matrix Biol* **71-72**, 40-50 (2018).

33. C. A. Poole, Articular cartilage chondrons: form, function and failure. *J Anat* **191 (Pt 1)**, 1-13 (1997).

34. I. Youn, J. B. Choi, L. Cao, L. A. Setton, F. Guilak, Zonal variations in the three-dimensional morphology of the chondron measured in situ using confocal microscopy. *Osteoarthritis Cartilage* **14**, 889-897 (2006).

35. E. M. Darling, R. E. Wilusz, M. P. Bolognesi, S. Zauscher, F. Guilak, Spatial mapping of the biomechanical properties of the pericellular matrix of articular cartilage measured in situ via atomic force microscopy. *Biophys J* **98**, 2848-2856 (2010).

36. J. P. White *et al.*, TRPV4: Molecular Conductor of a Diverse Orchestra. *Physiol Rev* **96**, 911-973 (2016).

37. Z. Deng *et al.*, Cryo-EM and X-ray structures of TRPV4 reveal insight into ion permeation and gating mechanisms. *Nature Structural & Molecular Biology* **25**, 252-260 (2018).

38. A. Mizuno, N. Matsumoto, M. Imai, M. Suzuki, Impaired osmotic sensation in mice lacking TRPV4. *Am J Physiol Cell Physiol* **285**, C96-101 (2003).

39. W. Liedtke *et al.*, Vanilloid receptor-related osmotically activated channel (VR-OAC), a candidate vertebrate osmoreceptor. *Cell* **103**, 525-535 (2000).

40. W. Liedtke, J. M. Friedman, Abnormal osmotic regulation in trpv4-/- mice. *Proc Natl Acad Sci U S A* **100**, 13698-13703 (2003).

41. R. Strotmann, C. Harteneck, K. Nunnenmacher, G. Schultz, T. D. Plant, OTRPC4, a

nonselective cation channel that confers sensitivity to extracellular osmolarity. *Nat Cell Biol* **2**, 695-702 (2000).

42. B. Nilius, A. Szallasi, Transient receptor potential channels as drug targets: from the science of basic research to the art of medicine. *Pharmacol Rev* **66**, 676-814 (2014).

43. W. Everaerts, B. Nilius, G. Owsianik, The vanilloid transient receptor potential channel TRPV4: From structure to disease. *Progress in Biophysics and Molecular Biology* **103**, 2-17 (2010).

44. R. Masuyama *et al.*, TRPV4-mediated calcium influx regulates terminal differentiation of osteoclasts. *Cell Metab* **8**, 257-265 (2008).

45. S. K. Sonkusare *et al.*, Elementary Ca2+ signals through endothelial TRPV4 channels regulate vascular function. *Science* **336**, 597-601 (2012).

46. L. Ye *et al.*, TRPV4 is a regulator of adipose oxidative metabolism, inflammation, and energy homeostasis. *Cell* **151**, 96-110 (2012).

47. N. Alessandri-Haber *et al.*, Transient receptor potential vanilloid 4 is essential in chemotherapy-induced neuropathic pain in the rat. *J Neurosci* **24**, 4444-4452 (2004).

48. N. Alessandri-Haber *et al.*, Hypotonicity induces TRPV4-mediated nociception in rat. *Neuron* **39**, 497-511 (2003).

49. A. D. Guler *et al.*, Heat-evoked activation of the ion channel, TRPV4. *J Neurosci* **22**, 6408-6414 (2002).

50. H. Watanabe *et al.*, Heat-evoked activation of TRPV4 channels in a HEK293 cell expression system and in native mouse aorta endothelial cells. *J Biol Chem* **277**, 47044-47051 (2002).

51. X. Gao, L. Wu, R. G. O'Neil, Temperature-modulated diversity of TRPV4 channel gating: activation by physical stresses and phorbol ester derivatives through protein kinase C-dependent and -independent pathways. *J Biol Chem* **278**, 27129-27137 (2003).

52. R. Kohler *et al.*, Evidence for a functional role of endothelial transient receptor potential V4 in shear stress-induced vasodilatation. *Arterioscler Thromb Vasc Biol* **26**, 1495-1502 (2006).

53. C. J. O'Conor, H. A. Leddy, H. C. Benefield, W. B. Liedtke, F. Guilak, TRPV4-mediated mechanotransduction regulates the metabolic response of chondrocytes to dynamic loading. *Proc Natl Acad Sci U S A* **111**, 1316-1321 (2014).

54. M. Jin *et al.*, Determinants of TRPV4 Activity following Selective Activation by Small Molecule Agonist GSK1016790A. *PLoS ONE* **6**, e16713 (2011).

55. S. Sun, in *Mutagenesis,* Kang, Ed. (InTech, 2012).

56. B. Nilius, T. Voets, The puzzle of TRPV4 channelopathies. *EMBO Rep* **14**, 152-163 (2013).

57. W. Tian *et al.*, A loss-of-function nonsynonymous polymorphism in the osmoregulatory TRPV4 gene is associated with human hyponatremia. *Proc Natl Acad Sci U S A* **106**, 14034-14039 (2009).

58. G. Zhu *et al.*, Association of TRPV4 gene polymorphisms with chronic obstructive pulmonary disease. *Hum Mol Genet* **18**, 2053-2062 (2009).

59. J. Dai *et al.*, TRPV4-pathy, a novel channelopathy affecting diverse systems. *J Hum Genet* **55**, 400-402 (2010).

60. C. J. Frijns, J. Van Deutekom, R. R. Frants, F. G. Jennekens, Dominant congenital benign spinal muscular atrophy. *Muscle Nerve* **17**, 192-197 (1994).

61. M. E. McEntagart *et al.*, Confirmation of a hereditary motor and sensory neuropathy IIC locus at chromosome 12q23-q24. *Ann Neurol* **57**, 293-297 (2005).

62. M. Auer-Grumbach *et al.*, Alterations in the ankyrin domain of TRPV4 cause congenital distal SMA, scapuloperoneal SMA and HMSN2C. *Nat Genet* **42**, 160-164 (2010).

63. P. J. Dyck *et al.*, Hereditary motor and sensory neuropathy with diaphragm and vocal cord paresis. *Ann Neurol* **35**, 608-615 (1994).

64. M. Donaghy, R. Kennett, Varying occurrence of vocal cord paralysis in a family with autosomal dominant hereditary motor and sensory neuropathy. *J Neurol* **246**, 552-555 (1999).

65. C. J. Klein *et al.*, TRPV4 mutations and cytotoxic hypercalcemia in axonal Charcot-Marie-Tooth neuropathies. *Neurology* **76**, 887-894 (2011).

66. D. H. Chen *et al.*, CMT2C with vocal cord paresis associated with short stature and mutations in the TRPV4 gene. *Neurology* **75**, 1968-1975 (2010).

67. G. Landoure *et al.*, Mutations in TRPV4 cause Charcot-Marie-Tooth disease type 2C. *Nat Genet* **42**, 170-174 (2010).

68. H. X. Deng *et al.*, Scapuloperoneal spinal muscular atrophy and CMT2C are allelic disorders caused by alterations in TRPV4. *Nat Genet* **42**, 165-169 (2010).

69. S. R. Lamande *et al.*, Mutations in TRPV4 cause an inherited arthropathy of hands and feet. *Nat Genet* **43**, 1142-1146 (2011).

70. M. J. Rock *et al.*, Gain-of-function mutations in TRPV4 cause autosomal dominant brachyolmia. *Nat Genet* **40**, 999-1003 (2008).

71. D. Krakow *et al.*, Mutations in the gene encoding the calcium-permeable ion channel TRPV4 produce spondylometaphyseal dysplasia, Kozlowski type and metatropic dysplasia. *Am J Hum Genet* **84**, 307-315 (2009).

72. S. Unger *et al.*, Fetal akinesia in metatropic dysplasia: The combined phenotype of chondrodysplasia and neuropathy? *Am J Med Genet A* **155A**, 2860-2864 (2011).

73. M. Beck, M. Roubicek, J. G. Rogers, P. Naumoff, J. Spranger, Heterogeneity of metatropic dysplasia. *Eur J Pediatr* **140**, 231-237 (1983).

74. S. D. Boden *et al.*, Metatropic dwarfism. Uncoupling of endochondral and perichondral growth. *J Bone Joint Surg Am* **69**, 174-184 (1987).

75. N. Camacho *et al.*, Dominant TRPV4 mutations in nonlethal and lethal metatropic dysplasia. *Am J Med Genet A* **152A**, 1169-1177 (2010).

76. J. Dai *et al.*, Novel and recurrent TRPV4 mutations and their association with distinct phenotypes within the TRPV4 dysplasia family. *J Med Genet* **47**, 704-709 (2010).

77. A. N. Doman, P. Maroteaux, E. D. Lyne, Spondyloepiphyseal dysplasia of Maroteaux. *J*

Bone Joint Surg Am **72**, 1364-1369 (1990).

78. A. Megarbane, P. Maroteaux, C. Caillaud, M. Le Merrer, Spondyloepimetaphyseal dysplasia of Maroteaux (pseudo-Morquio type II syndrome): report of a new patient and review of the literature. *Am J Med Genet A* **125A**, 61-66 (2004).

79. G. Nishimura *et al.*, Spondylo-epiphyseal dysplasia, Maroteaux type (pseudo-Morquio syndrome type 2), and parastremmatic dysplasia are caused by TRPV4 mutations. *Am J Med Genet A* **152A**, 1443-1449 (2010).

80. G. Nishimura *et al.*, Spondyloepiphyseal dysplasia Maroteaux type: report of three patients from two families and exclusion of type II collagen defects. *Am J Med Genet A* **120A**, 498-502 (2003).

81. L. O. Langer, D. Petersen, J. Spranger, An unusual bone dysplasia: parastremmatic dwarfism. *Am J Roentgenol Radium Ther Nucl Med* **110**, 550-560 (1970).

82. S. Muramatsu *et al.*, Functional gene screening system identified TRPV4 as a regulator of chondrogenic differentiation. *J Biol Chem* **282**, 32158-32167 (2007).

83. C. J. O'Conor, T. M. Griffin, W. Liedtke, F. Guilak, Increased susceptibility of Trpv4-deficient mice to obesity and obesity-induced osteoarthritis with very high-fat diet. *Ann Rheum Dis* **72**, 300-304 (2013).

84. R. J. Nims *et al.*, A synthetic mechanogenetic gene circuit for autonomous drug delivery in engineered tissues. *Sci Adv* **7**, (2021).

85. S. Woods *et al.*, Regulation of TGFbeta Signalling by TRPV4 in Chondrocytes. *Cells* **10**, (2021).

86. M. N. Phan *et al.*, Functional characterization of TRPV4 as an osmotically sensitive ion channel in porcine articular chondrocytes. *Arthritis Rheum* **60**, 3028-3037 (2009).

87. M. Lv *et al.*, Calcium signaling of in situ chondrocytes in articular cartilage under compressive loading: Roles of calcium sources and cell membrane ion channels. *J Orthop Res* **36**, 730-738 (2018).

88. M. R. Servin-Vences, M. Moroni, G. R. Lewin, K. Poole, Direct measurement of TRPV4 and PIEZO1 activity reveals multiple mechanotransduction pathways in chondrocytes. *Elife* **6**, (2017).

89. A. L. Clark, B. J. Votta, S. Kumar, W. Liedtke, F. Guilak, Chondroprotective role of the osmotically sensitive ion channel transient receptor potential vanilloid 4: age- and sex-dependent progression of osteoarthritis in Trpv4-deficient mice. *Arthritis Rheum* **62**, 2973-2983 (2010).

90. C. J. O'Conor *et al.*, Cartilage-Specific Knockout of the Mechanosensory Ion Channel TRPV4 Decreases Age-Related Osteoarthritis. *Sci Rep* **6**, 29053 (2016).

91. Y. Krishnan, A. J. Grodzinsky, Cartilage diseases. *Matrix Biol* **71-72**, 51-69 (2018).

92. F. C. Breedveld, Osteoarthritis--the impact of a serious disease. *Rheumatology (Oxford)* **43 Suppl 1**, i4-8 (2004).

93. J. S. Smolen, D. Aletaha, I. B. McInnes, Rheumatoid arthritis. *Lancet* **388**, 2023-2038 (2016).

94. K. A. Theis, D. W. Roblin, C. G. Helmick, R. Luo, Prevalence and causes of work disability among working-age U.S. adults, 2011-2013, NHIS. *Disabil Health J* **11**, 108-115 (2018).

95. K. E. Barbour *et al.*, Geographic Variations in Arthritis Prevalence, Health-Related Characteristics, and Management - United States, 2015. *MMWR Surveill Summ* **67**, 1-28 (2018).

96. J. M. Hootman, C. G. Helmick, K. E. Barbour, K. A. Theis, M. A. Boring, Updated Projected Prevalence of Self-Reported Doctor-Diagnosed Arthritis and Arthritis-Attributable Activity Limitation Among US Adults, 2015-2040. *Arthritis Rheumatol* **68**, 1582-1587 (2016).

97. V. Y. Ma, L. Chan, K. J. Carruthers, Incidence, prevalence, costs, and impact on disability of common conditions requiring rehabilitation in the United States: stroke, spinal cord injury, traumatic brain injury, multiple sclerosis, osteoarthritis, rheumatoid arthritis, limb loss, and back pain. *Arch Phys Med Rehabil* **95**, 986-995 e981 (2014).

98. K. E. Barbour, C. G. Helmick, M. Boring, T. J. Brady, Vital Signs: Prevalence of Doctor-Diagnosed Arthritis and Arthritis-Attributable Activity Limitation - United States, 2013-2015. *MMWR Morb Mortal Wkly Rep* **66**, 246-253 (2017).

99. L. B. Murphy, J. J. Sacks, T. J. Brady, J. M. Hootman, D. P. Chapman, Anxiety and depression among US adults with arthritis: prevalence and correlates. *Arthritis Care Res (Hoboken)* **64**, 968-976 (2012).

100. S. E. Furner, J. M. Hootman, C. G. Helmick, J. Bolen, M. M. Zack, Health-related quality of life of US adults with arthritis: analysis of data from the behavioral risk factor surveillance system, 2003, 2005, and 2007. *Arthritis Care Res (Hoboken)* **63**, 788-799 (2011).

101. R. L. Taruc-Uy, S. A. Lynch, Diagnosis and treatment of osteoarthritis. *Prim Care* **40**, 821-836, vii (2013).

102. F. Berenbaum, T. M. Griffin, R. Liu-Bryan, Review: Metabolic Regulation of Inflammation in Osteoarthritis. *Arthritis Rheumatol* **69**, 9-21 (2017).

103. J. Lieberthal, N. Sambamurthy, C. R. Scanzello, Inflammation in joint injury and post-traumatic osteoarthritis. *Osteoarthritis Cartilage* **23**, 1825-1834 (2015).

104. T. K. Kvien, Epidemiology and burden of illness of rheumatoid arthritis. *PharmacoEconomics* **22**, 1-12 (2004).

105. A. Courties, J. Sellam, F. Berenbaum, Metabolic syndrome-associated osteoarthritis. *Curr Opin Rheumatol* **29**, 214-222 (2017).

106. B. O. Diekman, F. Guilak, Stem cell-based therapies for osteoarthritis: challenges and opportunities. *Curr Opin Rheumatol* **25**, 119-126 (2013).

107. J. A. Martin, J. A. Buckwalter, Roles of articular cartilage aging and chondrocyte senescence in the pathogenesis of osteoarthritis. *Iowa Orthop J* **21**, 1-7 (2001).

108. T. D. Spector, F. Cicuttini, J. Baker, J. Loughlin, D. Hart, Genetic influences on osteoarthritis in women: a twin study. *BMJ* **312**, 940-943 (1996).

109. L. Punzi *et al.*, Post-traumatic arthritis: overview on pathogenic mechanisms and role of inflammation. *RMD Open* **2**, e000279 (2016).

110. C. Palazzo, C. Nguyen, M. M. Lefevre-Colau, F. Rannou, S. Poiraudeau, Risk factors and burden of osteoarthritis. *Ann Phys Rehabil Med* **59**, 134-138 (2016).

111. L. S. Lohmander, P. M. Englund, L. L. Dahl, E. M. Roos, The long-term consequence of anterior cruciate ligament and meniscus injuries: osteoarthritis. *Am J Sports Med* **35**, 1756-1769 (2007).

112. B. D. Springer, W. M. Sotile, The Psychology of Total Joint Arthroplasty. *J Arthroplasty* **35**, S46-S49 (2020).

113. K. T. Kim *et al.*, Causes of failure after total knee arthroplasty in osteoarthritis patients 55 years of age or younger. *Knee Surg Relat Res* **26**, 13-19 (2014).

114. S. Kurtz, K. Ong, E. Lau, F. Mowat, M. Halpern, Projections of primary and revision hip and knee arthroplasty in the United States from 2005 to 2030. *J Bone Joint Surg Am* **89**, 780-785 (2007).

115. A. Superti-Furga, S. Unger, Nosology and classification of genetic skeletal disorders: 2006 revision. *Am J Med Genet A* **143A**, 1-18 (2007).

116. D. Krakow, D. L. Rimoin, The skeletal dysplasias. *Genet Med* **12**, 327-341 (2010).

117. A.-V. Ngo, M. Thapa, J. Otjen, S. Kamps, Skeletal Dysplasias: Radiologic Approach with Common and Notable Entities. *Seminars in Musculoskeletal Radiology* **22**, 066-080 (2018).

118. S. F. Nemec *et al.*, The importance of conventional radiography in the mutational analysis of skeletal dysplasias (the TRPV4 mutational family). *Pediatr Radiol* **42**, 15-23 (2012).

119. I. M. Orioli, E. E. Castilla, J. G. Barbosa-Neto, The birth prevalence rates for the skeletal dysplasias. *J Med Genet* **23**, 328-332 (1986).

120. D. L. Rimoin *et al.*, The Skeletal Dysplasias: Clinical Molecular Correlations. *Annals of the New York Academy of Sciences* **1117**, 302-309 (2007).

121. J. M. Bauer, C. P. Ditro, W. G. Mackenzie, The Management of Kyphosis in Metatropic Dysplasia. *Spine Deform* **7**, 494-500 (2019).

122. A. Wada *et al.*, Operative treatment of bilateral hip dislocations in a child with metatropic dysplasia. *J Pediatr Orthop B* **16**, 94-97 (2007).

123. B. A. McCray, A. Schindler, J. E. Hoover-Fong, C. J. Sumner, in *GeneReviews((R)),* M. P. Adam *et al.*, Eds. (Seattle (WA), 1993).

124. S. E. Jennings *et al.*, Prevalence of mental health conditions and pain in adults with skeletal dysplasia. *Quality of Life Research* **28**, 1457-1464 (2019).

125. S. S. Kang, S. H. Shin, C.-K. Auh, J. Chun, Human skeletal dysplasia caused by a constitutive activated transient receptor potential vanilloid 4 (TRPV4) cation channel mutation. *Experimental & Molecular Medicine* **44**, 707 (2012).

126. S. Loukin, Z. Su, C. Kung, Increased basal activity is a key determinant in the severity of human skeletal dysplasia caused by TRPV4 mutations. *PLoS One* **6**, e19533 (2011).

127. H. A. Leddy *et al.*, Follistatin in chondrocytes: the link between TRPV4 channelopathies and skeletal malformations. *FASEB J* **28**, 2525-2537 (2014).

128. H. A. Leddy, A. L. McNulty, F. Guilak, W. Liedtke, Unraveling the mechanism by which

TRPV4 mutations cause skeletal dysplasias. *Rare Dis* **2**, e962971 (2014).

129. A. L. McNulty, H. A. Leddy, W. Liedtke, F. Guilak, TRPV4 as a therapeutic target for joint diseases. *Naunyn Schmiedebergs Arch Pharmacol* **388**, 437-450 (2015).

130. S. Thirion, F. Berenbaum, Culture and phenotyping of chondrocytes in primary culture. *Methods Mol Med* **100**, 1-14 (2004).

131. B. T. Estes, B. O. Diekman, J. M. Gimble, F. Guilak, Isolation of adipose-derived stem cells and their induction to a chondrogenic phenotype. *Nat Protoc* **5**, 1294-1311 (2010).

132. D. B. Katz, N. P. T. Huynh, A. Savadipour, I. Palte, F. Guilak, An immortalized human adipose-derived stem cell line with highly enhanced chondrogenic properties. *Biochem Biophys Res Commun* **530**, 252-258 (2020).

133. N. P. Huynh *et al.*, Long non-coding RNA GRASLND enhances chondrogenesis via suppression of the interferon type II signaling pathway. *Elife* **9**, (2020).

134. B. L. Larson *et al.*, Chondrogenic, hypertrophic, and osteochondral differentiation of human mesenchymal stem cells on three-dimensionally woven scaffolds. *J Tissue Eng Regen Med* **13**, 1453-1465 (2019).

135. D. Nasrabadi, S. Rezaeiani, M. B. Eslaminejad, A. Shabani, Improved Protocol for Chondrogenic Differentiation of Bone Marrow Derived Mesenchymal Stem Cells -Effect of PTHrP and FGF-2 on TGFbeta1/BMP2-Induced Chondrocytes Hypertrophy. *Stem Cell Rev Rep* **14**, 755-766 (2018).

136. Q. Lian *et al.*, Functional mesenchymal stem cells derived from human induced pluripotent stem cells attenuate limb ischemia in mice. *Circulation* **121**, 1113-1123 (2010).

137. A. I. Caplan, Mesenchymal Stem Cells: Time to Change the Name! *Stem Cells Transl Med* **6**, 1445-1451 (2017).

138. K. Drela, L. Stanaszek, A. Nowakowski, Z. Kuczynska, B. Lukomska, Experimental Strategies of Mesenchymal Stem Cell Propagation: Adverse Events and Potential Risk of Functional Changes. *Stem Cells Int* **2019**, 7012692 (2019).

139. Y. K. Yang, C. R. Ogando, C. Wang See, T. Y. Chang, G. A. Barabino, Changes in phenotype and differentiation potential of human mesenchymal stem cells aging in vitro. *Stem Cell Res Ther* **9**, 131 (2018).

140. S. Yumlu *et al.*, Gene editing and clonal isolation of human induced pluripotent stem cells using CRISPR/Cas9. *Methods* **121-122**, 29-44 (2017).

141. K. Musunuru, Genome editing of human pluripotent stem cells to generate human cellular disease models. *Dis Model Mech* **6**, 896-904 (2013).

142. S. P. Medvedev, A. I. Shevchenko, S. M. Zakian, Induced Pluripotent Stem Cells: Problems and Advantages when Applying them in Regenerative Medicine. *Acta Naturae* **2**, 18-28 (2010).

143. K. Takahashi *et al.*, Induction of pluripotent stem cells from adult human fibroblasts by defined factors. *Cell* **131**, 861-872 (2007).

144. B. O. Diekman *et al.*, Cartilage tissue engineering using differentiated and purified induced pluripotent stem cells. *Proc Natl Acad Sci U S A* **109**, 19172-19177 (2012).

145. A. M. Craft *et al.*, Generation of articular chondrocytes from human pluripotent stem cells. *Nat Biotechnol* **33**, 638-645 (2015).

146. K. M. Loh *et al.*, Mapping the Pairwise Choices Leading from Pluripotency to Human Bone, Heart, and Other Mesoderm Cell Types. *Cell* **166**, 451-467 (2016).

147. H. Nejadnik *et al.*, Improved approach for chondrogenic differentiation of human induced pluripotent stem cells. *Stem Cell Rev Rep* **11**, 242-253 (2015).

148. A. Yamashita *et al.*, Generation of scaffoldless hyaline cartilaginous tissue from human iPSCs. *Stem Cell Reports* **4**, 404-418 (2015).

149. Q. Zhao *et al.*, MSCs derived from iPSCs with a modified protocol are tumor-tropic but have much less potential to promote tumors than bone marrow MSCs. *Proc Natl Acad Sci U S A* **112**, 530-535 (2015).

150. J. Lee *et al.*, Early induction of a prechondrogenic population allows efficient generation of stable chondrocytes from human induced pluripotent stem cells. *FASEB J* **29**, 3399-3410 (2015).

151. W. M. Suchorska, E. Augustyniak, M. Richter, T. Trzeciak, Comparison of Four Protocols to Generate Chondrocyte-Like Cells from Human Induced Pluripotent Stem Cells (hiPSCs). *Stem Cell Rev Rep* **13**, 299-308 (2017).

152. M. Xu, G. Shaw, M. Murphy, F. Barry, Induced Pluripotent Stem Cell-Derived Mesenchymal Stromal Cells Are Functionally and Genetically Different From Bone Marrow-Derived Mesenchymal Stromal Cells. *Stem Cells* **37**, 754-765 (2019).

153. K. Umeda *et al.*, Human chondrogenic paraxial mesoderm, directed specification and prospective isolation from pluripotent stem cells. *Sci Rep* **2**, 455 (2012).

154. R. A. Oldershaw *et al.*, Directed differentiation of human embryonic stem cells toward chondrocytes. *Nat Biotechnol* **28**, 1187-1194 (2010).

155. S. S. Adkar *et al.*, Step-Wise Chondrogenesis of Human Induced Pluripotent Stem Cells and Purification Via a Reporter Allele Generated by CRISPR-Cas9 Genome Editing. *Stem Cells* **37**, 65-76 (2019).

156. J. Lim *et al.*, BMP-Smad4 signaling is required for precartilaginous mesenchymal condensation independent of Sox9 in the mouse. *Dev Biol* **400**, 132-138 (2015).

157. A. S. Patil, R. B. Sable, R. M. Kothari, An update on transforming growth factor-beta (TGF-beta): sources, types, functions and clinical applicability for cartilage/bone healing. *J Cell Physiol* **226**, 3094-3103 (2011).

158. Q. O. Tang *et al.*, TGF-beta3: A potential biological therapy for enhancing chondrogenesis. *Expert Opin Biol Ther* **9**, 689-701 (2009).

159. B. Johnstone, T. M. Hering, A. I. Caplan, V. M. Goldberg, J. U. Yoo, In vitro chondrogenesis of bone marrow-derived mesenchymal progenitor cells. *Exp Cell Res* **238**, 265-272 (1998).

160. A. Yamashita *et al.*, Considerations in hiPSC-derived cartilage for articular cartilage repair. *Inflamm Regen* **38**, 17 (2018).

161. C. Murphy, A. Mobasheri, Z. Tancos, J. Kobolak, A. Dinnyes, The Potency of Induced

Pluripotent Stem Cells in Cartilage Regeneration and Osteoarthritis Treatment. *Adv Exp Med Biol* **1079**, 55-68 (2018).

162. V. P. Willard *et al.*, Use of cartilage derived from murine induced pluripotent stem cells for osteoarthritis drug screening. *Arthritis Rheumatol* **66**, 3062-3072 (2014).

163. S. S. Adkar *et al.*, Genome Engineering for Personalized Arthritis Therapeutics. *Trends Mol Med* **23**, 917-931 (2017).

164. S. K. O'Connor, D. B. Katz, S. J. Oswald, L. Groneck, F. Guilak, Formation of Osteochondral Organoids from Murine Induced Pluripotent Stem Cells. *Tissue Eng Part A*, (2020).

165. B. Saitta *et al.*, Patient-derived skeletal dysplasia induced pluripotent stem cells display abnormal chondrogenic marker expression and regulation by BMP2 and TGFbeta1. *Stem Cells Dev* **23**, 1464-1478 (2014).

166. Y. Nur Patria *et al.*, CRISPR/Cas9 gene editing of a SOX9 reporter human iPSC line to produce two TRPV4 patient heterozygous missense mutant iPSC lines, MCRIi001-A-3 (TRPV4 p.F273L) and MCRIi001-A-4 (TRPV4 p.P799L). *Stem Cell Res* **48**, 101942 (2020).

167. H. Liu *et al.*, The potential of induced pluripotent stem cells as a tool to study skeletal dysplasias and cartilage-related pathologic conditions. *Osteoarthritis Cartilage* **25**, 616-624 (2017).

168. C. Sanjurjo-Rodriguez *et al.*, Versatility of Induced Pluripotent Stem Cells (iPSCs) for Improving the Knowledge on Musculoskeletal Diseases. *Int J Mol Sci* **21**, (2020).

169. A. Yamashita *et al.*, Statin treatment rescues FGFR3 skeletal dysplasia phenotypes. *Nature* **513**, 507-511 (2014).

170. Y. Matsumoto *et al.*, Induced pluripotent stem cells from patients with human fibrodysplasia ossificans progressiva show increased mineralization and cartilage formation. *Orphanet J Rare Dis* **8**, 190 (2013).

171. E. E. Miller *et al.*, EIF4A3 deficient human iPSCs and mouse models demonstrate neural crest defects that underlie Richieri-Costa-Pereira syndrome. *Hum Mol Genet* **26**, 2177-2191 (2017).

172. M. Okada *et al.*, Modeling type II collagenopathy skeletal dysplasia by directed conversion and induced pluripotent stem cells. *Hum Mol Genet* **24**, 299-313 (2015).

173. R. Torres-Ruiz, S. Rodriguez-Perales, CRISPR-Cas9 technology: applications and human disease modelling. *Brief Funct Genomics* **16**, 4-12 (2017).

174. J. M. Brunger, A. Zutshi, V. P. Willard, C. A. Gersbach, F. Guilak, CRISPR/Cas9 Editing of Murine Induced Pluripotent Stem Cells for Engineering Inflammation-Resistant Tissues. *Arthritis Rheumatol* **69**, 1111-1121 (2017).

175. L. Pferdehirt, A. K. Ross, J. M. Brunger, F. Guilak, A Synthetic Gene Circuit for Self-Regulating Delivery of Biologic Drugs in Engineered Tissues. *Tissue Eng Part A* **25**, 809-820 (2019).

176. F. Guilak *et al.*, Designer Stem Cells: Genome Engineering and the Next Generation of

Cell-Based Therapies. *J Orthop Res* **37**, 1287-1293 (2019).

Chapter 2

Prospective Isolation of Chondroprogenitors from Human iPSCs Based on Cell Surface Markers Identified using a CRISPR-Cas9-Generated Reporter

2.1 Abstract

2.1.1 Background

Articular cartilage shows little or no capacity for intrinsic repair, generating a critical need of regenerative therapies for joint injuries and diseases such as osteoarthritis. Human induced pluripotent stem cells (hiPSCs) offer a promising cell source for cartilage tissue engineering and *in vitro* human disease modeling; however, off-target differentiation remains a challenge during hiPSC chondrogenesis. Therefore, the objective of this study was to identify cell surface markers that define the true chondroprogenitor population and use these markers to purify iPSCs as a means of improving homogeneity and efficiency of hiPSC chondrogenic differentiation.

2.1.2 Methods

We used a CRISPR-Cas9-edited *COL2A1-GFP* knock-in reporter hiPSC line, coupled with a surface marker screen, to identify a novel chondroprogenitor population. Single-cell RNA sequencing was then used to analyze the distinct clusters within the population. An unpaired t-

test with Welch's correction or an unpaired Kolmogorov-Smirnov test was performed with significance reported at a 95% confidence interval.

2.1.3 Results

Chondroprogenitors expressing CD146, CD166, and PDGFRβ, but not CD45, made up an average of 16.8% of the total population. Under chondrogenic culture conditions, these triple positive chondroprogenitor cells demonstrated decreased heterogeneity as measured by single-cell RNA sequencing with fewer clusters (9 clusters in unsorted vs. 6 in sorted populations) closer together. Additionally, there was more robust and homogenous matrix production (unsorted: 1.5 ng/ng vs. sorted: 19.9 ng/ng sGAG/DNA; $p < 0.001$) with significantly higher chondrogenic gene expression (i.e., *SOX9*, *COL2A1*, *ACAN*; $p < 0.05$).

2.1.4 Conclusions

Overall, this study has identified a unique hiPSC-derived subpopulation of chondroprogenitors that are CD146$^+$/CD166$^+$/PDGFRβ$^+$/CD45$^-$ and exhibit high chondrogenic potential, providing a purified cell source for cartilage tissue engineering or disease modeling studies.

2.2 Introduction

Articular cartilage is the load-bearing tissue that lines the ends of long bones in diarthrodial joints, serving to resist compression and provide a nearly frictionless surface during joint loading and movement (*1, 2*). The extracellular matrix of cartilage is comprised primarily of type II collagen and proteoglycans, which are synthesized by the main residing cell type, chondrocytes (*3, 4*). However, because it is aneural and avascular, cartilage shows little or no capacity for intrinsic repair (*4*). Traumatic injury and a chronic inflammatory state lead to irreversible degeneration of the tissue, driving diseases such as osteoarthritis (OA) (*5, 6*). Current treatments

only target disease symptoms, creating a great demand for tissue-engineered cartilage as a system for disease modeling, drug testing, and tissue replacement.

Human induced pluripotent stem cells (hiPSCs) offer a promising source for cartilage tissue engineering and *in vitro* disease modeling (*7*) as they have virtually unlimited expansion capacity, can be genetically modified, and avoid many of the ethical considerations associated with embryonic stem cells (*8, 9*). Despite reports of several chondrogenic differentiation protocols for pluripotent stem cells (*10-15*), incomplete differentiation and cell heterogeneity remain major obstacles for iPSC chondrogenesis (*16, 17*). This challenge has been addressed in other stem and progenitor cell types by prospectively isolating cells that exhibit chondrogenic lineage commitment using surface marker expression. For example, previous studies have identified chondroprogenitors within adult articular cartilage that can be isolated using fibronectin adhesion assays since progenitors express integrins $\alpha5$ and $\beta1$ (*18, 19*). Additionally, mesenchymal progenitor cells, which express CD105, CD166, and CD146, have been reported to have a high chondrogenic potential (*19-21*). Adult multipotent cells, such as bone marrow mesenchymal stem cells (MSCs) or adipose stem cells (ASCs), exhibit chondrogenic potential and have been used extensively for cartilage tissue engineering. They are often characterized by a range of cell surface marker expression, including CD105, CD73, CD90, CD271, CD146, Stro-1, and SSEA-4 (*22*). In an effort to identify a more developmentally-relevant progenitor population, self-renewing human skeletal stem cells characterized by CD164$^+$, CD73$^-$, and CD146$^-$ showed chondrogenic differentiation when implanted in a mouse renal capsule (*23*). In another study, limb bud cells expressing CD73 and BMPR1β while having low to no expression of CD166, CD146, and CD44 were proposed to be the earliest cartilage committed cells (prechondrocytes) in human embryonic development (*24*). However, surface markers

characteristics of hiPSC-derived chondroprogenitors or chondrocytes remain to be identified.

Previously, our lab used green fluorescent protein (GFP) reporter systems to track the expression of collagen type II alpha 1 chain (*COL2A1*) in mouse (*25*) and human (*26*) iPSCs, allowing for the prospective isolation and purification of *COL2A1-GFP+* chondrogenic cells during the differentiation process. Despite the fact that this approach significantly enhanced homogeneity of iPSC chondrogenesis (*26*), genome editing is required to create a reporter line, hindering potential clinical translation. In this regard, the identification of cell surface markers that are directly representative of this *COL2A1*-positive population could greatly enhance the prospective isolation and purification of chondroprogenitors, without requiring genetic modifications to the cell line.

In this study, we used a *COL2A1*-GFP knock-in reporter hiPSC line as a tool to identify cell surface markers that are highly co-expressed with *COL2A1* to test the hypothesis that this sub-population of chondroprogenitor cells will show increased purity and chondrogenic capacity. Single-cell RNA sequencing (scRNA-seq) was then used to investigate the gene expression profile of this population and to identify subsets within it. Matrix production, cell morphology, and gene expression were measured to evaluate chondrogenic ability of unsorted and sorted chondroprogenitor cells. This chondroprogenitor population appears to represent an intermediate step in the developmental pathway of *in vitro* hiPSC chondrogenesis in which off-target differentiation also occurs. The identification of surface markers to purify this population of chondroprogenitor cells via sorting will enhance the efficiency of hiPSC-chondrogenic differentiation for use in tissue engineering, *in vitro* disease modeling, and drug testing.

2.3 Methods

2.3.1 hiPSC lines and culture

Two hiPSC lines were used in the current study: RVR *COL2A1-GFP* knock-in line (RVR) and

BJFF.6 line (BJFF). The RVR line was retrovirally reprogrammed from BJ fibroblasts and

characterized as previously described (*12, 27*). Using CRISPR-Cas9 genome editing, a GFP

reporter allele was added to the *COL2A1* gene as previously reported (*26*). The cells were

cultured in mTeSR1 medium (StemCell Technologies, Canada, 85857). The BJFF line was

derived using Sendai viral transfection of foreskin fibroblasts from a newborn male and cultured

in Essential 8 Flex medium (E8; Gibco, USA, A2858501). Both lines were maintained on

vitronectin coated plates (VTN-N; Fisher Scientific, USA, A14700) with daily medium changes.

Cells were passaged at approximately 90% confluency and induced into mesodermal

differentiation at 40% confluency.

2.3.2 Mesodermal differentiation

hiPSCs were induced into mesodermal differentiation in monolayer according to the previously

published protocol (*26*). In brief, cells were fed daily with various cocktails of growth factors

and small molecules driving stepwise lineage differentiation (anterior primitive streak, paraxial

mesoderm, early somite, sclerotome, and chondroprogenitor) in differentiation medium

composed of IMDM GlutaMAX (IMDM; Gibco, USA, 31980097) and Ham's F12 Nutrient Mix

(F12; Gibco, USA, 11765062) with 1% chemically defined lipid concentrate (Gibco, USA,

11905031), 1% insulin/human transferrin/selenous acid (ITS+; Corning, USA, 354352), 1%

penicillin/steptomycin (P/S; Gibco, USA, 15070063), and 450 µM 1-thioglycerol (Sigma–

Aldrich, USA, M6145-25ML). Upon differentiation into the chondroprogenitor stage, cells were

dissociated using TrypLE (Gibco, USA, 12563029) at 37ºC followed by neutralization with

equal parts of DMEM/F-12, GlutaMAX™ (DMEM/F12; Gibco, USA, 10565042) with 10% fetal

bovine serum (FBS; Atlanta Biologicals, USA, S11550) and 1% P/S. The dissociated cells were used for cell sorting and chondrogenic differentiation as appropriate.

2.3.3 Fluorescent activated cell sorting (FACS)

Chondroprogenitor cells were resuspended in FACS Buffer (PBS-/- with 1% FBS and 1% penicillin/steptomycin/fungizone (P/S/F; Gibco, USA, 15-240-062) at approximately 40×10^6 / mL. The cells were treated with ~6.5% of Human TruStain FcX^{TM} (BioLegend, USA, 422302) for 10 min at RT. Approximately 5×10^4 cells in 100 µl were used for each compensation. Cells were labeled with appropriate antibodies including an isotype control. A table of the antibodies used can be found in Table 2.1. Cells were incubated for 30 minutes at 4ºC and washed with FACS buffer twice. Samples were resuspended in sorting medium consisting of DMEM/F12 with 2% FBS, 2% P/S/F, 2% Hepes (Gibco, USA, 15-630-080), and DAPI (BioLegend, USA, 422801) at 4×10^6 cells / mL and filtered through a 40 µm cell strainer. Cells were stored on ice prior to sorting.

Table 2.1 Antibodies used for flow cytometry and sorting.

Marker	Color	Company	Catalog Number	
			Antibody	Isotype
CD45	FITC	BioLegend	304006	400110
CD166	PE	BioLegend	343904	400112
CD146	PE/Cy7	BioLegend	361008	400126
PDGFRβ	APC	BioLegend	323608	400121
CD271	PE/Cy7	BioLegend	345110	400126
CD105	PE	BioLegend	323206	400113
CD73	Pacific Blue	BioLegend	244012	400151
BMPR1β	APC	R&D Systems	FAB5051A	IC0041A

An Aria-II FACS machine was used to compensate and gate the samples. Sorted cells were collected in collection media composed of DMEM/F12, 20% FBS, 1% P/S/F, 1% ITS+, 1% MEM non-essential amino acids (NEAA; Gibco, USA, 11140050), and 0.1% ROCK inhibitor (Stemcell Technologies, Canada, NC0791122). Data was analyzed using FlowJo software.

2.3.4 10X chromium platform scRNA-seq

Cells were thawed at 37ºC and resuspended in PBS + 0.01% BSA at concentration of 2,000 cells/µl. Cell suspension were submitted to the Genome Technology Access Center (GTAC sequencing core) at Washington University in St. Louis for library preparation and sequencing. In brief, 10,000 cells per sample were loaded on a Chromium Controller (10x Genomics, USA) for single capture. Libraries were prepared using Single Cell 3′ Library & Gel Bead Kit v2 (10x Genomics, USA, 120237) following manufacture's instruction. A single cell emulsion (Gel Bead-In-Emulsions, GEMs) is created by making barcoded cDNA unique to each individual emulsion. Recovery agent was added to break GEM and cDNA was then amplified. A library is produced via end repair, dA-tailing, adaptor ligation, post-ligation cleanup with SPRIselect, and sample index PCR. The quality and concentration of the amplified cDNA was evaluated by Bioanalyzer (Agilent Technologies, USA, 2100) on a High Sensitivity DNA chip (Agilent Technologies, USA, 5065-4401). Only cDNA with average library size 260-620 bp were used for sequencing. Sequencing was performed by HiSeq2500 (Illumina, USA) with the following read length: 26 bp for Read1, 8 bp for i7 Index, and 98 bp for Read2. A species mixing experiment (mouse and human) was also performed prior to running on actual sample to ensure good single cell capture (i.e., cell doublet rate < 5%).

2.3.5 Preprocessing of scRNA-seq data

Paired-end sequencing reads were processed by Cell Ranger (10x Genomics software, version 2.0.0). Briefly, reads were aligned to the GRCh38 (version 90) for genome annotation, demultiplexing, barcode filtering and gene quantification. Cell Ranger also removes any barcode that has less than 10% of the 99th percentile of total unique molecular identifiers (UMI) counts per barcode as these barcodes are associated with empty droplets. After this quality control, gene barcode matrix for sorted and unsorted cells were generated by counting the number of UMIs for a given gene (as row) in individual cell (as column). For sorted cell sample, 8,682 cells with 19,140 genes were captured, while for unsorted cell sample, we obtained 8,220 cells with 19,604 genes.

2.3.6 Unsupervised clustering analysis and cell cluster annotation

To assess the difference in composition of cell populations due to sorting for selective markers, we performed global unsupervised clustering analysis on data sets of scRNA-seq from sorted and unsorted cells. First, gene barcode matrices from were input into Seurat R package (version 2.4) (*28*). We then removed the low-quality cells with less than 200 or more than 7,000 detected genes, or if their mitochondrial gene content was more than 5%. Genes were filtered out that were detected in less than 3 cells. After filtering out low-quality cells or cell doublets, the gene expression was then natural log transformed and normalized for scaling the sequencing depth to 10,000 molecules per cell. Next, to reduce the variance introduced by "unwanted" sources, we regressed out variation in gene expression driven by cell cycle stages and mitochondrial gene expression with *vars.to.regress* argument in function *ScaleData* in Seurat. We then used *FindVariableGenes* function in Seurat to identify highly variable genes across cells for downstream analysis. These quality control steps resulted in 4,173 cells with 1,833 highly variable

genes for sorted cell sample, and 8,630 cells with 3,009 highly variable genes for unsorted cell sample. Dimensionality reduction on the data was then performed by computing the significant principal components on highly variable genes. We then performed unsupervised clustering by using *FindClusters* function in Seurat with the resolution argument set to 0.6, and clusters were then visualized in t-distributed Stochastic Neighbor Embedding (tSNE) plot (*29*).

Differentially expressed genes (DEGs) among each cell cluster were determined using *FindAllMarkers* function in Seurat. DEGs expressing at least in 25% cells within the cluster and with a fold change of more than 0.25 in log scale were considered to be marker genes of the cluster. To determine the biology functions of the marker genes from a given cluster, we performed Gene Ontology (GO) enrichment analysis by using The DAVID Gene Functional Classification Tool (http://david.abcc.ncifcrf.gov; version 6.8) (*30*). By comparing these unique biological GO terms with existing RNA-seq datasets and the literature, we were able to annotate cell clusters. Additionally, the top 10 enriched GO terms from biological function category with associated p values were visualized by GraphPad Prism (version 8.0; GraphPad Software).

2.3.7 Canonical correlation analysis for integrated analysis of sorted and unsorted scRNA-seq data

To compare cell types and to identify their associated DEGs between sorted and unsorted cells, we applied canonical correlation analysis (CCA), a computational strategy implemented in Seurat for integrated analysis of multiple datasets, on the scRNA-seq datasets from the cells with or without sorting. First, top 1,000 highly variable genes from two datasets were selected. We then use *RunCCA* function to identify common sources of variation between the two datasets and to merge the two objects into a single dataset. We next determined the top principal components of the CCA by examining a saturation in the relationship between the number of principle components and the percentage of the variance explained using the *MetageneBicorPlot* function.

By using selected top principal components, we aligned the CCA subspaces with *AlignSubspace* function, which returns a new dimensional reduction matrix allowing for downstream clustering and DEG analyses. DEG analysis was performed on the cells from different datasets but grouped in the same cluster (i.e. conserved cell types between two conditions) after CCA alignment. The methods for cell clustering, identification of conserved cells types and DEGs as well as annotation of cell clusters were similar to the ones mentioned previously. DEGs in each conserved cell types in response to sorting were visualized by ComplexHeatmap R package (*31*).

2.3.8 Expansion of chondroprogenitor cells

Sorted and unsorted chondroprogenitor cells were plated on non-coated flasks and cultured in MEM alpha media (Gibco, USA, 12571048) with 1% penicillin/streptomycin (P/S; Gibco, USA, 15070063), 50 µg/ml L-ascorbic acid 2-phosphate (ascorbate; Sigma-Aldrich, USA, A4544), and 10 ng/ml basic fibroblast growth factor (bFGF; R&D Systems, USA, 233FB001MGC). Cells were fed every three days until 80-90% confluency prior to further expansion or chondrogenesis. chondroprogenitor cells were passaged up to four times.

2.3.9 Chondrogenic differentiation

Sorted, unsorted, and expanded chondroprogenitor cells were re-suspended at 2.5×10^5 cells / mL in chondrogenic medium composed of DMEM/F-12, 1% FBS, 1% ITS+, 55 µM β-mercaptoethanol (Gibco, USA, 21985-023), 100 nM dexamethasone (DEX; Sigma-Aldrich, USA, D4902), 1% NEAA, 1% P/S, 10 ng/ml human transforming growth factor beta 3 (TGF-β3; R&D Systems, USA, 24-3B3-200CF), 50 µg/ml L-ascorbic acid 2-phosphate (ascorbate; Sigma-Aldrich, USA, A4544), and 40 µg/ml L-Proline (proline; Sigma-Aldrich, USA, P5607). 2 mL of the cell solution was added to a 15mL conical tube and centrifuged for 5 min at 300g to form a pellet. Chondrogenic pellets were cultured at 37ºC for 28 days. Medium was changed every 3-4

days.

2.3.10 Histology

After chondrogenic differentiation, pellets were collected in 10% neutral buffered formalin for fixation for 24 hours. Pellets were then transferred to 70% ethanol, dehydrated, and embedded in paraffin wax. Wax blocks were sectioned at 8 µm and stained for glycosaminoglycans and cell nuclei according to the Safranin-O and hematoxylin standard protocol.

2.3.11 Immunohistochemistry

Histologic sections were washed with xylene three times and rehydrated before labeling against COL1A1, COL2A1, COL6A1, and COL10A1. Antigen retrieval was performed with 0.02% proteinase K for 3 min at 37ºC for COL2A1 and COL6A1 and with pepsin for 5 min at RT for COL1A1 and COL10A1 followed by peroxidase quench then serum blocking for 30 min at RT each. Samples were labeled for 1 hour with the primary antibody (COL1A1: 1:800 Abcam, UK, 90395; COL2A1: 1:10 Developmental Studies Hybridoma Bank, USA, II-II6B3-s; COL6A1 1:1000 Fitzgerald, USA, 70F-CR009X; COL10A1 1:200 Sigma, USA, C7974) and for 30 min with the secondary antibody (COL1A1, COL2A1, COL10A1: 1:500 Goat Anti-Mouse Abcam, UK, 97021; COL6A1: 1:500 Goat Anti-Rabbit Abcam, UK, 6720). Reagent C was then used for enzyme conjugation for 20 min at RT followed by AEC for 2.5 min (COL2A1 and COL6A1) or 2 min (COL1A1 and COL10A1) at RT. Finally, samples were counterstained with hematoxylin to reveal cell nuclei for 45 sec.

2.3.12 Biochemical analysis

Pellets were rinsed with PBS after chondrogenic differentiation and digested at 65ºC overnight in 200 µl of 125 µg/ml papain (Sigma-Aldrich, USA, P4762), 100 mM sodium phosphate (Sigma-Aldrich, USA, 71507), 5 mM ethylenediaminetetraacetic acid (EDTA; Sigma-Aldrich, USA,

ED2SS), and 5 mM L-cysteine hydrochloride (Sigma-Aldrich, USA, C1276) at 6.5 pH. Samples

were stored at -80ºC before thawing to measure double stranded DNA and sulfated

glycosaminoglycans (sGAG). The PicoGreen (Invitrogen, USA, P7589) and 1,9-

dimethylmethylene blue (Sigma-Aldrich, USA, 341088), with chondroitin-4-sulfate (Sigma-

Aldrich, USA, C9819) as a standard, assays were used according to the protocols to quantify

DNA and sGAG respectively.

2.3.13 Gene expression

Day 28 pellets were rinsed with PBS-/- and snap frozen in 300 µl of Buffer RL (from Total RNA

Purification Kit, Norgen Biotek, Canada, 37500) and stored at -80ºC. Samples were thawed and

homogenized with zirconia beads (BioSpec Products, USA, 11079124zx) and a miniature bead

beater. RNA was isolated from the samples using the Total RNA Purification Kit according to

the manufacture's protocol (Norgen Biotek, Canada, 37500). Reverse transcription of the RNA

was performed using SuperScript VILO Master Mix (Thermo Fisher, USA, 11755500) to

maintain cDNA. Fast SYBR Green Master Mix (Thermo Fisher, USA, 4385617) was used for

quantitative real time polymerase chain reaction (RT-qPCR) according to manufacturer's

instructions on the QuantStudio 3 (Thermo Fisher, USA). Gene expression was analyzed using

the $\Delta\Delta C_T$ method relative to undifferentiated hiPSCs with the reference gene TATA-box-binding

protein (*TBP*) (*32*). Sequences of primers can be found in the Table 2.2.

Table 2.2 Human primer sequences. Primers were used for RT-qPCR and are listed as 5' to 3'.

Gene	Forward Sequence	Reverse Sequence
ACAN	CACTTCTGAGTTCGTGGAGG	ACTGGACTCAAAAAGCTGGG
COL1A1	TGTTCAGCTTTGTGGACCTC	TTCTGTACGCAGGTGATTGG
COL2A1	GGCAATAGCAGGTTCACGTA	CTCGATAACAGTCTTGCCCC

COL5A1	GGCTCCCGAGAGCAACCT	CGGGACACTCACGAACGAA
COL6A1	TCAAGAGCCTGCAGTGGATG	TGGACACTTCTTGTCTATGCAG
COL10A1	CATAAAAGGCCCACTACCCAAC	ACCTTGCTCTCCTCTTACTGC
IGFBP5	TCCCCACGTGTGTTCATCTG	AAATGGGATGGACTGAGGCG
NES	CAGGGGCAGACATCATTGGT	CACTCCCCCATTCACATGCT
NKX3-2	GCTGGGAGCTTTCTGCACTA	TTCGCACCCCTTGGTTACAA
OTX1	AGACGCATCAGACCCTGAAGGACT	CCAGACCTGGACTCTAGACTC
PRRX1	GCAGGCTTTGGAGCGTGTCT	TCCTGCGGAACTTGGCTCTT
SOX9	CGTCAACGGCTCCAGCAAGAACAA	GCCGCTTCTCGCTCTCGTTCAGAAGT
TBP	AACCACGGCACTGATTTTCA	ACAGCTCCCCACCATATTCT

2.3.14 Statistical analysis

Quantification of surface marker expression was performed 8 separate times with technical

replicates of n = 3-4 for each experiment. Biochemical analysis and RT-qPCR were performed

on the pellets collected from two independent sorting experiments (n = 3-4 samples per group

per experiment). Gene expression and sGAG/DNA data were tested for normality using the

Shapiro-Wilk test. An unpaired t-test with Welch's correction was then performed assuming a

Gaussian distribution. If data was not normal, an unpaired Kolmogorov-Smirnov test was

performed. All calculations were performed using GraphPad Prism (GraphPad Software; version

8.0). Two-tailed p values were calculated and reported at a 95% confidence interval.

2.4 Results

2.4.1 *COL2A1*-positive chondroprogenitor cells express PDGFRβ, CD146, and CD166

COL2A1-GFP reporter hiPSCs were differentiated into chondroprogenitor cells along the

mesodermal lineage for 12 days as previously described (*26*). After the 12 days of

differentiation, flow cytometric analysis showed that, on average, 4.27% of the population

expressed *COL2A1* based on *GFP* expression (Figure 2.1A). The *COL2A1*-positive cells were

assumed to be chondroprogenitors with a unique surface marker profile. The cells were labeled

for surface markers commonly associated with MSCs and/or chondroprogenitors in the

developing limb bud: BMPR1β, CD73, CD105, CD146, CD166, CD271, and PDGFRβ (*22-24*).

Of the total population, less than 1% expressed *COL2A1* in addition to either CD271 (0.4%),

CD105 (0.16%), CD73 (0.09%), or BMPR1β (0%) (Figure 2.1B). Interestingly, 2.32%, 2.17%,

or 1.32% of the total population co-expressed *COL2A1* with PDGFRβ, CD146, or CD166

respectively (Figure 2.1C). Since these markers appear to be the most highly correlated with

COL2A1 expression of the previously identified as MSC and/or chondroprogenitor markers

selected, cells were sorted based on expression of these markers for this study. Sorting also

removed cells expressing CD45 (< 15% of total cells) to eliminate any non-chondrogenic

hematopoietic stem cells potentially derived during mesoderm differentiation (Figure 2.1D).

2.4.2 PDGFRβ, CD146, and CD166 enriched chondroprogenitor cells

The BJFF hiPSC line (wildtype without genome editing) was differentiated into

chondroprogenitor cells accordingly (12 days in monolayer). Cells either directly underwent

chondrogenic pellet culture, were expanded, were saved for scRNA-seq, or were labeled for the

surface markers of interest (Figure 2.1D). Fluorescent activated cell sorting (FACS) was used to

sort live chondroprogenitor cells negative for CD45 and positively expressing PDGFRβ and

CD146, followed by expression of CD166 (Figure 2.1E). Cells not expressing any of these

surface markers were also analyzed as a negative control. Approximately 16.5% of the total

chondroprogenitor cell population was triple positive for PDGFRβ, CD146, and CD166, which

was significantly higher than the percentage of the cells (7.2% of total cell population) that were

triple-negative for these markers (Figure 2.1F). As with unsorted cells, sorted cells were also

collected and either pelleted for chondrogenesis, expanded, or saved for scRNA-seq, as described in Figure 2.1D.
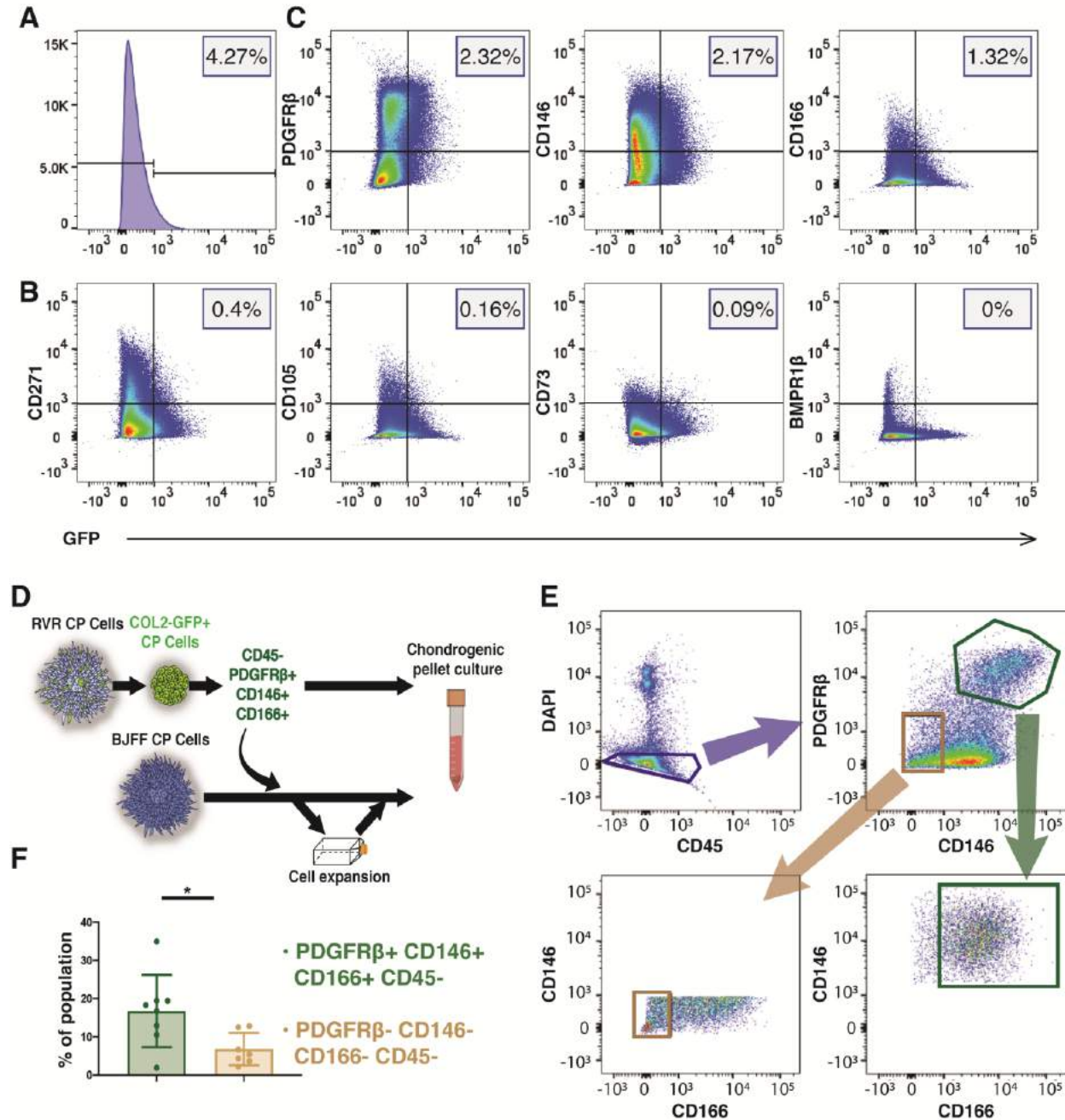
Figure 2.1 Surface marker analysis and sorting strategy to identify progenitors with robust chondrogenic potential from heterogenous chondroprogenitor (CP) cells. (**A**) Flow cytometry showed approximately 4.27% of cells expressed *COL2A1-GFP*. (**B-C**) Chondroprogenitors were labeled for various surface markers and analyzed for co-expression with *COL2A1-GFP*. (**B**) Most *COL2A1-GFP+* cells did not express CD271, CD105, CD73, and BMPR1β. (**C**) PDGFRβ,

CD146, and CD166 were co-expressed with *COL2A1-GFP*. (**D**) A schematic representing the experimental design. The RVR cell line with the *COL2A1-GFP* reporter was differentiated into chondroprogenitor cells. Surface marker analysis indicated that PDGFRβ, CD146, and CD166 expression were highly co-expressed with *COL2A1* but not CD45. (**E**) Cells expressing these desired markers were sorted from wildtype BJFF chondroprogenitor cells. To evaluate chondrogenic potential of the sorted cells, pellets from the sorted cells were either made immediately post-sorting or formed after *in* vitro expansion. (**F**) A higher percentage of the total cell population (~16.8%) were triple positive for the desired markers compared to the population not expressing any of these markers. * $p < 0.05$. Data represented as mean ± SEM. n = 7-8 independent experiments.

2.4.3 scRNA-seq reveals that unsorted chondroprogenitor cells contained diverse cell populations

We next used scRNA-seq to explore the cell diversity and genetic profiles of unsorted

chondroprogenitor cells. At least 9 distinct cell populations (cell clusters) were observed in

unsorted chondroprogenitor cells (Figure 2.2A). Among these populations, 5 of them were

enriched for a variety of neural cell markers such as *SOX2, OTX1, NES*, and *PAX6* (Figure 2.2B),

likely representing populations of the neurogenic lineage. Of these, *SOX2, OTX1,* and PAX6

expression were significantly downregulated with sorting according to RT-qPCR (Figure S2.2A).

Furthermore, we found that 3 cell populations exhibited high expression levels of several

mesenchyme markers including *PRRX1, COL1A1, COL5A1*, and *COL6A1* which were

comparable between sorted and unsorted groups, while only a small cell population (2.3% of

total cells) expressed chondrogenic markers such as *SOX9, COL2A1, IGFBP5*, and *NKX3-2*

(Figure 2.2B, 2.2C, S2.2B, and S2.2C). Using Gene Ontology (GO) enrichment analysis of the

gene sets representing each cell cluster (Figure 2.2D and S2.1A) we observed that cells

expressing *SOX9* and *COL2A1* demonstrated gene sets enriched for protein translation and

skeletal system development.

A Unsorted

Neurogenic lineage
Chondrogenic lineage
Mesenchyme

SOX9/COL2A1
SOX2/TTR/NES+
SOX2/SOX3/TOP2A+
SOX2/OTX2+
PAX6/OTX2+
SPP1/CRYAB/NES+
PRRX1/COL6A1+
PRRX1/COL1A1/COL3A1
PRRX1/HIST1H4C/CDK1+

B

Neurogenic markers
SOX2 *OTX1* *NES* *PAX6*

Mesenchyme markers
PRRX1 *COL6A1* *COL1A1* *COL5A1*

Chondrogenic markers
SOX9 *COL2A1* *IGFBP5* *NKX3-2*

tSNE2
tSNE1

C

Fraction of unsorted Cp cells

SOX2/TTR/NES+
PRRX1/COL1A1/COL3A1+
PRRX1/COL6A1+
PAX6/OTX2+
SOX2/OTX2+
SOX2/SOX3/TOP2A+
PRRX1/HIST1H4C/CDK1+
SPP1/CRYAB/NES+
SOX9/COL2A1+

D

SOX9/COL2A1+

GO:0006614 SRP-dependent Cotranslational Protein Targeting to Membrane
GO:0019083 Viral Transcription
GO:0000184 Nuclear-transcribed mRNA Catabolic Process, Nonsense-mediated Decay
GO:0006413 Translational Initiation
GO:0006364 rRNA Processing
GO:0006412 Translation
GO:0030199 Collagen Fibril Organization
GO:0001501 Skeletal System Development
GO:0003007 Heart Morphogenesis
GO:0030198 Extracellular Matrix Organization

-log(p value)

SOX2/TTR/NES+

GO:0030900 Forebrain Development
GO:0000086 G2/M Transition of Mitotic Cell Cycle
GO:0002576 Platelet Degranulation
GO:0045893 Positive Regulation of Transcription
GO:0007411 Axon Guidance
GO:0030902 Hindbrain Development
GO:0045665 Negative Regulation of Neuron Differentiation
GO:0006357 Regulation of Transcription from RNA Polymerase II Promoter
GO:0048754 Branching Morphogenesis of an Epithelial Tube
GO:0007399 Nervous System Development

-log(p value)

SOX2/SOX3/TOP2A+

GO:0006260 DNA Replication
GO:0000082 G1/S Transition of Mitotic Cell Cycle
GO:0042769 DNA Damage Response, Detection of DNA Damage
GO:0000722 Telomere Maintenance via Recombination
GO:0051301 Cell Division
GO:0006296 Nucleotide-excision Repair, DNA Incision, 5'-to Lesion
GO:0033683 Nucleotide-excision Repair, DNA Incision
GO:0006297 Nucleotide-excision Repair, DNA Gap Filling
GO:0019985 Translesion Synthesis
GO:0042276 Error-prone Translesion Synthesis

-log(p value)

PRRX1/COL1A1/COL3A1+

GO:0030199 Collagen Fibril Organization
GO:0070527 Platelet Aggregation
GO:0002576 Platelet Degranulation
GO:0098609 Cell-cell Adhesion
GO:0030198 Extracellular Matrix Organization
GO:0006936 Muscle Contraction
GO:0034329 Cell Junction Assembly
GO:0001525 Angiogenesis
GO:0006928 Movement of Cell or Subcellular Component
GO:0036498 IRE1-mediated Unfolded Protein Response

-log(p value)

PRRX1/HIST1H4C/CDK1+

GO:0006260 DNA Replication
GO:0000082 G1/S transition of Mitotic Cell Cycle
GO:0000083 Regulation of Transcription Involved in G1/S Transition of Mitotic Cell Cycle
GO:0051301 Cell Division
GO:0007062 Sister Chromatid Cohesion
GO:0006270 DNA Replication Initiation
GO:0070527 Platelet Aggregation
GO:0030198 Extracellular Matrix Organization
GO:0006936 Muscle Contraction
GO:0006281 DNA Repair

-log(p value)

43

Figure 2.2 Cell populations and GO enrichment analysis of unsorted chondroprogenitor cells. (**A**) scRNA-seq identified unsorted chondroprogenitor cells contained at least 9 populations, which could be further categorized into 3 broad classes: neurogenic cells (blue dashed circle), chondrogenic cells (green dashed circle), and mesenchyme (brown dashed circle). (**B**) Expression of signature genes of each cell lineage. (**C**) GO terms analysis (biological process) of each unique population. (**D**) Percentage of total unsorted chondroprogenitor cells in each unique cell population. More than 20% of the unsorted chondroprogenitors were *SOX2/TTR/NES+* neurogenic cells, while only small number of unsorted cells expressed *SOX9* and *COL2A1*.

2.4.4 scRNA-seq reveals that sorting enriched *SOX9/COL2A1+* cells

scRNA-seq of sorted chondroprogenitor cells indicated that there were at least 6 cell populations

consisting of PDGFRβ$^+$/CD146$^+$/CD166$^+$ cells (Figure 2.3A). Surprisingly, there was still a

small percentage of cells (4% of total sorted cells) expressing *SOX2* and *NES*, despite the

stringent sorting regime (Figures 2.3B and 2.3C). We also observed that *SOX2*/*NES+* cells

exhibited high expression of CD47, an integrin-associated protein (*33*) (Figure S2.1B).

Nevertheless, sorting still significantly enriched cells positive for *SOX9* and *COL2A1* by > 11-

fold (27% of total sorted cells vs. 2.3% of total unsorted cells). Interestingly, overall gene

expression of these chondrogenic genes was not increased, in fact *COL2A1* was decreased with

sorting when evaluated by RT-qPCR (Figure S2.2C). We observed that sorting slightly increased

the percentage of the cells expressing ALCAM (22.1% of the unsorted cells vs. 28.3% of the

sorted cells). However, 9.9% of the total sorted cells were triple positive for

SOX9/COL2A1/ALCAM, while only 0.8% of the total unsorted cells co-expressed these three

genes. Interestingly, we also found that ALCAM was also expressed by both chondrogenic and

neurogenic progenitors (e.g., 31.9% of SOX9/COL2A1$^+$ cells and 44.9% of SOX2/TTR$^+$ cells

were positive for ALCAM in the sorted group), implying ALCAM alone may not be used as a

sole marker for chondroprogenitor cells. Additionally, we also observed that gene expression

levels of the sorting makers were enriched in the sorted population, with *ALCAM* (CD166)

highest in the *SOX9* and *COL2A1* cluster compared to the enrichment of all three in the unsorted

mesenchyme population (Figure 2.3D). Similarly, there was enrichment of some previously

reported pro-chondrogenic markers (*18, 19, 21, 24*) in the sorted chondroprogenitor population;

specifically *ITGA5* and *ENG* (CD105) (Figure S2.3). Skeletal system development, as expected,

emerged as a significant GO term in *SOX9/COL2A1+* cells, while *HMGB2/TOP2A+* and

LGALS1/PTTG1+ cells were enriched in gene sets of cell division (Figure 2.3E and S2.1C).

A Sorted

ACTA2/COL3A1+

ANKRD1/S100A10+

SOX9/COL2A1+

LGALS1/PTTG1+

SOX2/TTR+

HMGB2/TOP2A+

B

Neurogenic markers

SOX2   OTX1   NES   PAX6

Mesenchyme markers

PRRX1   COL6A1   COL1A1   COL5A1

Chondrogenic markers

SOX9   COL2A1   IGFBP5   NKX3-2

tSNE2

tSNE1

C

Fraction of sorted Cp cells

SOX9/COL2A1+
HMGB2/TOP2A+
ACTA2/COL3A1+
LGALS1/PTTG1+
ANKRD1/S100A10+
SOX2/TTR+

D

Unsorted cells

MCAM (CD146)   ALCAM (CD166)

PDGFRB

Sorted cells

MCAM (CD146)   ALCAM (CD166)

PDGFRB

tSNE2

tSNE1

E

SOX9/COL2A1+

GO:0001501 Skeletal System Development
GO:0045893 Positive Regulation of Transcription, DNA-templated
GO:0014032 Neural Crest Cell Development
GO:0060021 Palate Development
GO:0006366 Transcription from RNA Polymerase II Promoter
GO:0045944 Positive Regulation of Transcription from RNA Polymerase II Promoter
GO:0060174 Limb Bud Formation
GO:0050680 Negative Regulation of Epithelial Cell Proliferation
GO:0061029 Eyelid Development in Camera-type Eye
GO:0009612 Response to Mechanical Stimulus

-log(p value)

HMGB2/TOP2A+

GO:0051301 Cell Division
GO:0007067 Mitotic Nuclear Division
GO:0006260 DNA Replication
GO:0007062 Sister Chromatid Cohesion
GO:0000082 G1/S Transition of Mitotic Cell Cycle
GO:0006281 DNA Repair
GO:0006302 Double-strand Break Repair
GO:0007059 Chromosome Segregation
GO:0000722 Telomere Maintenance via Recombination
GO:0034080 CENP-A Containing Nucleosome Assembly

-log(p value)

LGALS1/PTTG1+

GO:0051301 Cell Division
GO:0000086 G2/M transition of Mitotic Cell Cycle
GO:0031145 Anaphase-promoting Complex-dependent Catabolic Process
GO:0007017 Microtubule-based Process
GO:1904668 Positive Regulation of Ubiquitin Protein Ligase Activity
GO:0007067 Mitotic Nuclear Division
GO:0030705 Cytoskeleton-dependent Intracellular Transport
GO:0051439 Regulation of Ubiquitin-protein Ligase Activity Involved in Mitotic Cell Cycle
GO:0008283 Cell Proliferation
GO:0051726 Regulation of Cell Cycle

-log(p value)

SOX2/TTR+

GO:0051301 Cell Division
GO:0007067 Mitotic Nuclear Division
GO:0007062 Sister Chromatid Cohesion
GO:0000086 G2/M Transition of Mitotic Cell Cycle
GO:0031145 Anaphase-promoting Complex-dependent Catabolic Process
GO:0098609 Cell-cell Adhesion
GO:0051437 Positive Regulation of Ubiquitin-protein Ligase Activity for Mitotic Cell Cycle Transition
GO:0001764 Neuron Migration
GO:0097150 Neuronal Stem Cell Population Maintenance
GO:1904668 Positive Regulation of Ubiquitin Protein Ligase Activity

-log(p value)

46

Figure 2.3. Cell populations and GO enrichment analysis of sorted chondroprogenitor cells. (**A**) scRNA-seq identified PDGFRβ^{+}/CD146^{+}/CD166^{+} cells contained at least 6 populations. (**B**) Expression of signature genes of each cell lineage. The sorted cells were enriched for mesenchymal and chondrogenic genes. (**C**) Percentage of total sorted chondroprogenitor cells in each unique cell population. 27% of the sorted were *SOX9/COL2A1*. Interestingly, a small percentage of cells (4% of total sorted cells) expressing *SOX2* and *NES* was still observed. (**D**) PDGFRβ^{+}/CD146^{+}/CD166^{+} sorted cells may belong to mesenchymal population (brown dashed circle) in unsorted cells. Green dashed circle indicates the population that was positive for *SOX9* and *COL2A1.* (**E**) GO terms analysis (biological process) showing skeletal system development was highlighted in *SOX9/COL2A1+* cells, while *HMGB2/TOP2A+* and *LGALS1/PTTG1+* cells were enriched in gene sets of cell division.

2.4.5 Canonical correlation analysis (CCA) demonstrates high enrichment of proliferative and mesenchymal genes in sorted chondroprogenitor cells

CCA, a machine-learning method that performs linear combinations of features across data sets

that are maximally correlated, was used to integrate scRNA-seq datasets from sorted and

unsorted cells (*28*). Five major conserved populations were identified after CCA alignment of the

sorted and unsorted chondroprogenitor cells (Figure 2.4A). Among these populations,

HIST1H4C+ cells accounted for the largest conserved population, while the *IGFBP5/COL2A1+*

cluster was the smallest. We next performed differentially expression gene (DEG) analysis to

explore how sorting enriches or depletes the levels of gene expression within each individual

population (Figure 2.4B). Within the *IGFBP5/COL2A1+* population, sorted cells exhibited

significantly up-regulated expression of several mesenchymal genes including *TPM1, TAGLN*

and *TMSB10* (indicated by brown circle), which have been suggested to be essential in

chondrogenesis (*34, 35*). Furthermore, within the *IGFBP5/COL2A1+* population, sorted cells

demonstrated significantly down-regulated expression of *IGFBP5* (indicated by blue circle), an

important transcription factor inducing chondroprogenitor cells into the chondrogenic lineage

(*36*).
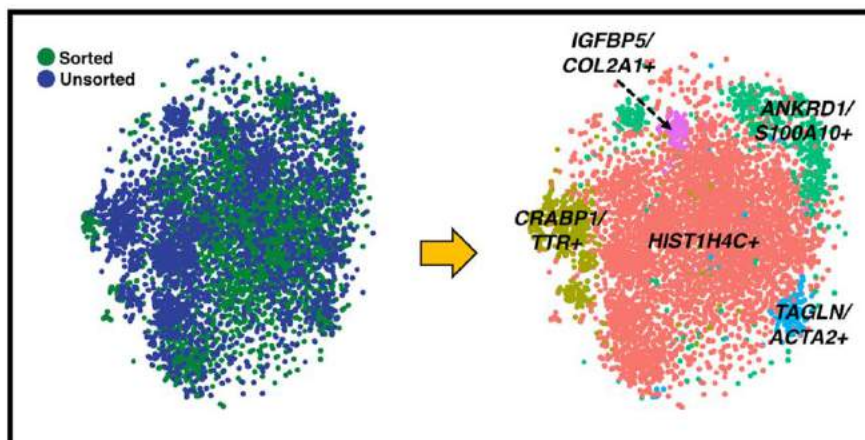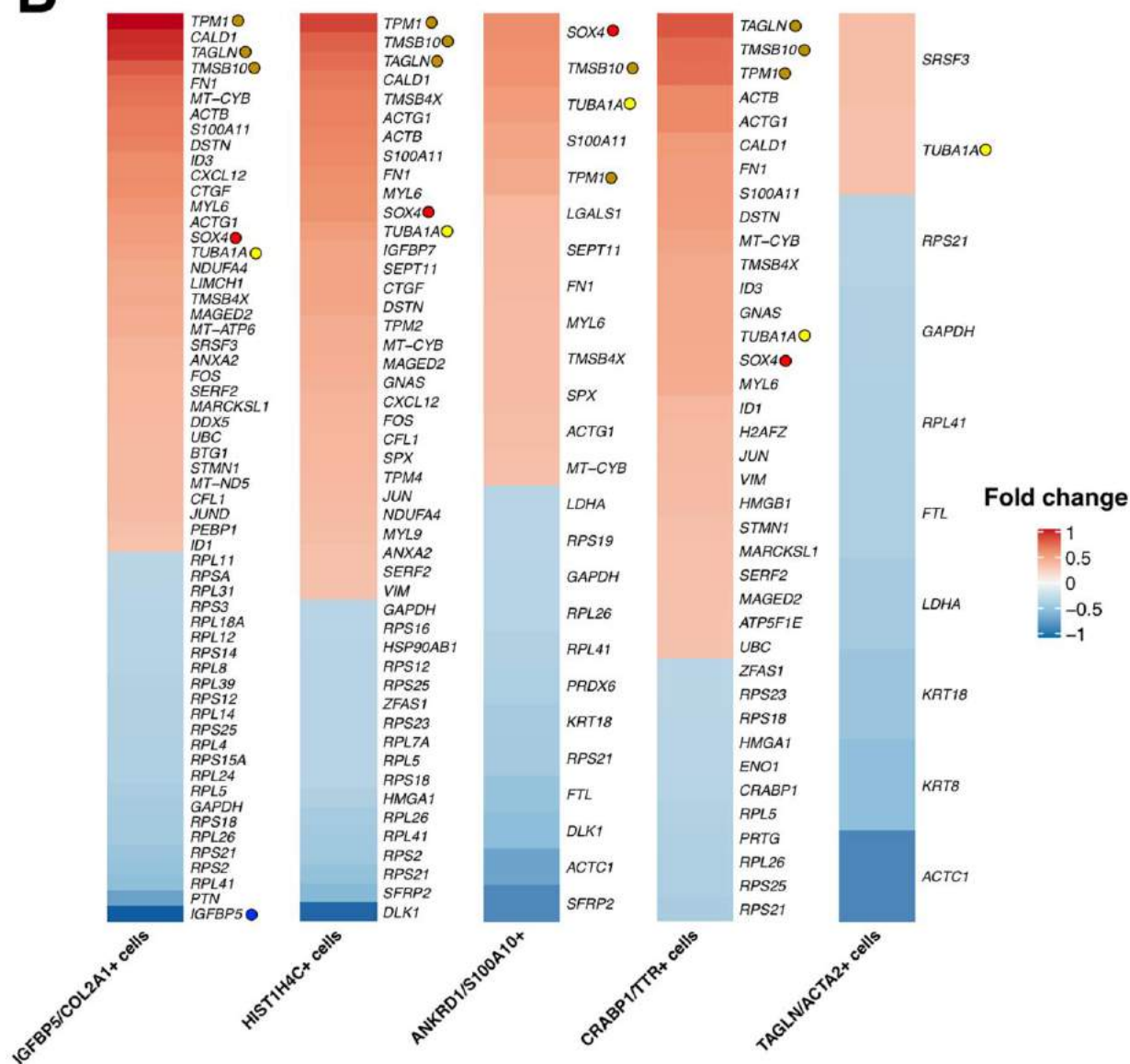
Figure 2.4 CCA for integrated analysis of sorted and unsorted scRNA-seq datasets. (**A**) Five major conserved populations were identified after CCA alignment of the sorted and unsorted chondroprogenitor cells (**B**) DEG analysis indicated that sorted cells exhibited significantly up-regulated expression of several mesenchymal genes including *TPM1*, *TAGLN* and *TMSB10* (brown circle), which have been suggested to be essential in chondrogenesis. Proliferative markers including *SOX4* (red circle) and *TUBA1A* (yellow circle) were increased, but *IGFBP5* (blue circle) and several ribosomal genes were decreased in sorted cells.

2.4.6 Sorting improved matrix production and homogeneity in cartilaginous pellets

Sorted and unsorted cells from both the reporter and wildtype lines underwent chondrogenesis in pellet culture for 28 days. Pellets stained with safranin-O for sulfated glycosaminoglycans (sGAGs) showed that sorting increased matrix production as well as homogeneity of cell morphology (Figure 2.5A and S2.4). Additionally, the layer of non-cartilaginous-like cells surrounding unsorted cell pellets was eliminated in the pellets derived from sorted cells. Biochemical analysis demonstrated that sorting significantly increased the ratio of sGAGs to DNA in pellets by almost 15-fold (unsorted: 1.5 ng/ng vs. sorted: 19.89 ng/ng, Figure 2.6A). Similarly, there was an increase in production and homogeneity observed in sorted pellets labeled for COL2A1 (Figure 2.5B). In addition, IHC labeling for COL1A1 showed a slight decrease at the perimeter of the pellet while the labeling for COL10A1 showed an increase in the respective matrix proteins with sorting (Figure 2.5C and 2.5D). Additionally, pellets formed with sorted cells had more localized staining of COL6A1 around the cells as shown with IHC compared to the more diffused pattern observed with unsorted cells (Figure S2.5).

49
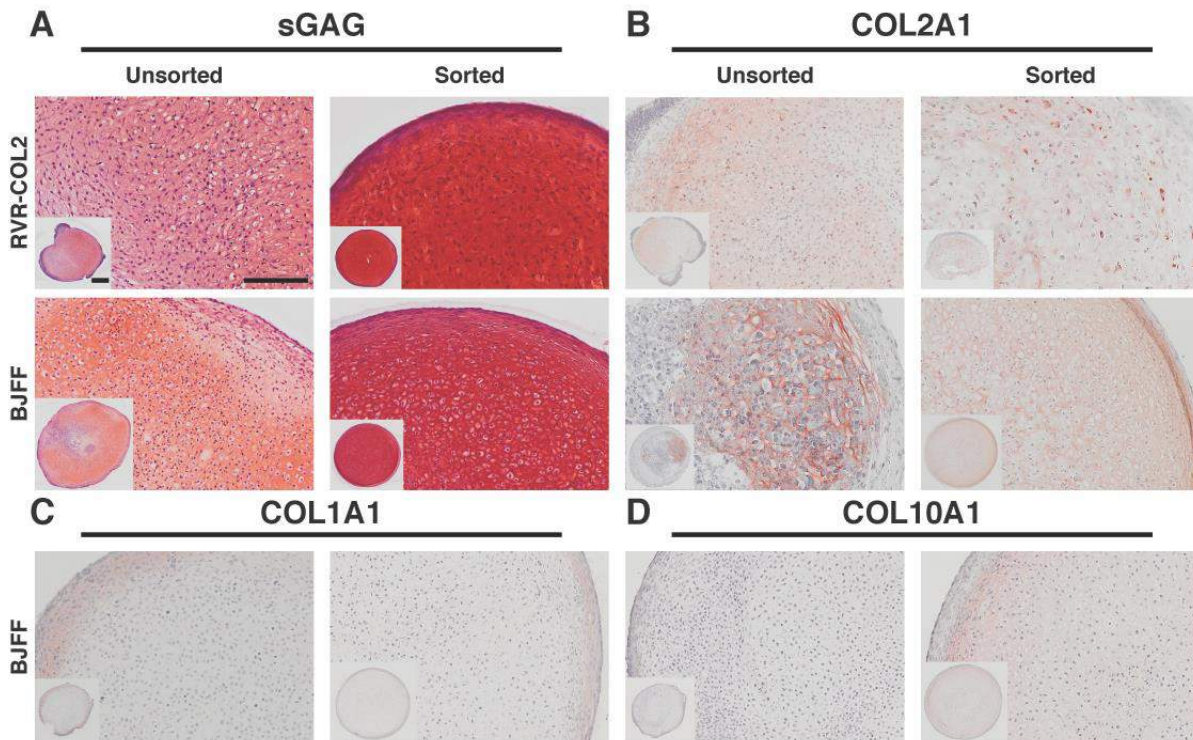
Figure 2.5 Histology and IHC for matrix proteins in RVR-COL2 and BJFF pellets. (**A**) Safranin-O staining for sGAG showing pellets derived from sorted chondroprogenitor cells had more robust staining and homogenous cell morphology compared to pellets derived from unsorted cells in both lines. (**B**) Labeling of COL2A1 showed similar results with an increase in COL2A1 in sorted pellets as opposed to unsorted which has isolated areas of staining. (**C**) There was little labeling of COL1A1 for both unsorted and sorted cell pellets. (**D**) Labeling for COL10A1 was increased with sorting. Scale bar = 200 µm. Inset scale bar = 400 µm.

2.4.7 Expression of cartilaginous genes was significantly higher in pellets derived from triple positive chondroprogenitor cells

Gene expression in pellets derived from unsorted and triple positive-sorted chondroprogenitor cells was analyzed using RT-qPCR. Chondrogenic genes *SOX9* (unsorted: 0.88-fold change vs. sorted: 6.62 fold change), *ACAN* (unsorted: 7.22-fold change vs. sorted: 1614-fold change), and *COL2A1* (unsorted: 0.68-fold change vs. sorted: 1667-fold change) were significantly increased in sorted pellets (Figure 2.6B-D). Additionally, *COL1A1* (unsorted: 0.74-fold change vs. sorted: 25.91-fold change) and *COL10A1* (unsorted: 2.69-fold change vs. sorted: 54.32-fold change) were significantly higher in sorted pellets compared to unsorted (Figure 2.6E-F). Statistical

significance was maintained for all genes when analyzed alternatively (Figure S2.6).
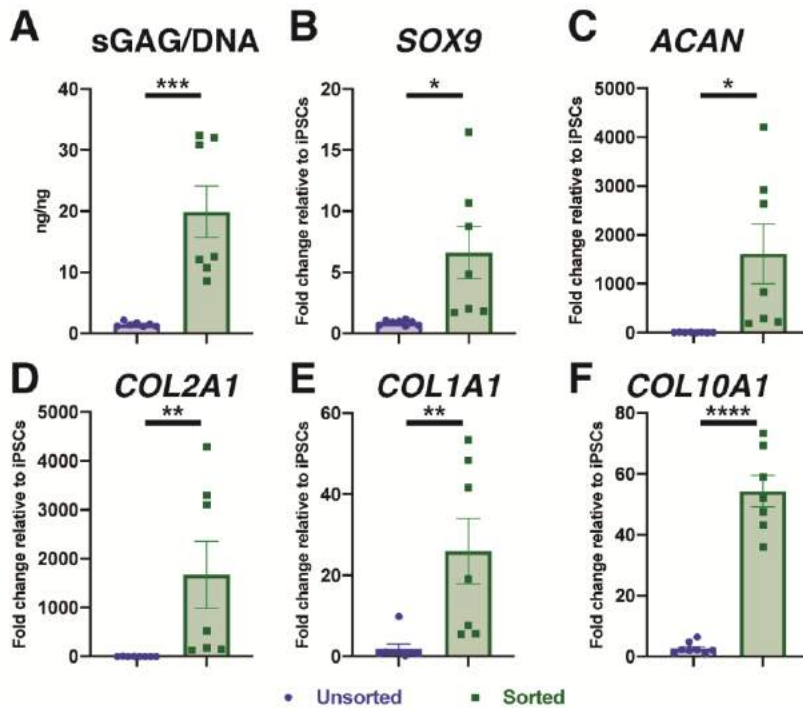
Figure 2.6. Quantitative analysis of matrix production and gene expression. (**A**) Sorting of chondroprogenitor cells prior to chondrogenesis significantly increased the sGAG/DNA ratio to approximately 20 ng/ng. (**B-D**) Expression of chondrogenic genes *ACAN, SOX9,* and *COL2A1* was significantly increased with sorting. (**E-F**) Sorting significantly unregulated fibrocartilage and bone matrix marker *COL1A1*, and hypertrophic cartilage marker *COL10A1*. Gene expression in reference to undifferentiated hiPSCs with housekeeping gene TBP. * $p < 0.05$. ** $p < 0.01$. *** $p < 0.001$. **** $p < 0.0001$. Data represented as mean ± SEM. n = 6-7 per group: 2 experimental replicates, 3-4 technical replicates (pellets).

2.4.8 Chondrogenic capacity was maintained through one passage of unsorted and sorted chondroprogenitor cells

Pellets derived from passage 1 (p1) sorted cells exhibited the most robust and homogenous

safranin-O staining as compared to the pellets derived from sorted cells of later passages and to

the pellets derived from unsorted cells of a similar passage (Figure S2.7). Pellets derived from

p2-4 unsorted and sorted chondroprogenitor cells had comparable staining and cell morphology

with decreased chondrogenic capacity (Figure S2.7).

2.5 Discussion

Using a *COL2A1*-GFP reporter line, we have identified a novel combination of surface markers (i.e., PDGFRβ$^+$/CD146$^+$/CD166$^+$/CD45$^-$) depicting a unique progenitor population with robust chondrogenic potential in hiPSC chondrogenesis. This finding was further confirmed by significantly increased cartilaginous matrix production of the prospectively isolated cells with these selected markers from a wildtype, non-edited hiPSC line. The results of scRNA-seq of sorted cells revealed that cells positive for PDGFRβ, CD146, and CD166 exhibited enhanced cell homogeneity with decreased neurogenic subpopulations. These findings support the hypothesis that sorting of hiPSC-derived chondroprogenitor cells using surface markers can be used to purify progenitor cells with enhanced chondrogenic potential, without the need for genetic modification to improve hiPSC chondrogenesis (*25, 26*).

We previously reported that chondroprogenitor cells at the end of mesodermal lineage differentiation had high expression of CD146 and CD166 (*26*). In the present study, we observed that these markers were also co-expressed with *COL2A1*. CD146 and CD166, along with CD105, have also been shown to be expressed in chondroprogenitors in articular cartilage (*19-21*). While our chondroprogenitor cells did not co-express CD105 (ENG) with *COL2A1,* sorting did enrich *CD105* gene expression. Interestingly, it has been shown that CD105 itself may not indicate chondrogenic potential (*37*). In addition, scRNA-seq showed that sorted cells exhibited increased expression of *ITGB1* (*CD29*) and *ITGA5* (*CD49e*), which have been deemed necessary for chondrogenic differentiation in progenitor cells and MSCs (*18, 19, 38*). Nevertheless, our chondroprogenitor cells had somewhat different expression profiles than skeletal progenitor cells identified previously *in vivo* (*23, 24*). Moderate expression of CD164, a surface marker of the skeletal stem cell (*23*), was conserved between the unsorted and sorted chondroprogenitor cells

52

while many other markers described were absent from both populations including prechondrocyte markers BMPR1β and CD73 (NT5E) (*24*). Therefore, the chondroprogenitor population described in this study is a distinct, unique subpopulation of iPSCs that possesses robust chondrogenic potential.

Several factors may contribute to the differences in cell surface markers that have been. identified as markers of chondrogenesis in these different cell types. First, in our study we used a differentiation protocol which follows the paraxial mesodermal lineage of cartilage (*26, 39*). Different types of cartilage follow various developmental pathways (e.g., paraxial mesoderm vs. lateral plate mesoderm) and therefore the other studies could be investigating these lineages, thus the cells would have different surface marker expression during differentiation (*39-41*). Another explanation may be the time point along the developmental pathway in which the cells are being investigated. Our surface marker profiles are based on the expression of *COL2A1*. While COL2A1 is one of the most prominent matrix proteins in articular cartilage (*4*) and can indicate chondrogenic potential and determination of a chondrogenic fate (*42*), *COL2A1* is a relatively late marker of chondrogenesis (*43*). Therefore, differences between the cell surface markers identified in our study as compared to other previous work may reflect differences in the prescribed differentiation pathway or the specific subpopulation identified.

In addition to the fact that *COL2A1* expression is a later chondrogenic marker, *COL2A1* expression was found throughout the entire unsorted population including neurogenic cells and sorting significantly decreased its overall expression indicating that *COL2A1*+ cells were heterogenous. This finding is consistent with studies showing that *COL2A1* expression may be a broader indicator for the initial lineage specification of a variety of tissues rather than a sole marker for chondrogenesis during embryonic development (*43-45*). Indeed, it has been reported

53

that *COL2A1* is expressed in the floor plate of the central nervous system (*46*), which provides a

plausible explanation for our observation of *COL2A1* expression in neurogenic cells. This may

also explain why there are many *COL2A1* positive cells not expressing the selected surface

markers. CD146, CD166, and PDGFRβ may be specific to chondroprogenitors as opposed to

cells of other lineages also expressing collagen type II thus purifying the population as shown

with increased COL2A1 IHC labeling when compared to sorting for *COL2A1* alone. Following

sorting for these markers, the size of the chondrogenic *SOX9/COL2A1* population was increased

and, while the neural *SOX2* populations were reduced, a *SOX2/TTR* population remained. In fact,

this population had high expression of CD47, an integrin-associated and modulating protein (*33*)

that could be used as an additional marker for sorting in future experiments to improve

homogeneity. The expression of nestin and several mesenchyme markers appeared to be

permissive in sorted cells, suggesting that PDGFRβ/CD146/CD166 triple-positive cells may still

have a similar signature as neural crest cells (*47, 48*) and might come primarily from

mesenchyme populations in unsorted cells. Nonetheless, despite the presence of 6 unique cell

clusters, including the *SOX2/TTR* population, sorted chondroprogenitor cells showed robust

chondrogenic capacity.

The sorted chondroprogenitors, which all express PDGFRβ, CD146, and CD166, were

found to be localized in the mesenchyme clusters of unsorted cells. Alignment of the unsorted

and sorted populations by CCA allowed us to compare similarities and differences between the

two groups. After alignment, the largest cell cluster expressed histone H4 (*HIST1H4C*). Histones

are primarily synthesized during the S-phase of the cell cycle to package the replicated DNA

(*49*), thus indicating the large portion of cells in both sorted and unsorted populations are

proliferative. Furthermore, there was a decrease in insulin-like growth factor binding protein-5

(*IGFBP5*) expression in sorted cells among the *IGFBP5/CO2A1* population compared to unsorted. IGFBP5 plays a role in insulin-like growth factor-1 (IGF-1)-dependent chondrocyte proliferation (*50*) and protects cartilage during OA-induced degeneration (*51*). This may imply that sorted cells may be precursors not fully committed into chondrogenic linage in comparison with unsorted cells. This could be further supported by the observation that sorted cells had increased expression in neural crest and proliferation markers (i.e., *SOX4* and *TUBA1A*, respectively) (*52*). Indeed, for all populations identified in the sorted cells, we found that they exhibited elevated expression in proliferative and mesenchymal genes, further suggesting that sorted cells were primarily derived from mesenchyme populations in unsorted cells. Nonetheless, subpopulations in sorted cells still expressed unique gene signatures as shown by the clustering. This finding implies that chondrocytes may differentiate from mesenchyme cells with a variety of transcriptomic profiles if given the correct signaling cues with appropriate timing.

Cartilaginous pellets derived from sorted chondroprogenitor cells showed a significant increase in chondrogenic matrix production and gene expression along with the elimination of a surrounding layer of non-chondrocyte-like cells. Despite the increase in *COL1A1* gene expression, COL1A1 protein, as indicated by IHC labeling, does not reflect its gene expression, implying a potential possibility of post-transcriptional regulation of COL1A1 in protein translation (*53*). This results also suggest that the matrix produced by the hiPSC-derived chondrocytes is similar to hyaline cartilage instead of fibrocartilage which is rich in COL1A1 protein. Surprisingly, there was also a relatively small increase in IHC labeling of COL10A1, a matrix protein often associated with hypertrophic chondrocytes (*54, 55*). Interestingly, COL6A1 was observed to be more localized around the cells in pellets derived from sorted cells. In developing neonatal cartilage, COL6A1 is found throughout the matrix, but with maturity it is

55

only found in the pericellular matrix surrounding the chondrocytes (*56-58*). The increased expression in COL10A1 at both mRNA and protein levels alongside the co-localization of COL6A1 around chondrocytes suggests that the chondrocytes derived from the sorted cells were at more mature stages as compared to the chondrocytes derived from unsorted cells after 28 days of chondrogenic culture. With maturity and COL10A1 secretion, there is a possibility that these cells may further differentiate into hypertrophic chondrocytes and undergo endochondral ossification. Future studies could be done to investigate the differentiation trajectory with more time in culture and *in vivo*.

As cell sorting can significantly reduce the number of functional cells (*59*), we also examined the effects of cell expansion on differentiation potential of the sorted cells prior to chondrogenesis. Cells in the first passage following sorting exhibit high chondrogenic potential and sGAG staining in pellet culture. However, in subsequent passages, cells showed signs of dedifferentiation and loss of chondrogenic capacity, similar to that observed in primary chondrocytes (*60*) as well as similarly sorted mouse iPSCs (*25*). The decreased chondrogenic potential of sorted cells may result from telomere erosion (*61*), plating density (e.g., cell-cell and cell-matrix interactions) (*60, 62-64*), mechanobiological factors (e.g., plate stiffness and/or coating) (*65, 66*), or culture medium (e.g., low vs. high glucose, growth factors) (*62, 65*). While we used an expansion media similar to MSC expansion media due to similarities of the cells, in the future, the media could be altered by changing the glucose level (*64*) and/or adding growth factors such as fibroblastic growth factor (FGF)-2 and FGF-4, bone morphogenic protein (BMP)-2 and BMP-3, transforming growth factor beta (TGFβ)-3, heparin-binding epidermal growth factor (EGF), and platelet derived growth factor (PDGF)-ββ (*62, 65, 67*) as these have been shown to maintain and improve multipotency and chondrogenic capacity.

2.6 Supplemental Figures
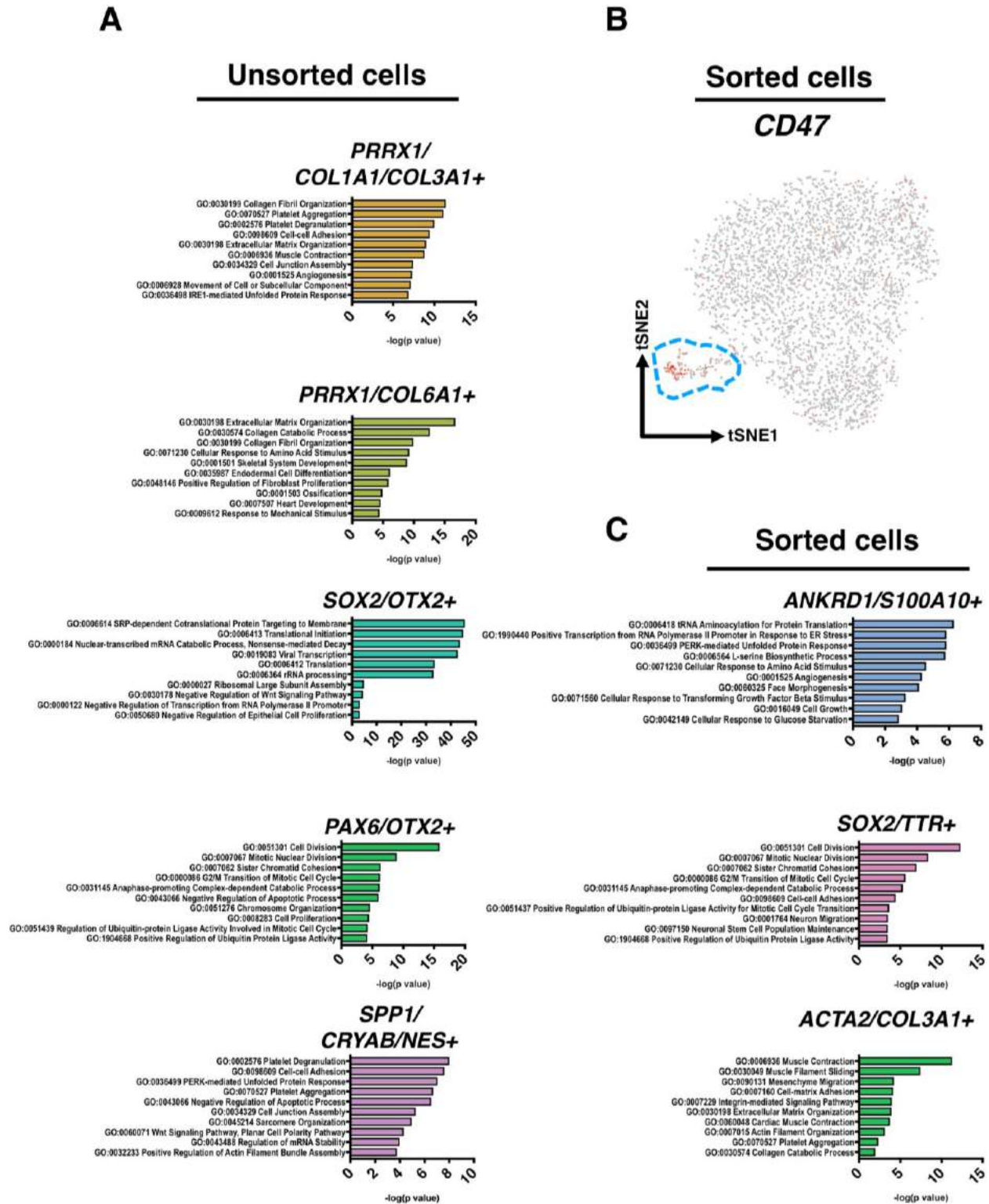
Figure S2.1 GO enrichment analysis of unsorted and sorted cells. Related to Figure 2 and 3. (**A**) Top 10 GO terms (biological process) that were associated with each population in unsorted cells. (**B**) CD47 was highly expressed in SOX2/TTR+ cells. (**C**) Top 10 GO terms (biological process) that were associated with each population in sorted cells.
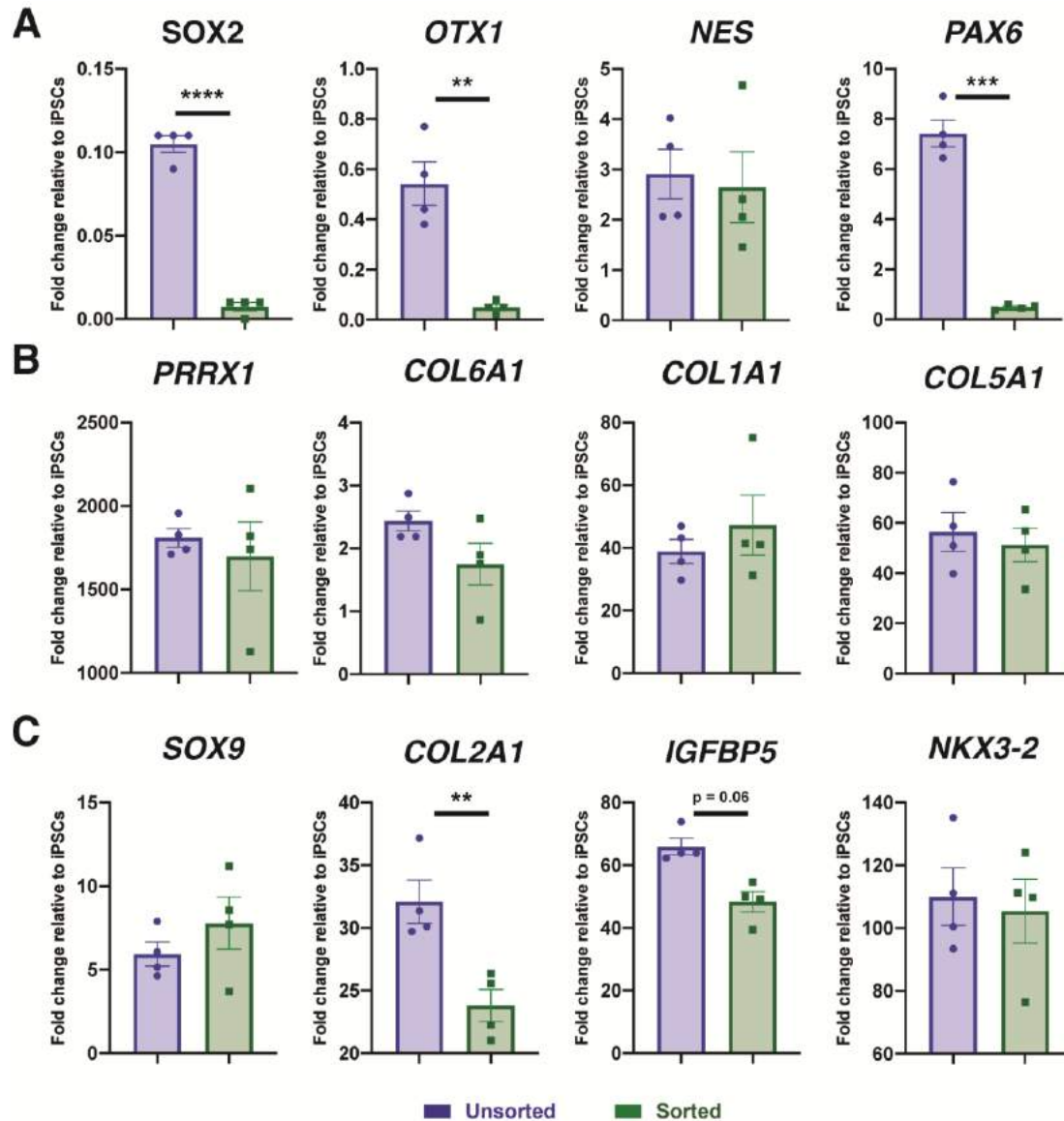
Figure S2.2 Overall gene expression of sorted and unsorted chondroprogenitors. Related to Figure 2 and 3. RT-qPCR reveals differences between sorted and unsorted chondroprogenitor cells in overall expression of (**A**) neurogenic, (**B**) mesenchymal, and (**C**) chondrogenic genes. Gene expression in reference to undifferentiated hiPSCs with housekeeping gene TBP. * $p < 0.05$. *** $p < 0.001$. Data represented as mean ± SEM. n = 4 samples/group.
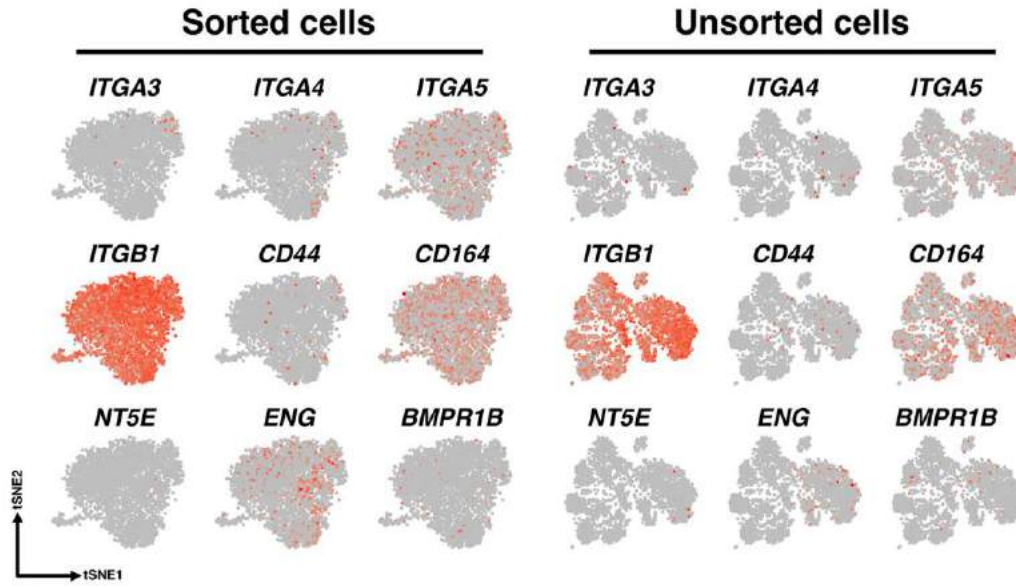
Figure S2.3 Expression profiles of pro-chondrogenic genes in sorted and unsorted chondroprogenitor cells. Related to Figure 2 and 3. scRNA-seq reveals that sorted and unsorted cells had distinct gene expression patterns of several markers that were proposed to be pro-chondrogenic identified by previous studies.
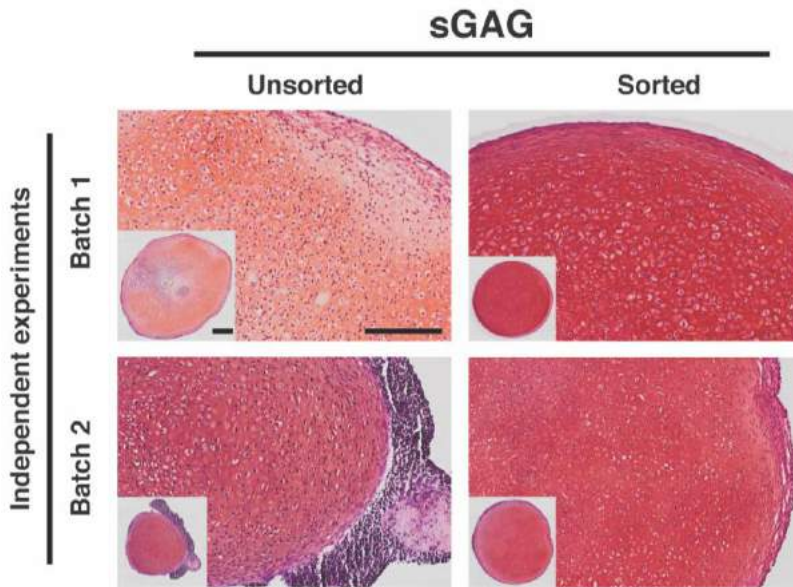
Figure S2.4 Histology for matrix proteins. Related to Figure 5. Safranin-O staining for sGAG showing pellets derived from sorted chondroprogenitor cells had more robust staining and homogenous cell morphology compared to pellets derived from unsorted cells in two individual experimental replicates. Scale bar = 200 µm. Inset scale bar = 400 µm.

COL6A1

Unsorted — Sorted

BJFF
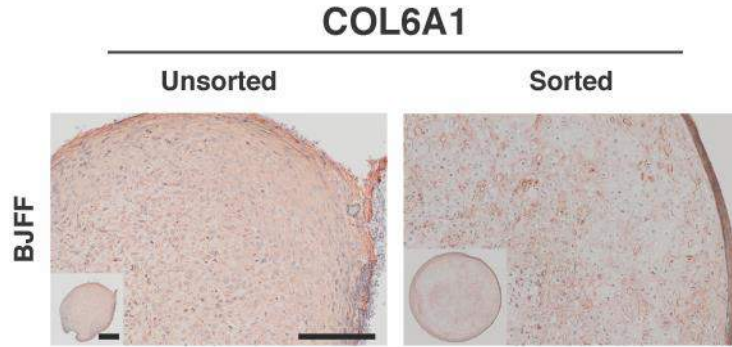
Figure S2.5 IHC labeling for COL6A1. Related to Figure 5. There was more distributed labeling for COL6A1 in unsorted chondroprogenitor pellets compared to the localization around cells in sorted chondroprogenitor pellets. Scale bar = 200 µm. Inset scale bar = 400 µm.
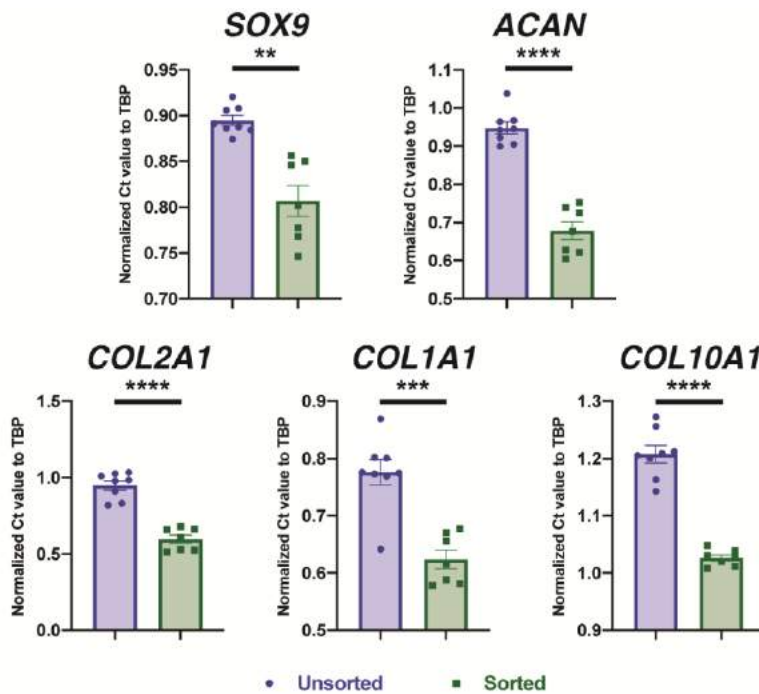
Figure S2.6 Alternative analysis of gene expression. Related to Figure 6. Expression of chondrogenic genes ACAN, SOX9, and COL2A1, fibrocartilage and bone matrix marker COL1A1, and hypertrophic cartilage marker COL10A1 was significantly increased with sorting. CT value of gene of interest was normalized to CT value of housekeeping gene TBP for each sample. ** $p < 0.01$. *** $p < 0.001$. **** $p < 0.0001$. Data represented as mean ± SEM. n = 6-7 per group: 2 experimental replicates, 3-4 technical replicates (pellets).

60
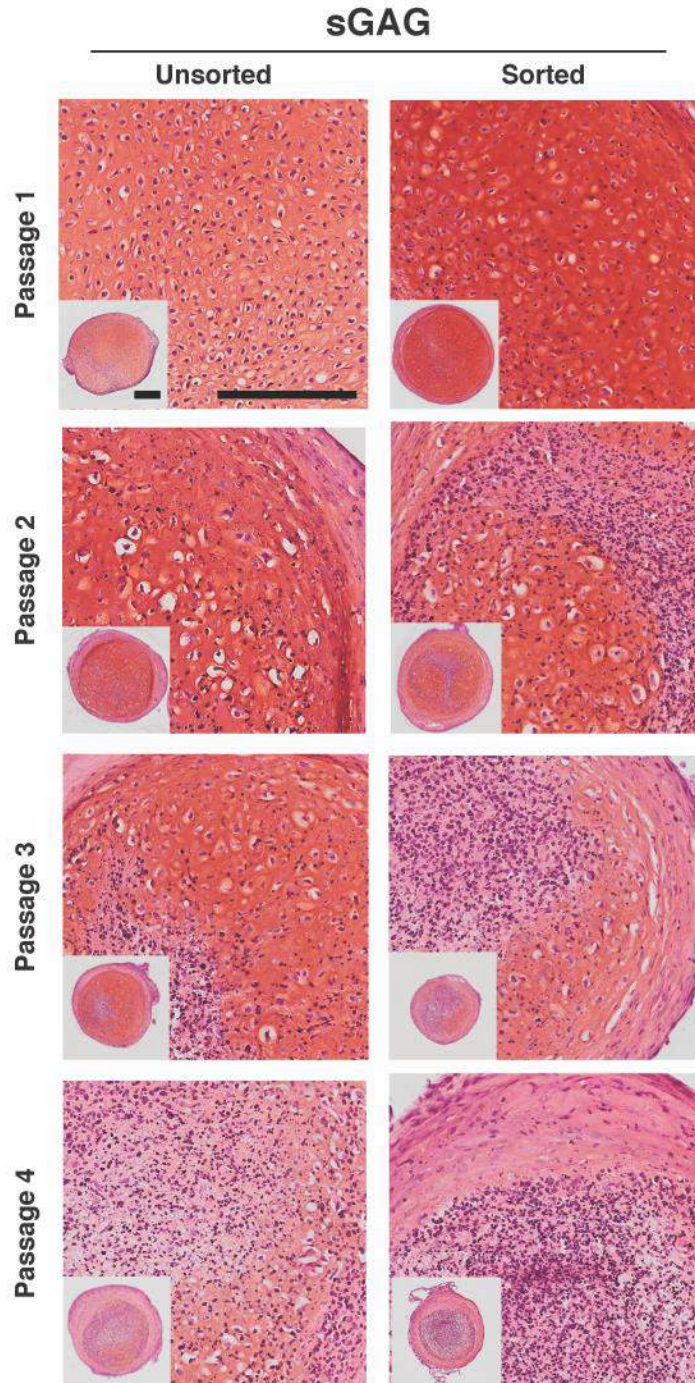
Figure S2.7. Histology of pellets derived from in vitro expanded unsorted and sorted chondroprogenitors. Chondrogenic capacity was maintained after one passage of both unsorted and sorted chondroprogenitor cells as shown by staining for sGAG. There was more robust staining in pellets derived from sorted cells. Safranin-O staining for sGAG showed similar loss of chondrogenic capacity for both unsorted and sorted chondroprogenitor cells through four passages.

2.7 Conclusion

In conclusion, we have identified a unique chondroprogenitor population from hiPSCs which expresses PDGFRβ, CD146, and CD166 and has strong chondrogenic potential. While the population does share some characteristics with previously defined chondroprogenitors and traditionally defined MSCs, it has a distinct profile. The methods and findings in this study will contribute to future cartilage tissue engineering and disease modeling studies to improve understanding and treatment of diseases such as osteoarthritis.

2.8 References

1. J. M. Mansour, in *Kinesiology: The Mechanics and Pathomechanics of Human Movement*. (2003), vol. 2e, chap. 5, pp. 66-75.

2. F. Guilak, Biomechanical factors in osteoarthritis. *Best Pract Res Clin Rheumatol* **25**, 815-823 (2011).

3. Z. Lin, C. Willers, J. Xu, M. H. Zheng, The chondrocyte: biology and clinical application. *Tissue Eng* **12**, 1971-1984 (2006).

4. A. J. Sophia Fox, A. Bedi, S. A. Rodeo, The basic science of articular cartilage: structure, composition, and function. *Sports Health* **1**, 461-468 (2009).

5. F. Berenbaum, T. M. Griffin, R. Liu-Bryan, Review: Metabolic Regulation of Inflammation in Osteoarthritis. *Arthritis Rheumatol* **69**, 9-21 (2017).

6. J. Lieberthal, N. Sambamurthy, C. R. Scanzello, Inflammation in joint injury and post-traumatic osteoarthritis. *Osteoarthritis Cartilage* **23**, 1825-1834 (2015).

7. K. Musunuru, Genome editing of human pluripotent stem cells to generate human cellular disease models. *Dis Model Mech* **6**, 896-904 (2013).

8. K. Takahashi *et al.*, Induction of pluripotent stem cells from adult human fibroblasts by defined factors. *Cell* **131**, 861-872 (2007).

9. S. Yumlu *et al.*, Gene editing and clonal isolation of human induced pluripotent stem cells using CRISPR/Cas9. *Methods* **121-122**, 29-44 (2017).

10. H. Nejadnik *et al.*, Improved approach for chondrogenic differentiation of human induced pluripotent stem cells. *Stem Cell Rev Rep* **11**, 242-253 (2015).

11. A. Yamashita *et al.*, Generation of scaffoldless hyaline cartilaginous tissue from human iPSCs. *Stem Cell Reports* **4**, 404-418 (2015).

12. J. Lee *et al.*, Early induction of a prechondrogenic population allows efficient generation of stable chondrocytes from human induced pluripotent stem cells. *FASEB J* **29**, 3399-3410 (2015).

13. W. M. Suchorska, E. Augustyniak, M. Richter, T. Trzeciak, Comparison of Four Protocols to

Generate Chondrocyte-Like Cells from Human Induced Pluripotent Stem Cells (hiPSCs). *Stem Cell Rev Rep* **13**, 299-308 (2017).

14. Q. Lian *et al.*, Functional mesenchymal stem cells derived from human induced pluripotent stem cells attenuate limb ischemia in mice. *Circulation* **121**, 1113-1123 (2010).

15. A. M. Craft *et al.*, Generation of articular chondrocytes from human pluripotent stem cells. *Nat Biotechnol* **33**, 638-645 (2015).

16. Y. Yoshida, S. Yamanaka, Recent stem cell advances: induced pluripotent stem cells for disease modeling and stem cell-based regeneration. *Circulation* **122**, 80-87 (2010).

17. P. Cahan, G. Q. Daley, Origins and implications of pluripotent stem cell variability and heterogeneity. *Nat Rev Mol Cell Biol* **14**, 357-368 (2013).

18. R. Williams *et al.*, Identification and clonal characterisation of a progenitor cell sub-population in normal human articular cartilage. *PLoS One* **5**, e13246 (2010).

19. E. Vinod, P. Boopalan, S. Sathishkumar, Reserve or Resident Progenitors in Cartilage? Comparative Analysis of Chondrocytes versus Chondroprogenitors and Their Role in Cartilage Repair. *Cartilage* **9**, 171-182 (2018).

20. X. Su *et al.*, CD146 as a new marker for an increased chondroprogenitor cell sub-population in the later stages of osteoarthritis. *J Orthop Res* **33**, 84-91 (2015).

21. S. Alsalameh, R. Amin, T. Gemba, M. Lotz, Identification of mesenchymal progenitor cells in normal and osteoarthritic human articular cartilage. *Arthritis Rheum* **50**, 1522-1532 (2004).

22. F. J. Lv, R. S. Tuan, K. M. Cheung, V. Y. Leung, Concise review: the surface markers and identity of human mesenchymal stem cells. *Stem Cells* **32**, 1408-1419 (2014).

23. C. K. F. Chan *et al.*, Identification of the Human Skeletal Stem Cell. *Cell* **175**, 43-56 e21 (2018).

24. L. Wu *et al.*, Human developmental chondrogenesis as a basis for engineering chondrocytes from pluripotent stem cells. *Stem Cell Reports* **1**, 575-589 (2013).

25. B. O. Diekman *et al.*, Cartilage tissue engineering using differentiated and purified induced pluripotent stem cells. *Proc Natl Acad Sci U S A* **109**, 19172-19177 (2012).

26. S. S. Adkar *et al.*, Step-Wise Chondrogenesis of Human Induced Pluripotent Stem Cells and Purification Via a Reporter Allele Generated by CRISPR-Cas9 Genome Editing. *Stem Cells* **37**, 65-76 (2019).

27. J. Lee *et al.*, Activation of innate immunity is required for efficient nuclear reprogramming. *Cell* **151**, 547-558 (2012).

28. A. Butler, P. Hoffman, P. Smibert, E. Papalexi, R. Satija, Integrating single-cell transcriptomic data across different conditions, technologies, and species. *Nat Biotechnol* **36**, 411-420 (2018).

29. L. van der Maaten, G. Hinton, Visualizing Data using t-SNE. *Journal of Machine Learning Research* **9**, 2579-2605 (2008).

30. D. W. Huang *et al.*, The DAVID Gene Functional Classification Tool: a novel biological module-centric algorithm to functionally analyze large gene lists. *Genome Biol* **8**, R183

(2007).

31. Z. Gu, R. Eils, M. Schlesner, Complex heatmaps reveal patterns and correlations in multidimensional genomic data. *Bioinformatics* **32**, 2847-2849 (2016).

32. K. J. Livak, T. D. Schmittgen, Analysis of relative gene expression data using real-time quantitative PCR and the 2(-Delta Delta C(T)) Method. *Methods* **25**, 402-408 (2001).

33. E. J. Brown, W. A. Frazier, Integrin-associated protein (CD47) and its ligands. *Trends Cell Biol* **11**, 130-135 (2001).

34. W. Zhang *et al.*, Deer thymosin beta 10 functions as a novel factor for angiogenesis and chondrogenesis during antler growth and regeneration. *Stem Cell Res Ther* **9**, 166 (2018).

35. A. Molnar *et al.*, Identification of differentially expressed genes in the developing antler of red deer Cervus elaphus. *Mol Genet Genomics* **277**, 237-248 (2007).

36. D. R. Clemmons, IGF binding proteins and their functions. *Mol Reprod Dev* **35**, 368-374; discussion 374-365 (1993).

37. M. A. Cleary *et al.*, Expression of CD105 on expanded mesenchymal stem cells does not predict their chondrogenic potential. *Osteoarthritis Cartilage* **24**, 868-872 (2016).

38. C. Cicione, S. Diaz-Prado, E. Muinos-Lopez, T. Hermida-Gomez, F. J. Blanco, Molecular profile and cellular characterization of human bone marrow mesenchymal stem cells: donor influence on chondrogenesis. *Differentiation* **80**, 155-165 (2010).

39. K. M. Loh *et al.*, Mapping the Pairwise Choices Leading from Pluripotency to Human Bone, Heart, and Other Mesoderm Cell Types. *Cell* **166**, 451-467 (2016).

40. R. S. Decker, E. Koyama, M. Pacifici, Genesis and morphogenesis of limb synovial joints and articular cartilage. *Matrix Biol* **39**, 5-10 (2014).

41. M. E. Bronner, N. M. LeDouarin, Development and evolution of the neural crest: an overview. *Dev Biol* **366**, 2-9 (2012).

42. T. D. Grant *et al.*, Col2-GFP reporter marks chondrocyte lineage and chondrogenesis during mouse skeletal development. *Dev Dyn* **218**, 394-400 (2000).

43. R. A. Kosher, M. Solursh, Widespread distribution of type II collagen during embryonic chick development. *Dev Biol* **131**, 558-566 (1989).

44. W. M. Kulyk, C. N. Coelho, R. A. Kosher, Type IX collagen gene expression during limb cartilage differentiation. *Matrix* **11**, 282-288 (1991).

45. H. D. Nah *et al.*, In situ hybridization analysis of the expression of the type II collagen gene in the developing chicken limb bud. *Coll Relat Res* **8**, 277-294 (1988).

46. Y. L. Yan, K. Hatta, B. Riggleman, J. H. Postlethwait, Expression of a type II collagen gene in the zebrafish embryonic axis. *Dev Dyn* **203**, 363-376 (1995).

47. J. Isern *et al.*, The neural crest is a source of mesenchymal stem cells with specialized hematopoietic stem cell niche function. *Elife* **3**, e03696 (2014).

48. C. Coste *et al.*, Human bone marrow harbors cells with neural crest-associated characteristics like human adipose and dermis tissues. *PLoS One* **12**, e0177962 (2017).

49. M. A. Osley, The regulation of histone synthesis in the cell cycle. *Annu Rev Biochem* **60**, 827-861 (1991).

50. D. Kiepe *et al.*, Intact IGF-binding protein-4 and -5 and their respective fragments isolated from chronic renal failure serum differentially modulate IGF-I actions in cultured growth plate chondrocytes. *J Am Soc Nephrol* **12**, 2400-2410 (2001).

51. D. R. Clemmons *et al.*, Inhibition of insulin-like growth factor binding protein 5 proteolysis in articular cartilage and joint fluid results in enhanced concentrations of insulin-like growth factor 1 and is associated with improved osteoarthritis. *Arthritis Rheum* **46**, 694-703 (2002).

52. E. V. Sviderskaya *et al.*, Functional neurons and melanocytes induced from immortal lines of postnatal neural crest-like stem cells. *FASEB J* **23**, 3179-3192 (2009).

53. R. I. Schwarz, Collagen I and the fibroblast: high protein expression requires a new paradigm of post-transcriptional, feedback regulation. *Biochem Biophys Rep* **3**, 38-44 (2015).

54. M. Pacifici *et al.*, Hypertrophic chondrocytes. The terminal stage of differentiation in the chondrogenic cell lineage? *Ann N Y Acad Sci* **599**, 45-57 (1990).

55. H. M. Kronenberg, Developmental regulation of the growth plate. *Nature* **423**, 332-336 (2003).

56. F. Guilak, R. J. Nims, A. Dicks, C. L. Wu, I. Meulenbelt, Osteoarthritis as a disease of the cartilage pericellular matrix. *Matrix Biol* **71-72**, 40-50 (2018).

57. E. H. Morrison, M. W. Ferguson, M. T. Bayliss, C. W. Archer, The development of articular cartilage: I. The spatial and temporal patterns of collagen types. *J Anat* **189 (Pt 1)**, 9-22 (1996).

58. A. F. Sherwin, D. H. Carter, C. A. Poole, J. A. Hoyland, S. Ayad, The distribution of type VI collagen in the developing tissues of the bovine femoral head. *Histochem J* **31**, 623-632 (1999).

59. C. W. t. Shields, C. D. Reyes, G. P. Lopez, Microfluidic cell sorting: a review of the advances in the separation of cells from debulking to rare cell isolation. *Lab Chip* **15**, 1230-1249 (2015).

60. E. M. Darling, K. A. Athanasiou, Rapid phenotypic changes in passaged articular chondrocyte subpopulations. *J Orthop Res* **23**, 425-432 (2005).

61. I. M. Khan, J. C. Bishop, S. Gilbert, C. W. Archer, Clonal chondroprogenitors maintain telomerase activity and Sox9 expression during extended monolayer culture and retain chondrogenic potential. *Osteoarthritis Cartilage* **17**, 518-528 (2009).

62. G. Schulze-Tanzil *et al.*, Redifferentiation of dedifferentiated human chondrocytes in high-density cultures. *Cell Tissue Res* **308**, 371-379 (2002).

63. I. Ustunel *et al.*, The immunohistochemical localization of notch receptors and ligands in human articular cartilage, chondroprogenitor culture and ultrastructural characteristics of these progenitor cells. *Acta Histochem* **110**, 397-407 (2008).

64. Y. Jiang *et al.*, Human Cartilage-Derived Progenitor Cells From Committed Chondrocytes for Efficient Cartilage Repair and Regeneration. *Stem Cells Transl Med* **5**, 733-744 (2016).

65. S. Kaitainen *et al.*, TiO2 coating promotes human mesenchymal stem cell proliferation

without the loss of their capacity for chondrogenic differentiation. *Biofabrication* **5**, 025009 (2013).

66. Y. Chen *et al.*, Morphology and adhesion of mesenchymal stem cells on PLLA, apatite and apatite/collagen surfaces. *J Mater Sci Mater Med* **19**, 2563-2567 (2008).

67. D. L. Coutu, J. Galipeau, Roles of FGF signaling in stem cell self-renewal, senescence and aging. *Aging (Albany NY)* **3**, 920-933 (2011).

Chapter 3

Single Cell Transcriptomic Analysis of Human Pluripotent Stem Cell Chondrogenesis

Partially adapted from: Wu CL*, Dicks A*, Steward N, Tang R, Katz DB, Choi YR, Guilak F.

Single cell transcriptomic analysis of human pluripotent stem cell chondrogenesis. *Nature*

Communications. 2021 Jan 13;12(1):362.

3.1 Abstract

The therapeutic application of human induced pluripotent stem cells (hiPSCs) for cartilage

regeneration is largely hindered by the low-yield of chondrocytes accompanied by unpredictable

and heterogeneous off-target differentiation of cells during chondrogenesis. Here, we combine

bulk RNA sequencing, single-cell RNA sequencing, and bioinformatic analyses, including

weighted gene co-expression analysis (WGCNA), to investigate the gene regulatory networks

regulating hiPSC differentiation under chondrogenic conditions. We identify specific *Wnt*s and

MITF as hub genes governing the generation of off-target differentiation into neural cells and

melanocytes during hiPSC chondrogenesis. With heterocellular signaling models, we further

show that Wnt signaling produced by off-target cells are responsible for inducing chondrocyte

hypertrophy. By targeting Wnts and MITF, we eliminate these cell lineages, significantly

enhancing the yield and homogeneity of hiPSC-derived chondrocytes. Collectively, our findings

identify the trajectories and molecular mechanisms governing cell fate decision in hiPSC

chondrogenesis, as well as dynamic transcriptome profiles orchestrating chondrocyte

proliferation and differentiation.

3.2 Introduction

Osteoarthritis (OA) is a debilitating joint disease characterized by cartilage degeneration as well as pathologic remodeling of other joint tissues. Cartilage has limited intrinsic healing capacity, motivating the application of stem cells for regenerative therapies. In this regard, the advent of human induced pluripotent stem cells (hiPSCs) has served as a major breakthrough towards cartilage regenerative therapies and *in vitro* disease modeling for OA drug discovery (*1*). However, the development of protocols to consistently differentiate hiPSCs into chondrocytes remains challenging. Early studies reported that chondrocytes can be generated from hiPSCs via embryoid body formation followed by monolayer expansion of mesodermal cells and three-dimensional cell pellet culture in chondrogenic induction medium (*2, 3*). Despite some success, this approach was proven difficult to reproduce across different iPSC lines, potentially due to variability in lots of fetal bovine serum generally used for cell expansion. Thus, recent strategies have sought to use serum-free and chemically defined medium (*4-6*). By coupling inductive and repressive signals required for mesoderm specification in embryonic development (*7*), we established a step-wise hiPSC chondrogenic differentiation protocol that was validated with multiple hiPSC lines and in several laboratories (*8*).

An important consideration in the differentiation process of hiPSCs is that they are considered to be in a primed pluripotent state with increased genome-wide DNA methylation compared to ground state naïve pluripotent cells, such as pre-implantation blastocysts (*9*). Therefore, even directed differentiation of hiPSCs can lead to unpredictable formation of off-target cell populations. However, the gene regulatory networks (GRNs) leading to on- or off-target differentiation of hiPSCs, as well as the effect of the undesired cells on hiPSC chondrogenesis (i.e., heterocellular signaling), remain to be elucidated, particularly at the single

cell level.

Here, we apply bulk RNA sequencing (bulk RNA-seq) and single-cell RNA sequencing (scRNA-seq) throughout the process of mesodermal and chondrogenic differentiation of hiPSCs to map the dynamics of gene expression. By exploiting single cell transcriptomics, we confirm the mesodermal and chondrogenic differentiation of hiPSCs in addition to identifying the GRNs and critical hub genes regulating the generation of heterogenous off-target cells. We demonstrate that homogeneity of hiPSC chondrogenesis can be significantly improved by inhibiting the molecular targets Wnts and MITF. In summary, this study develops and validates an enhanced hiPSC chondrogenic differentiation protocol.

3.3 Methods

3.3.1 hiPSC lines and culture

Three distinct hiPSC lines were used in the current study: STAN, ATCC, and BJFF. STAN line was purchased from WiCell (#STAN061i-164-1), ATCC line was acquired from ATCC (#ATCCACS-1019), and BJFF was obtained from the Genome Engineering and iPSC Core at Washington University in Saint Louis. All three lines were reprogrammed by Sendai virus from human foreskin fibroblasts and confirmed to be karyotypically normal and mycoplasma free. STAN and BJFF hiPSCs were maintained on vitronectin coated 6-well plates (Thermo Fisher Scientific, #A31804) in Essential 8 Flex medium (Thermo Fisher Scientific, #A2858501). ATCC hiPSCs were cultured on CellMatrix Basement Membrane Gel coated 6-well plates (ATCC, #ACS3035) in Pluripotent Stem Cell SFM XF/FF medium (ATCC, #ACS3002). Cells were fed daily, and passaged with ReLeSR (STEMCELL Technologies, #05872). All hiPSC lines were maintained below passage 30. Information regarding the cell lines can be found in Table 3.1.

3.3.2 hMSCs and culture

Discarded and deidentified waste tissue from the iliac crests of adult bone marrow transplant donors were collected in accordance with the institutional review board of Washington University in Saint Louis. Human bone marrow-derived MSCs (hMSCs) were isolated by their physical adherence to plastic culture vessels. (*10*) Cells were expanded and maintained in expansion medium consisting of DMEM-low glucose (Thermo Fisher Scientific, #11885092), 1% penicillin/streptomycin (P/S, Thermo Fisher Scientific, #15140-122), 10% lot-selected fetal bovine serum (FBS; Atlanta Biologicals, #S11550), and 1 ng ml^{-1} basic fibroblast growth factor (R&D Systems, #233-FB). Three individual donors were used as biologic replicates in subsequent experiments (Table 3.1).

Table 3.1 Subject details.

Donor ID	Study ID	Cell type	GenoType	Age, Sex
PHBI-BA-060	STAN	iPSC	wt/wt	1 yr, M
SCRC-1041	ATCC	iPSC	wt/wt	Newborn, M
BJFF.6	BJFF	iPSC	wt/wt	Newborn, M
hMSC3	Donor 1	MSC	wt/wt	51, F
hMSC4	Donor 2	MSC	wt/wt	38, M
hMSC6	Donor 3	MSC	wt/wt	26, F

3.3.3 Mesodermal differentiation

hiPSCs were induced into mesodermal differentiation in monolayer at 40% confluency (*7*). Each day, cells were rinsed with wash medium consisting of 50% IMDM GlutaMAX (IMDM, Fisher Scientific, #31980097) and 50% Ham's F12 Nutrient Mix (F12, Fisher Scientific, #31765092) to remove previous medium. hiPSCs were then fed daily to sequentially drive mesodermal differentiation similar to those identified in embryonic development with various sets of growth

factors and small molecules supplemented in mesodermal differentiation medium consisting of IMDM and F12 with 1% chemically defined lipid concentrate (Gibco), 1% insulin/human transferrin/selenous acid (ITS+, Corning, #354352), 1% P/S (Thermo Fisher Scientific, #15140-122), and 450 µM 1-thioglycerol (Sigma–Aldrich, #M6145). Cells were induced to the anterior primitive streak with 30 ng ml^{-1} of Activin A (R&D Systems, #338-AC), 4 µM CHIR99021 (Stemgent, #04-0004), and 20 ng ml^{-1} human fibroblast growth factor (FGF; R&D Systems, #233-FB-025/CF) for 24 hours. On the second day, cells were driven to paraxial mesoderm with 2 µM SB-505124 (Tocris, #3263), 3 µM CHIR99021, 20 ng ml^{-1} FGF, and 4 µM dorsomorphin (Stemgent, #04-0024). Then, cells were treated with 2 µM SB5, 4 µM DM, 1 µM Wnt-C59 (C59; Cellagent Technology, #C7641-2s), and 500 nM PD173074 (Tocris, #3044) to become early somite on the third day. For the fourth through sixth days, cells were driven to the sclerotome with daily feedings of 2 µM purmorphamine (Stemgent, #04-0009) and 1 µM C59. Finally, for six days, cells were driven to the chondroprogenitor stage (Cp) with 20 ng ml^{-1} of human bone morphogenetic protein 4 (BMP4; R&D Systems, #314-BP-010/CF) daily (Figure S3.1A).

At each stage, some cells were dissociated using TrypLE (Gibco, #12604013) at 37ºC for 3 mins followed by adding an equal part of neutralizing medium consisting of DMEM/F-12, GlutaMAXTM (DMEM/F12; Thermo Fisher Scientific, #10565042) with 10% FBS (Atlanta Biologicals) and 1% P/S. The dissociated cells were either used for bulk RNA-seq, scRNA-seq, chondrogenic differentiation, or fluorescence-activated cell sorting (FACS) as appropriate.

3.3.4 Chondrogenic differentiation

Cells dissociated at Cp stage were re-suspended at 5 x 10^5 cells per mL in chondrogenic medium consisting of DMEM/F-12, 1% FBS, 1% ITS+, 55 µM β-mertcaptoethanol, 100 nM dexamethasone (DEX; Sigma-Aldrich, #D4902), 1% NEAA (Gibco, #11140050), 1% P/S, 10 ng

ml^{-1} human transforming growth factor beta 3 (TGF-β3; R&D Systems, #243-B3-010), 50 µg ml^{-1} L-ascorbic acid 2-phosphate (ascorbate; Sigma-Aldrich, #A8960), and 40 µg ml^{-1} L-Proline (proline; Sigma-Aldrich, #P5607). Cells were then centrifuged for 5 min at 300x g to form a pellet. Chondrogenic pellets were cultured at 37ºC for up to 42 days.

On the day of collection for bulk RNA-seq experiments, 3-4 pellets per experimental group were pooled together and washed once with PBS, snap frozen in 300 µl of Buffer RL (Norgen Biotek), and stored at -80ºC until processing for RNA extraction. At harvesting time points for scRNA-seq experiments, 6-8 pellets per experimental group were pooled and digested with 0.04% type 2 collagenase solution in DMEM/F12 for 1hr. Cells were washed once with PBS, re-suspended in standard freezing medium, and stored in liquid nitrogen until needed.

3.3.5 C59 and ML329 treatment for Wnt and MITF inhibition

For C59 treatment for Wnt inhibition during chondrogenesis, pellets were treated with either 10 ng ml^{-1} TGF-β3 (control group) or a combination of 10 ng ml^{-1} TGF-β3 and 1 µM C59 in chondrogenic medium from d0 to d42 as appropriate. For C59 and ML329 treatment (ML, Axon Medchem, HY-101464) for Wnt and MITF inhibition during chondrogenesis, pellets were treated with either 10 ng ml^{-1} TGF-β3 (control group), a combination of 10 ng ml^{-1} TGF-β3 and 1 µM ML, a combination of 10 ng ml^{-1} TGF-β3 and 1 µM C59, or a combination of 10 ng ml^{-1} TGF-β3, 1 µM ML and 1 µM C59 in chondrogenic medium from d0 to d42 as appropriate.

3.3.6 Wnt ligands treatment during chondrogenesis

For Wnt ligands treatment during chondrogenesis, pellets were treated with either 10 ng/ml TGF-β3 (control group) or a combination of 10 ng ml^{-1} TGF-β3 and 100 ng ml^{-1} individual Wnt ligand (Wnt2B, Wnt3A, Wnt4, Wnt5B, or Wnt7B, all from R&D system) in chondrogenic medium from d0 to d42 as appropriate. For Wnt ligands treatment during the Cp stage, cells were

supplemented with either 20 ng ml^{-1} BMP4 (R&D Systems, #314-BP-010) alone (control group), a combination of 20 ng ml^{-1} BMP4 and 1 μM C59, or a combination of 20 ng ml^{-1} BMP4 and 100 ng ml^{-1} Wnt3A (R&D Systems, #5036-WN-010) in mesodermal differentiation medium from d7 to d12.

3.3.7 Animal experiments

All animal procedures were approved by Institutional Animal Care and Use Committee (IACUC) at Washington University in Saint Louis. Male NSG mice (NOD.Cg-*Prkdc^{scid} Il2rg^{tm1Wjl}*/SzJ, #005557, Jackson laboratory) at age of 18-20 weeks-old were used for human xenograft implantation in the in the dorsal region (subcutaneous) or in osteochondral defects in the knee joints of mice. Mice were housed under a 12hr light/12hr dark cycle with ambient temperature and humidity. NSG mice were anesthetized with 3% isoflurane in oxygen for all surgical procedures. For subcutaneous implantation, the skin was shaved and sterilized over the implantation site using standard sterile techniques. A mid-scapular incision was made, and a hemostat was inserted into the skin incision to create a pocket for implantation. A d14 hiPSC chondrogenic pellet was then inserted into the pockets. The incision of the skin was closed with 8-0 suture with taper point (PolysorbTM, Covidien, #L-2800). Tissue adhesive was applied to the skin wound area. For implantation in osteochondral defects in the knee, a 3 mm long medial parapatellar incision was made in the left hindlimb, and the knee joint was exposed via lateral dislocation of the patella. An osteochondral defect (1 mm in diameter and 1 mm in depth) in the trochlear groove of femur was created by a 1 mm micro bone drill (Roboz, #RS-6300A). All debris were removed by sterile PBS washes. Mild hemorrhage from the fat pad was controlled by epinephrine 1:1000 (International Medication Systems, #491590) followed by sterile PBS wash. A d14 hiPSC chondrogenic pellet was implanted into the defect, and the patella was re-

positioned to its original anatomical location. Mice with osteochondral defects that did not receive pellet implantation were used as control group. After implantation, the subcutaneous layer and skin were closed with 8-0 suture with taper point followed by the application of tissue adhesive to the skin wound area. After surgery, the mice were allowed to move freely within their cages. After 14- and 28-days post-implantation, mice were sacrificed for pellet harvest for histological analysis.

3.3.8 RNA isolation, library preparation, and bulk RNA-seq

To determine transcriptome profiles over the course of differentiation, three hiPSCs lines (ATCC, BJFF, and STAN) as biological replicates at various differentiation stages (6 mesodermal and 5 chondrogenic stages per cell line; i.e., total 33 samples) were collected for bulk RNA-seq. Cell samples were thawed on ice, and pellet samples were homogenized with zirconia beads (BioSpec Products, # 11079110zx) and a miniature bead beater. RNA was then isolated from all samples using the Total RNA Purification Kit according to the manufacture's protocol (Norgen Biotek, #37500). RNA was eluted in 20 μl of diethylpyrocarbonate-treated water. The quality and quantity of RNA from each sample was evaluated by RNA Analysis ScreenTape (Agilent, #5067-5576) on bioanalyzer (Agilent 4200 Tapestation). Only samples with a RIN value larger than 0.8 were submitted to the Genome Technology Access Center (GTAC sequencing core) at Washington University in St. Louis for library preparation and bulk RNA-seq. Libraries were prepared using TruSeq Stranded Total RNA with Ribo-Zero Gold kit (Illumina). Sequencing was performed on a HiSeq2500 instrument (Illumina) (1 x 50 bp reads) with a sequencing depth of 30 million reads per sample.

3.3.9 Preprocessing of bulk RNA-seq data

Reads were processed using an in-house pipeline and open-source R packages as previously

described (*11*). Raw reads were first trimmed using Cutadapt to remove low quality bases and

reads (*12*). After trimming, processed reads were aligned to the human reference genome

GRCh38 (version 90) by STAR (*13*), and the number of aligned reads to each annotated genes or

transcripts (GENCODE v21) was performed using *featureCounts* from the Subread package

(v1.4.6) (*14*).

3.3.10 DEGs and GO enrichment analysis and of bulk RAN-seq data

After quality control, un-normalized gene counts were read into DESeq2 R package by

DESeqDataSetFromMatrix function as instructed by the package tutorial (*15*). Genes that were

expressed by less than 10 cells were then removed. Next, we used *DESeq* and *results* functions

which implement Wald test in DESeq2 to determine the differentially expressed genes (DEGs)

between two consecutive differentiation stages. In this process, the estimation of size factors

(i.e., controlling for differences in the sequencing depth of the samples), the estimation of

dispersion values for each gene, and fitting a generalized linear model were performed. The

Gene counts were also averaged from three hiPSC lines. Top 20 DEGs between two consecutive

stages were selected and visualized using ComplexHeatmap R package. To observe the temporal

expression of a given gene for each hiPSC line, the count matrix was regularized-logarithm

transformed via *rlog* function first, and we used *plotCounts* function in DESeq2 to visualize the

expression pattern of the gene. Furthermore, regularized-logarithm transformed counts were also

used for principle component analysis (PCA) and PCA plots were visualized by *ggplot* function

in ggplot2 R package (*16*).

We next performed gene ontology (GO) enrichment analysis of the genes in mesodermal

and chondrogenic stages using GAGE R package (Generally Applicable Gene-set/Pathway

Analysis), whose algorism evaluates the coordinated up- or down-differential expression over

gene sets defined by GO terms (*17*). Significantly upregulated GO terms with their associated p

values in biological process, molecular function, and cellular component were plotted by

GraphPad Prism (version 8.0; GraphPad Software). Furthermore, GAGE analysis also reveals

that 134 out of 205 genes defined by GO term cartilage development (GO:0051216) were

significantly increased during our differentiation process. Thus, a heatmap was generated to

investigate the expression levels of these genes at various stages using ComplexHeatmap R

package (*18*).

3.3.11 10X chromium platform scRNA-seq

Cells were thawed at 37ºC and resuspended in PBS + 0.04% BSA at concentration of 2,000 cells

per μl. Cell suspensions were submitted to the GTAC sequencing core at Washington University

in St. Louis for library preparation and sequencing. In brief, 10,000 cells per sample were loaded

on a Chromium Controller (10x Genomics) for single capture. Libraries were prepared using

Single Cell 3′ Library & Gel Bead Kit v2 (#120237 10x Genomics) following manufacture's

instruction. A single cell emulsion (Gel Bead-In-EMulsions, GEMs) is created by making

barcoded cDNA unique to each individual emulsion. Recovery agent was added to break GEM

and cDNA was then amplified. A library is produced via end repair, dA-tailing, adaptor ligation,

post-ligation cleanup with SPRIselect, and sample index PCR. The quality and concentration of

the amplified cDNA was evaluated by Bioanalyzer (Agilent 2100) on a High Sensitivity DNA

chip (Agilent, #5065-4401). Only cDNA with average library size 260-620 bp were used for

sequencing. Sequencing was performed by Illumina HiSeq2500 with the following read length:

26 bp for Read1, 8 bp for i7 Index, and 98 bp for Read2. We generally acquired ~180 million

reads per library (sample). A species mixing experiment (mouse adipose stem cells and human

iPSCs, 1:1 mixture) was also performed prior to running on actual sample to ensure good quality

76

of single cell capture (i.e., cell doublet rate < 5%).

3.3.12 Preprocessing of scRNA-seq data

Paired-end sequencing reads were processed by Cell Ranger (10x Genomics software, version

2.0.0). Reads were aligned to the GRCh38 (version 90) for genome annotation, demultiplexing,

barcode filtering, and gene quantification. Cell Ranger also removes any barcode that has less

than 10% of the 99th percentile of total unique molecular identifiers (UMI) counts per barcode as

these barcodes are associated with empty droplets. After this quality control, gene barcode

matrices for each sample were generated by counting the number of UMIs for a given gene (as

row) in individual cell (as column). For each sample, ~2,200-2,500 cells were captured.

3.3.13 Unsupervised clustering analysis and annotation

To assess the difference in composition of cell populations, we performed global unsupervised

clustering analysis scRNA-seq datasets. First, gene barcode matrices were input into Seurat R

package (version 2.4) (*19*). We then removed the low-quality cells with less than 200 or more

than 7,000 detected genes, or if their mitochondrial gene content was more than 5%. Note that

the cutoff criteria were adjusted in few cases due to the sequencing depth and the variations in

mitochondrial gene content from datasets. Genes that were detected in less than 3 cells were

filtered out. After filtering out low-quality cells or cell doublets, the gene expression was then

natural log transformed and normalized for scaling the sequencing depth to 10,000 molecules per

cell. Next, to reduce the variance introduced by unwanted sources, we regressed out variation in

gene expression driven by cell cycle stages and mitochondrial gene expression with

vars.to.regress argument in function *ScaleData* in Seurat. We then used *FindVariableGenes*

function in Seurat to identify highly variable genes across cells for downstream analysis. These

steps resulted in (1) total 8,547 cells with average 1,882 highly variable genes from stages of

hiPSCs, Scl, and CP, (2) total 10,648 cells with average 2,061 highly variable genes from stages

of TGF-β3-treated pellets (d1, d3, d7, d14, d28, and d42), and (3) total 7,997 cells with average

1,886 highly variable genes from TGF-β3+C59-treated pellets (d7, d14, d28, and d42) for

downstream analysis. Detailed cells numbers passed quality control steps for each stage are listed

in Table S3.1. Dimensionality reduction on the data was then performed by computing the

significant principal components on highly variable genes. We then performed unsupervised

clustering by using *FindClusters* function in Seurat with the resolution argument set to 0.6 and

clusters were then visualized in tSNE plot (*20*).

DEGs among each cell cluster were determined using *FindAllMarkers* function in Seurat.

DEGs expressed in at least 25% cells within the cluster and with a fold change of more than 0.25

in log scale were considered marker genes of the cluster. To determine the biology functions of

the marker genes from a given cluster, we performed Gene Ontology (GO) enrichment analysis

by using The DAVID Gene Functional Classification Tool (http://david.abcc.ncifcrf.gov; version

6.8) (*21*). By comparing these unique biological GO terms with existing RNA-seq datasets and

the literature, we were able to annotate cell clusters. Additionally, the top 10 enriched GO terms

from biological function category with associated p values were visualized GraphPad Prism

(version 8.0; GraphPad Software).

3.3.14 Cell cycle analysis of scRNA-seq data

CellCycleScoring function in Seurat was used to determine a cell cycle score on each cell

according to its gene expression of G2/M phase (54 genes) and S phase (43 genes) markers (*22*).

Based on this scoring system, fractions of each cell cluster with given cell cycle score in total

cell population were computed and plotted.

3.3.15 CCA for integrated analysis of multiple scRNA-seq datasets

To compare cell types and to identify their associated DEGs between distinct experimental

conditions such as batch effect, C59 treatment, or differentiation stages (i.e., time points), we

applied canonical correlation analysis (CCA), a computational strategy implemented in Seurat

for integrated analysis of multiple datasets. First, the top 1,000 highly variable genes from each

dataset were selected. We then use *RunCCA* function or *RunMultiCCA* function (if more than 2

datasets) to identify common sources of variation resulting from experimental conditions and to

merge the multiple objects into a single dataset. We next determined the top principal

components of the CCA by examining a saturation in the relationship between the number of

principle components and the percentage of the variance explained using the *MetageneBicorPlot*

function. By using selected top principal components, we aligned the CCA subspaces with

AlignSubspace function, which returns a new dimensional reduction matrix allowing for

downstream clustering and DEG analyses. DEG analysis was performed on the cells from

different datasets but grouped in the same cluster (i.e., conserved cell types between two

conditions) after CCA alignment. The methods for cell clustering, identification of conserved

cell types and DEGs, as well as annotation of cell clusters were similar to the ones mentioned

previously. DEGs in each conserved cell types in response to differentiation stages or C59

treatment were visualized by ComplexHeatmap R package (*18*). In some cases, gene of interests

such as Wnts and various lineage markers were also visualized using the *FeatureHeatmap* and

DotPlot function in Seurat.

3.3.16 Pseudotemporal ordering and lineage trajectories

We used Monocle2 R package to reconstruct differentiation trajectories by computing and

ordering the sequence of gene expression changes of the cells collected from different time

79

points in an unsupervised manner (*23, 24*). First, scRNA-seq datasets from different timepoints

underwent several quality control steps as mentioned previously. These multiple scRNA-seq

datasets were then merged into one single object using *MergeSeurat* function in Seurat. The

merged matrix was then converted into Monocle object using *importCDS* and *newCellDataSet*

functions in Monocle2. We then identified a set of DEGs between the cells collected at the

beginning of the process to those at the end using *differentialGeneTest* function with argument

qval < 0.01 in Monocle. The dimensions of the dataset were then reduced using first two

principal components with 'DDRTree' method. Next, we used *orderCells* function to order the

cells based on the selected DEGs and the trajectory of the cells was visualized by

plot_cell_trajectory function in Monocle. The temporal expression of the gene of interests was

visualized using the *plot_genes_in_pseudotime* function in Monocle. Additionally, to observe

dynamic changes in the expression levels of the genes that were branch dependent (i.e., along

with specific lineage), we used *plot_genes_branched_heatmap* function in Monocle to construct

a special type of heatmap in which genes that had similar lineage-dependent expression patterns

were clustered together.

3.3.17 WGCNA reconstruction of GRNs and hub genes

We used Weighted Gene Co-expression Network Analysis (WGCNA), an algorithm

implemented in WGCNA R package, to reconstruct GRNs and to identify their associated hub

genes that regulate cell differentiation (*38*). First, the dataset of interest (e.g., a given timepoint)

created in Seurat was converted into a plain matrix for a given gene (in column) in an individual

cell (in row). The dataset was then cleaned by removing cells with too many missing values

using *goodSamplesGenes* function in WGCNA. Next, we used *pickSoftThreshold* function in

WGCNA to determine the proper soft-thresholding power (β) that fits the criterion of

approximate scale-free topology of the network, and an adjacency matrix was then built with soft-thresholding power of 8 in our study. Hierarchical clustering and GRN were constructed by using *blockwiseModules* function with arguments *TOMType* set to unsigned, *networkType* set to signed, and *mergeCutHeight* set to 0.25 in WGCNA. Modules containing genes that were highly associated with each other were identified in this process. Gene lists of interesting modules were extracted and submitted to DAVID for GO term analysis to retrieve their biological process and molecular functions. We then identified transcription factors (TFs) and TF regulators from the genes based on the GO terms in molecular functions. We then selected top 100 genes that have highest weight (i.e., high correlation coefficient) connected to a given TF or TF regulator. Finally, the GRN based on these TFs and TF regulators then underwent cluster analysis using community cluster (GLay) (*25*) and was then visualized using Cytoscape (*26*). Hub genes for each GRN were identified as genes with high weight (summed correlation coefficients), high degree (summed connectivity, i.e., total numbers genes connected to this specific gene), and high betweenness centrality (BC) measure of the network. The hub gene of a given GRN were visualized by ComplexHeatmap R package (*18*).

3.3.18 Multicellular signaling and ligand-receptor models

To investigate the ligand-receptor interaction in heterogenous multicellular signaling systems, we used a list comprising of 2,557 human ligand–receptor pairs curated by Database of Ligand-Receptor Partners (DLRP), IUPHAR, and Human Plasma Membrane Receptome (HPMR) (*27, 28*). We first quantified the percentage of the cells (i.e., neural cells, melanocytes, and chondrocytes) that expressed a specific Wnt ligand and its associated frizzled (FZD) receptors using scRNA-seq datasets. To ensure the ligand and receptors are uniquely expressed, we required that their expression in fold change needs to more than 0.25 in log scale. We then used

Circlize R package to visualize the directions of the signaling in the cell type based on connections of ligand-receptor pairs (*29*).

3.3.19 RNA Fluorescence *in situ* hybridization (RNA-FISH)

To validate scRNA-seq findings and to visualize the spatial distribution of *Wnts* and *COL2A1* within pellets, we performed RNA-FISH for *Wnt3A*, *Wnt4*, and *COL2A1* expression. d28 pellets with or without C59 treatment were harvested (n = 3 time point) and snap frozen in liquid nitrogen. Pellets were cryo-sectioned at 10 μm thick and fixed using 4% paraformaldehyde in PBS on ice for 10 min. Sample pre-treatment and RNA probe hybridization, amplification, and signal development were performed using the RNAscope Multiplex Fluorescent Reagent Kit v1 (Advanced Cell Diagnostics, #320850) following the manufacturer's instruction. Samples were imaged with multi-channel confocal microscopy (Zeiss LSM 880). Tiled images with Z-stacks were taken at 20X magnification to capture the entire pellet. Maximum intensity projection, a process in which brightest pixel (voxel) in each layer along Z direction is projected in the final 2D image, was performed using Zeiss Zen Blue (version 2.5).

3.3.20 Fluorescent activated cell sorting (FACS) for progenitors

Cells at the Cp stage with treatment of BMP4, a combination of BMP4 and Wnt3A, or a combination of BMP4 and C59 were dissociated and resuspended in FACS Buffer (PBS$^{-/-}$ with 1% FBS and 1% penicillin/steptomycin/fungizone (P/S/F; Gibco) at approximately 40 x 10^6 cells per ml. The cells were treated with Human Tru Stain FC X^{TM} (BioLegend, #422302) for 10 min at room temperature. Approximately 10,000 cells in 100 μl were used for each compensation. Cells were labeled with appropriate antibodies including their associated isotype control (FITC-CD45, #304006; PE/Cy7-CD146, #361008; PE-CD166, #343904, all from BioLegend). Cells were incubated for 30 minutes at 4ºC and washed with FACS buffer twice. Samples were

resuspended in sorting medium consisting of DMEM/F12 with 2% FBS, 2% P/S/F, 2% HEPES (Gibco), and DAPI (BioLegend, #422801) at 4×10^6 cells per ml and filtered through a 40 µm cell strainer. Cells were stored on ice prior to sorting. Five µl of all antibodies were used per million cells in 100 µl staining volume, 10 µl of Tru Stain FC X^{TM} was used per million cells in 100 µl staining volume. DAPI was used at 3 µM. An Aria-II FACS machine was used to compensate the color overlapping and to gate the samples. Data was analyzed using FlowJo software (version 10.5.3).

3.3.21 Histology

Pellets were collected in 10% neutral buffered formalin for fixation for 24 hours. Pellets were then transferred to 70% ethanol, dehydrated, and embedded in paraffin wax. Pellet blocks were sectioned at 8 µm thickness and stained for proteoglycans and cell nuclei according to the Safranin-O and hematoxylin standard protocol.

3.3.22 Immunohistochemistry

Histologic sections (8 µm thick) of the pellets were rinsed with xylenes three times and rehydrated before labeling. Antigen retrieval was performed with 0.02% proteinase K for 3 min at 37ºC for COL2A1 and COL6A1 and with pepsin for 5 min at room temperature for COL1A1 and COL10A1 followed by peroxidase quench then serum blocking for 30 min at room temperature. Samples were labeled for 1 hour with the primary antibody against COL1A1 (1:800 Abcam #90395), COL2A1 (1:10 Iowa #II-II6B3-s), COL6A1 (1:1000 Fitzgerald #70F-CR009X), and COL10A1 (1:200 Sigma #C7974) and for 30 min with the secondary antibody goat anti-mouse (1: 500, Abcam #97021) or goat anti-rabbit (1:500 Abcam #6720) as appropriate. Histostain Plus Kit (Sigma, #858943) was then used for enzyme conjugation for 20 min at room temperature followed by AEC (ThermoFisher, #001111) for 2.5 min (COL2A1 and

COL6A1) or 2 min (COL1A1 and COL10A1) at RT. Finally, samples were counterstained with hematoxylin to reveal cell nuclei for 45 sec and mounted with Vector Hematoxylin QS (Vector lab, #H3404). Images were taken by Olympus VS120 microscope (VS120-S6-W).

3.3.23 Biochemical analysis of cartilaginous matrix production

Pellets were rinsed with PBS after chondrogenic differentiation and digested at 65ºC overnight in 200 µl papain solution consisting of 125 µg ml^{-1} papain (Sigma, P4762), 100 mM sodium phosphate, 5 mM EDTA, and 5 mM L-cysteine hydrochloride at 6.5 pH. Samples were stored at -80ºC before thawing to measure double stranded DNA by Quant-iT PicoGreen dsDNA Assya Kit (ThermoFisher, #P11496) and glycosaminoglycans (GAG) by the 1,9-dimethylmethylene blue assay at 525 nm wavelength (*30*). GAG content, as calculated based on the standard curve, was normalized to double stranded DNA content.

3.3.24 RT-qPCR

RNA of the pellets was isolated using the Total RNA Purification Kit according to the manufacture's protocol (Norgen Biotek, #37500). Reverse transcription of the RNA was performed using SuperScript VILO Master Mix (Thermo Fisher, # 11755050). Fast SYBR Green Master Mix (Thermo Fisher, # 4385614) was used for reverse transcription quantitative polymerase chain reaction (RT-qPCR) according to manufacturer's instructions on the QuantStudio 3 (Thermo Fisher). Gene expression was analyzed using the $\Delta\Delta C_T$ method relative to undifferentiated hiPSCs with the reference gene TATA-box-binding protein (*TBP*). Sequences of primers are listed in Table 3.2.

Table 3.2 qRT-PCR Primer Sequences. Primers are listed as 5' to 3'.

Gene	Forward Sequence	Reverse Sequence
ACAN	CACTTCTGAGTTCGTGGAGG	ACTGGACTCAAAAAGCTGGG
COL1A1	TGTTCAGCTTTGTGGACCTC	TTCTGTACGCAGGTGATTGG
COL2A1	GGCAATAGCAGGTTCACGTA	CTCGATAACAGTCTTGCCCC
COL10A1	CATAAAAGGCCCACTACCCAAC	ACCTTGCTCTCCTCTTACTGC
MITF	AGTTGCTGGCGTAGCAAGAT	AAAGTCAACCGCTGAAGAGC
PAX6	GAGTGCCCGTCCATCTTTG	GTCTGCGCCCATCTGTTGCTTTTC
SOX2	TACAGCATGATGCAGGACCA	CCGTTCATGTAGGTCTGCGA
SOX9	CGTCAACGGCTCCAGCAAGAACAA	GCCGCTTCTCGCTCTCGTTCAGAAGT
TBP	AACCACGGCACTGATTTTCA	ACAGCTCCCCACCATATTCT
Wnt2B	GTGTCCTGGCTGGTTCCTTA	AGCTGGTGCAAAGGAAAGAA
Wnt3A	CCTGCACTCCATCCAGCTACA	GACCTCTCTTCCTACCTTTCCCTTA
Wnt4	GATGTGCGGGAGAGAAGCAA	ATTCCACCCGCATGTGTGT
Wnt5B	CTGCCTTTCCAGCGAGAATT	AGGTCAAATGGCCCCCTTT
Wnt7B	CCCCCTCCCTGGATCATGCACA	GCCACCACGGATGACAGTGCT

3.3.25 Western blots

To examine the effect of C59 on Wnt inhibition in the pellets at protein levels, Western blot analysis was performed on d28 pellets with or without C59 treatments. 6-8 pellets per experimental group were pooled and digested with 0.04% type 2 collagenase solution in DMEM/F12 for 1hr. Cells were washed once with PBS and lyzed in RIPA buffer (Cell Signaling Technology, #9806S) with protease inhibitor (ThermoFisher, #87786) and phosphatase inhibitor (Santa Cruz Biotechnology, #sc-45044). Protein concentration was measured using the BCA Assay (Pierce). 10 μg of proteins for each well were separated on 10% SDS-PAGE gels with prestained molecular weight markers (Bio-Rad, 161-0374). and transferred to a PVDF

membrane. The PVDF membrane blots were incubated overnight at 4 °C with the following primary antibodies: anti-Wnt2B (1:350, abcam, ab178418), anti-Wnt3A (1:1000, abcam, ab81614), anti-Wnt4 (1:500, abcam, ab91226), anti-Wnt5B (1:500, abcam, ab93134), anti-Wnt7B (1:2000, abcam, ab155313) and anti-GAPDH (1:30000, Proteintech 60004-1-Ig) for loading control, respectively. Affinity purified horseradish peroxidase(HRP)-linked goat anti-rabbit IgG secondary antibody (1:3000, Cell Signaling, #7074) or horse anti-mouse IgG secondary antibody (1:3000, Cell Signaling, #7076) was added and incubated for 45 minutes at room temperature. Immunoblots were imaged and analyzed using the iBright FL1000 Imaging System (Thermo Fisher). After the Wnt proteins were imaged, the blots were then stripped by incubating with restore plus Western blot stripping buffer (ThermoFisher Scientific) at room temperature for 15 mins.

3.3.26 Statistical analysis

All data were presented as mean ± SEM. Analyses were performed using SPSS Statistics (version 25), with significance reported at the 95% confidence level. In the current study, the number of pellets per group or treatment condition are technical replicates, while number of the mice per group are biological replicates.

3.3.27 Data availability

We acquired RNA-seq datasets of human primary chondrocytes from a previously published study (NIH Gene Expression Omnibus (GEO) accession number GSE106292) (31), in which embryonic hind limb bud chondrocytes (age: 6 weeks, $n = 2$), adolescent knee chondrocytes (age: 17 weeks, $n = 2$), adult knee chondrocytes (age: 18-60 years, $n = 2$), and growth plate chondrocytes (age: 14 weeks, 15 weeks, and 18 weeks, $n = 1$ per age). For the datasets obtained from the previous mentioned study, gene expression counts were averaged if there were more

than 2 samples with the same age. We also harvested chondrocytes from human costal cartilage and performed bulk RNA-seq on these samples (age: ~70 years, n = 3). However, it was challenging to collect rib cartilage from young healthy donors; thus, aged 70-year-old costal cartilages were used. To compare the difference between the phenotypes of chondrocytes derived from hiPSCs and hMSCs, we also used bulk RNA-seq datasets of hMSC chondrogenesis from our recent study (GEO accession number GSE109503) (*10*). For the present study, our bulk RNA-seq and scRNA-seq datasets are available on GEO accession number GSE 160787.

3.4 Results

3.4.1 Bulk RNA-seq indicates successful differentiation of hiPSCs

Previously, we reported a robust differentiation protocol that can drive hiPSCs toward a chondrogenic lineage via the paraxial mesoderm (*8*) (Figure S3.1A-B). To determine transcriptome profiles over the course of differentiation, 3 independent hiPSCs lines (ATCC, BJFF, and STAN) were collected for bulk RNA-seq at various stages (Figure 3.1A). Principal component analysis (PCA) reveals that the 3 hiPSC lines follow similar mesodermal and chondrogenic differentiation trajectories (Figure 3.1B-C). Analysis of differentially expressed genes (DEGs) between each stage revealed upregulation of stage-specific markers. For example, T-box transcription factor T (*TBXT*) and mix paired-like homeobox (*MIXL1*) were upregulated at the stage of anterior primitive streak (anterior PS) compared to hiPSCs (*32*) (Figure 3.1D; Table 3.2). Markers representing mesodermal derivatives including T-box 6 (*TBX6*), UNC homeobox (*UNCX*), and paired box 9 (*PAX9*) were upregulated sequentially at the stages of paraxial mesoderm, early somite, and sclerotome, respectively (Figure 3.1C).

Chondrogenic markers such as matrilin 4 (*MATN4*), aggrecan (*ACAN*), collagen type VI alpha 3 chain (*COL6A3*), collagen type IX alpha 1 chain (*COL9A1*), and SRY-box 6 and 9

(*SOX6* and *SOX9*) were upregulated as early as at day 7 (d7), while the expression of collagen type II alpha 1 chain (*COL2A1*) was increased at d21 (Figure 3.1E; Table S3.3). Interestingly, microRNA 302a (*MIR302A*), reportedly down-regulated in osteoarthritic chondrocytes, had enhanced expression in d28 pellets (*33*). Interestingly, neuronal differentiation 4 (*NEUROD4*), a gene encoding a transcriptional activator essential for neuronal differentiation, had increased expression in d14 pellets (*34*).
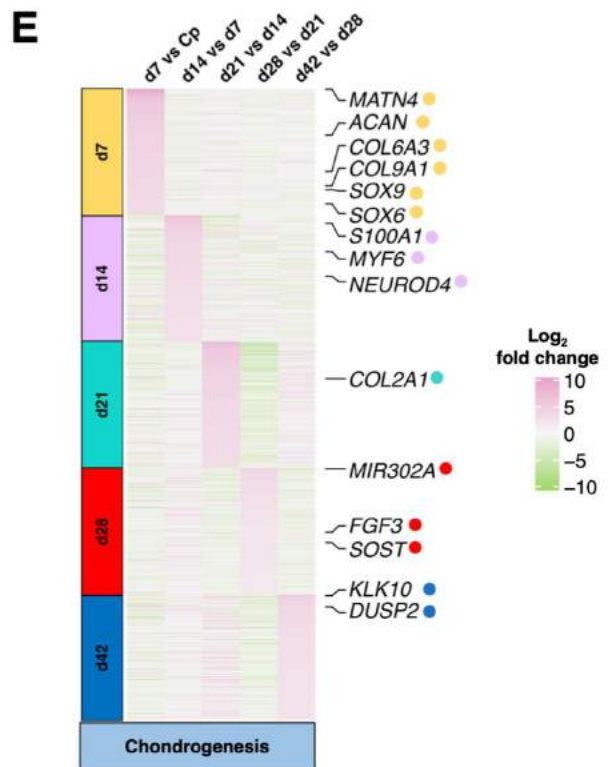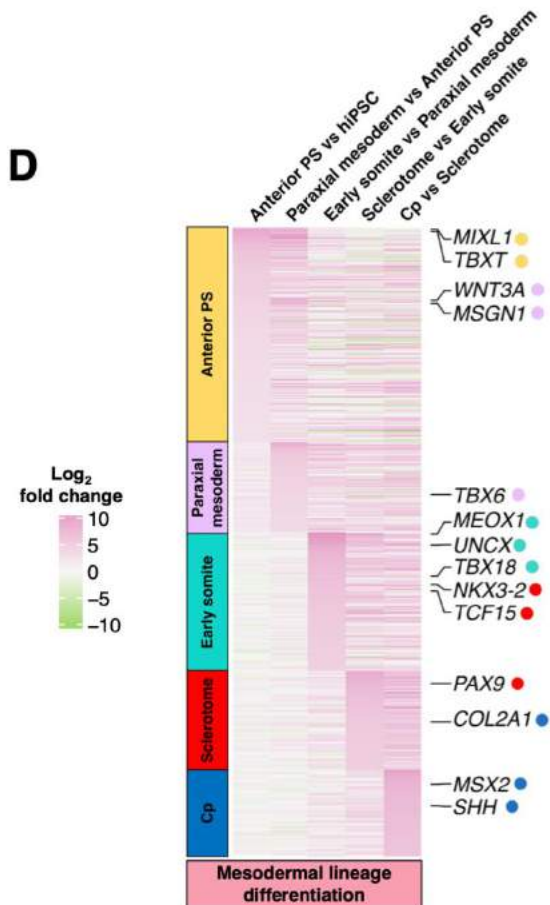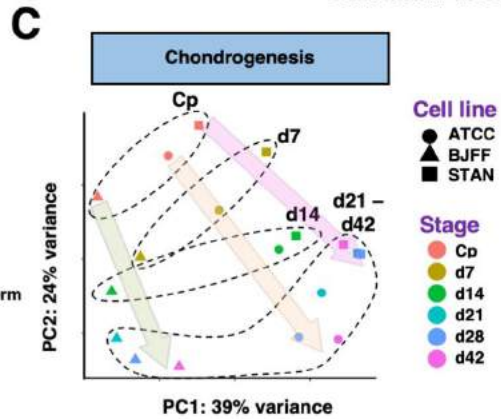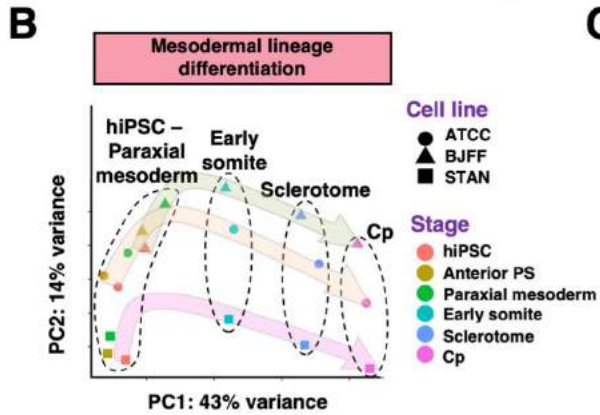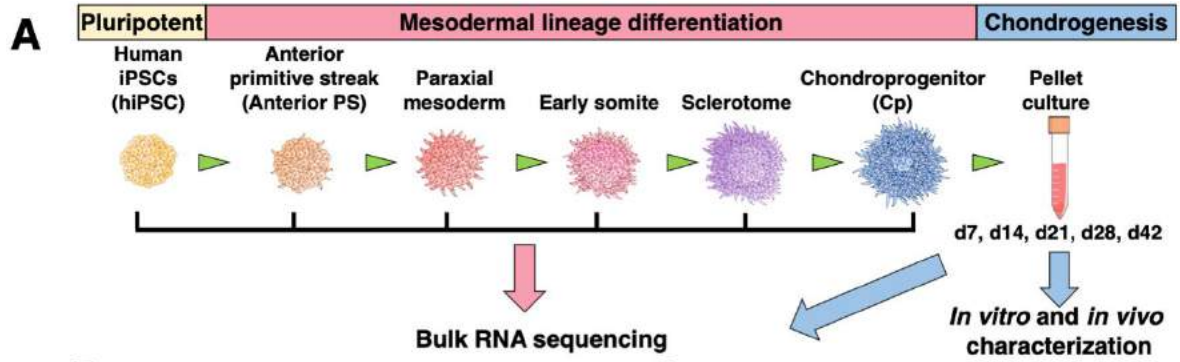
Figure 3.1 DEGs of mesodermal and chondrogenic differentiation of 3 hiPSC lines by bulk RNA-seq. (**A**) Schematic of chondrogenic differentiation protocol for hiPSCs. (**B-C**) PCA indicates that 3 unique hiPSC lines followed similar differentiation trajectories. (**D-E**) DEGs averaged from 3 unique hiPSC lines at each stage of differentiation, respectively. Each column of the heatmap represents a comparison between two stages/timepoints, and each gene presented was assigned a colored dot (following the gene label). The color of a dot matches the color of the timepoint label at the left side of the heatmap. When the color of a gene label and a timepoint label match, that gene was significantly upregulated at the corresponding time points and was thus detected as a differentially expressed gene.

3.4.2 *in vitro* characterization of hiPSC-derived chondrocytes

While temporal expression of chondrogenic markers such as *SOX9* and *COL2A1* were

upregulated in unique hiPSC lines, both the hypertrophic chondrocyte marker collagen type X

alpha 1 chain (*COL10A1*) and osteogenic marker collagen type I alpha 1 chain (*COL1A1*)

exhibited increased expression over time (Figure 3.2A). It is important to note that COL1A1 is

also a marker for fibrous tissues, perichondrium, and many other cell types. The d28 pellet

matrix also demonstrated rich proteoglycan staining using Safranin-O (Saf-O) as well as intense

labeling for COL2A1 and COL6A1 by immunohistochemistry (IHC). However, little labeling

for COL10A1 and COL1A1 was observed despite increased gene expression of *COL10A1* and

COL1A1 at later time points (Figure 3.2B). Gene ontology (GO) enrichment analysis of the

genes using R package GAGE was performed (*17*). Significantly upregulated GO terms in

Biological Process highlighted skeletal system and cartilage development (Figure S3.2A). GAGE

analysis also revealed that 134 out of the 205 genes defined by cartilage development

(GO:0051216) were significantly increased. Interestingly, in addition to upregulated *SOX5*, *6*,

and *9,* which are known to be master transcription factors (TFs) governing chondrogenesis, we

also observed several Wnts, including *Wnt2B,* had increased gene expression at different stages

during differentiation (Figure 3.2C).

To determine the phenotype of hiPSC-derived cartilage, we projected our bulk RNA-seq

data and publicly available sequencing datasets of primary chondrocytes from a variety of

cartilaginous tissues and chondrocytes derived from mesenchymal stem cells (MSCs) in a PCA

plot (Figure 3.2D) (*31*). We found that hiPSC-derived chondrocytes demonstrated a similar

phenotype to embryonic limb bud chondrocytes.

3.4.3 *in vivo* characterization of hiPSC-derived chondrocytes

To determine whether hiPSC-derived chondrocytes could maintain their phenotype *in vivo*, we

implanted d14 pellets subcutaneously in the dorsal region of immunodeficient NSG (NOD.Cg-

*Prkdc^{scid} Il2rg^{tm1Wjl}/*SzJ) mice (Figure S3.2B). The d14 pellets represented the earliest time point

when a chondrocyte-like phenotype was observed *in vitro*. After 14 days of implantation, pellets

were harvested and found to retain a cartilage phenotype, with rich proteoglycan and COL2A1

labeling. No endochondral ossification was observed during this relatively short-term

implantation period in our study.

To test whether hiPSC-derived chondrocytes can retain their phenotype within the joint,

we created an osteochondral defect in the femoral groove of the mouse (Figure 3.2E). Due to the

small size of the mouse knee, the osteochondral defect model here also involves a growth plate

defect. The defect was either left empty as a non-repair control group or filled with a d14 pellet.

Defects left untreated did not exhibit any repair with hyaline cartilage, and only fibrotic tissue

was observed. However, defects with pellet implantation demonstrated enhanced repair of the

focal cartilage lesion, which was filled with cartilaginous matrix rich in Saf-O staining at both

14- and 28-days post-implantation. While this finding provides proof-of-concept of the

maintenance of the chondrogenic phenotype over 28 days, future studies may wish to investigate

cell fate and implant properties after long-term implantation.
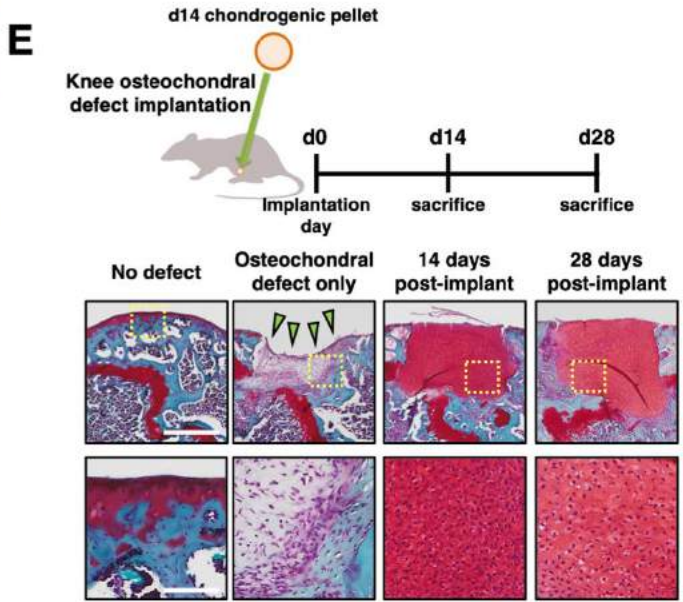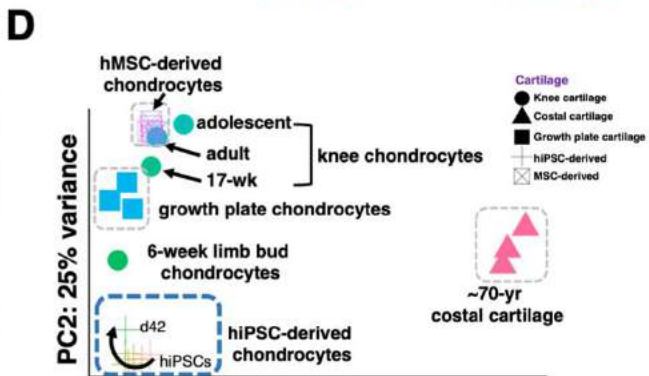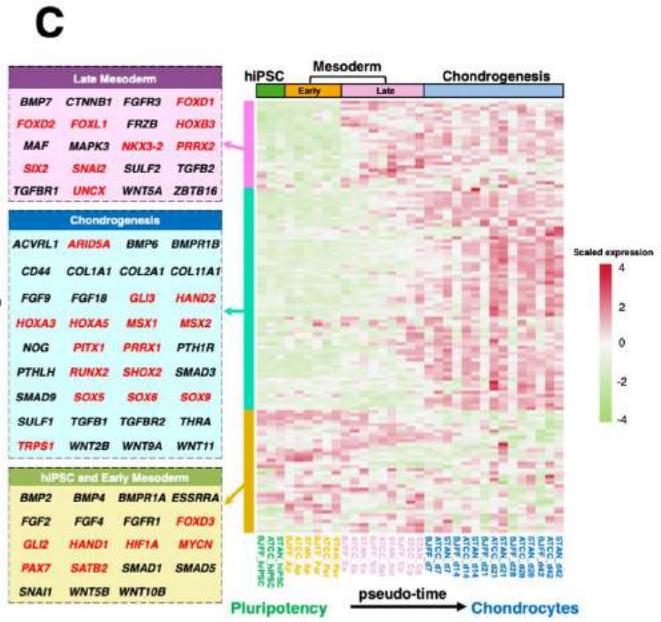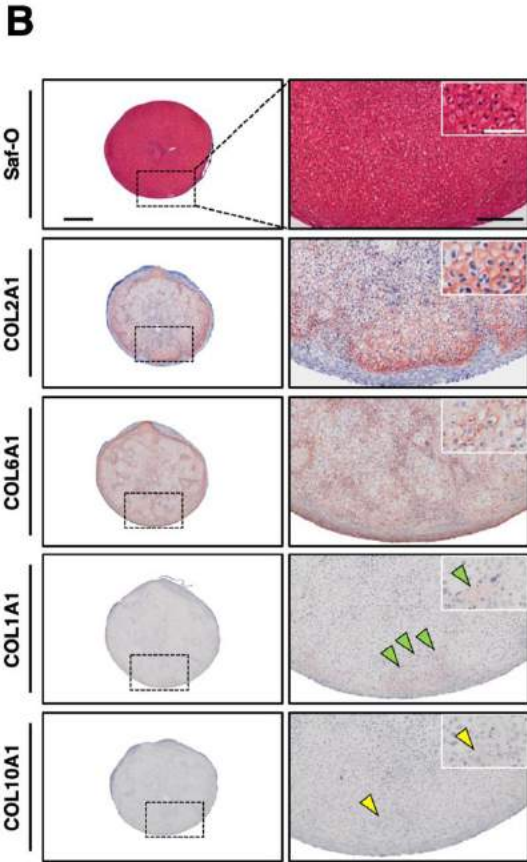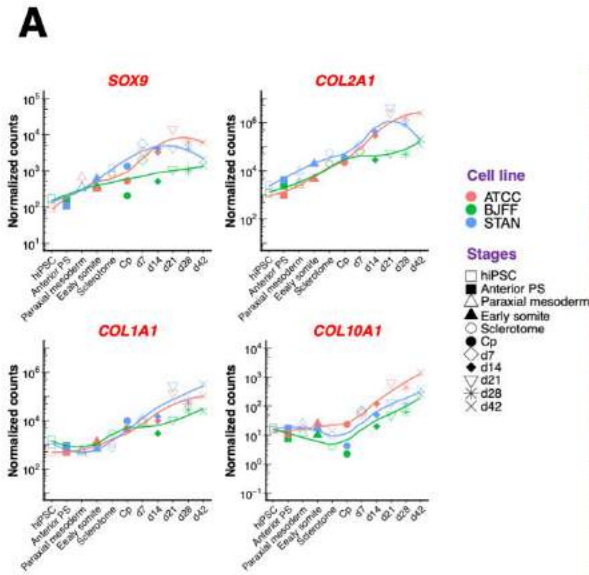
Figure 3.2 *In vitro* and *in vivo* characterization of hiPSC-derived chondrocytes (**A**) Temporal gene expression of chondrogenic markers *SOX9* and *COL2A1*, hypertrophic marker *COL10A1*, and osteogenic marker *COL1A1*. (**B**) Pellets showed enriched Saf-O, COL2A1, and COL6A1 staining. Most COL1A1 staining (green arrow) was located at the edge of the pellets, while faint COL10A1 (yellow arrowheads) was observed. Left column scale bar = 400 µm. Right column scale bar = 200 µm. Inset scale bar = 50 µm. Experiment was repeated 3 times with similar results. (**C**) Heatmap of 134 significantly upregulated genes identified in GO term cartilage development (GO:0051216). Genes in red font are either TFs or transcription regulators. (**D**) hiPSC-derived chondrocytes exhibit similar phenotype to embryonic limb bud chondrocytes. (**E**) hiPSC-derived chondrocytes repaired osteochondral defects in the cartilage of mouse knee joints and remained a chondrocyte phenotype 28-days post-implantation. n = 3 mice per group. Top row scale bar = 500 µm. Bottom row scale bar = 100 µm.

3.4.4 scRNA-seq mapping of cellular heterogeneity

Although our protocol generates a predominantly chondrocyte-like population as shown by IHC and bulk RNA-seq (Figure 3.2B), we often observed non-chondrocyte populations and occasional focal accumulation of black pigmented regions on the surface of the pellets (Figure S3.2C-D). These results suggest the presence of off-target differentiation, prompting us to seek their cellular identities. To dissect this cellular heterogeneity, 8 samples from the STAN cell line at different differentiation time points were collected for scRNA-seq (Figure 3.3A). Detailed cell numbers passed quality control steps and median genes per cell for each stage are listed in Table S3.1 (see Methods for quality control steps and criteria).

Sequencing of mixed species ensured a low cell multiplet rate (2.7%) (Figure S3.3A). To verify reproducibility of the differentiation, two batches of d28 samples were collected from independent experiments for scRNA-seq. Canonical correlation analysis (CCA) was used to align cells from the 2 batches (*19*) (Figure S3.3B). The cells in the same cluster from different batches exhibited high correlation in their gene expression (Spearman's rank coefficient $r_s > 0.87$ for all clusters) (Figure S3.3C). Furthermore, genes that were highly conserved in one particular cluster (using cluster 0 as an example) showed similar expression patterns in the clusters from distinct batches, suggesting that our differentiation is highly reproducible (Figure S3.3D).

3.4.5 Lineage bifurcation in hiPSC differentiation trajectory

We used the Monocle2 R package to reconstruct the differentiation trajectory from the stage of

hiPSCs to d42 chondrocytes with a total of 19,195 cells that passed quality control (Figure 3.3B)

(*23*). While cells following chondrogenic fate expressed chondrocyte markers including *ACAN*,

COL2A1, *SOX9,* and cartilage oligomeric matrix protein (*COMP*), we found one major

branchpoint, diverting cell fate toward neural lineage with the expression of neural cell markers

such as nestin (*NES*), orthodenticle homeobox 2 (*OTX2*), *SOX2*, and *Wnt3A* (Figure 3.3C). Other

neural cell markers such as *OTX1* and *PAX6* were also enriched in this branch (Figure S3.3E).

The off-target cell differentiation toward neurogenic lineage confirmed our findings of increased

NEUROD4 in the bulk RNA-seq data.

To explore distinct cell populations at each stage, scRNA-seq data were subjected to

unsupervised clustering and visualized using t-distributed stochastic neighbor embedding (tSNE)

plots (Figure 3.3D). By comparing DEGs with signature genes of cell types in the literature and

GO term analyses, we annotated broad cell populations by combining clusters expressing similar

marker genes. For example, 2 of 7 clusters identified at the chondroprogenitor (Cp) stage not

only had high expression levels of *SOX4* and *SOX9*, but were also enriched in several markers

resembling neural crest cells including *PAX3* and forkhead box D3 (*FOXD3*) (Figure S3.3F)

(*35*). Therefore, these two clusters were assigned to a broad cell population referred to as neural

crest cells. Similarly, 4 clusters at the Cp stage exhibited markers of neural lineage including

SOX2, *OTX1/2*, and *PAX6*, and thus were annotated as neurogenic lineage cells, while *PRRX1*,

COL1A1, and *COL3A1* are known markers for mesenchyme (Figure S3.3G) (*36*). Similar major

cell populations were also observed in d1 and d3 pellets, although it appeared that the percentage

of mesenchymal and neural cells increased in d1 and d3 while there was a decreased percentage

of neural crest cells (Figure S3.3H-I).

Of note, a cluster with high expression of melanocyte inducing transcription factor (*MITF*) was observed in d7 and d14 pellets. MITF is a master TF regulating development of melanocytes, cells that produce melanin (i.e., pigment) (*37*). IHC of the pellets labeling for NES and MITF further confirmed the presence of neural cells and melanocytes (Figure S3.3J), suggesting that the focal black dots observed at the surface of pellets are likely to be the pigment accumulation in melanocytes. Nevertheless, as distinct subtypes of hiPSC-derived chondrocytes and off-target cells were defined primarily based on marker genes, the complete functionality of these population require future investigation.

3.4.6 WGCNA identifies GRNs of neurogenesis and melanogenesis

Next, we aimed to improve hiPSC chondrogenesis by decreasing off-target differentiation. We performed weighted gene co-expression network analysis (WGCNA) to reconstruct GRNs and identify the hub genes that modulate neurogenesis and melanogenesis (38). scRNA-seq data of d14 pellets (with a total of 2,148 cells and 3,784 genes) was used for this computation due to the earliest presence of both chondrogenic and off-target populations detected. Five major gene modules (each containing > 150 genes) were identified, and based on GO enrichment analyses, they were categorized into: cell division, cilium movement and assembly, skeletal system development, nervous system development, and melanin biosynthetic process. The genes in the modules of nervous system development and melanin biosynthetic process were then used to build corresponding GRNs and subnetworks by Cytoscape, while hub genes were determined by degree (node connectivity), weight (association between two genes), and betweenness centrality measure of the network (Figure 3.3E and Figure S3.4A-C) (39). In the GRN of neurogenesis, Wnt4 was strongly associated with several TFs regulating neural differentiation. We also

observed that Wnt2B was associated with both MITF and ETS variant 1 (ETV1), a gene whose

activity has been reported to positively regulate MITF (40).
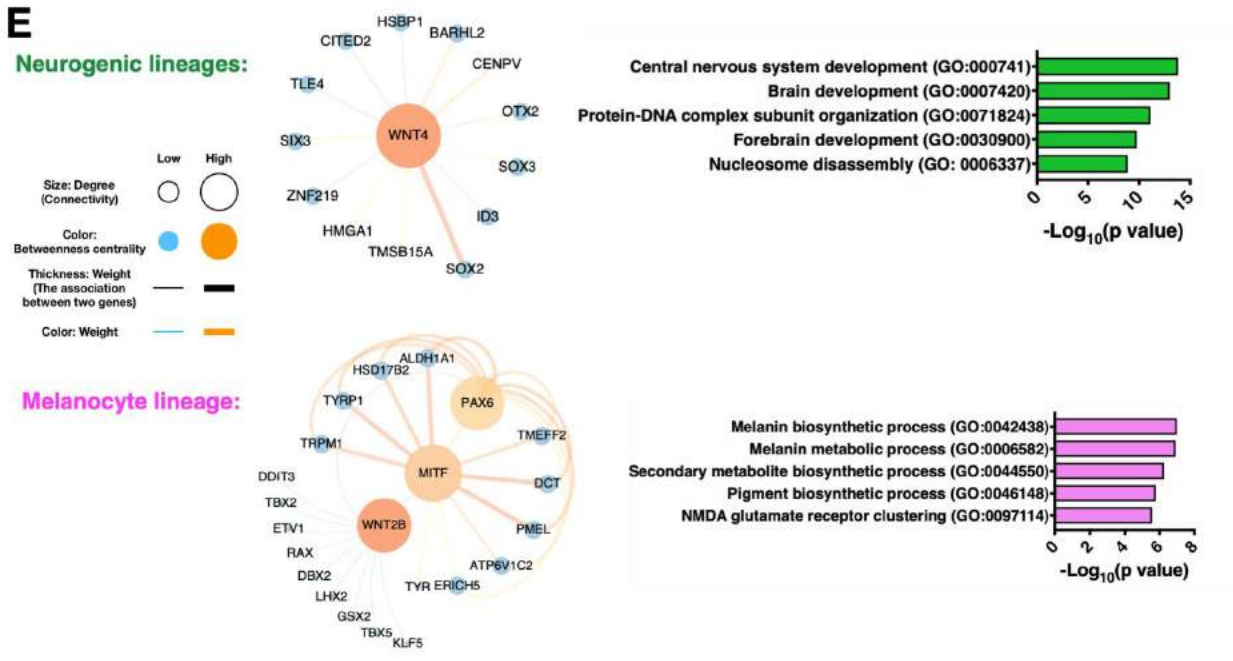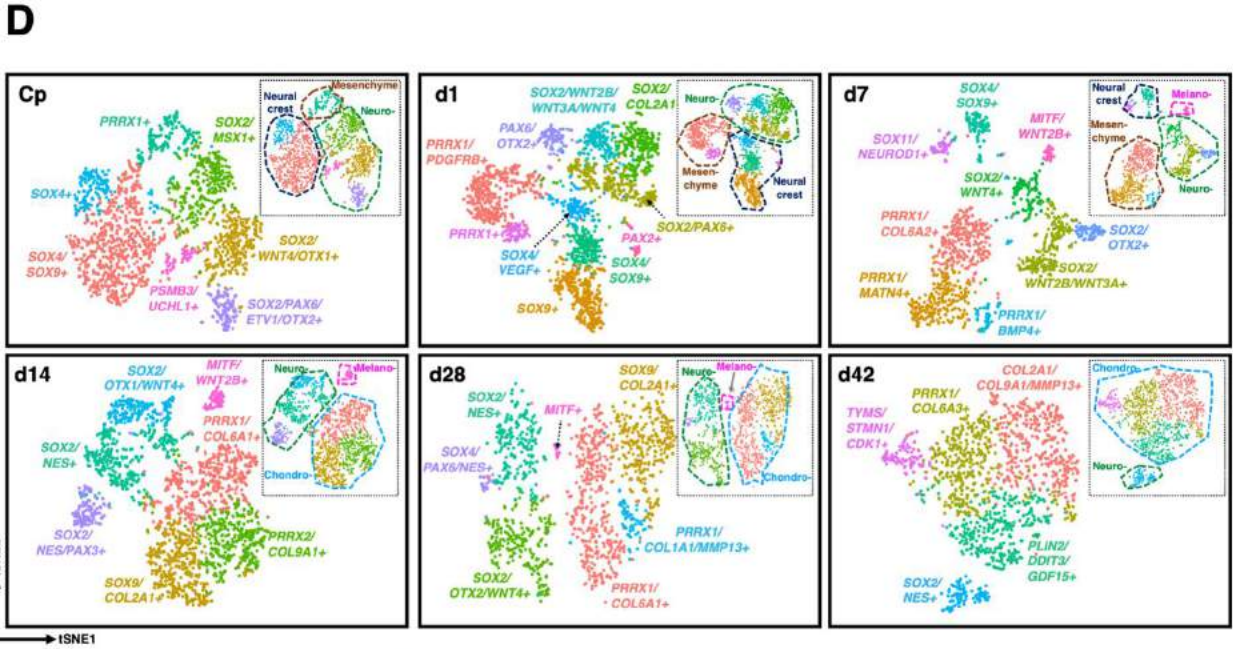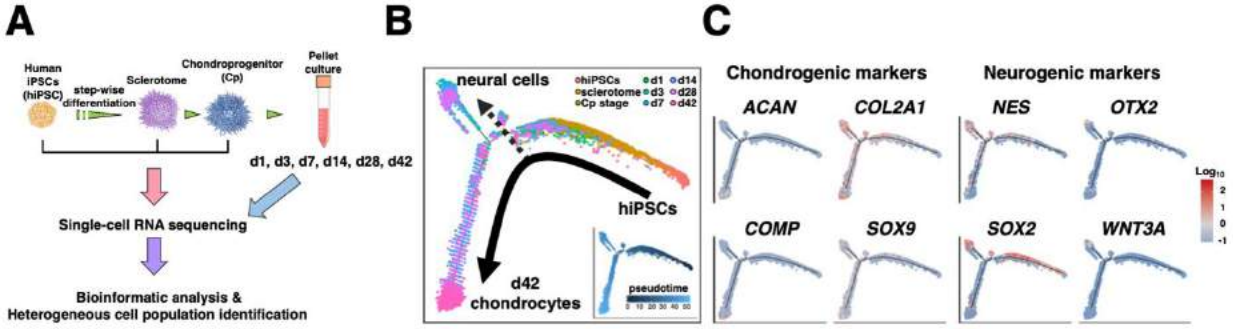
Figure 3.3 scRNA-seq and WGCNA reveal neural cells and melanocytes as off-target cells. (**A**) scRNA-seq was performed at hiPSC, Sclerotome, Cp, and 6 chondrogenic pellet time points. (**B**) Reconstruction of differentiation trajectory reveals an off-target lineage bifurcation toward neural cells. A total of 19,195 cells that passed quality control from the stage of hiPSC to d42 chondrogenic pellet was used to reconstructed differentiation trajectory. (**C**) Chondrogenic markers were enriched in the chondrogenic branch, while neurogenic markers were observed in the branch of neurogenesis. (**D**) Annotated cell populations at different timepoints during hiPSC chondrogenesis. Cells that passed quality are used for tSNE plots; Cp: 1,888 cells, d1: 2,216 cells, d7: 1,200 cells, d14: 2,148 cells, d28: 1,271 cells, and d42: 1,328 cells. (**E**) WGCNA and GO term analysis identified *Wnt4* as a hub gene of neurogenesis while *Wnt2B* was highly associated with melanocyte development. scRNA-seq data of d14 pellets (with a total of 2,148 cells and 3,784 genes) was used for this computation.

3.4.7 Inhibition of Wnt signaling enhances hiPSC chondrogenesis

As Wnts were identified as essential genes in the off-target cells, we hypothesized that inhibition

of Wnt signaling may improve hiPSC chondrogenesis by decreasing undesired cell populations.

It is known that Wnts are required to properly specify somites from pluripotent cells (*41*).

Therefore, we administrated Wnt-C59 (C59), a Wnt inhibitor, at either the Cp stage and/or

during the chondrogenic pellet culture (i.e., 4 different inhibition regimens; Figure 3.4A).

Chondrocyte homogeneity, as indicated by Saf-O staining, was increased if Wnt signaling was

inhibited during pellet culture (Figure 3.4B). This finding was reflected by increased production

of glycosaminoglycans per cell (GAG/DNA ratio) in the group receiving C59 during the pellet

culture (Figure 3.4C). However, inhibiting Wnts at the Cp stage severely impaired

chondrogenesis. Mesenchymal cells that are positive for CD146 and CD166 are proposed to be

putative chondroprogenitors due to their robust chondrogenic potential (*30*). Flow cytometric

analysis showed that C59 treatment largely decreased the percentage of CD146/CD166+ cells,

while Wnt3A supplementation increased this population at the Cp stage (Figure 3.4D). Similar

results were observed using two additional hiPSC lines (ATCC and BJFF) (Figure S3.4D-G).

Interestingly, pellets derived from hMSCs with Wnt inhibition also exhibited increased Saf-O

staining (Figure S3.4H-I). Additionally, hiPSC pellets receiving combined administration of C59

and ML329 (ML), an MITF antagonist, also exhibited enhanced chondrocyte homogeneity compared to standard TGF-β3 treatment (Figure S3.4G).

RNA fluorescence *in situ* hybridization (RNA-FISH) labeling of Wnts and *COL2A1* within d28 pellets indicated that although some labeling could be detected in the center of the pellets, most Wnts were in the perichondral layer, consistent to the inhomogeneous cell populations observed via IHC staining. Furthermore, C59-treated pellets showed a more homogenous distribution of *COL2A1* RNA-FISH labeling versus TGF-β3-treated pellets (Figure 3.4E and Figure S3.5).
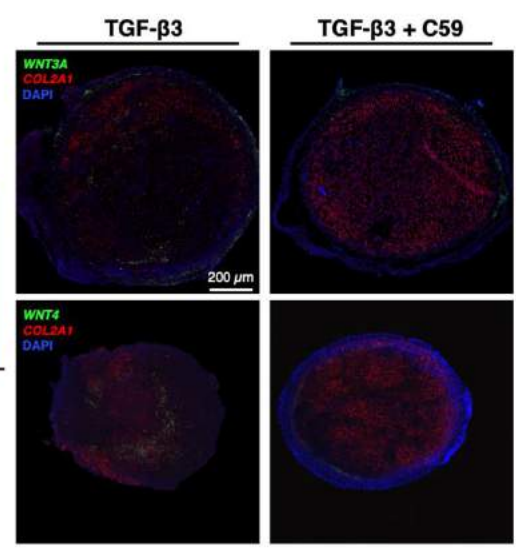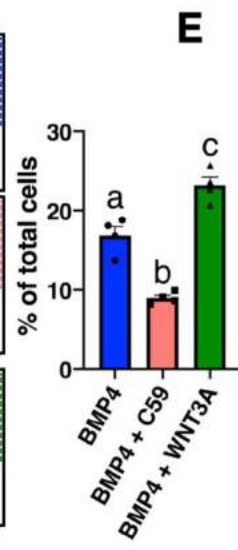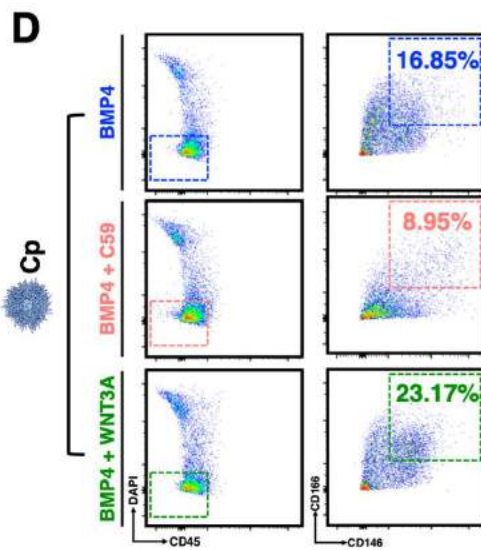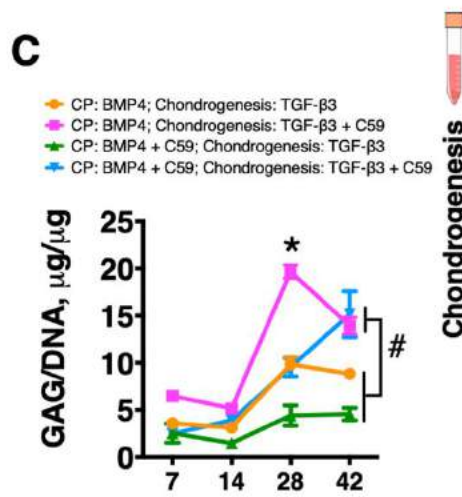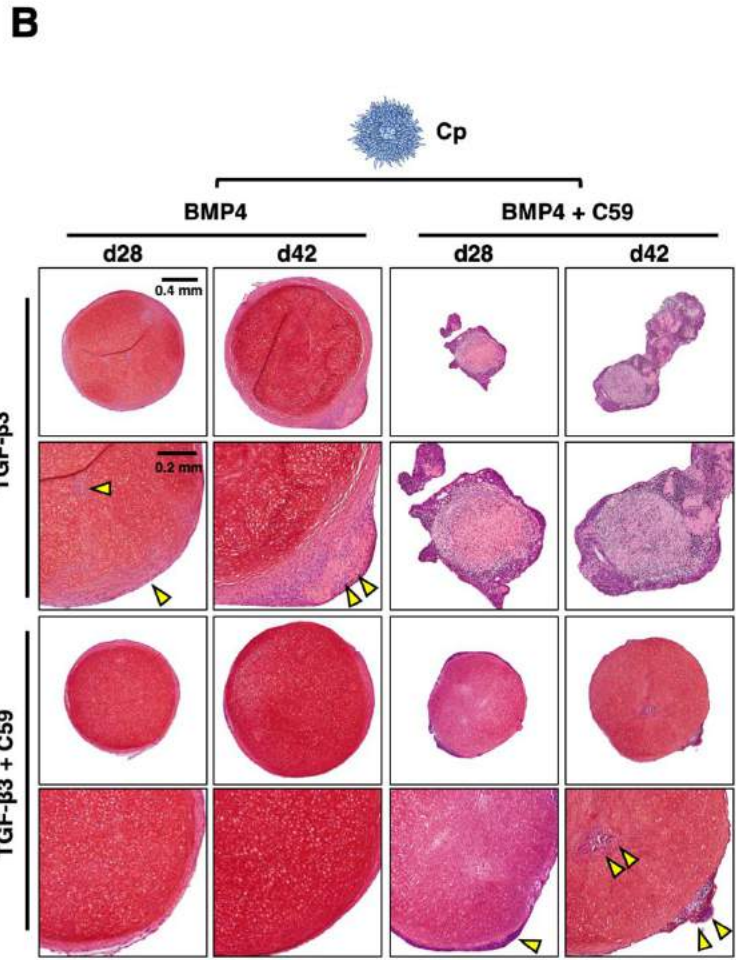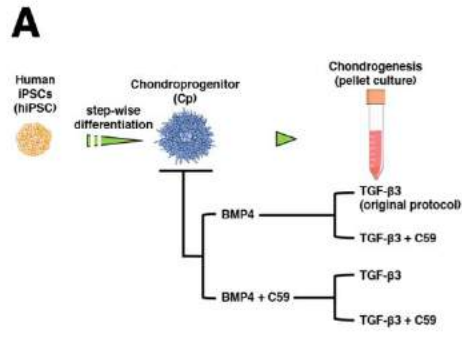
Figure 3.4 Wnt inhibition during pellet culture enhanced homogeneity of hiPSC chondrogenesis. (**A**) Experimental scheme of Wnt inhibition. (**B**) C59 treatment during pellet culture enhanced Saf-O staining and decreased off-target cells (yellow arrowheads) as compared to other Wnt inhibition culture regiments. Top row scale bar = 400 µm. Bottom row scale bar = 200 µm. Experiment was performed twice with similar results. (**C**) Pellets treated with C59 in pellet culture only exhibited an increased GAG/DNA ratio compared to pellets treated with other culture regiments. * p = 0.00001 at d28. # p = 0.0228 at d42. Mean ± SEM. n = 4 pellets per group. Statistical significance was determined by one-way ANOVA with Tukey's *post-hoc* test at specific timepoint. (**D**) C59 significantly decreased, but Wnt3A significantly increased, CD146/CD166+/CD45- progenitors at the Cp stage. Different letters are significantly different (a vs. b, p = 0.0005; a vs. c, p = 0.0021; b vs. c, p = 0.0001). Mean ± SEM. n = 3 per group (independent experiment). Statistical significance was determined by one-way ANOVA with Tukey's *post-hoc* test. (**E**) RNA-FISH of d28 pellets showing C59-treated pellets had decreased *Wnt3A* and *Wnt4* staining (green) but more homogenous *COL2A1* distribution (red) in the pellets. Scale bar = 200 µm. Experiment was performed twice with similar results.

3.4.8 scRNA-seq confirms Wnt inhibition enhances chondrogenesis

To determine how Wnt inhibition altered cell populations in chondrogenesis and to identify chondrocyte subpopulations, pellets treated with C59 were analyzed using scRNA-seq with a total of 12,795 cells from the stage of hiPSC, Cp as well as d7, d14, d28 and d42 C59-treated pellets (Figure 3.5A-B). We found the C59-treated pellets comprised two major cell populations: mesenchyme and chondrocytes. Mesenchyme exhibited high expression of actin (*ACTA2*), *PRRX1*, *COL1A1*, and *COL3A1*. Most importantly, neural cells and melanocytes were significantly decreased with Wnt inhibition. The differentiation trajectory of C59-treated chondrogenesis was reconstructed, using scRNA-seq datasets of hiPSC and Cp stages from previous sequencing (since they did not involve in C59 intervention) (Figure 3.5C). Compared to the trajectory built from TGF-β3-treated pellets, C59-treated pellets exhibited little, if any, neurogenic markers, but showed enriched expression for chondrogenic markers (Figure 3.5D). In pseudotime analysis, we found that C59-treatment led to earlier induction of *ACAN* expression, higher levels of *COL2A1* and *SOX9* expression, and an earlier decrease in *SOX2* expression as compared to pellets treated with TGF-β3 alone (Figure S3.6A).

Chondrocytes in C59-treated pellets comprised several subpopulations as identified by multiple CCA alignment of d7-d42 timepoints with a total of 7,997 cells (Figure 3.5E-F and Figure S3.6B-C), including one mesenchymal population and four conserved chondrocyte subsets with enriched *COL2A1* and *SOX9* expression. The chondrocyte subset enriched in cell cycling markers, such as high mobility group box 2 and cyclin dependent kinase 1 (*HMGB2/CDK1+*), is defined as proliferating chondrocytes (*42*). The second chondrocyte subset is enriched in IGF-binding protein-5 (*IGFBP5*). It has been previously reported that IGFBP5 is highly upregulated in early differentiating stage (*43*). Hence, the *IGFBP5+* chondrocyte subset is defined as a population of early differentiating chondrocytes. The third chondrocyte subset expresses leukocyte cell-derived chemotaxin 1, epiphycan, and frizzled related protein (*LECT1/EPYC/FRZB+*) and had the highest levels of *COL2A1* and *ACAN* expression among other chondrocyte subsets. Therefore, the *LECT1/EPYC/FRZB+* chondrocyte subset is defined as a population of early-mature chondrocytes. Finally, we identified a unique chondrocyte subset expressing interferon (IFN)-related genes including ISG15 ubiquitin-like modifier, interferon alpha inducible protein 6, and MX dynamin like GTPase 1 (*ISG15/IFI6/MX1+*). We observed that 4.6% of *ISG15/IFI6/MX1+* chondrocytes co-expressed terminal hypertrophic differentiation markers *VEGFA* and *MMP13*; thus, we defined the *ISG15/IFI6/MX1+* chondrocyte subset as mature-hypertrophic chondrocytes (Figure S3.6D).

At early timepoint d7, *HMGB2/CDK1+* proliferating chondrocytes was the main cell population (44.5%) within the pellets (Figure S3.6C). Interestingly, this population also had the highest numbers of *BMPR1B/ITGA4* double-positive cells, a rare osteochondral progenitor population found in articular cartilage (Figure S3.6E-F) (*31*). When proliferating chondrocytes differentiated toward maturity, potentially facilitated by IGFBP5 (*43*), *IGFBP5+* early

102

differentiating chondrocytes and *LECT1/EPYC/FRZB+* early-mature chondrocytes became

dominant (Figure S3.6C). The enriched expression of *FRZB*, which encodes a secretory Wnt

inhibitor, in early-mature chondrocytes might help stabilize this population by further

antagonizing Wnt signaling in addition to C59 treatment (Figure S3.6G). As

LECT1/EPYC/FRZB+ chondrocytes had the highest levels of *COL2A1* and *ACAN* expression,

we investigated the DEGs of this particular population at various time points (Figure 3.5G).

Among several early chondrogenic markers such as *COL9A1* and osteogenic markers such as

COL1A1, *IGFBP7* exhibited biphasic upregulation at both early and later time points of

chondrogenesis.

The percentage of *ISG15/IFI6/MX1+* mature-hypertrophic chondrocytes greatly

increased at d28 (Figure S3.6C). Although the downstream IFN regulatory molecules including

STAT1 and *PML* were elevated in this population, we could not detect any type of IFNs which

were conventionally believed to be the activators of IFN pathways (Figure S3.6H). Instead, we

observed that *IGFBP3* was enriched in *ISG15/IFI6/MX1+* chondrocytes, whereas *IGFBP5* was

highly expressed in early differentiating chondrocytes. In line with the results of previous

studies, we also observed that IGFBP3 inhibited expression of *FOS* (*C-FOS*), a possible driver of

chondrocyte hypertrophy when it dimerizes with *JUN* (*AP-1*) (Figure S3.6I) (*44*). This result

may provide some explanations for the finding that *ISG15/IFI6/MX1+* chondrocytes had variable

expression levels of hypertrophic chondrocyte markers (Figure S3.6J) (*45*).

During chondrogenic culture, pellets were generally surrounded by a fibrous layer,

resembling the cartilage anlage enclosed by fibroblastic cells (i.e., perichondrium). To determine

if the mesenchyme (i.e., *ACTA2/PRRX1/COL1A1+* cells) identified in pellets and the

mesenchyme (i.e., *PRRX1+* cells) identified at the Cp stage (monolayer culture) were similar to

the perichondrium, we benchmarked these mesenchymal cells, as well as various chondrocyte

subpopulations, against previously reported markers of perichondrial cells in rats and humans

(Figure S3.7) (*46, 47*). We found that *ACTA2/PRRX1/COL1A1+* cells in pellets, but not

PRRX1+ cells at the Cp stage, were enriched in genes of perichondrium, suggesting that the

mesenchymal populations at the Cp stage and in pellets had distinct phenotypes, despite their

shared mesenchymal genes such as *COL1A1* and *COL3A1*. These data were then used

reconstruct the GRN of hiPSC chondrogenesis, with minimal presence of off-target cells as

shown by WGCNA (Figure S3.8A).
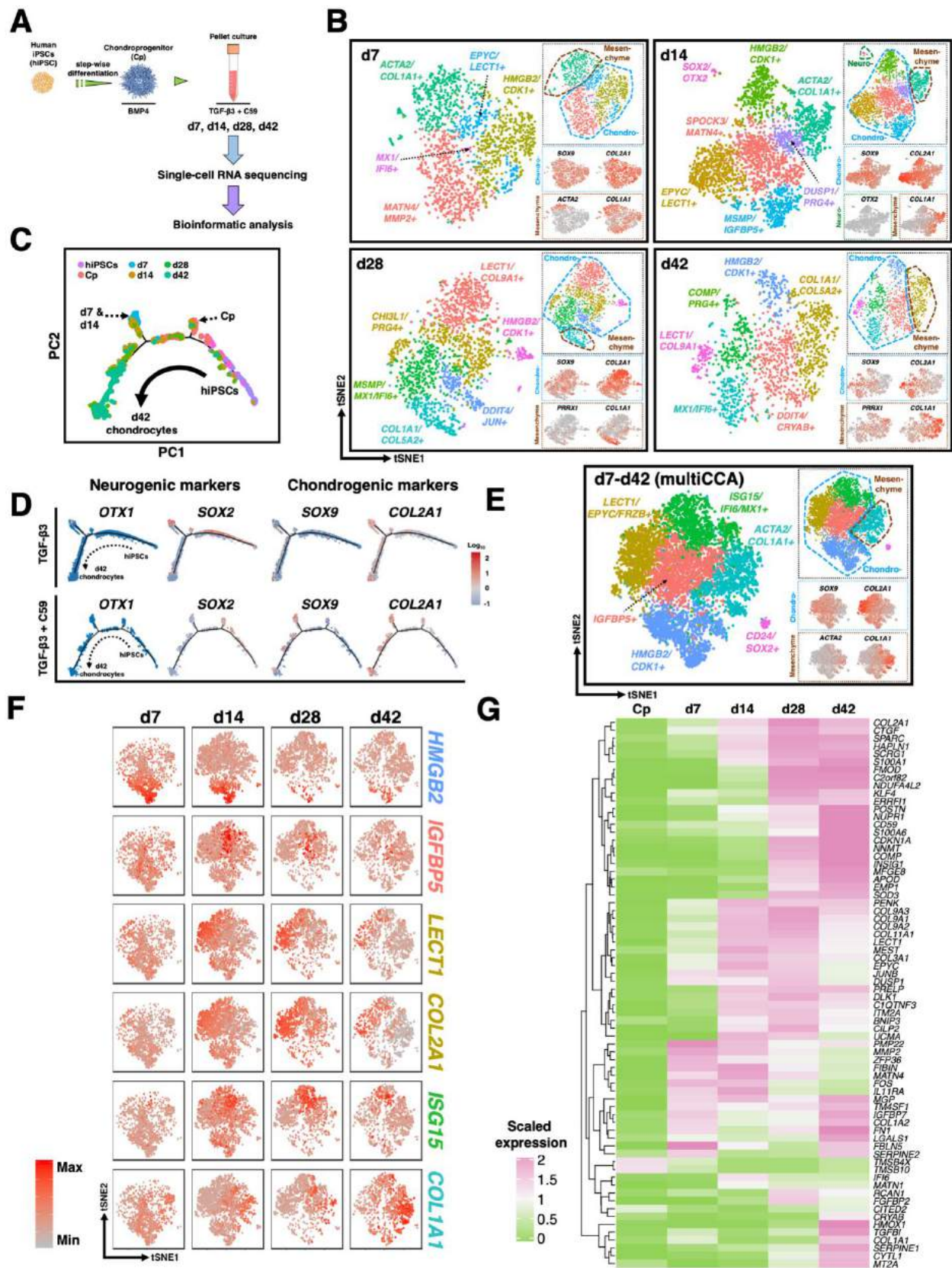
Figure 3.5 scRNA-seq of pellets with Wnt inhibition shows improved chondrogenesis. (**A**) scRNA-seq was performed on the pellets with Wnt inhibition. (**B**) Chondrocytes and mesenchymal cells were two major populations in C59-treated pellets. Cells that passed quality are used for tSNE plots; Cp: 1,888 cells, d7: 1,682 cells, d14: 3,076 cells, d28: 1,756 cells, and d42: 1,483 cells. (**C**) Differentiation trajectory of C59-treated pellets. scRNA-seq data with a total of 12,795 cells from the stage of hiPSC, Cp as well as d7, d14, d28 and d42 C59-treated pellets was used to reconstruct the differentiation trajectory. (**D**) C59-treated pellets exhibited decreased neurogenic markers but increased chondrogenic markers. (**E**) Multiple CCA alignment of d7-d42 pellets. A total of 7,977 cells from d7-d42 timepoints of C59-treated pellets was used to performed CCA alignment. (**F**) Dynamic changes in gene expression and percentages of chondrocyte subpopulations over time. (**G**) Heat map of top 20 DEGs at each timepoint for *LECT1/EPYC/FRZB+* early-mature chondrocytes.

3.4.9 Differential gene expression profiles after C59 treatment

Three major conserved populations were identified after CCA alignment of the d14 cells with or without C59 treatment (a total of 5,224 cells analyzed): proliferative cells, mesenchyme enriched, and chondrocytes (Figure 3.6A and 3.6B). C59-treated pellets contained more mesenchyme and chondrocytes at d14, while non-C59-treated (i.e., TGF-β3 only) pellets had more proliferative cells at the same time point (Figure 3.6C). Pellets with only TGF-β3 treatment not only showed elevated expression of *MITF* but also had more neural cells which were clustered in proliferative cells (Figure 3.6D). Chondrocytes and proliferative cells exhibited similar profiles of up- and down-regulated DEGs. For instance, both cell populations showed upregulated expression of *COL2A1* and *JUNB*, while exhibiting decreased expression of *SOX4* and several ribosomal genes (Figure S3.8B). Interestingly, *FRZB* was only upregulated in the chondrocyte population upon C59 treatment.

At d28, pellets treated with C59 exhibited increased expression of *ACAN* and *COMP* compared to the standard-treated pellets (Figure S3.8C-D). Importantly, we also observed that *IFI6* and *ISG15*, markers for mature-hypertrophic chondrocytes, were down-regulated in the C59-treated pellets, suggesting Wnt inhibition may decrease chondrocyte hypertrophy during chondrogenesis.

3.4.10 Wnt expression with neurogenesis

To determine the expression patterns of Wnts and to identify the cells responsible for Wnt production, we investigated Wnt expression levels in multiple cell populations of d14 and d28 pellets (Figure 3.6E and Figure S3.8E; a total of 5,224 d14 cells and a total of 3,027 d28 cells analyzed). In TGF-β3-treated pellets, several canonical Wnts such as *Wnt3*, *Wnt3A*, and *Wnt7B,* as well as non-canonical Wnts including *Wnt4,* were enriched in the proliferative population (where the neural cells clustered), while *Wnt2B* and *Wnt5B* could be found in proliferative cells, chondrocytes, and mesenchyme. We did not detect *Wnt1*, *Wnt2*, and *Wnt8* in any specimens. Upon C59 treatment, most Wnts showed decreased expression, particularly in proliferative cells. Western blots confirmed that C59-treated pellets had decreased protein levels of Wnt2B, Wnt3A, Wnt4, and Wnt7B (Figure 3.6F). Interestingly, C59 only moderately inhibited Wnt5B. We next plotted these Wnt ligands along with neurogenic and chondrogenic markers in pseudotime to investigate their expression patterns. We observed that *Wnt2B*, *Wnt3A*, *Wnt4*, and *Wnt7B* clustered with neurogenic markers, whereas Wnt5B was upregulated along chondrogenic differentiation, implying that individual Wnts may play distinct roles in regulating chondrogenesis (Figure 3.6G).
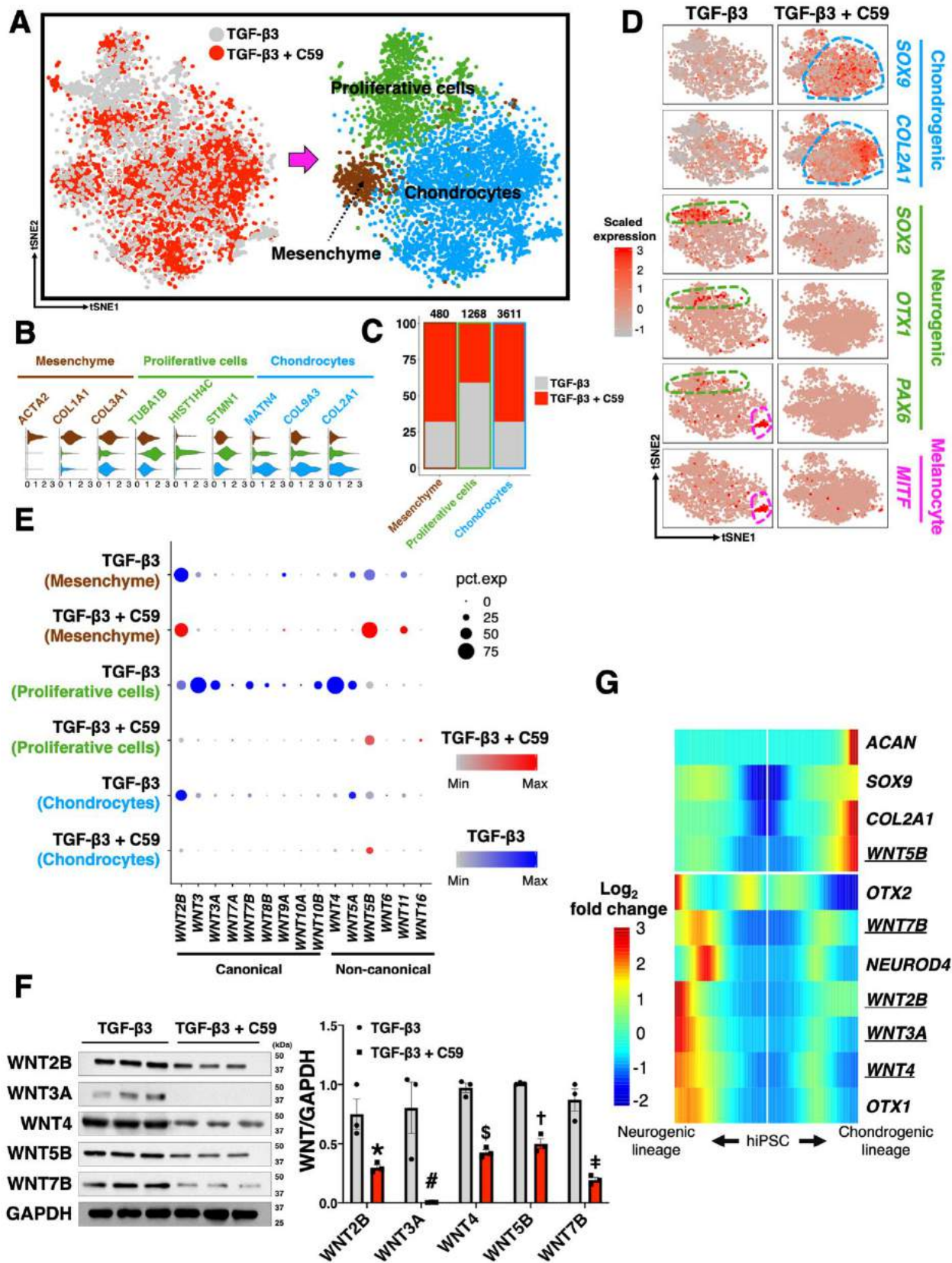
Figure 3.6 CCA analysis reveals that most Wnts, except Wnt5B, were secreted by off-target cells. (**A**) Three major conserved populations in d14 pellets. A total of 5,224 cells from the d14 pellets with or without C59 treatment was analyzed. (**B**) Violin plots of the specific markers for each conserved population. (**C**) C59-treated pellets comprised more chondrocytes and mesenchymal cells. (**D**) Expression levels of chondrogenic markers were higher in C59-treated pellets while expression of neurogenic markers and melanocyte markers was higher in TGF-β3-treated pellets. (**E**) Dotplot showing proliferative cells (mainly neural cells) from TGF-β3-treated pellets had high expression levels of Wnt ligands. Wnt inhibition largely decreased expression levels of Wnts in cells. (**F**) Western blots confirm that Wnt inhibition significantly decreased Wnts in cells at protein levels. * $p = 0.026$, # $p = 0.021$, \$ $p = 0.0003$, † $p = 0.00029$, ‡ $p = 0.021$ to its corresponding group. Mean ± SEM. n = 3 per treatment condition. Statistical significance was determined by two-tailed Student's t-test for the groups with or without specific Wnt inhibition. (**G**) Most Wnts were upregulated along the lineage of neural cells, where Wnt5B was clustered with chondrogenic differentiation in TGF-β3-treated pellets. A total of 2,148 cells from the TGF-β3-treated d14 pellets was analyzed and used to generate the heatmap.

3.4.11 Wnts alter GAG/DNA and collagen production

As C59 is a pan-Wnt signaling inhibitor, it therefore remained unknown which Wnt ligand had the most severe adverse effect on hiPSC chondrogenesis. To answer this question, we administrated a variety of Wnts during pellet culture (Figure S3.9A). RT-qPCR analysis showed that only Wnt7B significantly decreased chondrogenic markers (*SOX9*, *ACAN*, and *COL2A1*), hypertrophic marker (*COL10A1*), and osteogenic marker (*COL1A1*) when compared to TGF-β3 only pellets (Figure 3.7A). Interestingly, the pellets treated with Wnt2B and Wnt3A exhibited increased *COL2A1*, *COL1A1,* and *COL10A1* expression versus TGF-β3 pellets. However, only the pellets with Wnt3A treatment had a significantly decreased GAG/DNA ratio compared to the pellets with TGF-β3 only treatment (Figure 3.7B). Wnt2B-treated pellets also showed a trend toward increasing expression of neurogenic markers (*PAX6* and *SOX2*), although not statistically significant. Furthermore, Wnt2B- and Wnt7B-treated pellets had significantly lower expression of *MITF* relative to TGF-β3 pellets. We also observed that Wnt ligands may not only regulate their own expression but may also modulate the expression of other Wnt ligands (Figure S3.9B).

While all pellets had comparable Saf-O staining, Wnt treatment increased off-target cells

within the pellets (Figure 3.7C). Furthermore, these off-target cells exhibited lower production of COL2A1 compared to chondrocytes. Additionally, pellets treated with Wnts, particularly Wnt3A, exhibited higher intensity of COL1A1 and COL10A1 staining, which was observed near off-target cells and perichondrium. On the contrary, C59 pellets had low COL1A1 and COL10A1 production and the staining was mainly at the perichondrium. Together, these results indicate that Wnts increased non-chondrogenic cells and modulated collagen production. The histological images in Figure 3.7C were quantified using a published ImageJ protocol (Figure S3.9C) (*48*).

3.4.12 Heterocellular Wnt signaling may regulate chondrogenesis

To investigate which cell populations are the main sources for the endogenous production of specific Wnts during chondrogenesis, a heatmap in which the expression of Wnt ligands against multiple cell populations at the d28 timepoint was plotted (Figure 3.7D and Figure S3.9D). We found that 30% of melanocytes expressed *Wnt2B*, while *Wnt3A*, *Wnt4*, and *Wnt7B* were mainly expressed in neural cells. *Wnt5B* was expressed primarily by chondrocytes (about 10% of chondrocyte population) providing a possible explanation for the upregulation of *Wnt5B* during chondrogenesis. As Wnts are secretory proteins, we next aimed to identify the potential cell populations receiving Wnt signaling based on published lists of ligand-receptor pairs (*27*). We found that 31.6% of chondrocytes expressed *FZD2*, the highest expression of a Wnt receptor in chondrocytes (Figure 3.7E). Thus, we created the multicellular signaling for *Wnt3A-FZD2* pair and identified that 9.9% of neural cells expressed *Wnt3A* while more than a third of chondrocytes (36.1%) were capable of receiving this ligand (Figure 3.7F). Additionally, we also observed that although chondrocytes were the major contributor for Wnt5B production, melanocytes (30%) might be the main receiving cell type. Furthermore, while 30% of melanocytes may secrete

Wnt2B, only 1% of chondrocytes expressed *FZD4*, one of the main Wnt2B receptors (Figure

3.7G).
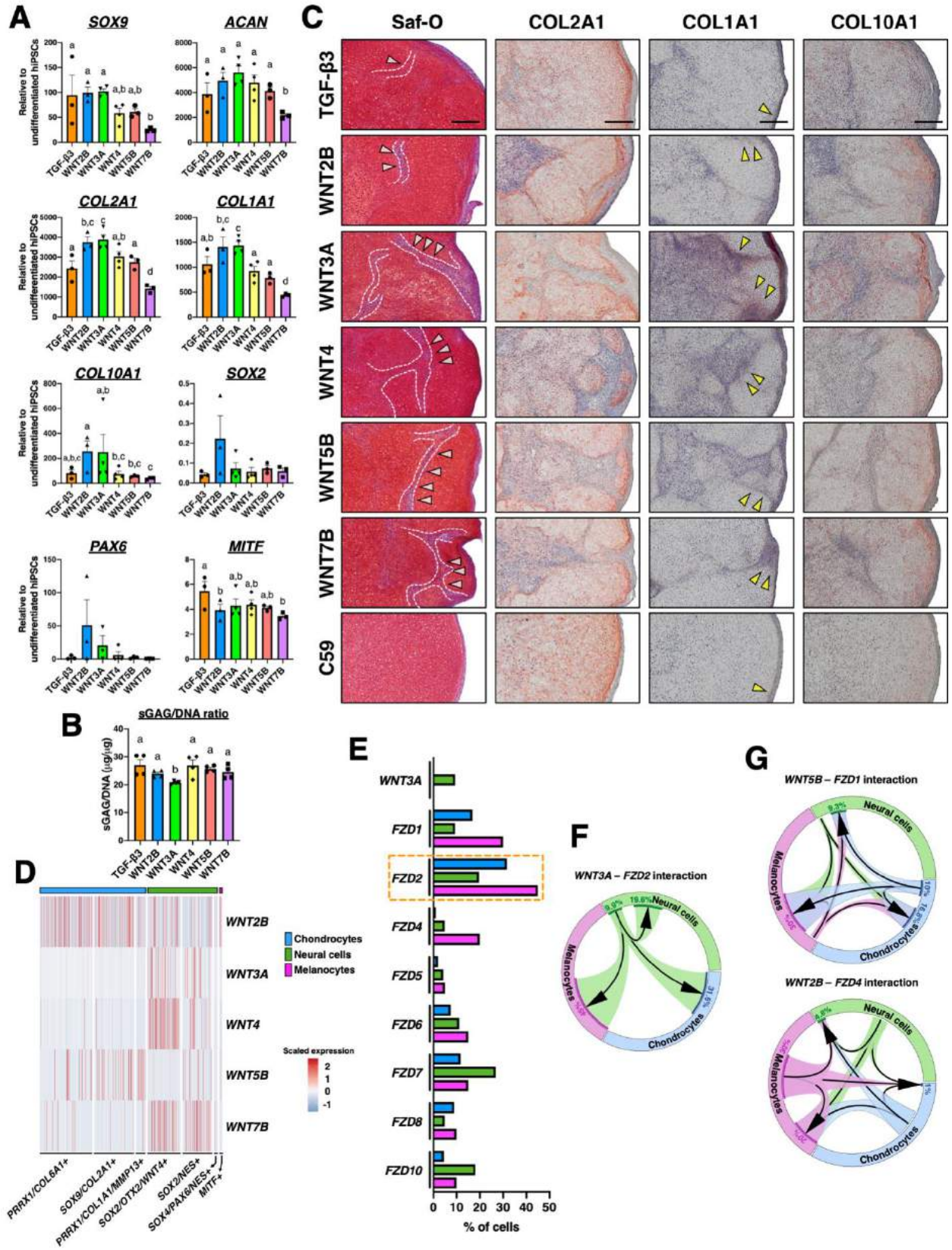
Figure 3.7 Heterogenous multicellular Wnt signaling models. (**A-B**) RT-qPCR and GAG/DNA ratios of pellets treated with various Wnts during pellet culture. Different letters are significantly different from each other ($p < 0.05$). Mean ± SEM. n = 3-4 pellets per group. Statistical significance was determined by one-way ANOVA with Tukey's *post-hoc* test. (**C**) Wnt treatment increased infiltration of off-target cells (pink arrowheads and white dashed lines) into the pellets, decreased COL2A1 staining, but increased COL1A1 (yellow arrowheads) and COL10A1 staining in the pellets. The pellets with C59 treatment exhibited homogenous COL2A1 staining and decreased COL1A1 and COL10A1 staining. Scale bar = 0.2 mm. Experiment was performed twice with similar results. (**D**) Heatmap showing distinct expression levels of various Wnts in d14 TGF-β3-treated pellets. A total of 2,148 cells from the TGF-β3-treated d14 pellets was analyzed and used to generate the heatmap. (**E**) Percentage of the cells expressing *Wnt3A* and its putative receptors in d14 TGF-β3-treated pellets. (**F-G**) Heterogenous multicellular signaling models in d14 TGF-β3-treated pellets.

3.4.13 BMP/GDF differential expression after C59 treatment

While the precise mechanisms of enhanced chondrogenesis remain to be determined, our CCA analysis showed that six chondrocyte subpopulations and 1 mesenchymal population were conserved between TGF-β3 and C59 conditions in d14 pellets: 1) *HMGB2/CDK1+* proliferating chondrocytes, 2) *UBE2C/CCNB1+* proliferating chondrocytes, 3) *LECT1/EPYC/FRZB+* early-mature chondrocytes, 4) *ISG15/IFI6/MX1+* mature-hypertrophic chondrocytes, 5) *FTL/MT-CO2+* stressed chondrocytes, 6) *BNIP3/FAM162A+* apoptotic chondrocytes, and *ACTA2/PRRX1/COL1A1+* mesenchymal cells (Figure S3.10A; CCA was performed with a total of 1,335 cells from mesenchymal and chondrocyte populations from d14 TGF-β3 pellets and with a total of 3,047 cells from mesenchymal and chondrocyte populations from d14 C59 pellets). Interestingly, C59 treatment differentially influenced the expression of various growth factors and receptor in the TGF-β superfamily essential in regulating chondrogenesis (*49*) (Figure S3.11A-B and Figure S3.12A-B).

In addition to exogenous TGF-β3 stimulation, endogenous signaling from other members of the TGF-β superfamily (e.g., bone morphogenetic proteins (BMPs), growth and differentiation factors (GDFs)) is also essential for regulating chondrogenesis. To investigate how C59

treatment alters gene expression profiles of these families and their associated receptors (including Type I and Type II receptors), we used CCA to align chondrocytes populations and mesenchymal cells from d14 pellets with or without C59 treatment. We also observed that C59 treatment decreased *BMP2*, *BMP4*, *BMP6,* and *BMP7* gene expression, but it increased *GDF5* and *GDF10* gene expression. For receptors, C59 treatment enhanced expression levels of *BMPR1B* and *ACVR1*, but it decreased *BMPR2*, *ACVR2A*, and *ACVR2B* expression (Figure S3.11A-B and S3.12A-B). *BMP8A*, *BMP10*, *BMP11*, and *BMP15*, as well as *GDF2*, *GDF4*, *GDF6*, and *GDF8* were not detected in our datasets.

To investigate how C59 treatment affects the percentage of cells expressing genes of interest within a specific chondrocyte subpopulation, we used *BMP4*, *GDF5*, *BMPR1B* (type I receptor), and *BMPR2* (type II receptor) as examples (Figure S3.10B-E). For BMP4, C59-treated pellets had a decreased percentage of *BMP4*-expressing cells within all chondrocyte subpopulations except *ISG15/IFI6/MX1+* mature-hypertrophic chondrocytes as compared to pellets treated with TGF-β3 only condition. In addition, C59-treated pellets also demonstrated a remarkably increased percentage of *GDF5* and *BMPR1B* expressing cells within all chondrocyte populations versus TGF-β3-treated pellets. Furthermore, C59 decreased the percentage of the cells expressing *BMPR2* in *LECT1/EPYC/FRZB+* early-mature, *ISG15/IFI6/MX1+* mature-hypertrophic chondrocytes, *BNIP3/FAM162+* chondrocytes, and *HMGB2/CDK1+* and *UBE2C/CCNB1+* proliferating chondrocytes. Interestingly, it appeared that C59 treatment did not significantly affect the contribution of a chondrocyte subpopulation to the cells expressing a given gene (i.e., the cells expressing the genes of interests mainly came from *LECT1/EPYC/FRZB+* early-mature chondrocytes regardless of the treatments as presented in the pie charts in Figure S3.10B-E).

114

3.5 Discussion

The therapeutic applications of hiPSCs for cartilage regeneration or disease modeling have been limited by the low-yield of *bona fide* chondrocytes, accompanied by off-target populations during chondrogenic differentiation. Our GRN analysis revealed two major off-target cell populations, neural cells and melanocytes, which showed high association with Wnt4 and Wnt2B signaling, respectively. By building heterocellular signaling models, we showed that off-target cells were the main source of several canonical and non-canonical Wnt ligands that were implicated in chondrocyte hypertrophic differentiation. Importantly, inhibition of Wnt and MITF, the master regulator of melanocyte development, significantly enhanced homogeneity of hiPSC chondrogenesis by decreasing off-target cells, circumventing the need for prospective sorting and expansion of isolated progenitor cells.

An important finding of this study was the identification of distinct subtypes of hiPSC-derived chondrocytes, as shown in depth by the comprehensive transcriptomic profiles of each cell type at various differentiation stages. We also observed that inhibition of Wnt signaling during chondrogenesis alters gene expression levels of BMPs/GDFs (e.g., decreasing *BMP4* and *BMP7* levels) in chondrocytes, which is consistent with a recent study demonstrating decreased BMP activity during MSC chondrogenesis due to Wnt inhibition (*50*). Another intriguing finding is the discovery of *ISG15/IFI6/MX1+* mature-hypertrophic chondrocytes as, without scRNA-seq, this unique population has not been reported before. Although the signature genes of this chondrocyte population (e.g., *STAT-1*) were generally believed to be downstream of IFN-related pathways, we did not detect IFN expression. The high expression of *IGFBP3* in *ISG15/IFI6/MX1+* chondrocytes may provide an explanation for this observation, as IGFBP3 can activate *STAT-1* expression without the presence of IFN molecules in chondrogenesis (*51*).

Additionally, *IGFBP3*-enriched chondrocytes also had decreased expression of *FOS,* essential in driving chondrocytes toward hypertrophy (*44*). It has been reported that chondrocyte hypertrophy was largely prevented upon *IGFBP3* knockdown in the ATDC5 line (*52*). Thus, low FOS expression in *ISG15/IFI6/MX1+* chondrocytes provides a plausible explanation for their low expression of hypertrophic markers. Nevertheless, the causal relationship between the dual function of *IGFBP3* in chondrocyte hypertrophy and Wnt inhibition merits further study.

The finding that melanocytes and neural cells were the major off-target cells imply that some, if not all, progenitors may acquire the phenotype of neural crest cells, a transient stem cell population that can give rise to neurons and melanocytes. This differentiation pathway likely occurs at the Cp stage, where we first observed cell populations expressing several markers of neural crest cells. It is likely that the neural crest cells observed in the current study were also off-target cells (i.e., non-paraxial mesodermal lineage) generated during early stages of mesodermal differentiation and amplified due to BMP4 treatment at the Cp stage. It has been reported that the *Bmp4-Msx1* signaling axis inhibits Wnt antagonists such as Dkk2 and Sfrp2 in dental mesenchyme in mice (*53*), implying BMP4 activating Wnt signaling that is essential for the proliferation of neural crest cells.

Additionally, our sorting results showed that supplementation of Wnt increased, but inhibition of Wnt decreased, the proportion of CD146/CD166+ cells, suggesting that Wnt signaling is required to maintain progenitors at the Cp stage. This finding is in agreement with a recent study showing that Wnt3A supports multipotency of hMSCs during *in vitro* expansion (*54*). In our recent publication using a CRISPR-Cas9-edited reporter hiPSC line and scRNA-seq techniques, we identified that mesenchymal cells triple-positive for CD146, CD166, and PDGFRβ, but negative for CD45, at the Cp stage showed robust chondrogenic potential but little

osteogenic capacity compared to unsorted cells, suggesting that CD146/CD166/PDGFRβ+ mesenchymal cells may be a unique chondroprogenitor population (*55*). However, whether the CD146/CD166+ progenitor population identified in the current study functions like MSCs with multilineage potential warrants future investigation. Furthermore, as distinct subtypes of hiPSC-derived chondrocytes were defined primarily based on marker genes, the complete functionality of these subsets require future investigation.

An important contribution of this study is the construction of the GRN of hiPSC chondrogenesis with the presence of minimal off-target cells, ensuring the hub genes identified are truly governing differentiation. In addition to conventional master TFs such as SOX9, we also identified several additional hub genes associated with chondrogenesis. For instance, the expression levels of complement C1q like 1 (*C1QL1*) was highly correlated with those of *COL2A1* in our model. *C1QL1* encodes a secreted protein with Ca^{2+} binding sites that regulates synaptogenesis in neuronal cells (*56*). However, how C1QL1 affects chondrogenesis or if it plays a role in synovial joint innervation is currently unknown. Additionally, our finding of the melanogenic GRN during hiPSC chondrogenesis suggests an off-target cell fate decision in differentiation. This result is further corroborated by the study of Yamashita and colleagues demonstrating the presence melanin or lipofuscin on the surface of hiPSC-derived cartilage pellet using rigorous histological staining (*57*). Furthermore, we also revealed the significant association between *Wnt2B* and *MITF*, providing insights into melanogenesis. Indeed, a recent study proposed genetic variants in *Wnt2B* may serve as a biomarker to predict survival rate of the patients with cutaneous melanoma (*58*). We also identified *Wnt4* as a hub gene in the GRN of neurogenesis and observed that *Wnt3A* was enriched in the cell populations expressing neural markers. These results are consistent with the previously identified roles for these Wnts in

117

promoting forebrain development (*59, 60*).

Heterogenous multicellular signaling models indicate that although most Wnts were produced by off-target cells, these ligands may signal though chondrocytes. It is well recognized that Wnt signaling not only blocks *SOX9* expression in limb bud mesenchymal cells but also regulates chondrocyte maturation, driving them toward hypertrophy (*61, 62*). In agreement with these findings, hiPSC-derived chondrogenic pellets treated with individual Wnts exhibited increased COL10A1 staining. We also demonstrated that blocking endogenous Wnt signaling significantly improved chondrogenesis in hMSCs. These findings reveal the potential modulatory effects of off-target cells on chondrocytes through Wnt signaling pathway, indicating that inhibition of Wnt has dual beneficial effects on hiPSC chondrogenesis as it not only removes off-target cells but also prevents chondrocyte hypertrophy.

These findings not only identify the mechanisms regulating the heterogeneity in hiPSC chondrogenesis but, more importantly, provide an enhanced chondrogenic differentiation protocol capable of generating homogenous chondrocytes by removing off-target cells without cell sorting. Furthermore, this protocol has been validated in multiple unique lines, demonstrating its robustness and efficiency in deriving chondrocytes from hiPSCs. We also established a comprehensive map of single-cell transcriptome profiles and GRNs governing cell fate decision during hiPSC chondrogenesis. These findings provide insights into dynamic regulatory and signaling pathways orchestrating hiPSC chondrogenesis, thereby advancing a further step of cartilage regenerative medicine toward therapeutic applications. This approach also provides a roadmap for the use of single-cell transcriptomic methods for the study and optimization of other *in vitro* or *in vivo* differentiation processes.

3.6 Supplemental Figures and Tables
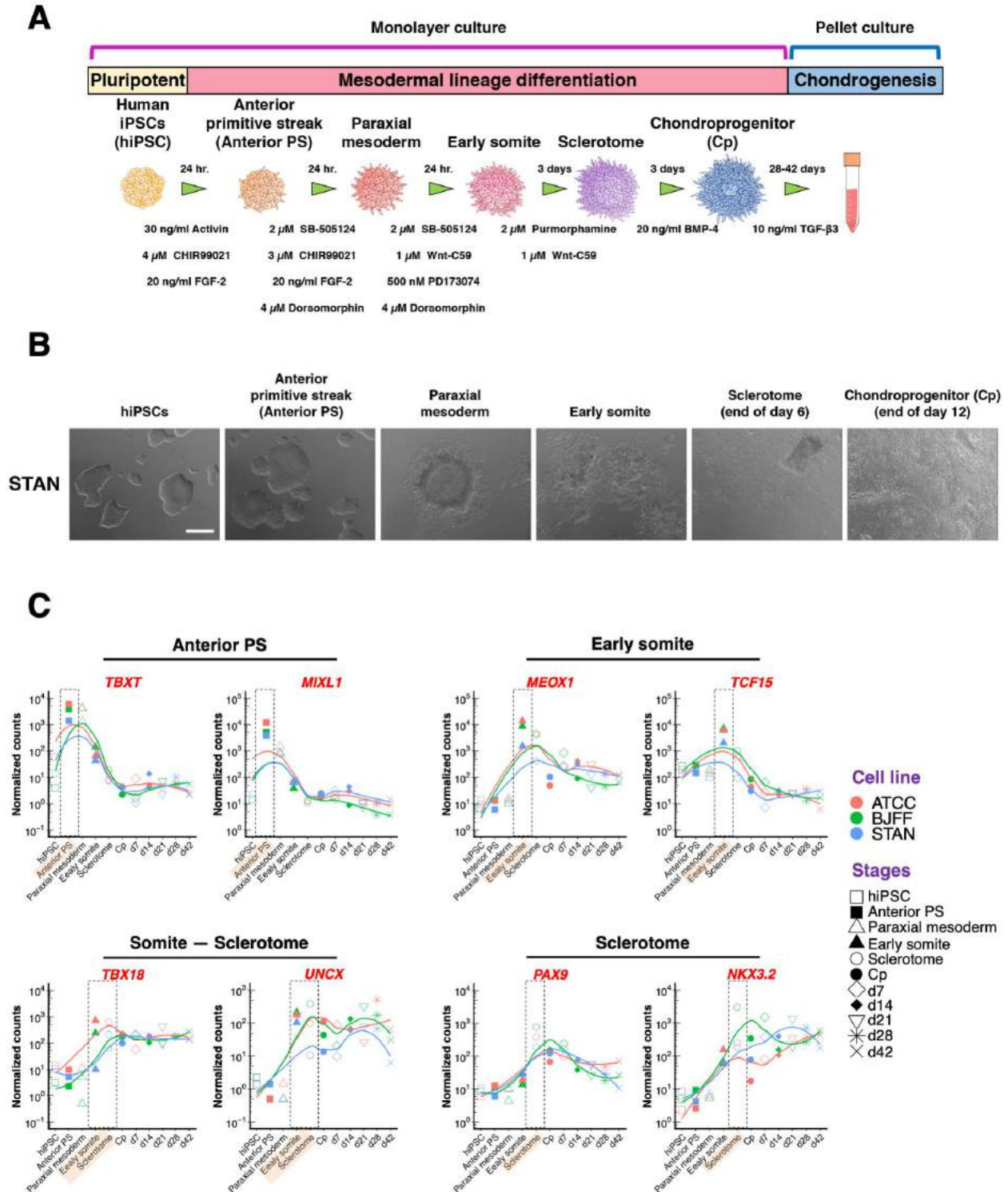
Figure S3.1 Step-wise differentiation of hiPSCs toward chondrocytes via specification of mesoderm. (**A**) Differentiation protocol of hiPSCs into chondrocytes. (**B**) Cell morphology at each stage during mesodermal differentiation. Please note that low cell density at hiPSC stage is required to obtain successful mesodermal differentiation. Scale bar = 500 µm. (**C**) Up-regulation of stage-specific markers for 3 unique hiPSC lines.
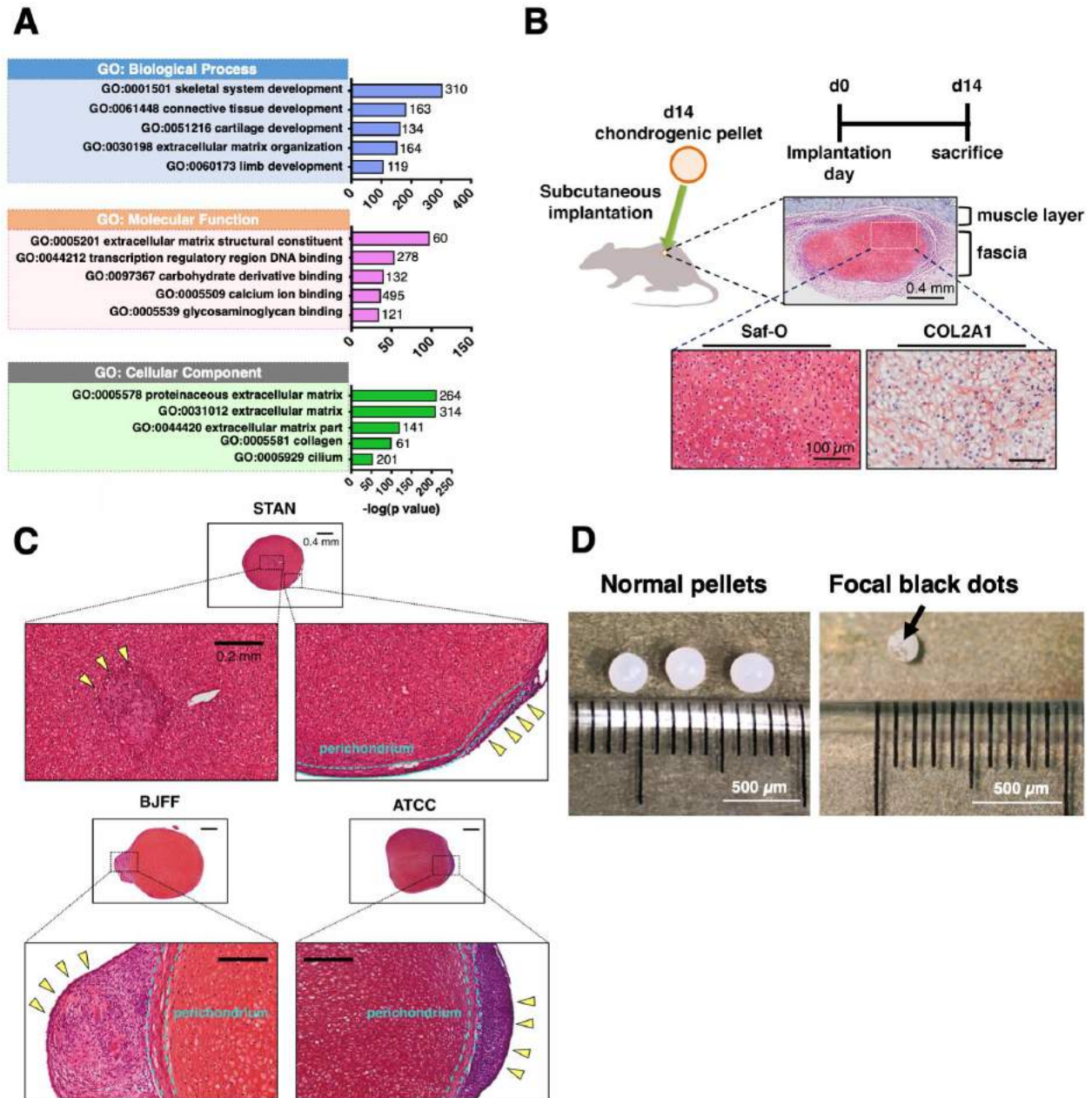
Figure S3.2 GO enrichment analysis of bulk RNA-seq data and subcutaneous implantation of hiPSC-derived chondrocytes in mice. (**A**) GO enrichment analysis of bulk RNA-seq data showing that up-regulated genes were involved in skeletal system and cartilage development. (**B**) d14 chondrogenic pellets maintained a cartilage phenotype indicated by intense Saf-O and COL2A1 staining after 14 days of subcutaneous implantation in mice. n = 3 mice. (**C**) The off-target cells (mostly located at the edge of perichondrium, yellow arrowheads) were observed in the pellets derived from 3 distinct hiPSC lines. (**D**) Focal black dots were occasionally observed on the surface of the pellets.
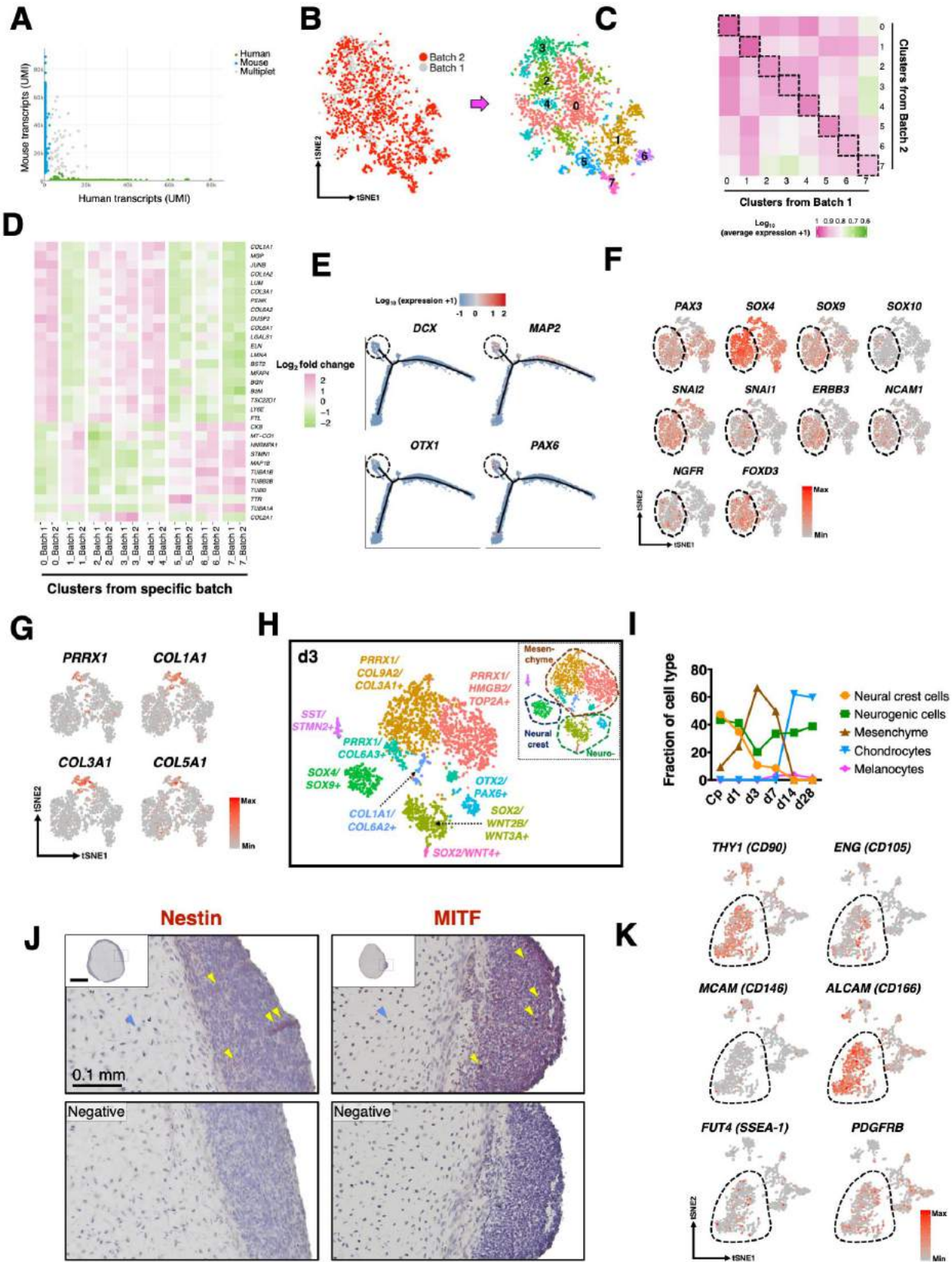
Figure S3.3 Analysis of scRNA-seq data reveals diverse cell populations in hiPSC-derived chondrogenic pellets. (**A**) scRNA-seq of mixed specie samples showing low multiplet rates (< 2.7%). (**B**) CCA of scRNA-seq data from d28 chondrogenic pellets from 2 independent experiments (i.e., 2 batches). 8 conserved cell clusters were identified in both batches. (**C**) Cells in the same cluster from different batches exhibited high correlation in their gene expression (Spearman's rank coefficient $r_s > 0.87$ for all clusters). (**D**) Cells in the clusters from distinct batches demonstrated similar gene expression patterns. (**E**) Additional neural cell markers such as *DCX*, *MAP2*, *OTX1,* and *PAX6* were also enriched in the branch of neurogenic differentiation. (**F**) *SOX4+* and *SOX4/SOX9+* cells at the Cp stage had high expression of neural crest cell markers. A total of 1,888 cells at the Cp stage that passed quality control was analyzed. (**G**) Cells that are enriched for *PRRX1, COL1A1, COL3A1,* and *COL5A1* were annotated as "mesenchyme" at the Cp stage. A total of 1,888 cells at the Cp stage that passed quality control was analyzed. (**H**) Three major cell populations observed in d3 pellets. A total of 2,485 cells from d3 pellets that passed quality control was used to generate the tSNE plot. (**I**) Fraction of major cell types over the course of differentiation (Cp – d28). A total of 11,208 cells from the Cp stage to d28 pellets was analyzed. (**J**) IHC against nestin and MITF confirms the presence of neural cells and melanocytes in pellets. (**K**) Mesenchymal cells in d14 pellets expressed several conventionally recognized MSC markers. However, whether these mesenchymal cells exhibit multipotency like MSCs requires further investigation. A total of 2,148 cells from d14 pellets was analyzed.

A GRN of neurogenesis

B GRN of melanocyte development

C
Hub genes of neurogenesis

Hub genes of melanocyte development

D STAN cell line

E BJFF cell line

F ATCC cell line

G

H MSCs
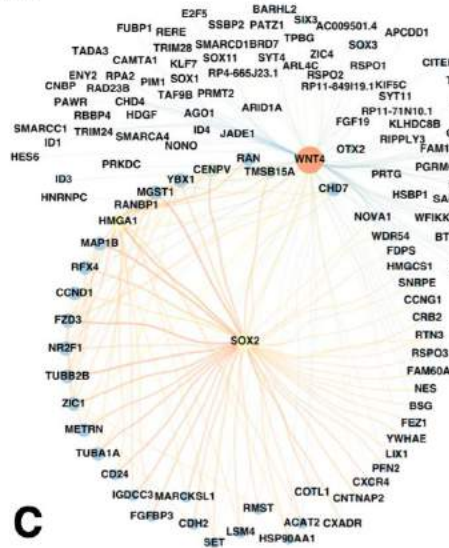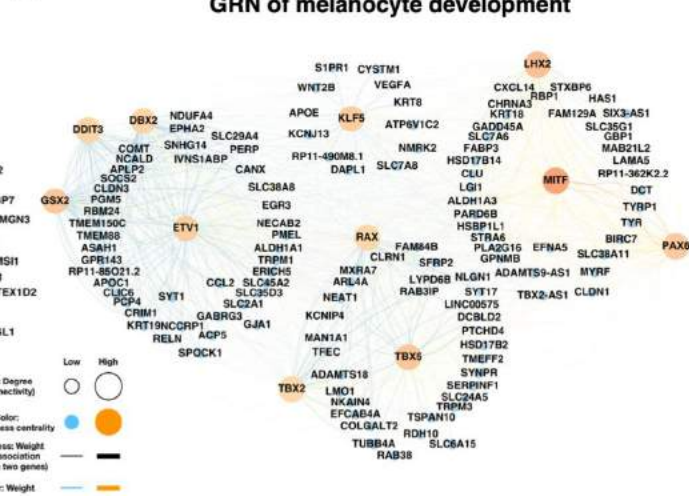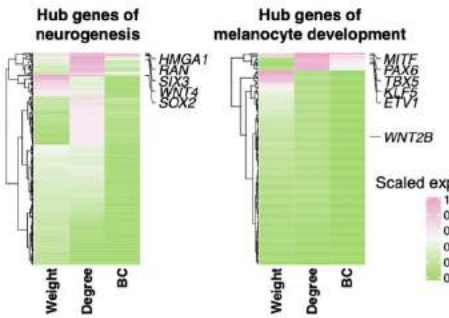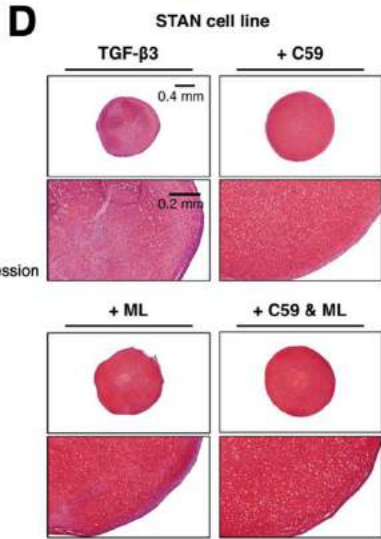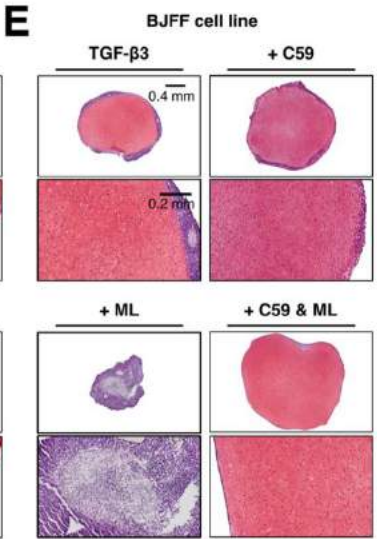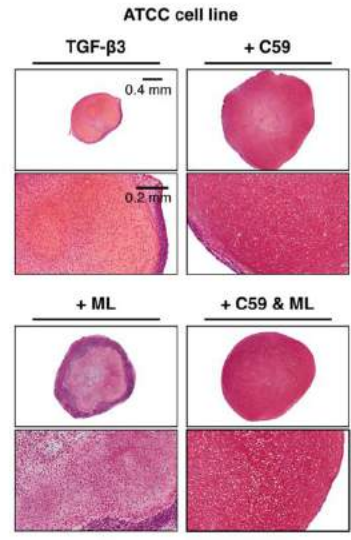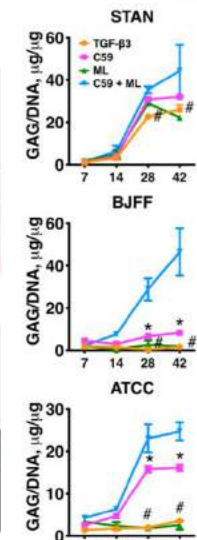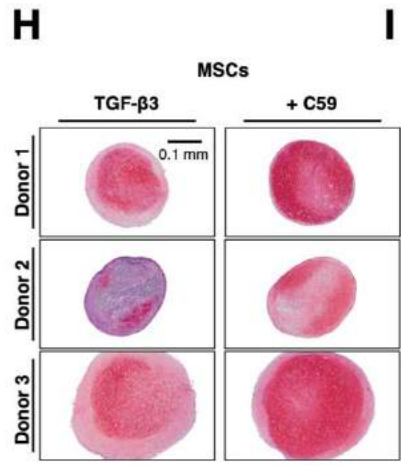
I
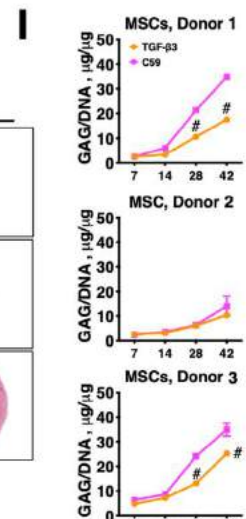
Figure S3.4 WGCNA reconstructed GRNs of neurogenesis and melanogenesis and identified the hub genes in each network. (**A-B**) GRNs of neurogenesis and melanogenesis. Topological analysis (community cluster) was performed to visualize subnetworks. (**C**) *Wnt4* was among the hub genes in the GRN of neurogenesis while *Wnt2B* was associated with the GRN of melanocyte development. (**D-F**) Representative d28 pellet images showing that C59 or a combination of C59 and ML treatment during pellet culture enhanced the homogeneity of chondrogenesis by removing off-target cells. This was validated in 3 unique hiPSC lines. (**G**) The pellets treated with C59 or a combination of C59 and ML treatment exhibited significantly increased GAG/DNA ratios compared to the pellets treated with ML and the pellets treated TGF-β3. * C59 vs. TGF-β3 (p = 0.01) at a specific timepoint. # C59 + ML vs. TGF-β3 (p = 0.001) at a specific timepoint. Mean ± SEM. n = 4 pellets per treatment condition. One-way ANOVA with *Fisher's LSD* was performed at d28 and d42. (**H**) hMSCs harvested from 3 distinct donors exhibited increased chondrogenesis when treated with C59 during pellet culture. (**I**) hMSCs harvested from donor 1 and donor 3 had significantly increased GAG/DNA ratios when treated with C59 compared to with TGF-β3 alone. # C59 vs. TGF-β3 (p = 0.01) at specific time point. Mean ± SEM. n = 4 pellets per treatment condition. Two-tailed Student's t-test was performed at d28 and d42.
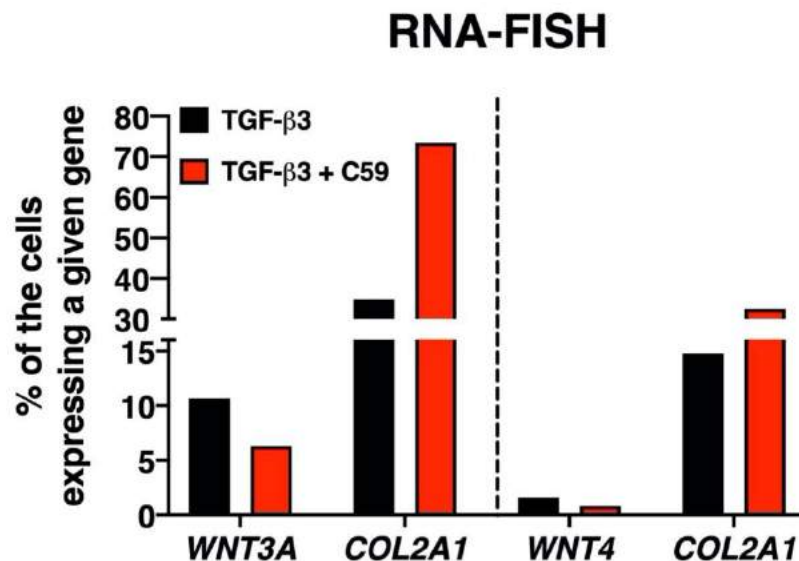
Figure S3.5 Semi-quantification of RNA-FISH against Wnts and COL2A1. C59-treated pellets showed decreased *Wnt3A* and *Wnt4* expression but increased *COL2A1* RNA-FISH labeling versus TGF-β3-treated pellets.
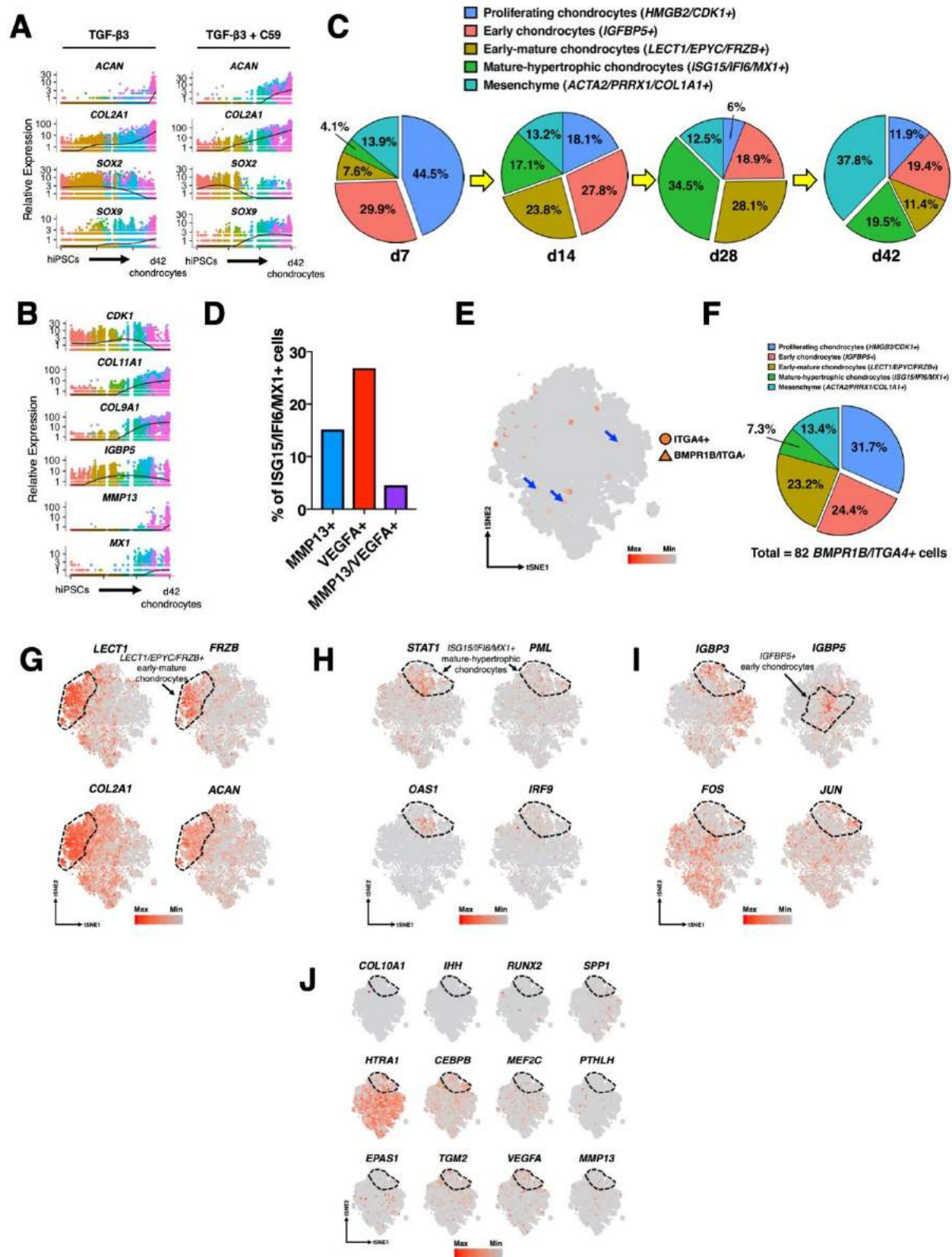
Figure S3.6 Multiple CCA alignment of d7-d42 pellets reveals that 4 conserved chondrocyte

subpopulations and 1 conserved mesenchymal population were observed in C59-treated pellets. (**A**) Jitter plots showing that C59-treated pellets had increased expression of *ACAN, COL2A1,* and *SOX9* but decreased *SOX2* versus Standard TGF-β3-treated pellets. (**B**) Temporal expression profiles of signature genes of each chondrocyte subpopulation. *CDK1* and *IGFBP5* showed transient upregulation while *COL9A1* and *COL11A1* remained up-regulated once activated. *MMP13* and *MX1* showed increased expression levels at later time points. (**C**) Dynamic changes in the percentage of the cell population within the pellets over the course of differentiation. (**D**) *ISG15/IFI6/MX1+* chondrocytes contained 4.6% cells expressing both *VEGF*A and *MMP13*. (**E-F**) *BMPR1B/ITGA4+* progenitors previously identified in articular cartilage were mostly observed in *HMGB2/CDK1+* proliferating chondrocytes. (**G**) *LECT1/EPYC/FRZB+* early-mature chondrocytes had the highest levels of *COL2A1* and *ACAN* expression among other chondrocyte subpopulations. (**H**) *ISG15/IFI6/MX1+* mature-hypertrophic chondrocytes expressed several IFN-related genes. (**I**) In comparison with *IGFBP5+* early chondrocytes, *ISG15/IFI6/MX1+* mature-hypertrophic chondrocytes showed high expression in *IGFBP3* but decreased expression in *FOS*. (**J**) The expression of various hypertrophic chondrocyte markers. For scRNA-seq analysis of C59 treated pellets, total 7,997 cells (from d7-d42) passed quality control and thus were analyzed for this figure. (**E-F**) A total of 7,977 cells from d7-d42 timepoints of C59-treated pellets was used to performed CCA alignment.
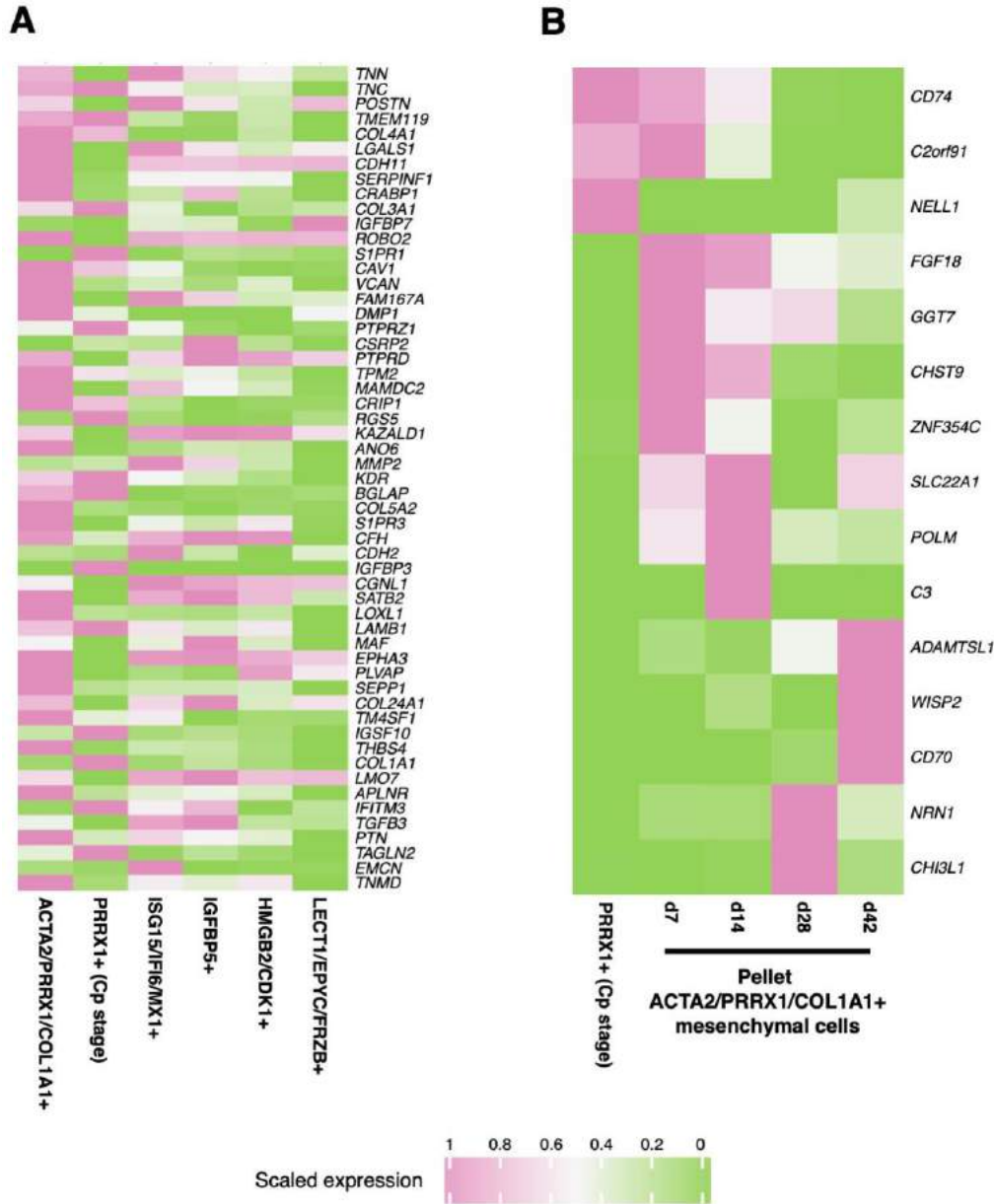
Figure S3.7 *ACTA2/PRRX1/COL1A1+* mesenchymal cells in the pellets, but not mesenchymal cells at the Cp stage, exhibit similar gene expression profile to perichondrial cells. (**A**) *ACTA2/PRRX1/COL1A1+* mesenchymal cells in the pellets expressed markers of rat perichondrial cells. (**B**) *ACTA2/PRRX1/COL1A1+* mesenchymal cells from d7 and d14 pellets were enriched with 8 of 15 differentially expressed genes in the perichondrium-like membrane of the human chondrogenic pellet. Particularly, d7 *ACTA2/PRRX1/COL1A1+* mesenchymal cells had the highest expression of *C2orf91*, *FGF18*, *GGT7*, *CHST9*, and *ZNH354C*. Interestingly, we also observed that there was gradual shift in the gene expression profile of *ACTA2/PRRX1/COL1A1+* mesenchymal cells from d28 to d42. For example, d28 *ACTA2/PRRX1/COL1A1+* mesenchymal cells were enriched in *NRN1* and *CH3L1* while d42 cells had the highest expression of *ADAMTSL1*, *WISP2*, and *CD70*.

127

A The GRN of chondrogenesis

B d14 TGF-β3 + C59 v.s. TGF-β3

Chondrocytes   Proliferative cells   Mesenchyme

Scaled expression

C

Mesenchyme   Proliferative cells   Chondrocytes

D d28 TGF-β3 + C59 v.s. TGF-β3

Chondrocytes

Scaled expression
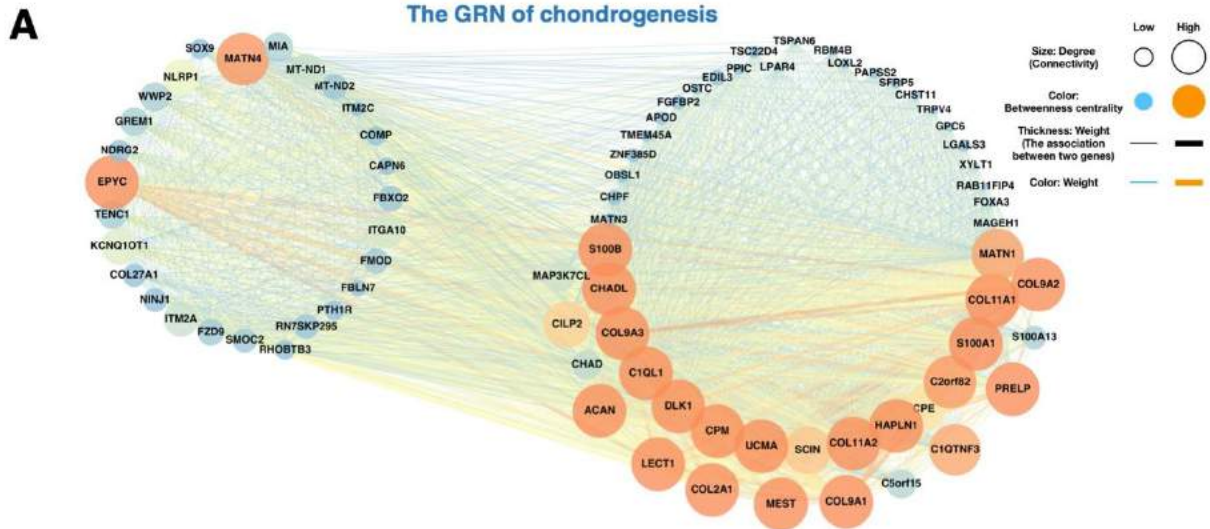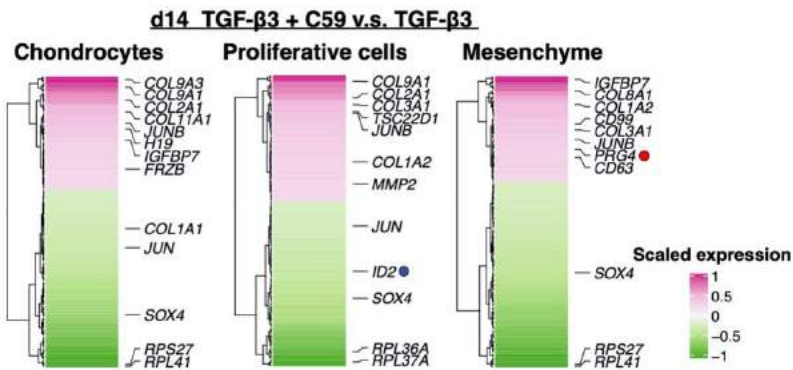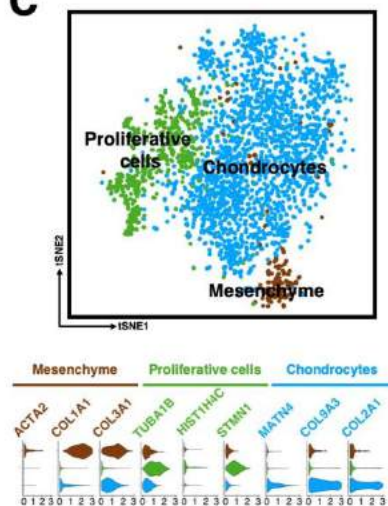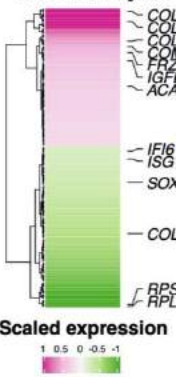
E
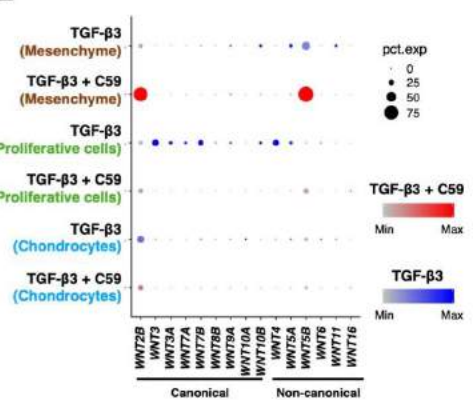
Figure S3.8 The GRN of hiPSC chondrogenesis. (**A**) The GRN and hub genes of hiPSC chondrogenesis. (**B**) CCA was used to identify DEGs of each subpopulation between d14 pellets with and without C59 treatment. *ID2*, a neurogenic marker (blue circle), was decreased in proliferative cells in C59-treated pellets, while *PRG4* (red circle) was increased in mesenchymal cells in C59-treated pellets. (**C**) CCA alignment of cells from d28 pellets with and without C59 treatment. A total of 3,027 cells from d28 pellets with and without C59 treatment was used to performed CCA alignment. (**D**) CCA was used to identify DEGs of chondrocytes between d28 pellets with and without C59 treatment. Markers for mature-hypertrophic chondroocytes, such as *IFI6* and *ISG15* (blue circles), were decreased while *ACAN* and *COMP* (red circles) were increased in C59-treated pellets. (**E**) Similar to the Wnt expression profiles in d14 pellets, most Wnts were expressed by proliferative cells in the d28 pellets treated with TGF-β3.
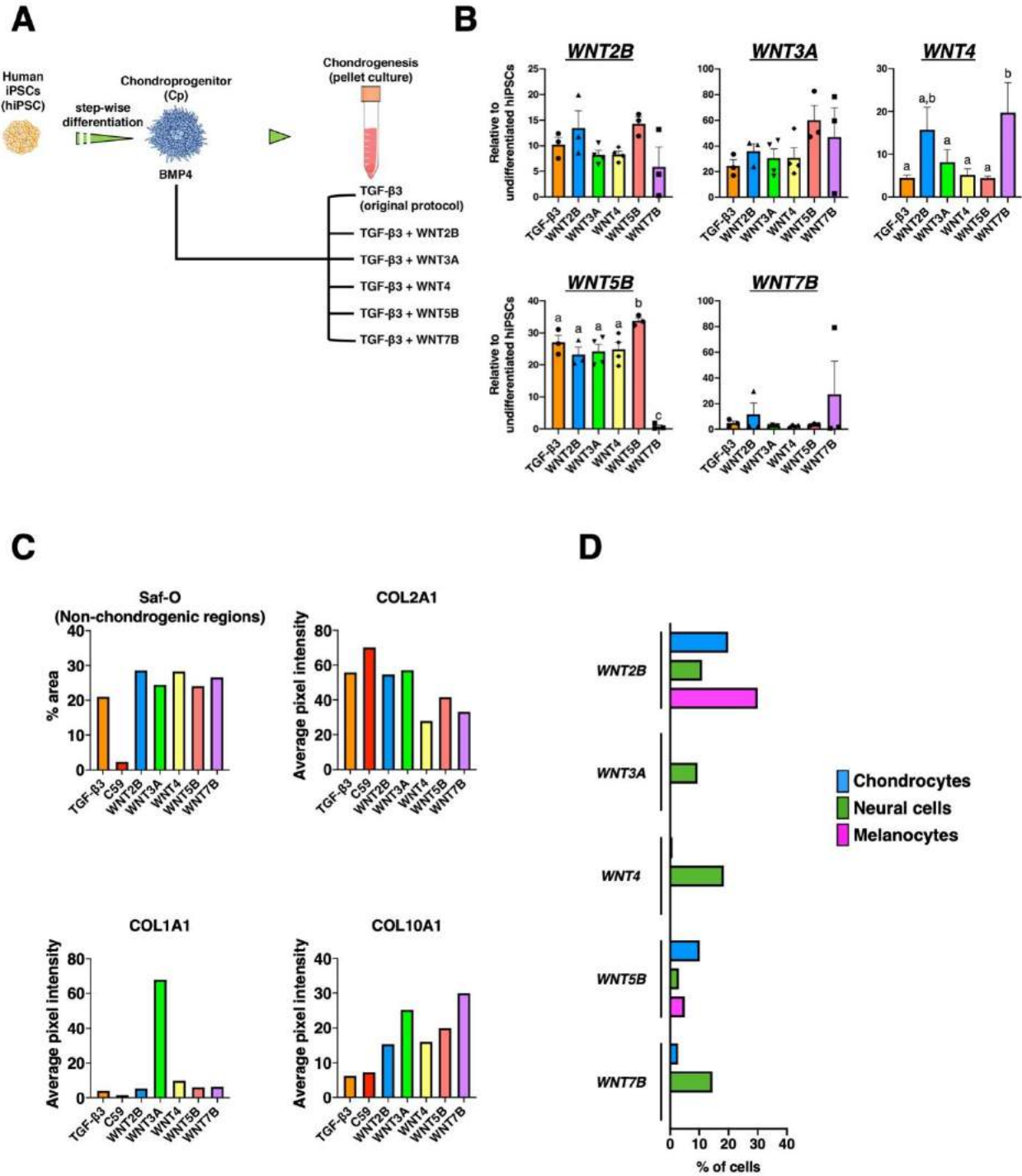
Figure S3.9 Effect of Wnts on chondrogenesis. (**A**) Schematic of Wnt treatment during chondrogenic pellet culture. (**B**) RT-qPCR of d14 pellets treated various Wnts showing that gene expression of Wnts can be modulated by other Wnt ligands. Different letters are significantly different from each other ($p < 0.05$). Mean ± SEM. n = 3-4 pellets per group. Statistical significance was determined by one-way ANOVA with Tukey's *post-hoc* test. (**C**) Semi-quantification of Saf-O and IHC labeling against various collagens. (**D**) Percentage of the cells

expressing a variety of Wnts in d14 pellets treated with TGF-β3. For scRNA-seq analysis of d14 TGF-β3 treated pellets, total 2,148 cells passed quality control and thus were analyzed.
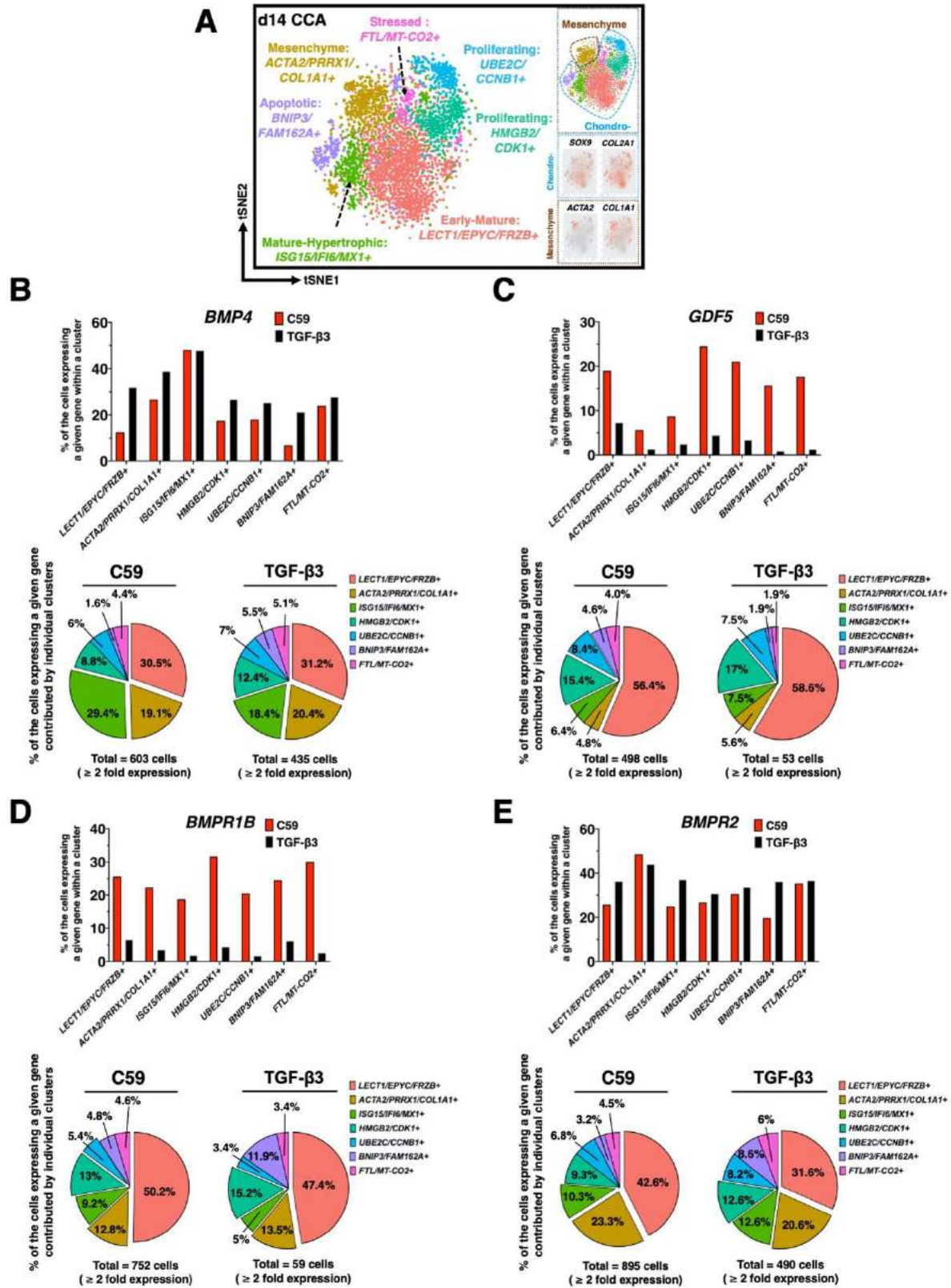
Figure S3.10 Differential expression of BMPs/GDFs and receptors in response to Wnt inhibition. (**A**) CCA alignment of chondrocyte and mesenchymal populations from TGF-β3 only and C59 conditions. (**B**) C59-treated pellets had a decreased percentage of *BMP4* expressing cells within all clusters except within *ISG15/IFI6/MX1+* mature-hypertrophic chondrocytes. (**C-D**) C59-treated pellets demonstrated a remarkably increased percentage of *GDF5* and *BMPR1B* expressing cells within all clusters versus TGF-β3-treated pellets. (**E**) C59 treatment decreased percentage of cells expressing *BMPR2* in *LECT1/EPYC/FRZB+* early-mature chondrocytes, *ISG15/IFI6/MX1+* mature-hypertrophic chondrocytes, *BJIP3/FAM162+* apoptotic chondrocytes, as well as *HMGB2/CDK1+* and *UBE2C/CCNB1/KPNA2+* proliferating chondrocytes. (**B-E**) Note that C59 treatment did not significantly affect the contribution of a cluster to the cells expressing *BMP4*, *GDF5, BMPR1B,* and *BMPR2* as presented in the pie charts. For bioinformatic analysis, CCA was performed with a total of 1,335 cells from mesenchymal and chondrocyte populations from d14 TGF-β3 pellets and with a total of 3,047 cells from mesenchymal and chondrocyte populations from d14 C59 pellets.
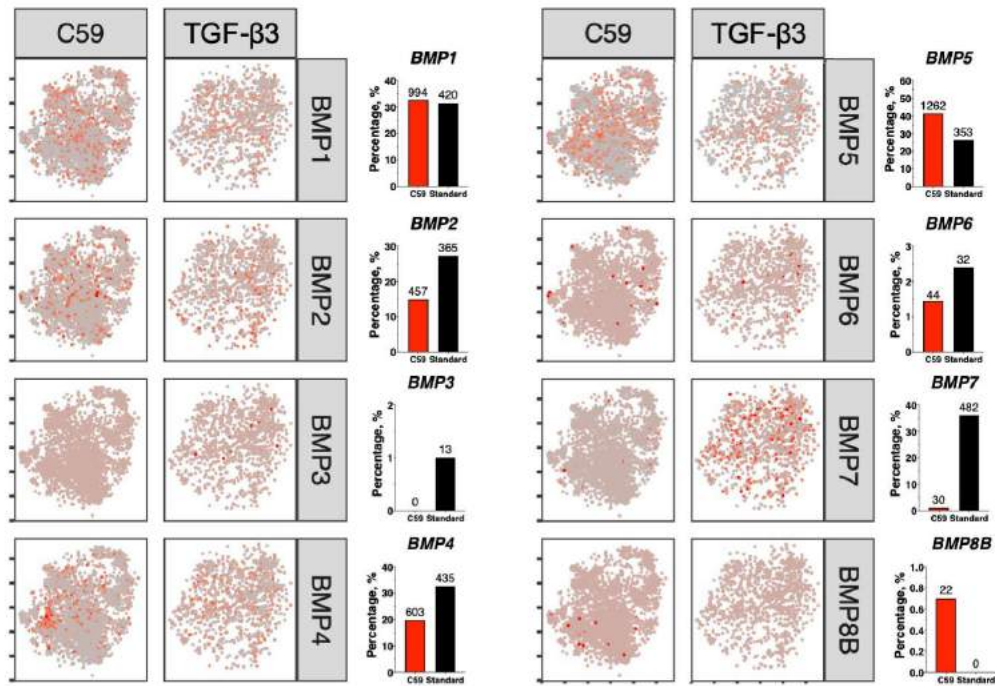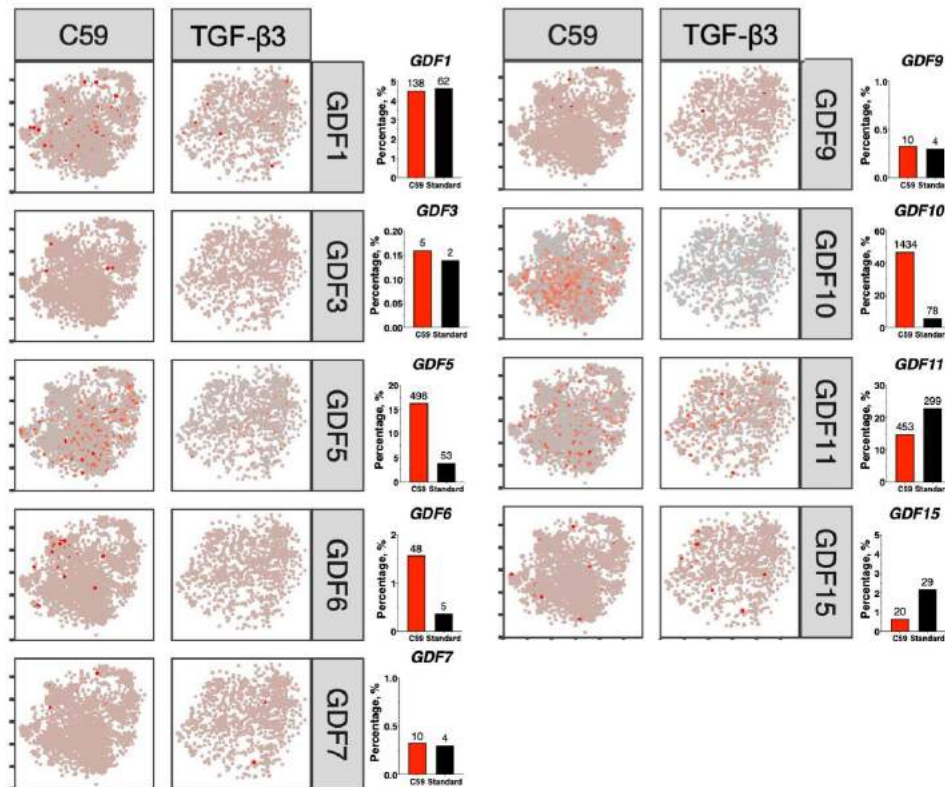
Figure S3.11 CCA analysis showing differential gene expression with C59 treatment. (**A**) BMP and (**B**) GDF families in chondrocyte subpopulations due to C59 treatment. Numerical value on

133

top of each bar in the bar graph indicates cell numbers expressing a given gene. For bioinformatic analysis, CCA was performed with a total of 1,335 cells from mesenchymal and chondrocyte populations from d14 TGF-β3 pellets and with a total of 3,047 cells from mesenchymal and chondrocyte populations from d14 C59 pellets.

Figure S3.12 CCA analysis showing differential receptor gene expression with C59 treatment. (**A**) Type I and (**B**) type II receptors for the BMP/GDF family in chondrocyte subpopulations due to C59 treatment. Numerical value on top of each bar in the bar graph indicates cell numbers expressing a given gene. For bioinformatic analysis, total 2,148 cells from d14 TGF-β3 treated pellets and total 3,076 cells from d14 C59+TGF-β3 treated pellets passed quality control and thus were analyzed for this figure.

Table S3.1 Numbers of the cells passed quality control (QC) for each stage and associated highly variable genes.

	Detected cells	Cells passed QC	Median genes/cell	Highly variable genes
Monolayer culture				
hiPSC	6258	4798	1688	1651
Sclerotome	2237	1861	3107	2240
Cp	2536	1888	3443	1754
Sum	11031	8547	8238	5645
Average	3677	2849	2746	1882
TGF-β3 chondrogenic pellets				
d1	2418	2216	3447	2097
d3	2810	2485	3357	1835
d7	1369	1200	4049	2302
d14	2266	2148	3784	2001
d28	1321	1271	2900	2178
d42	1355	1328	2324	1955
Sum	11539	10648	19861	12368
Average	1923	1775	3310	2061
TGF-β3 + C59 chondrogenic pellets				
d7	2191	1682	4030	1733
d14	3461	3076	2718	1693
d28	1881	1756	2714	1991
d42	1926	1483	3003	2126
Sum	9459	7997	12456	7543
Average	2365	1999	3116	1886

Table S3.2 Top 10 up-regulated genes in fold change in mesodermal phase. Related to Figure 1.

Ensembl	Symbol	AP vs hiPSC	PM vs AP	ES vs Par	Scl vs ES	ES vs Cp
ENSG00000113722	CDX1	7.47	1.28	-5.77	-1.90	-2.03
ENSG00000185155	MIXL1	7.32	-2.67	-4.09	-2.29	0.91
ENSG00000222033	LINC01124	7.32	0.31	-5.65	-2.48	2.72
ENSG00000164458	T	7.19	-0.13	-5.22	-2.84	-1.81
ENSG00000104371	DKK4	7.13	-2.61	-5.28	-0.92	1.07
ENSG00000274981		6.99	-0.44	-4.38	-2.01	-0.10
ENSG00000241345	LOC105375483	6.80	1.09	-5.53	-1.25	2.06
ENSG00000253308		6.75	2.33	-7.08	-1.82	2.23
ENSG00000106038	EVX1	6.51	0.01	-5.38	-2.44	1.48
ENSG00000105991	HOXA1	6.34	3.87	-2.36	-1.99	-1.85
ENSG00000049249	TNFRSF9	1.16	6.93	-5.79	-0.95	3.01
ENSG00000120094	HOXB1	2.25	6.54	-3.53	-3.39	-0.37
ENSG00000151379	MSGN1	3.11	6.23	-5.27	-3.42	-0.60
ENSG00000137252	HCRTR2	0.01	6.01	-2.13	-0.74	1.57
ENSG00000179111	HES7	0.97	5.54	-2.97	-2.34	-0.34
ENSG00000253552		2.07	5.13	0.68	-2.19	-0.52
ENSG00000182742	HOXB4	1.54	4.93	1.00	-1.24	-0.41
ENSG00000129654	FOXJ1	-2.73	4.73	-2.53	1.02	1.48
ENSG00000163083	INHBB	-2.68	4.55	-0.68	-2.63	1.58
ENSG00000100678	SLC8A3	-0.89	4.53	-0.27	-0.63	-1.42
ENSG00000147223	RIPPLY1	-0.02	-0.99	11.49	-8.93	-1.53
ENSG00000005102	MEOX1	0.06	0.37	9.05	-1.35	-5.05
ENSG00000164853	UNCX	-1.66	0.00	8.92	-0.59	-1.21
ENSG00000136698	CFC1	-2.67	2.82	8.33	-4.80	-1.36
ENSG00000224865	LOC101928782	0.07	0.01	8.17	-2.92	-4.34

ENSG00000168269	FOXI1	1.00	-0.91	8.12	-4.89	-3.26
ENSG00000102837	OLFM4	0.99	-0.16	7.77	-4.75	-0.94
ENSG00000176692	FOXC2	0.89	0.83	7.24	-1.11	-2.23
ENSG00000176678	FOXL1	-0.32	0.94	7.15	-2.86	-1.48
ENSG00000213931	HBE1	1.07	0.33	7.12	-1.58	-0.82
ENSG00000136327	NKX2-8	2.46	-0.32	-2.04	9.99	-3.90
ENSG00000184302	SIX6	0.22	-1.31	-3.65	8.29	-0.28
ENSG00000008196	TFAP2B	2.42	0.63	-4.51	7.30	1.47
ENSG00000274021		-0.86	0.85	-6.19	6.97	-1.09
ENSG00000064218	DMRT3	0.99	0.80	-2.70	6.97	-3.17
ENSG00000139318	DUSP6	-0.39	0.72	-6.78	6.96	-1.03
ENSG00000176165	FOXG1	0.14	0.67	-0.64	6.81	-3.11
ENSG00000244405	ETV5	-0.05	0.62	-6.23	6.76	-1.15
ENSG00000152785	BMP3	-0.82	0.49	0.16	6.63	-3.57
ENSG00000178235	SLITRK1	-0.99	0.33	-2.34	6.62	-2.86
ENSG00000180828	BHLHE22	2.88	-1.47	-2.00	-3.08	7.73
ENSG00000167941	SOST	-1.11	0.36	5.37	-4.87	7.09
ENSG00000188620	HMX3	-2.25	-0.08	2.35	-3.91	6.47
ENSG00000164125	FAM198B	0.87	-0.59	-0.25	1.80	6.30
ENSG00000163132	MSX1	4.90	0.75	-2.60	-1.44	6.30
ENSG00000175899	A2M	-0.10	-0.72	-0.41	1.55	6.29
ENSG00000165092	ALDH1A1	-0.27	-1.01	-1.47	0.82	6.20
ENSG00000109846	CRYAB	-1.24	-0.25	-0.09	-0.25	6.12
ENSG00000107984	DKK1	5.15	-0.85	-3.78	-2.19	6.10
ENSG00000122641	INHBA	-1.45	-1.94	1.50	-0.96	6.07

AP: anterior primitive streak; **PM**: paraxial mesoderm; **ES**: early somite, **Scl**: Sclerotome; **Cp**: Chondroprogenitor

Table S3.3 Top 10 up-regulated genes in fold change in chondrogenic phase. Related to Figure 1.

Ensembl	Symbol	d7 vs Cp	d14 vs d7	d21 vs d14	d28 vs d21	d42 vs d28
ENSG00000124159	*MATN4*	7.69	1.22	0.73	-1.28	-0.68
ENSG00000181195	*PENK*	7.65	1.16	-0.23	-0.15	-0.51
ENSG00000008441	*NFIX*	7.08	-0.36	1.15	-0.69	0.43
ENSG00000006611	*USH1C*	7.01	-0.34	-0.37	-0.64	0.73
ENSG00000157554	*ERG*	6.44	-0.47	-0.45	-0.25	-0.51
ENSG00000171812	*COL8A2*	6.19	-0.01	0.68	-1.48	0.21
ENSG00000124134	*KCNS1*	6.18	0.48	0.42	-0.68	-1.88
ENSG00000121898	*CPXM2*	5.87	0.80	1.01	-0.05	0.52
ENSG00000224765		5.75	-0.37	0.53	-0.83	-0.15
ENSG00000145708	*CRHBP*	5.66	-2.59	0.34	0.56	-3.25
ENSG00000249945		-2.48	5.07	-4.36	-0.50	0.13
ENSG00000135480	*KRT7*	-2.54	4.98	1.00	-0.08	-0.17
ENSG00000278530	*CHMP1B2P*	-0.11	4.80	-4.40	-1.15	-1.39
ENSG00000234787	*LINC00458*	-2.38	4.34	-2.06	0.93	-0.91
ENSG00000182798	*MAGEB17*	-3.16	4.24	-1.13	-1.02	2.03
ENSG00000278840		-2.23	4.19	0.70	-0.59	0.73
ENSG00000253507		-0.90	4.00	-2.28	-0.13	0.48
ENSG00000187569	*DPPA3*	0.15	3.96	-1.73	0.95	-0.79
ENSG00000196767	*POU3F4*	2.51	3.94	-1.98	-0.60	-2.49
ENSG00000101842	*VSIG1*	-1.03	3.81	-1.35	-0.37	2.15
ENSG00000011083	*SLC6A7*	-0.34	-1.09	6.22	-1.47	-0.62
ENSG00000205890	*LOC100128770*	-2.25	1.60	5.78	-3.33	-1.20
ENSG00000152213	*ARL11*	-1.54	-1.42	5.10	-4.03	1.23
ENSG00000233841	*HLA-C*	-0.97	0.94	5.06	-5.06	1.81
ENSG00000117091	*CD48*	0.74	-0.73	4.77	-3.40	-1.04

ENSG00000166869	CHP2	-3.55	0.82	4.70	-4.51	1.21
ENSG00000204121		-3.93	1.36	4.51	-3.57	1.80
ENSG00000224865	LOC101928782	0.13	-0.54	4.48	-4.29	2.13
ENSG00000182912		-0.87	-1.29	4.45	-2.86	0.11
ENSG00000188257	PLA2G2A	2.84	-1.28	4.22	1.86	-0.02
ENSG00000213931	HBE1	-3.49	1.31	-0.55	3.12	-4.81
ENSG00000207927	MIR302A	-0.72	0.80	-1.84	2.87	0.72
ENSG00000120094	HOXB1	-0.17	1.40	-1.90	2.82	-3.71
ENSG00000164746	C7orf57	-0.30	-0.16	-0.92	2.77	-0.75
ENSG00000183463	URAD	-2.49	-0.82	0.69	2.68	-3.05
ENSG00000203635		-0.46	0.86	-2.09	2.66	-1.49
ENSG00000131095	GFAP	0.18	0.65	1.11	2.65	0.93
ENSG00000255282	WTAPP1	-2.90	-1.23	0.75	2.62	-0.60
ENSG00000101276	SLC52A3	-1.43	1.12	-1.39	2.57	-0.83
ENSG00000277060	NLRP2	-1.14	1.39	-1.19	2.56	-2.86
ENSG00000166828	SCNN1G	-2.23	0.06	-0.22	0.46	4.32
ENSG00000129451	KLK10	-2.31	-0.66	1.84	0.73	3.96
ENSG00000168447	SCNN1B	-1.71	0.49	3.90	-3.56	3.84
ENSG00000176654		-1.05	2.23	1.68	-4.23	3.50
ENSG00000234745	HLA-B	0.48	-0.20	0.68	-1.09	3.48
ENSG00000013588	GPRC5A	0.83	-0.05	1.38	0.16	3.45
ENSG00000105392	CRX	0.14	1.54	-1.45	-1.03	3.32
ENSG00000137265	IRF4	-1.02	-0.43	3.20	-1.55	3.27
ENSG00000123689	G0S2	-2.25	0.07	1.75	0.99	3.25
ENSG00000161652	IZUMO2	-1.81	-1.56	0.78	0.27	3.02

3.7 Conclusion

In conclusion, we used next generation sequencing to map the transcriptomic profile of hiPSC

chondrogenesis. This allowed us to identify Wnt and MITF as the drivers of off-target differentiation resulting in neurogenic and melanocytic cell populations, respectively. By inhibiting these signaling pathways during chondrogenesis, we significantly improved the homogeneity and robustness of the hiPSC-derived cartilage. The extensive data gathered about chondrogenesis via the mesodermal lineage will provide insights and preliminary data for future studies investigating chondrogenic differentiation and optimizing cartilage tissue engineering. Furthermore, the hiPSC-derived cartilage can serve as an *in vitro* disease model for developmental and degenerative cartilage diseases.

3.8 References

1. S. S. Adkar *et al.*, Genome engineering for personalized arthritis therapeutics. *Trends in molecular medicine* 23, 917-931 (2017).

2. Y. Nam, Y. A. Rim, S. M. Jung, J. H. Ju, Cord blood cell-derived iPSCs as a new candidate for chondrogenic differentiation and cartilage regeneration. *Stem cell research & therapy* 8, 16 (2017).

3. N. Koyama *et al.*, Human induced pluripotent stem cells differentiated into chondrogenic lineage via generation of mesenchymal progenitor cells. *Stem cells and development* 22, 102-113 (2012).

4. A. M. Craft *et al.*, Generation of articular chondrocytes from human pluripotent stem cells. *Nature biotechnology* 33, 638 (2015).

5. A. Yamashita *et al.*, Generation of scaffoldless hyaline cartilaginous tissue from human iPSCs. *Stem cell reports* 4, 404-418 (2015).

6. C. K. Chan *et al.*, Identification of the human skeletal stem cell. *Cell* 175, 43-56. e21 (2018).

7. K. M. Loh *et al.*, Mapping the pairwise choices leading from pluripotency to human bone, heart, and other mesoderm cell types. *Cell* 166, 451-467 (2016).

8. S. S. Adkar *et al.*, Step-Wise Chondrogenesis of Human Induced Pluripotent Stem Cells and Purification Via a Reporter Allele Generated by CRISPR-Cas9 Genome Editing. *STEM CELLS* 37, 65-76 (2019).

9. T. W. Theunissen *et al.*, Molecular criteria for defining the naive human pluripotent state. *Cell stem cell* 19, 502-515 (2016).

10. N. P. Huynh, B. Zhang, F. Guilak, High-depth transcriptomic profiling reveals the temporal gene signature of human mesenchymal stem cells during chondrogenesis. *The FASEB Journal* 33, 358-372 (2018).

11. F. Qu, I. C. Palte, P. M. Gontarz, B. Zhang, F. Guilak, Transcriptomic analysis of bone and

fibrous tissue morphogenesis during digit tip regeneration in the adult mouse. *The FASEB Journal* 34, 9740-9754 (2020).

12. M. Martin, Cutadapt removes adapter sequences from high-throughput sequencing reads. *EMBnet. journal* 17, 10-12 (2011).

13. A. Dobin *et al.*, STAR: ultrafast universal RNA-seq aligner. *Bioinformatics* 29, 15-21 (2013).

14. Y. Liao, G. K. Smyth, W. Shi, The Subread aligner: fast, accurate and scalable read mapping by seed-and-vote. *Nucleic acids research* 41, e108-e108 (2013).

15. M. I. Love, W. Huber, S. Anders, Moderated estimation of fold change and dispersion for RNA-seq data with DESeq2. *Genome biology* 15, 550 (2014).

16. H. Wickham, *ggplot2: elegant graphics for data analysis*. (Springer, 2016).

17. W. Luo, M. S. Friedman, K. Shedden, K. D. Hankenson, P. J. Woolf, GAGE: generally applicable gene set enrichment for pathway analysis. *BMC bioinformatics* 10, 161 (2009).

18. Z. Gu, R. Eils, M. Schlesner, Complex heatmaps reveal patterns and correlations in multidimensional genomic data. *Bioinformatics* 32, 2847-2849 (2016).

19. A. Butler, P. Hoffman, P. Smibert, E. Papalexi, R. Satija, Integrating single-cell transcriptomic data across different conditions, technologies, and species. *Nature biotechnology* 36, 411 (2018).

20. L. v. d. Maaten, G. Hinton, Visualizing data using t-SNE. *Journal of machine learning research* 9, 2579-2605 (2008).

21. D. W. Huang *et al.*, The DAVID Gene Functional Classification Tool: a novel biological module-centric algorithm to functionally analyze large gene lists. *Genome biology* 8, R183 (2007).

22. I. Tirosh *et al.*, Dissecting the multicellular ecosystem of metastatic melanoma by single-cell RNA-seq. *Science* 352, 189-196 (2016).

23. C. Trapnell *et al.*, The dynamics and regulators of cell fate decisions are revealed by pseudotemporal ordering of single cells. *Nature biotechnology* 32, 381 (2014).

24. X. Qiu *et al.*, Single-cell mRNA quantification and differential analysis with Census. *Nature methods* 14, 309 (2017).

25. G. Su, A. Kuchinsky, J. H. Morris, D. J. States, F. Meng, GLay: community structure analysis of biological networks. *Bioinformatics* 26, 3135-3137 (2010).

26. P. Shannon *et al.*, Cytoscape: a software environment for integrated models of biomolecular interaction networks. *Genome research* 13, 2498-2504 (2003).

27. J. A. Ramilowski *et al.*, A draft network of ligand–receptor-mediated multicellular signalling in human. *Nature communications* 6, 7866 (2015).

28. S. Hrvatin *et al.*, Single-cell analysis of experience-dependent transcriptomic states in the mouse visual cortex. *Nature neuroscience* 21, 120 (2018).

29. Z. Gu, L. Gu, R. Eils, M. Schlesner, B. Brors, circlize implements and enhances circular visualization in R. *Bioinformatics* 30, 2811-2812 (2014).

30. L. Wu *et al.*, Human developmental chondrogenesis as a basis for engineering chondrocytes from pluripotent stem cells. *Stem cell reports* 1, 575-589 (2013).

31. G. B. Ferguson *et al.*, Mapping molecular landmarks of human skeletal ontogeny and pluripotent stem cell-derived articular chondrocytes. *Nature communications* 9, 3634 (2018).

32. H. Kempf *et al.*, Bulk cell density and Wnt/TGFbeta signalling regulate mesendodermal patterning of human pluripotent stem cells. *Nature communications* 7, 13602 (2016).

33. N. Akhtar *et al.*, MicroRNA-27b regulates the expression of matrix metalloproteinase 13 in human osteoarthritis chondrocytes. *Arthritis & Rheumatism* 62, 1361-1371 (2010).

34. N. E. Baker, N. L. Brown, All in the family: proneural bHLH genes and neuronal diversity. *Development* 145, dev159426 (2018).

35. M. Simões-Costa, M. E. Bronner, Establishing neural crest identity: a gene regulatory recipe. *Development* 142, 242-257 (2015).

36. D. ten Berge, A. Brouwer, J. Korving, J. F. Martin, F. Meijlink, Prx1 and Prx2 in skeletogenesis: roles in the craniofacial region, inner ear and limbs. *Development* 125, 3831-3842 (1998).

37. J. Vachtenheim, J. Borovanský, "Transcription physiology" of pigment formation in melanocytes: central role of MITF. *Experimental dermatology* 19, 617-627 (2010).

38. P. Langfelder, S. Horvath, WGCNA: an R package for weighted correlation network analysis. *BMC bioinformatics* 9, 559 (2008).

39. M. Barthelemy, Betweenness centrality in large complex networks. *The European physical journal B* 38, 163-168 (2004).

40. J. Jané-Valbuena *et al.*, An oncogenic role for ETV1 in melanoma. *Cancer research* 70, 2075-2084 (2010).

41. T. Nakajima *et al.*, Modeling human somite development and fibrodysplasia ossificans progressiva with induced pluripotent stem cells. *Development* 145, dev165431 (2018).

42. M. Saito *et al.*, The indispensable role of cyclin-dependent kinase 1 in skeletal development. *Scientific reports* 6, 1-10 (2016).

43. D. Kiepe, S. Ciarmatori, A. Haarmann, B. Tönshoff, Differential expression of IGF system components in proliferating vs. differentiating growth plate chondrocytes: the functional role of IGFBP-5. *American Journal of Physiology-Endocrinology and Metabolism* 290, E363-E371 (2006).

44. E. Wagner, Functions of AP1 (Fos/Jun) in bone development. *Annals of the rheumatic diseases* 61, ii40-ii42 (2002).

45. P. Van der Kraan, W. Van den Berg, Chondrocyte hypertrophy and osteoarthritis: role in initiation and progression of cartilage degeneration? *Osteoarthritis and cartilage* 20, 223-232 (2012).

46. S. S. Späth, A. C. Andrade, M. Chau, M. Baroncelli, O. Nilsson, Evidence That Rat Chondrocytes Can Differentiate Into Perichondrial Cells. *JBMR plus* 2, 351-361 (2018).

47. X. Chen *et al.*, Integration Capacity of Human Induced Pluripotent Stem Cell-Derived

Cartilage. *Tissue Engineering Part A* 25, 437-445 (2019).

48. G. Haimovich, S. Sonam, Semi-quantitative Determination of Protein Expression Using Immunohistochemistry Staining and Analysis: An Integrated Protocol.

49. V. Dexheimer *et al.*, Differential expression of TGF-β superfamily members and role of Smad1/5/9-signalling in chondral versus endochondral chondrocyte differentiation. *Scientific reports* 6, 1-14 (2016).

50. S. Diederichs *et al.*, Regulation of Wnt5A and Wnt11 during MSC in vitro chondrogenesis: Wnt inhibition lowers BMP and hedgehog activity, and reduces hypertrophy. *Cellular and Molecular Life Sciences* 76, 3875-3889 (2019).

51. A. Spagnoli *et al.*, Identification of STAT-1 as a molecular target of IGFBP-3 in the process of chondrogenesis. *Journal of Biological Chemistry* 277, 18860-18867 (2002).

52. D. S. Evans *et al.*, Genome-wide association and functional studies identify a role for IGFBP3 in hip osteoarthritis. *Annals of the rheumatic diseases* 74, 1861-1867 (2015).

53. S. Jia *et al.*, Bmp4-Msx1 signaling and Osr2 control tooth organogenesis through antagonistic regulation of secreted Wnt antagonists. *Developmental biology* 420, 110-119 (2016).

54. R. Narcisi *et al.*, Long-term expansion, enhanced chondrogenic potential, and suppression of endochondral ossification of adult human MSCs via Wnt signaling modulation. *Stem cell reports* 4, 459-472 (2015).

55. A. Dicks *et al.*, Prospective isolation of chondroprogenitors from human iPSCs based on cell surface markers identified using a CRISPR-Cas9-generated reporter. *Stem cell research & therapy* 11, 1-14 (2020).

56. S. Ressl *et al.*, Structures of C1q-like proteins reveal unique features among the C1q/TNF superfamily. *Structure* 23, 688-699 (2015).

57. A. Yamashita *et al.*, Considerations in hiPSC-derived cartilage for articular cartilage repair. *Inflammation and regeneration* 38, 1-7 (2018).

58. Q. Shi *et al.*, Genetic variants in Wnt2B and BTRC predict melanoma survival. *Journal of Investigative Dermatology* 137, 1749-1756 (2017).

59. S. J. Harrison-Uy, S. J. Pleasure, Wnt signaling and forebrain development. *Cold Spring Harbor perspectives in biology* 4, a008094 (2012).

60. C. Elizalde *et al.*, Distinct roles for Wnt-4 and Wnt-11 during retinoic acid-induced neuronal differentiation. *Stem cells* 29, 141-153 (2011).

61. Y. Deng *et al.*, Engineering hyaline cartilage from mesenchymal stem cells with low hypertrophy potential via modulation of culture conditions and Wnt/β-catenin pathway. *Biomaterials* 192, 569-578 (2019).

62. D. Kumar, A. B. Lassar, Fibroblast growth factor maintains chondrogenic potential of limb bud mesenchymal cells by modulating DNMT3A recruitment. *Cell reports* 8, 1419-1431 (2014).

Chapter 4

Chondrogenic Differentiation of Human Induced Pluripotent Stem Cells

4.1 Abstract

The generation of large quantities of genetically defined human chondrocytes remains a critical step for the development of tissue engineering strategies for cartilage regeneration and high-throughput drug screening. This protocol describes chondrogenic differentiation of human induced pluripotent stem cells (hiPSCs), which can undergo genetic modification and the capacity for extensive cell expansion. The hiPSCs are differentiated in a stepwise manner in monolayer through the mesodermal lineage for 12 days using defined growth factors and small molecules. This is followed by 28 days of chondrogenic differentiation in a 3D pellet culture system using transforming growth factor beta 3 and specific compounds to inhibit off-target differentiation. The 6-week protocol results in hiPSC-derived cartilaginous tissue that can be characterized by histology, immunohistochemistry, and gene expression or enzymatically digested to isolate chondrocyte-like cells. Investigators can use this protocol for experiments including genetic engineering, in vitro disease modeling, or tissue engineering.

4.2 Introduction

Articular cartilage is the tissue lining the ends of long bones in synovial joints, providing a nearly frictionless surface for joint motion while withstanding millions of cycles of loading per

year (*1, 2*). The unique mechanical properties of cartilage (*3*) are due to the composition and structure of the cartilage matrix – predominantly a variety of proteoglycans and collagens as well as hyaluronate and fibronectin (*4*). Glycosaminoglycans (GAGs), largely comprising the large aggregating proteoglycan aggrecan (ACAN), make up 4-7% of the tissue (*4-6*). Due to their negative charge, GAGs retain water, which composes 65-80% of the tissue weight, contributing to the compressive properties of cartilage (*4-6*). Type II collagen, making up approximately 10-20% of cartilage matrix, primarily contributes to the shear and tensile properties of the tissue (*4-6*).

Chondrocytes, the sole cell type in articular cartilage, are responsible for maintaining the homeostasis of cartilage matrix proteins in response to genetic and environmental signals, such as growth factors or physiologic loading (*7, 8*). However, under pathologic, injurious loading, the chondrocytes shift to a degradative and inflammatory phenotype (*9*). Since the cartilage is avascular and aneural, it is susceptible to degeneration in an inflammatory environment, while lacking the ability to regenerate, leading to diseases such as arthritis (*4, 10*).

Arthritis is a family of joint diseases characterized degradation of the cartilage matrix, which leads to joint space narrowing, along with osteophyte formation, bone remodeling, and synovitis. These progressive changes which are associated with pain, swelling, and loss of motion (*11, 12*). There is a variety of types of arthritis, affecting approximately 54 million adults in the United States (*13*), with osteoarthritis (OA) and rheumatoid arthritis (RA) as the most common. OA affects the largest number of people with increasing age, female sex, genetics, joint injury, and obesity as the primary risk factors (*11, 14*). RA is an autoimmune disease (*12*), where the immune system leads to the inflammatory environment and onset of degeneration and symptoms (*12*). Unfortunately, current treatment for OA is limited to non-steroidal, anti-

146

inflammatory drugs for mild to moderate cases and joint replacements for severe cases (*11*).

Disease-modifying antirheumatic drugs have been developed to treat RA; however, they are

effective in only a fraction of individuals and have been associated with significant side effects

(*12*). Therefore, there remains a need for improved therapies for cartilage injury or arthritis. In

this regard, cartilage tissue engineering not only provides a potential regenerative therapy for

joint diseases but can also provide *in vitro* model systems for disease modeling and drug

development (*15-17*). Furthermore, such *in vitro* models can be used to elucidate mechanisms of

and develop treatments for a variety of other cartilage-associated diseases (*18-25*). In this regard,

the availability of large numbers of genetically-defined cells that can be chondrogenically

differentiated could serve as a critical component in the development of new cell-based therapies

or *in vitro* disease models for drug screening.

4.2.1 Development of the protocol

This protocol was developed based on a series of previous studies that elucidated the sequence of

signaling cues required for cartilage development *in vivo* coupled with various reports of *in vitro*

chondrogenic differentiation of mouse and human pluripotent stem cells (*26-29*). In previous

studies, we developed a method to derive chondrocytes from hiPSCs in a stepwise manner via

the paraxial mesodermal lineage (*30*) based on the mesodermal roadmap developed by Loh, et al.

using embryonic stems cells and iPSCs (*26*). The next steps toward directed chondrogenic

differentiation were induced using bone morphogenic protein 4 (BMP4) and transforming

growth factor beta 3 (TGF-β3), given their known roles in pre-cartilaginous mesenchymal

condensation and chondrogenic differentiation (*29, 31-36*). In this process, hiPSC-derived

sclerotome cells were treated with BMP4. The resulting chondroprogenitor cells were then

cultured in a conventional 3D pellet system with TGF-β3 to further specify mesodermal cells

147

into the chondrogenic fate. However, despite the robust generation of chondrocytes from hiPSCs using BMP4 and TGF-β3, we and others have shown significant and unpredictable cellular heterogeneity within newly formed cartilaginous tissues (*30, 37-40*).

To determine the identity of such non-chondrocytic cells, bulk and single-cell RNA sequencing were applied at multiple time points throughout the course of hiPSC chondrogenesis. These studies revealed that the primary off-target cells were of neural and melanocytic lineages (*37, 38*). With the analysis of the gene regulatory networks, we identified that *Wnts* and melanocyte inducing transcription factor (*MITF*) are the primary hub genes responsible for off-target neurogenesis and melanogenesis during hiPSC chondrogenic differentiation, respectively. Thus, in the improved protocol, we use small molecules to inhibit Wnt and MITF signaling during chondrogenic pellet culture, significantly enhancing the efficiency and homogeneity of hiPSC chondrogenesis. We further validated our optimized protocol using multiple hiPSC lines, histological and quantitative biochemical analysis of cartilage matrix production, and real-time quantitative polymerase chain reaction (RT-qPCR) and single-cell RNA sequencing techniques to evaluate gene expression (Figure 4.1).
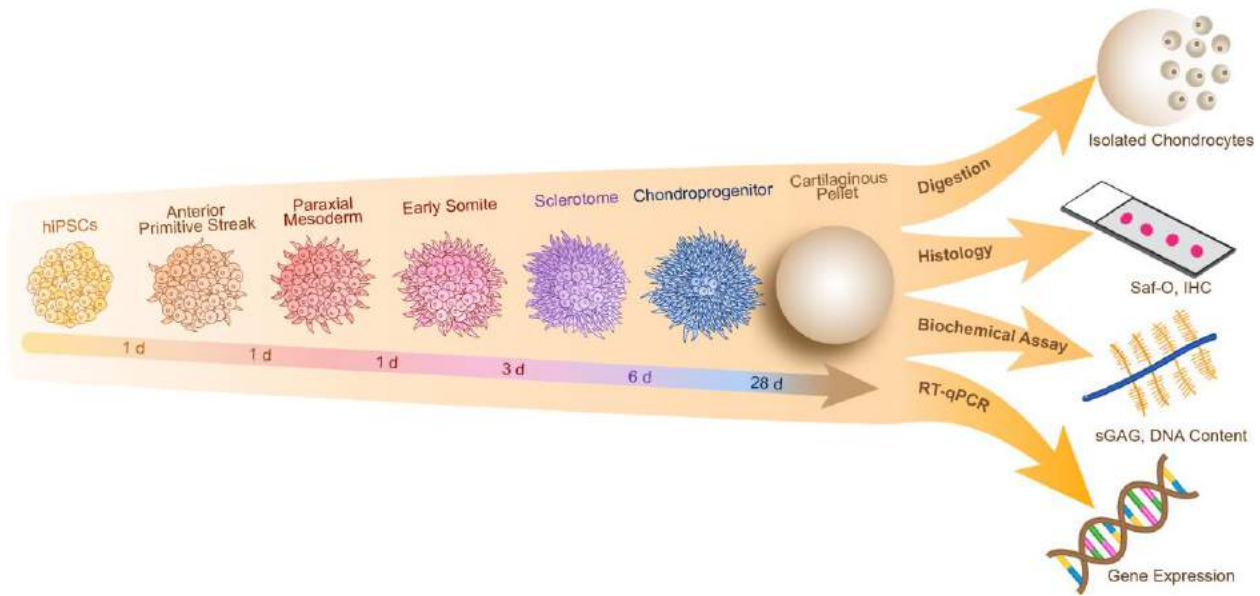
Figure 4.1 Overview schematic of the protocol. hiPSCs undergo mesodermal differentiation in monolayer for twelve days. The cells go through the anterior primitive streak, paraxial mesoderm, early somite, sclerotome, and finally chondroprogenitor stage. Cells are then cultured in a 3D pellet culture to become chondrocytes and synthesize cartilaginous matrix. The protocol then has 4 options to either digest the tissue to isolate single cells or validate chondrogenesis with histology (Saf-O and IHC), biochemical assays (DMMB for sGAG and PicoGreen for dsDNA), and/or RT-qPCR.

4.2.2 Applications of the protocol

The hiPSC-derived chondrocytes and tissue-engineered cartilage from this protocol can facilitate the development of patient-specific regenerative approaches for a variety of cartilaginous disorders including, but not limited to, arthritis, osteochondritis dissecans, relapsing polychondritis, chondrocalcinosis, cartilaginous tumors, and arthropathies (*41*). Particularly, our protocol can allow for *in vitro* disease modeling and high throughput drug screening (*15*). Furthermore, *in vitro* modeling of specific genetic conditions can be established through targeted genome engineering of the cells (e.g., CRISPR-Cas9 genome editing) with isogenic controls or patient-derived iPSCs, in conjunction with simulation of a diseased environment (e.g., inflammatory cytokines) (*16, 42, 43*). Furthermore, since the protocol follows the developmental lineage, such models allow investigation of the mechanisms underlying developmental disorders,

such as skeletal dysplasias, chondrodysplasias, collagenopathies, and aggrecanopathies (*41*).

Additionally, the protocol can be applied to cartilage tissue engineering and other topics in the musculoskeletal field. Studies can be developed to investigate mechanisms that promote or repress chondrogenic differentiation to improve tissue engineering and regenerative strategies. For example, various forms of loading such as osmotic, compressive, and shear forces can be applied at different magnitudes, time points, and regimens to optimize matrix production and mechanical properties (*44*). The similarity between hiPSC-derived chondrocytes and primary chondrocytes allows for the study of fundamental questions regarding cell physiology, such as mechanisms of chondrocyte mechanobiology (e.g., role of ion channels, integrins, and other mechanotransduction pathways) (*45, 46*), the development and physiology of the chondrocyte circadian rhythm, and the cells' responses to metabolic syndrome and inflammation. Furthermore, the rapid expansion of genome engineering in the cartilage field provides the opportunity to apply principals of synthetic biology for the development of "smart," self-regulating cells or mechanogenetic gene circuits in human cells (*45, 47-49*). Therefore, the ability to generate a large number of chondrogenically differentiated cells from hiPSCs provides the opportunity for numerous advances in cartilage research, including other types of cartilaginous tissues (*50*).

4.2.3 Comparison with other methods

To tissue-engineer cartilage, a culture system is needed to differentiate and culture chondrocytes that can synthesize and accumulate cartilaginous matrix, with or without a biomaterial scaffold (*6*). A variety of cell types have also been used for this purpose including primary chondrocytes, adult multipotent stem cells, and pluripotent stem cells (*6*). While primary chondrocytes can synthesize a cartilaginous matrix in 3D, they are limited in their expansion potential and undergo

dedifferentiation with passage in monolayer (*51*). Additionally, harvesting of human

chondrocytes from a patient results in donor site morbidity, while other sources (e.g., cadaveric,

surgical waste) are difficult to obtain (*6*). Therefore, adult stem cells, such as bone marrow-

derived mesenchymal stem cells (*52*) and adipose-derived stem cells (*53*), have been used for

cartilage tissue engineering. While these methods have been optimized to successfully produce

cartilage-like tissue, adult stem cells represent a heterogeneous population of cells and show

significant donor-to-donor variability. Furthermore, they have limited *in vitro* expansion

capacity, making it difficult to perform gene editing and clonal isolation (*54-56*). Induced

pluripotent stems cells have high proliferation and differentiation capacities, allowing for the

study of genetic perturbations. Furthermore, they can be derived in a patient-specific manner

with low or no donor morbidity, and they do not have the ethical concerns associated with

embryonic stem cells (*42, 43, 57*).

Previously published chondrogenesis protocols of stem cells, including ours, have greatly

extended our knowledge in chondrocyte biology and cartilage tissue engineering; however, many

of these approaches rely on the application of fetal bovine serum (FBS) in culture medium.

While it may enhance cell viability, FBS may also lead to off-target differentiation because of its

undefined chemical composition. Furthermore, lot-to-lot variability of FBS may also make the

protocols difficult to reproduce in different laboratories (*34, 35, 58-62*). Here, we have

established a chondrogenic differentiation protocol for hiPSCs, using serum-free, chemically

defined medium, that we have validated with 8 hiPSC lines with and without genetic mutations.

4.3 Experimental Design

4.3.1 Cell source

hiPSC lines derived from foreskin or skin fibroblasts with either retroviral or Sendai viral

induction of the Yamanaka factors (i.e., *OCT3/4*, *SOX2*, *KLF4*, and *c-MYC*) (*56*) have been tested with this protocol. Sendai-viral hiPSCs are free from genomic integration of the Yamanaka factors, unlike retrovirally-transduced hiPSCs, which have the genes integrated in their genome (*62*). The cells are maintained in hiPSC-maintenance medium, avoiding overcrowding and spontaneous differentiation. In some cases, cleaning, either colony picking or scraping of differentiated cells, can be carried out. hiPSC maintenance, expansion, and mesodermal differentiation are performed on vitronectin-coated plates.

4.3.2 Mesodermal differentiation

Approximately 48 hours after passaging, when the hiPSCs have reached 30-40% confluency, the cells should be induced for mesodermal differentiation in monolayer. The cells are fed every 24 hours with a defined growth factor and small molecule cocktail to guide differentiation. First, basic fibroblast growth factor (FGF) alongside activation of the TGF and Wnt-signaling pathways drive the cells into the anterior primitive streak. Wnt activation and FGF are continued while the TGF/BMP pathway is inhibited on the second day to derive paraxial mesodermal cells. Next, all these pathways (i.e., FGF, Wnt, and TGF/BMP) are inhibited for differentiation into the early somite. Wnt inhibition is continued in combination with sonic hedgehog (SHH) activation for the next three days achieving sclerotome cells. The following 6 days drive the cells into chondroprogenitors by adding BMP4 each day (Figure 4.1). Notably, mesodermal differentiation begins along the perimeter of the hiPSC colonies, and cell morphology will change from the small, round, colonized hiPSCs into longer, more fibrotic cells which spread throughout the culture plate.

4.3.3 Chondrogenic differentiation

After the 12-day mesodermal differentiation in monolayer, chondroprogenitor cells are

disassociated with TrypLE into single cells. Cells are resuspended at a concentration of 5×10^5

cells/mL using complete chondrogenic medium containing TGF-β3. These cells

are transferred to a 15-mL conical tube and centrifuged to form the 3D chondrogenic pellet

culture (Figure 4.1). The media is replaced every 3-4 days with complete chondrogenic medium

until the time point of interest, typically 28 days after chondrogenic induction.

4.3.4 Chondrogenic validation

We use five different methods to validate the outcome of the chondrogenic differentiation:

isolated single cells (chondrocytes), histology, immunohistochemistry (IHC), biochemical

analysis, and RT-qPCR (Figure 4.1).

The chondrogenic pellets are digested to obtain hiPSC-derived chondrocytes at the single

cell level (Figure 4.1). Pellets are washed with DPBS$^{-/-}$ and transferred into a 0.4% (wt/vol) type

II collagenase solution in a conical tube. The tubes are vortexed and placed on an orbital shaker

in a 37 ℃ incubator. The tubes should be vortexed every 20 minutes until the pellets are

digested. After pellet digestion, the collagenase solution with single cell suspension is

neutralized with medium containing 10% FBS. Cells are then resuspended in the appropriate

serum-free culture medium for follow up experiments.

Pellets are fixed in 10% neutral buffered formalin overnight, dehydrated in 70% ethanol

at 4 ℃, processed following standard histological protocol (including multiple dehydration

steps), and embedded in paraffin wax. Wax blocks containing the pellets are cut into 8 µm

sections, and sections are placed on microscope slides. Histological slides are stained for the

nuclei and proteoglycans with hematoxylin and Safranin-O, respectively. For IHC, slides are

rehydrated, prepared for staining with a primary antibody of interest, visualized with a secondary

antibody, enzyme conjugation, and a chromogen substrate, and then counterstained for the

nucleus. Slides are mounted with paramount and cover slipped for imaging and storage. IHC can be semi-quantified using the previously published ImageJ protocol (*64*).

For a more quantitative analyses and validation of our protocol, we recommend two additional methods. The first is the biochemical assay using dimethylmethylene blue (DMMB) and PicoGreen for quantitative measures of sulfated GAG (sGAG) and DNA contents, respectively (*53*). Chondrogenic pellets are washed in DPBS$^{-/-}$, transferred into a 1.7-mL tube containing 200 µL of 125 µg/mL papain, vortexed, and digested at 65 ºC overnight to release DNA and sGAG content. The following day, the digested samples are vortexed again and can be frozen until needed. This protocol measures the sGAG content which can then be normalized to DNA. The second method is to quantify gene expression using RT-qPCR (*53, 65*). Each pellet is washed with DPBS$^{-/-}$ and transferred into a 2-mL tube to be snap frozen in liquid nitrogen and stored at -80ºC until the RNA isolation.

4.4 Materials

4.4.1 hiPSC culture

1. hiPSC lines. This protocol has been validated with hiPSCs derived from fibroblasts reprogrammed using Sendai virus or retrovirus. It has also been successful with CRISPR-Cas9-edited hiPSCs.

2. Culture dishes: 6-well cell culture plate or T75 or T225 cm^2 cell culture flask

3. Matrix substrate: 1 µg/mL vitronectin recombinant human protein, truncated (Invitrogen) in DPBS. Coat plate at 0.5 µg/cm^2 and distribute by rocking plate to ensure surface is coated and incubate at room temperature 1 hour. Plates can be used immediately or stored at 2-8 °C wrapped in plastic film. If stored, warm for 1 hour at room temperature before using. Aspirate vitronectin solution and discard before culturing cells.

4. hiPSC culture medium: Essential 8 flex media (E8; Gibco). Prepare according to

   manufacturer instruction and store at 4 ℃ for up to 2 weeks. Add 10 µM Y-27632

   (STEMCELL Technologies) to E8 medium for first 24 hours after thawing or passaging.

5. Disassociation solution: ReLeSR (STEMCELL Technologies).

6. Cryomedium: PSC cryopreservation kit (Gibco).

7. 2-ml cryotubes.

4.4.2 Mesodermal differentiation

1. Differentiation medium: 242.5 mL Iscove's Modified Dulbecco's

   Medium, glutaMAX (IMDM; Gibco), 242.5 mL Ham's F-12 nutrient

   mix, glutaMAX (F12; Gibco), 5 mL penicillin-streptomycin (P/S; Gibco), 5 mL Insulin-

   Transferrin-Selenium (ITS+; Gibco), 19.5 µL 1-Thioglycerol (Millipore Sigma),

   chemically defined concentrated lipids (Thermo Fisher Scientific). Store at 4 ℃ for up to

   2 weeks.

2. Wash medium: 248.5 mL IMDM, 248.5 mL F12, 5 mL P/S. Store at. 4 ℃ for up to 2

   weeks.

3. Anterior primitive streak differentiation medium (day 1): 30 ng/mL activin A protein

   (R&D Systems), 20 ng/mL recombinant human fibroblast growth factor basic protein

   (FGF2; R&D Systems), 4 µM CHIR99021 (Reprocell) in differentiation medium.

4. Paraxial mesoderm differentiation medium (day 2): 20 ng/mL FGF2, 3 µM CHIR99021,

   2 µM SB505124 (Tocris Bioscience), 4 µM dorsomorphin (Reprocell) in differentiation

   medium.

5. Early somite differentiation medium (day 3): 2 µM SB505124, 4 µM dorsomorphin, 500 nM PD173074 (Tocris Bioscience), 1 µM Wnt-C59 (Cellagen Technologies) in differentiation medium.

6. Sclerotome differentiation medium (days 4-6): 1 µM Wnt-C59, 2 µM purmorphamine (Reprocell) in differentiation medium.

7. Chondroprogenitor differentiation medium (days 7-12): 20 ng/mL recombinant human bone morphogenic protein 4 (BMP4, R&D Systems) in differentiation medium.

8. Disassociation reagent: TrypLE Select enzyme (Gibco).

9. Neutralization medium: 494 mL Dulbecco's Modified Eagle Medium/F12, glutaMAX (DMEM/F12; Gibco), 5 mL fetal bovine serum (FBS; Atlanta Biologicals).

10. Trypan blue stain (Invitrogen).

11. Cell counter.

12. 50-mL conical tubes.

13. Cryomedium: 16 mL FBS, 2 mL DMEM, 2 mL dimethylsulfoxide (DMSO).

14. 2-ml cryotubes.

4.4.3 Chondrogenic differentiation

1. Dexamethasone: 100 µM. Add 19.62 mg dexamethasone powder (Millipore Sigma) to 1 mL absolute ethanol. Transfer 0.8 mL of the ethanol solution to 39.2 mL DMEM/F12 for a 1-mM solution. Transfer 4 mL of the 1-mM solution to 36 mL DMEM/F12 to make a 100-µM solution. Store aliquots at -80 °C up to 1 year.

2. Ascorbic acid solution: 50 mg/mL ascorbic acid (Millapore Sigma) in DMEM/F12. Store aliquots at -80 ºC for up to 3 months.

3. Proline: 40 mg/mL proline (Millapore Sigma) in DMEM/F12. Store aliquots at -80 ℃ for up to 3 months.

4. Chondrogenic medium: 483 mL DMEM/F12, 5 mL P/S, 5 mL ITS+, 5 mL Modified Eagle Medium (MEM) with nonessential amino acids (Gibco), 0.5 mL dexamethasone, 0.5 mL 2-Mercaptoethnol (Gibco). Store at 4 ℃ for up to 2 weeks.

5. Complete chondrogenic medium: 10 ng/mL recombinant human transforming growth factor beta 3 protein (TGF-β3; R&D Systems), 1 µM Wnt-C59, 1 µM ML329 (Cayman Chemical), 0.1% ascorbic acid, 0.1% proline in chondrogenic medium.

6. 15-ml conical tubes.

4.4.4 Chondrogenic validation

Digestion of chondrogenic pellets

1. DPBS$^{-/-}$.

2. Neutralization medium.

3. Digestion medium: 0.4% wt/vol type II collagenase (Worthington Biochemical, activity 225 units/mL) in warm neutralization medium. Sterile filter and use immediately.

4. 15-mL or 50-mL conical tubes.

5. Orbital shaker.

Histology preparation

1. DPBS$^{-/-}$.

2. 20-ml glass scintillation vials.

3. 10% neutral buffered formalin.

4. Paraffin.

5. Ethanol, 200 proof.

6. Xylenes.

7. Microscope slides.

8. Microtome.

Safranin-O staining

1. Safranin-O solution (Millipore Sigma).

2. Harris hematoxylin with glacial acetic acid (Poly Scientific).

3. Ethanol, 200 proof.

4. Xylenes.

5. Differentiation solution (Millipore Sigma).

6. Permount mounting media.

7. Glass cover slips.

Immunohistochemistry

1. Ethanol, 200 proof.

2. Xylenes.

3. COL1A1 antibody (Abcam, cat. no. ab90395).

4. COL2A1 antibody (Iowa Hybridoma Bank, cat. no. II-II6B3-s).

5. COL6A1 antibody (Fitzgerald Industries, cat. no. 70F-CR009X).

6. COL10A1 antibody (Millipore Sigma, cat. no. C7974).

7. Goat anti-mouse antibody (Abcam, cat. no. ab97021).

8. Goat anti-rabbit antibody (Abcam, cat. no. ab6720).

9. Hydrogen peroxide.

10. Methanol.

11. 10% goat serum (Thermo Fisher Scientific).

12. Pepsin (Thermo Fisher Scientific).

13. Proteinase K (Millipore Sigma): 0.5% wt/vol in TE buffer. Prepare fresh.

14. Quenching solution: 3% hydrogen peroxide in methanol.

15. Histostain Plus Kit (Thermo Fisher Scientific).

16. AEC substrate solution (Abcam).

17. Vector hematoxilyn QS counterstain (Vector Laboratories).

18. VectaMount AQ aqueous mounting medium (Vector Laboratories).

19. Glass cover slips.

20. Aluminum foil.

Biochemical analysis preparation

1. DPBS$^{-/-}$.

2. Papain solution: 125 mg/L papain, pH 6.5. Weigh 125 mg of papain (Millapore Sigma), 13.8 g of sodium phosphate, 1.46 g ethylenediaminetetraacetic acid (EDTA), and 0.79 g cysteine hydrochloric acid (HCl). Mix reagents using a stir bar and plate at room temperature with 1 L ultrapure distilled water. Reagents may take 1.5-2 hours to dissolve. Adjust pH to 6.5 using approximately 38 mL of 1 N NaOH. Aliquot and store at -20°C for up to 3 months.

3. 1.7-mL tubes.

RT-qPCR preparation

1. DPBS$^{-/-}$.

2. 2-ml screw-top tubes.

3. Liquid nitrogen.

4. Primers. See Table 4.1 for suggested chondrogenic primers.

Table 4.1 RT-qPCR primers.

Target gene	Forward primer (5'-3')	Reverse primer (5'-3')
ACAN	CACTTCTGAGTTCGTGGAGG	ACTGGACTCAAAAAGCTGGG
COL1A1	TGTTCAGCTTTGTGGACCTC	TTCTGTACGCAGGTGATTGG
COL2A1	GGCAATAGCAGGTTCACGTA	CTCGATAACAGTCTTGCCCC
COL10A1	CATAAAAGGCCCACTACCCAAC	ACCTTGCTCTCCTCTTACTGC
SOX9	CGTCAACGGCTCCAGCAAGAACAA	GCCGCTTCTCGCTCTCGTTCAGAAGT
TBP	AACCACGGCACTGATTTTCA	ACAGCTCCCCACCATATTCT

4.5 Methods

4.5.1 hiPSC culture

≥ 1 hour for coating plate(s), 30 minutes for plating/passaging, 30 minutes for feeding, 2-7 days

for culture

1. Coat a 6-well plate with vitronectin.

2. Thaw a vial of hiPSCs in a 37 °C water bath.

3. Transfer the cells using sterile serological plastic pipettes into 10 mL of room-
    temperature hiPSC maintenance medium in a 15 mL-conical tube.

4. Centrifuge cells at 200 g for 5 min at 23 °C.

5. Aspirate the supernatant.

6. Add 13 mL hiPSC maintenance medium containing 10 μM of Y-27632 to the cell pellet.
    Do not pipette up and down, instead gently rock the tube back and forth twice. This will
    prevent breaking up the colonies into single cells.

7. Aspirate the vitronectin-PBS$^{-/-}$ solution from plate.

8. Add 2 mL of cell solution to each well. Gently tilt the plate in a circular motion to distribute the cells evenly throughout the wells. Failure to do so will cause the cells to cluster in one area, preventing proper proliferation, which may lead to spontaneous differentiation.

9. Incubate the plate at 37 ℃.

10. After 24 hours, aspirate the medium from the plate and feed with hiPSC maintenance medium without Y-27632.

11. Continue cell culture, feeding every day until cells reach approximately 80% confluency. Cells can be frozen in cryopreservation medium. We typically freeze cells sufficient for one 6-well plate in 1 mL of cryopreservation medium for future passaging. The split ratio may vary depending on hiPSC lines.

12. Before passaging, coat the appropriate number of 6-well plates and/or T225 flasks with vitronectin.

13. Aspirate medium from cell plate.

14. Wash each well with 2 mL of DPBS$^{-/-}$.

15. Add 1.5 mL of ReLeSR for 1 min at RT.

16. Aspirate off ReLeSR.

17. Incubate plate for 2 min at 37 ℃. If the cells are ≥ 85% confluent or if there is spontaneous differentiation, the time can be shortened to 1 min.

18. Pipette 2 mL of hiPSC maintenance medium onto the bottom of each well, you should see the cells lift off with the medium, and transfer into a conical tube using sterile

serological plastic pipettes. Do not pipette up and down.

19. Tap the plate several times.

20. Centrifuge cells at 200 g for 5 min at 23 ºC.

21. Aspirate the supernatant.

22. Resuspend cells in hiPSC maintenance medium containing 10 μM of Y-27632. Do not pipette up and down, instead gently rock the tube back and forth twice. This will prevent breaking up the colonies into single cells.

23. Aspirate the vitronectin-PBS$^{-/-}$ solution from plate(s) / flask(s).

24. Add cell solution to plate(s) / flask(s). Gently tilt the plate(s) / flask(s) in a circular motion to distribute the cells throughout the wells. Failure to do so will cause the cells to cluster, preventing proper proliferation and leading to spontaneous differentiation

25. Check cell density in microscope. If too confluent, remove some of the cell solution and add up volume with maintenance medium containing Y-27632.

26. Culture for at least 48 h until 30-40% confluent. Too high cell density inhibits mesodermal differentiation. Too low cell density prevents adhesion and increases cell death. (*see* **Notes 1-3**)

4.5.2 Mesodermal differentiation

30 minutes – 1 hour for feeding, 12 days for culture

1. Warm appropriate volume of wash and differentiation medium in 37 ºC water bath. For days 2-12: if fed medium changes from orange to yellow in color after 24 h, suggesting high metabolic activity of the cells, increase differentiation medium volume by 1 mL per

well and / or 5 mL per flask.

2. Make the appropriate differentiation medium for the corresponding day by adding the correct growth factors. Day 1: anterior primitive streak; day 2: paraxial mesoderm; day 3: early somite; days 4-6: sclerotome; days7-12: chondroprogenitor.

3. Aspirate maintenance media from plate(s) / flask(s).

4. Rinse plate(s) / flask(s) with wash medium.

5. Add complete differentiation medium.

6. Incubate plate at 37 ℃.

7. Feed the cells every 24 h with mesodermal differentiation medium supplemented with the appropriate growth factor and small molecule cocktails. Note that more-than-usual cell death may be observed after day 3 due to the inhibition of several major signaling pathways. When switching to a new set of the growth factors and small molecules (i.e., days 1, 2, 3, 4, and 7), it is critical to feed at the 24-hour time points to ensure proper lineage specification. Cells can be harvested after days 1, 2, 3, 6, and 12 if the specific lineage stages are of interest to the experiment (e.g., RT-qPCR). (*see* **Notes 4-7**)

8. On day 13, aspirate medium from cell plate(s) / flask(s).

9. Wash with DPBS$^{-/-}$

10. Pipette TrypLE disassociation reagent onto plate(s) / flask(s).
    2 mL per well of 6-well plate and 20-25 mL per T225 flask.

11. Incubate for 3 min at 37 ℃.

12. Gently tap plate(s) / flask(s) several times to disassociate cells. You should see cells

floating in medium (*see* **Note 8**).

13. Add slightly more than an equal volume of neutralization media.

14. Pipette half of the medium into a conical tube.

15. Pipette up and down the other half in the wells / flask(s) twice to lift any remaining cells. Transfer to a conical tube.

16. Rinse the wells / flask(s) twice with neutralization medium and transfer to tubes each time.

17. Centrifuge cell tubes at 300 g for 5 min at 23 ºC.

18. Aspirate supernatant.

19. Chondroprogenitor cells can undergo chondrogenesis or frozen in cryomedium for future chondrogenesis.

4.5.3 Chondrogenic differentiation

1-3 hours for pelleting, 28 days for differentiation

1. Warm neutralization and chondrogenic medium in 37 ºC water bath.

2. Add TGF-β3, ascorbate, proline, Wnt-C59, and ML329 to make complete chondrogenic medium.

3. Resuspend chondroprogenitor cells in complete chondrogenic medium. Combine cells if you have multiple tubes.

4. Stain 10 µL of the cell solution with 10 µL of Trypan Blue to count cell number on an automated cell counter or hemocytometer.

5. Using the cell count, calculate the volume needed for a concentration of 5×10^5 cells per

1 mL of complete chondrogenic medium (*see* **Note 9**).

6. Pipette the cell solution to make pellet cultures – 1 mL per 15 mL conical tube.

7. Centrifuge tubes at 300 g for 5 min at 23 ℃.

8. Loosen the caps of the tubes in the biosafety cabinet. The tubes must be loosened to provide oxygen supply to the cells. The cap should however still be screwed on so that it cannot be lifted off to prevent contamination.

9. Incubate the tubes at 37 ℃.

10. Check tubes to confirm pellet formation after 24 hours (*see* **Note 10**).

11. Feed pellets every 3 – 4 days.

12. Warm incomplete chondrogenic medium in 37 ℃ water bath.

13. Add TGF-β3, ascorbate, proline, Wnt-C59, and ML329 to make complete chondrogenic medium.

14. Aspirate medium from the conical tube with a 9" Pasteur pipette.

15. Use at 12-mL stereological pipette to feed 6 tubes at a time with 2 mL per pellet. Ensure lids remain loose (*see* **Notes 11-12**).

16. Chondrogenic pellets can be harvested at various time points as desired. Proceed to section 3.4. We recommend weekly harvest on days 7, 14, 21, 28, and 42. In general, cells start to deposit matrix 14 days post-chondrogenic induction (i.e., apparent pellet enlargement). Additionally, chondrocytes usually can be observed approximately 14-21 days post-chondrogenic induction.

17. 28 days after chondrogenic induction, most of the cells should have differentiated into

chondrocytes and formed cartilaginous matrix. We recommend digesting the chondrogenic pellet to retrieve the chondrocytes at a single cell level (3.4.1) for further experimentation or using histology/IHC (3.4.2-4), biochemical assays (3.4.5), and/or RT-qPCR (3.4.6) to confirm and study chondrogenic differentiation.

4.5.4 Chondrogenic validation

Digestion of chondrogenic pellets

3 hours

1. Warm neutralization and desired medium for the experiment. If plating the cells, we recommend using the neutralization medium.

2. Prepare digestion medium.

3. Aspirate medium from pellets.

4. Wash each pellet with 2-3 mL of DPBS$^{-/-}$.

5. Transfer pellets into a tube with digestion medium. Use an equal volume of digestion medium to the number of pellets being digested ($\pm$ 1 mL). A 15-mL or 50-mL tube should not exceed 8 mL or 25 mL of digestion medium, respectively.

6. Vortex the tube(s) and shake manually then place on an orbital shaker (80 RPMs) in a 37 ºC incubator.

7. Every 20 min remove the tube(s) from the incubator to vortex and check digestion progress.

8. After approximately 2 h, the matrix of chondrogenic pellets should be mostly digested. The length of digestion time needed depends on harvest time point and size of the tube.

For example, pellets harvested prior 28 days post-chondrogenic induction may only require 1 hr to achieve full digestion. Additionally, we have observed faster digestion using 50-mL conical tubes (*see* **Note 13**).

9. Add neutralization medium to the tube(s) bringing the volume to 12 mL or 45 mL.

10. Centrifuge tube(s) at 300 g for 5 min at 23 ºC.

11. Aspirate supernatant.

12. Resuspend in neutralization medium.

13. Stain 10 µL of the cell solution with 10 µL of Trypan Blue to count on an automated cell counter or hemocytometer.

14. Centrifuge at 300 g for 5 min at 23 ºC.

15. Resuspend the cells at the desired concentration. The number of cells retrieved per pellet may depend on hiPSC lines. On average, we get approximately 6.5×10^5 cells per pellet. The cell recovery rate may be increased if multiple pellets from the same group are pooled and digested together. If plating the chondrocytes, we recommend adding the cells to desired dish(s) and incubating for 6-8 h. This provides sufficient time for the cells to adhere without dedifferentiating and losing their phenotype.

Histology preparation

At least 3 days

1. Transfer pellet(s) into a scintillation vial with 10% (vol/vol) neutral buffered formalin.

2. Store at 4 ºC overnight.

3. Remove formalin and add 70% (vol/vol) ethanol. Pellets can be stored in 70% (vol/vol)

ethanol at 4ºC long term.

4. Transfer pellet into a plastic cassette for processing. Biopsy foam pads can be used to sandwich the chondrogenic pellet within the cassette to prevent it from falling out. Processing can be done by hand or using a tissue processor.

5. Dehydrate the chondrogenic pellet for 30 min in 80% (vol/vol) ethanol followed by 30 min in 100% (vol/vol) ethanol. Exchange the 100% (vol/vol) ethanol for another 30 min. Pellets can be stored in 100% (vol/vol) ethanol overnight.

6. Clear the pellet for 30 min with a 1:1 solution of ethanol and xylene followed by 30 min of 100% (vol/vol) xylene. Exchange the 100% (vol/vol) xylene for another 30 min.

7. Begin embedding the pellet for 1 h with a 1:1 solution of xylene and paraffin wax at 60 ºC followed by 1 h with 100% (vol/vol) paraffin at 60 ºC. Exchange the 100% (vol/vol) paraffin for another 1 h at 60 ºC.

8. Transfer pellet into an embedding tray, place cassette on top, and fill with paraffin wax.

9. Store for a few hours or overnight at 4 ºC to harden wax. Pellets can be stored in wax long term at RT.

10. Cut the wax blocks in 8-µm-thick sections and place a short ribbon of sections in a 42 ºC water bath.

11. Remove a ribbon of sections from the water bath by allowing it to attach to a microscope slide. In general, there should be 3-5 sections per ribbon on each slide. Slides can be stored long term at RT.

12. Dry slides in a warmer at 37 ºC for staining or in a drying rack at RT for storage overnight.

13. Perform desired histology such as staining for sGAGs with Safranin-O or labeling of collagenous proteins with immunohistochemistry.

Safranin-O and hematoxylin staining

1-2 hours

1. Remove paraffin wax with 3 rounds of soaking slide(s) in xylene for 5 min.

2. Rehydrate tissue with 100% (vol/vol) ethanol for 2 min followed by 50% (vol/vol) ethanol for 2 min.

3. Rinse slide(s) in tap water for 2 min.

4. Remove all excess water.

5. Stain slide(s) with Harris hematoxylin for 3 min (nuclei will be stained purple). Filter Harris hematoxylin staining solution before each use to remove potential precipitations and avoid deposition of particulates on slide. Do not reuse stain more than ten times.

6. Rinse slide(s) in tap water for 3 min.

7. Differentiate slide(s) in differentiation solution (acid alcohol) for 15 sec.

8. Rinse slide(s) in tap water for 3 min.

9. Stain slide(s) with Safranin-O for 3-5 min (sGAGs will be stained pink/red). Do not reuse stain more than 10 times.

10. Rinse slide(s) multiple times with 100% (vol/vol) ethanol until no excess stain remains.

11. Let slide(s) partially dry before rinsing with xylene for 30 sec.

12. Mount slide(s) with permount, coverslip, let dry, and image (*see* **Note 14**).

Immunohistochemistry

4-5 hours

1. Remove paraffin wax with 3 rounds of soaking slide(s) in xylene for 5 min.

2. Rehydrate tissue by washing slide(s) with 100% (vol/vol) ethanol for 5 min twice, 95% (vol/vol) ethanol for 5 min twice, 70% (vol/vol) ethanol for 5 min, 50% (vol/vol) ethanol for 5 min, and then tap water for 5 min. Do not let the slides dry out. Place slide(s) in a container with a hydrated paper towel.

3. Perform antigen retrieval by adding 100 µL of proteinase K or pepsin on the slide and incubating (see Table 4.2 for recommended reagent, timing, and temperature).

4. Wash the slide(s) with DPBS$^{-/-}$ for 5 min twice.

5. Quench the slide(s) for 1 h in 3% (vol/vol) hydrogen peroxide in methanol.

6. Wash the slide(s) with DPBS$^{-/-}$ for 5 min three times.

7. Use a Pap-pen to circle each piece of tissue on the slide(s) to prevent solution spreading.

8. Perform blocking by adding a couple drops (enough to cover the tissue) of 2.5% (vol/vol) goat serum to each piece of tissue for 1 h at RT.

9. Blot excess serum from bottom of inclined slide. Do not rinse.

10. Stain tissue with primary antibody for 1 h at RT in hydrated container. See Table 4.2 for antibodies and dilutions. Do not add primary antibody to one piece of tissue. Instead add more goat serum from step viii to serve as negative control.

11. Wash the slide(s) with DPBS$^{-/-}$ for 5 min three times.

12. Add a couple drops (enough to cover the tissue) of the proper secondary antibody at a

1:500 dilution for 30 min at RT (Table 4.2).

13. Wash the slide(s) with DPBS for 5 min three times.

14. Combine 5 mL of ImmPact AEC diluent, 2 drops of AEC reagent 1, 3 drops of AEC
    reagent 2, and 2 drops of AEC reagent 3. Mix well.

15. Add AEC solution to the slide(s) and incubate at RT. See Table 4.2 for timing (*see* **Note
    15**).

16. Wash the slide(s) with distilled water for 5 min.

17. Rinse the slide(s) in tap water.

18. Cover tissue sections with Vector Hematoxylin QS counterstain for 45 sec.

19. Rinse the slide(s) in tap water for 10 sec. Do not dehydrate slides.

20. Mount the slide(s) with VectaMount AQ aqueous mounting medium, coverslip, let dry,
    and image.

Table 4.2 IHC antibodies.

Antibody	Host	Manufacturer	Cat. No.	Retrieval (Time, Temp)	Dilution	AEC Time
COL1A1	Mouse	Abcam	ab90395	Pepsin (5 min, RT)	1:800	2 min
COL2A1	Mouse	Iowa Hybridoma Bank	II-II6B3-s	Proteinase K (3 min, 37 ºC)	1:10	2.5 min
COL6A1	Rabbit	Fitzgerald Industries	70F-CR009X	Proteinase K (3 min, 37 ºC)	1:1000	2.5 min
COL10A1	Mouse	Millipore Sigma	C7974	Pepsin (5 min, RT)	1:200	2 min
Goat anti-mouse IgG, biotin	Goat	Abcam	ab97021		1:500	

Goat anti-rabbit IgG, biotin	Goat	Abcam	ab6720	1:500

Biochemical assay preparation

1 day for sample preparation, 2-3 hour for assay

1. Wash chondrogenic pellets with 2-3 mL of DPBS$^{-/-}$.

2. Transfer each pellet into a 1.7-mL tube with 200 µL of papain and vortex.

3. Digest tissue at 65 ℃ overnight and vortex. Use of cap-lock on the tubes may help securely seal the tube at high temperatures. Samples can be stored at -20 ℃ until analysis.

4. Follow previously published protocol to determine sGAG/DNA ratio using DMMB and PicoGreen Assays (*53*).

RT-qPCR Preparation

1-2 days

1. Clean work area with RNaseZap solution.

2. Wash chondrogenic pellets with 2-3 mL DPBS.

3. Transfer pellet into a tube and snap freeze in liquid nitrogen. We generally use screw-top microcentrifuge tubes with O-ring cap. Samples can be frozen at -80 ℃ until analysis.

4. Follow previously published protocol to determine gene expression using RT-qPCR (*53, 65*).

4.6 Anticipated Results

During regular culture, the hiPSCs have a small, round phenotype, and they grow in dense, round colonies (Figure 4.2a). When passaging and plating, caution must be taken to prevent from

breaking up the colonies too much as the hiPSCs tend to trigger cell death or spontaneously differentiate if cultured as single cells. In our laboratory, most hiPSC lines had optimal survival and growth on vitronectin-coated 6-well plates while there was lower viability when cultured on 10-cm dishes. Some hiPSC lines that were originally maintained on other substrates (e.g., Matrigel) were able to be switched onto vitronectin substrate by culturing cells on vitronectin-coated plates for several passages before mesodermal differentiation. After mesodermal induction, hiPSCs begin to differentiate at the edges of the colonies. As the cells become more elongated and spread out, the center of the colony begins to differentiate as well (Figure 4.2b-e). Some cell death may be observed after the third day of mesodermal induction due to the inhibition of multiple essential pathways; however, the remaining cells should recover and differentiate as expected. Excess cell death may occur if hiPSCs are induced at too low of a cell density. In our previous study, we have demonstrated a decrease in pluripotent genes *OCT4* and *NANOG* throughout the mesodermal differentiation with an upregulation of *MIXL1* indicating anterior primitive streak cells after day 1, *MSGN1* indicating the paraxial mesoderm after day 2, and *PARAXIS* indicating the early somite state after day 3 (*30*). After day 6, the cells are committed into the sclerotome lineage with an upregulation of *SOX9*, *PDGFRA*, and *PDGFRB*. The upregulation of *PDGFRβ* continues through the chondroprogenitor stage alongside *COL2A1* expression after day 12 of mesodermal induction (*30*). We have also demonstrated that the chondroprogenitors express the surface markers CD166, CD146, and PDGFRβ, but not CD45, using flow cytometric analysis (*37*). Cells in the chondroprogenitor stage should be fully differentiated and spread out throughout the dish with an elongated phenotype (Figure 4.2f). If the mesodermal differentiation is induced at too high of a cell density; however, one might observe formation of nodules in the center of cell colonies (Figure 4.2g) and/or formation of a

173

cell "sheet" that often spontaneously lifts off the culture plates, resulting into failed mesodermal

lineage commitment.
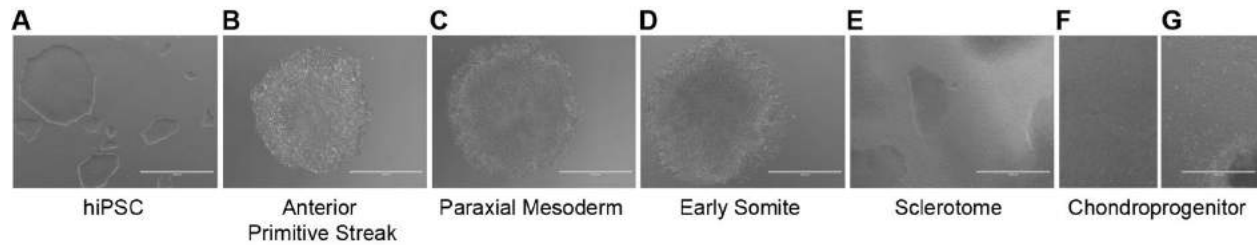
Figure 4.2 Phase contrast images of cells throughout mesodermal differentiation. (**A**) Induce cells when they are 30-40% confluent. (**B-F**) As cells differentiate, from (**B**) anterior primitive streak, (**C**) paraxial mesoderm, (**D**) early somite, (**E**) sclerotome, to (**F**) chondroprogenitor, they spread and become more spindled. (**G**) If cells are induced at too high of a density, they may not fully differentiate and form nodules in the center of the colonies. Scale bar = 1 mm.

Chondroprogenitor cells in monolayer culture (i.e., day 12 of mesodermal differentiation)

should be disassociated into single cells to form 3D, chondrogenic pellets for chondrogenesis.

Cells should lift off the bottom of the culture dish in the TrypLE solution after a 3 min

incubation and gentle tapping. If cells do not lift off, increase the time of incubation. We have

tried using cell scrapers in instances where cells do not lift after 8 min of incubation; however,

the cells had poor viability and failed to form chondrogenic pellets. We average a yield of 6 x

10^7 chondroprogenitor cells per T225 flask; however, this value may vary due to different hiPSC

lines and plating density used. Approximately 24 h after chondrogenic induction, we observe the

formation of a spherical pellet in the bottom of the conical tube. Occasionally, the pellet may

need additional time before the proper shape is visible. Pellets that do not form after 48 h should

be discarded. This may be caused by improper mesodermal differentiation or incompatible

disassociation reagent (cell line specific). In some cell lines, we have found disassociating

chondroprogenitor cells in 0.05 mM EDTA and/or differentiating cells on Matrigel has improved

pelleting and chondrogenesis. As pellet cultures approach 28 days, the medium may begin to turn

yellow due to increased cellular metabolic activity, which can be prevented by increasing the

174

volume of chondrogenic medium during feeding. In other cases, some excess matrix may have

formed apart from the pellet in the tube; removing this during feeding will also reduce the rate

the culture medium is metabolized. If black dots appear on the pellets, suggestive of off-target

differentiation and presence of melanocytes, increasing the concentration of ML329 will inhibit

MITF and potential melanin production. Throughout chondrogenic culture, the pellets should

grow due to accumulation of cartilaginous matrix but maintain a relatively spherical shape. We

have reported a significant increase in chondrogenic genes *SOX9*, *COL2A1*, and *ACAN* from the

chondroprogenitor stage through day 42 culture, while fibrocartilage and hypertrophic cartilage

markers *COL1A1* and *COL10A1*, respectively, remain relatively low until later time points

(Figure 4.3a-e) (*30, 37*).
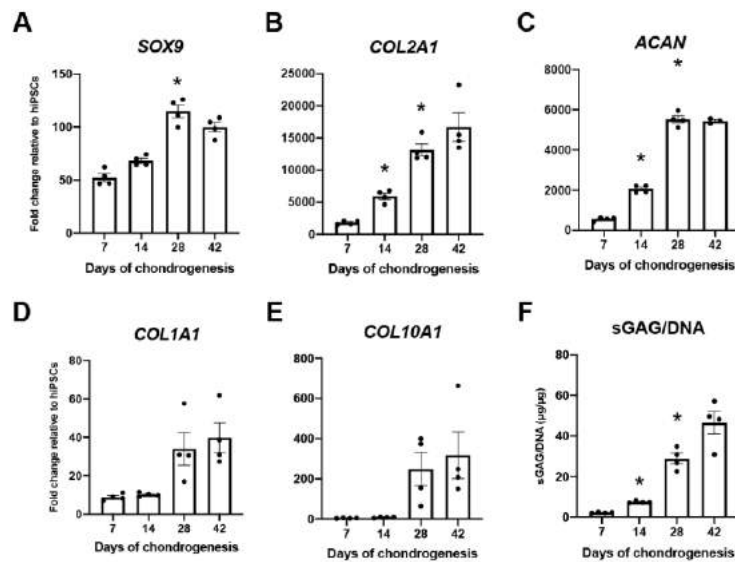
Figure 4.3 Anticipated results – gene expression and matrix quantification. (**A-C**) Chondrogenic transcription factor *SOX9* gene expression should increase early, followed by matrix genes *COL2A1* and *ACAN*. (**D-E**) Relative to the expression of *COL2A1*, lower gene expression of fibrocartilage and hypertrophic cartilage markers *COL1A1* and *COL10A1*, respectively, was observed. (**F**) sGAG/DNA ratio should increase throughout chondrogenesis, reaching 20-30 ng/ng at day 28 and over 40 ng/ng at day 42. Mean ± SEM, n=4. *p<0.05 compared to previous time point.

To obtain hiPSC-derived chondrocytes, day 28 chondrogenic pellets can be digested with

type 2 collagenase. Vortexing the tubes every 20 min will facilitate the breakdown of the tissue

matrix, thus increasing digestion efficiency. However, if the chunks of pellets remain intact after

a lengthy period of digestion, "smashing" the pellets using a tool with a flat surface (e.g., spatula

with shovel head, or lid of an Eppendorf tube) in a sterile Petri dish may help break up the tissue

matrix. We do not recommend digesting for longer than 2.5 h as it may decrease the cell

viability. Occasionally, small pieces of tissue may still be visible after the digestion process;

however, most of the cells will be dissociated from the matrix. We average a cell viability of

85% and approximately 6.5×10^5 cells per digested pellet. We found an increase in viability and

efficiency when more pellets are digested at a time and 50-mL conical tubes are used.

To validate and visualize the cartilage matrix produced by hiPSC-derived chondrocytes,

we use Safranin-O staining to reveal the presence of sGAGs (Figure 4.4a-c), IHC to label various

types of collagens (Figure 4.4d-f), biochemical DMMB assay to quantify sGAG production

(Figure 4.3f), and RT-qPCR to analyze gene expression (Figure 4.3a-e). We normally observe

round chondrocyte-like cells within cartilaginous matrix with robust, homogenous Safranin-O

staining (Figure 4.4a-c). If cellular heterogeneity is observed, concentration of Wnt-C59 and

ML329 can be increased to further prevent off-target differentiation. If there is little or no sGAG

staining, differentiation was unsuccessful, which can be attributed to several issues addressed in

Notes. If hiPSCs have successfully differentiated into chondrocytes, there should also be

significant labeling for COL2A1 (Figure 4.4d), with minimal labeling of COL1A1 (Figure 4.4e)

and COL10A1 (Figure 4.4f). Biochemical analysis and RT-qPCR for these genes can further

support successful chondrogenesis. Chondrogenic pellets typically have an sGAG/DNA ratio

between 20-30 ng/ng in day 28 pellet samples, which can continue to increase with more time in

culture (Figure 4.3f). A significant upregulation of *SOX9*, *COL2A1*, and *ACAN* gene expression

176

should be detected in the pellets at day 28 versus day 0 pellet samples (Figure 4.3a-c), while the

expression levels of *COL1A1* and *COL10A1* remain low until later time points (Figure 4.3d-e).

The hiPSC-derived chondrocytes and cartilage matrix generated using this protocol can be used

for a variety of experiments including genetic engineering, in vitro disease modeling, and tissue

engineering.
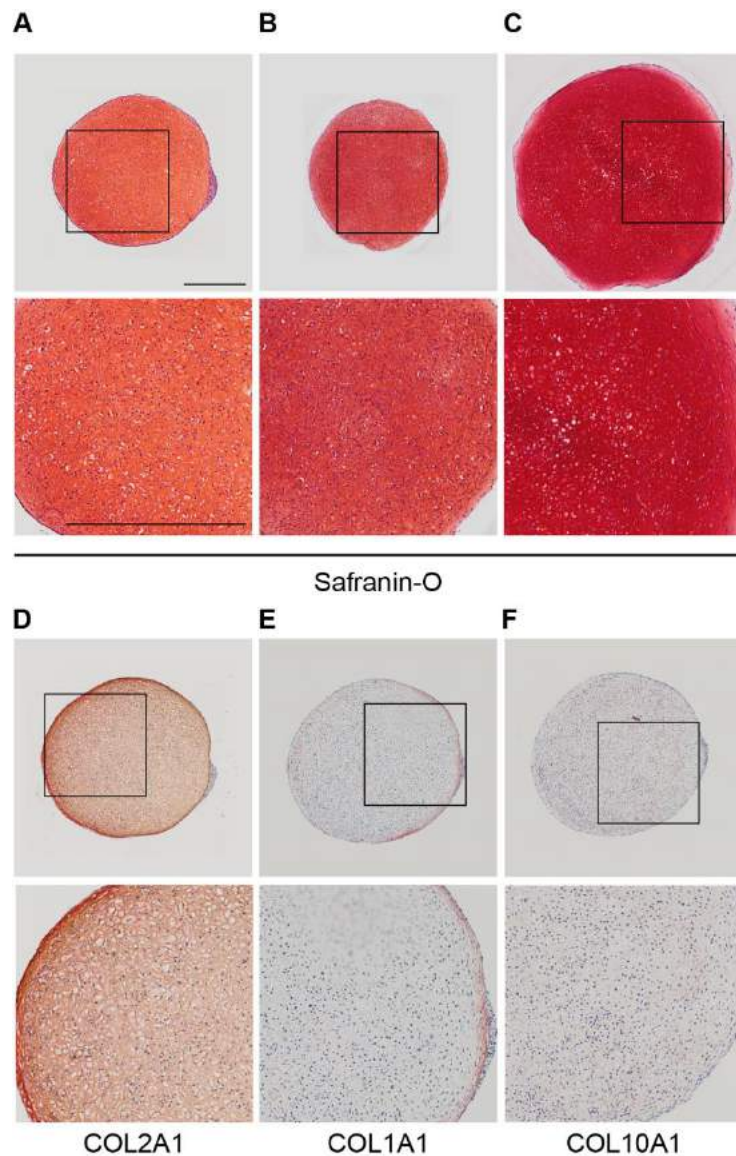
Figure 4.4 Anticipated results – histology. (**A-C**) Robust, homogenous safranin-O staining for sGAGs in three different cell lines. (**D-F**) Pellet in panel a with IHC labeling of COL2A1 (**D**), COL1A1 (**E**), and COL10A1 (**F**). Scale bar = 500 µm.

4.7 Troubleshooting Notes

1. If hiPSCs are confluent in 2-3 days, the cell concentration of the frozen stock is too high. Plate one vial to more than one 6-well plate (e.g., 1.5 or 2 x 6-well plates).

2. If there is hiPSC death, cells were plated at too low of a density, media was changed too soon, Y-27632 was not added, cells were washed and fed too aggressively, or the cell line is not compatible with vitronectin. Reduce number of wells and/or flasks you are plating, make sure media is changed 24 hours after plating (or try extending the time slightly longer than 24 hours), make sure to add Y-27632 to media for the first 24 hours, pipette media slowly and onto the side of the dish (not directly on the cells), or try other matrix substrates such as Matrigel.

3. If there is spontaneous differentiation, colonies were not maintained but broken into single cells or cells were plated at an incorrect density. Do not pipette up and down when plating and passaging hiPSCs or change the number of wells you plate per cell vial/plate. You can scrape differentiated cells to clean the wells.

4. If there is cell death, cells were induced at too low of a density or there was spontaneous differentiation. Wait longer after passaging to increase cell density before induction or clean wells before passaging by scraping differentiated cells.

5. If cells are not differentiating or nodules form in the center of colonies, cells were induced at too high of a density. Passage cells at a lower density and induce cells 48 hours after passaging.

6. If cells lift off the culture surface, cells were induced at too high of a density or were washed and fed too aggressively. Passage cells at a lower density, induce 48 hours after

passaging, and pipette media slowly on the side of the dish (not directly on cells).

7. If media is yellow, cells were metabolic and fed too low of a media volume. Increase

   volume by 1 mL per well (6-well plate) or 5 mL per T225 flask.

8. If cells are still stuck to the dish, they did not fully lift off the plate during disassociation.

   Place dishes with fresh TrypLE back in the incubator for 2 min and increase the force of

   slap without causing media to splash on top of dish.

9. If you do not have enough cells to create the desired number of chondrogenic pellets,

   reduce the number of cells per chondrogenic pellet (e.g., 2.5×10^5 or 3×10^5).

10. If pellets have not formed, wait an additional 24 hours to allow them to form. Otherwise,

    dissociation reagent (TrypLE) was too aggressive, cells did not differentiate properly, or

    the cell line is incompatible with vitronectin. Use a milder disassociation reagent (e.g.,

    0.05 mM EDTA), decrease cell density at time of mesodermal induction, or try a

    different matrix substrate such as Matrigel.

11. If media is yellow, pellets have grown significantly and are metabolically active or extra

    matrix is being produced around walls of the conical tube in addition to the pellet.

    Increase chondrogenic medium volume by 1 mL per tube or aspirate away excess matrix

    with Pasteur pipette during aspiration.

12. If black spots appear on pellet, melanin is being produced. Increase concentration of

    ML329.

13. If chondrogenic pellets are not fully digested, the collagenase solution is not strong

    enough or the matrix is too dense. Ensure proper ratio of collagenase to medium was used

    and test different lots of collagenase. Remove pellets from tube and place in an empty

well of 6-well plate. Use a closed, sterile 1.7-mL Eppendorf to gently "smash" pellets. Use collagenase solution to rinse the well and transfer back to tube. Digest an additional 20 min.

14. If there is cell and matrix heterogeneity in chondrogenic pellet, Wnt and MITF signaling is occurring and causing off-target differentiation. Increase concentrations of Wnt-C59 and ML329.

15. If the positive control is not showing stain, development time is too short. Increase time of development with AEC.

4.8 References

1. J. M. Mansour, in *Kinesiology: The Mechanics and Pathomechanics of Human Movement*. (2003), vol. 2e, chap. 5, pp. 66-75.

2. F. Guilak, Biomechanical factors in osteoarthritis. *Best Pract Res Clin Rheumatol* **25**, 815-823 (2011).

3. J. Antons *et al.*, Zone-dependent mechanical properties of human articular cartilage obtained by indentation measurements. *J Mater Sci Mater Med* **29**, 57 (2018).

4. A. J. Sophia Fox, A. Bedi, S. A. Rodeo, The basic science of articular cartilage: structure, composition, and function. *Sports Health* **1**, 461-468 (2009).

5. Y. Xia *et al.*, in *Biophysics and Biochemistry of Cartilage by NMR and MRI*. (The Royal Society of Chemistry, 2017), pp. 1-43.

6. L. Zhang, J. Hu, K. A. Athanasiou, The role of tissue engineering in articular cartilage repair and regeneration. *Crit Rev Biomed Eng* **37**, 1-57 (2009).

7. F. Guilak, C. Hung, in *Basic Orthopaedic Biomechanics and Mechanobiology,* V. Mow, R. Huiskes, Eds. (Lippincott-Raven Publishers, Philadelphia, 2005), pp. 179-207.

8. A. C. Shieh, K. A. Athanasiou, Principles of cell mechanics for cartilage tissue engineering. *Ann Biomed Eng* **31**, 1-11 (2003).

9. J. Sanchez-Adams, H. A. Leddy, A. L. McNulty, C. J. O'Conor, F. Guilak, The mechanobiology of articular cartilage: bearing the burden of osteoarthritis. *Curr Rheumatol Rep* **16**, 451 (2014).

10. F. Berenbaum, T. M. Griffin, R. Liu-Bryan, Review: Metabolic Regulation of Inflammation in Osteoarthritis. *Arthritis Rheumatol* **69**, 9-21 (2017).

11. F. C. Breedveld, Osteoarthritis--the impact of a serious disease. *Rheumatology (Oxford)* **43 Suppl 1**, i4-8 (2004).

12. J. S. Smolen, D. Aletaha, I. B. McInnes, Rheumatoid arthritis. *Lancet* **388**, 2023-2038 (2016).

13. K. E. Barbour *et al.*, Geographic Variations in Arthritis Prevalence, Health-Related Characteristics, and Management - United States, 2015. *MMWR Surveill Summ* **67**, 1-28 (2018).

14. C. Palazzo, C. Nguyen, M. M. Lefevre-Colau, F. Rannou, S. Poiraudeau, Risk factors and burden of osteoarthritis. *Ann Phys Rehabil Med* **59**, 134-138 (2016).

15. V. P. Willard *et al.*, Use of cartilage derived from murine induced pluripotent stem cells for osteoarthritis drug screening. *Arthritis Rheumatol* **66**, 3062-3072 (2014).

16. S. S. Adkar *et al.*, Genome Engineering for Personalized Arthritis Therapeutics. *Trends Mol Med* **23**, 917-931 (2017).

17. S. K. O'Connor, D. B. Katz, S. J. Oswald, L. Groneck, F. Guilak, Formation of Osteochondral Organoids from Murine Induced Pluripotent Stem Cells. *Tissue Eng Part A*, (2020).

18. B. Saitta *et al.*, Patient-derived skeletal dysplasia induced pluripotent stem cells display abnormal chondrogenic marker expression and regulation by BMP2 and TGFbeta1. *Stem Cells Dev* **23**, 1464-1478 (2014).

19. Y. Nur Patria *et al.*, CRISPR/Cas9 gene editing of a SOX9 reporter human iPSC line to produce two TRPV4 patient heterozygous missense mutant iPSC lines, MCRIi001-A-3 (TRPV4 p.F273L) and MCRIi001-A-4 (TRPV4 p.P799L). *Stem Cell Res* **48**, 101942 (2020).

20. H. Liu *et al.*, The potential of induced pluripotent stem cells as a tool to study skeletal dysplasias and cartilage-related pathologic conditions. *Osteoarthritis Cartilage* **25**, 616-624 (2017).

21. C. Sanjurjo-Rodriguez *et al.*, Versatility of Induced Pluripotent Stem Cells (iPSCs) for Improving the Knowledge on Musculoskeletal Diseases. *Int J Mol Sci* **21**, (2020).

22. A. Yamashita *et al.*, Statin treatment rescues FGFR3 skeletal dysplasia phenotypes. *Nature* **513**, 507-511 (2014).

23. Y. Matsumoto *et al.*, Induced pluripotent stem cells from patients with human fibrodysplasia ossificans progressiva show increased mineralization and cartilage formation. *Orphanet J Rare Dis* **8**, 190 (2013).

24. E. E. Miller *et al.*, EIF4A3 deficient human iPSCs and mouse models demonstrate neural crest defects that underlie Richieri-Costa-Pereira syndrome. *Hum Mol Genet* **26**, 2177-2191 (2017).

25. M. Okada *et al.*, Modeling type II collagenopathy skeletal dysplasia by directed conversion and induced pluripotent stem cells. *Hum Mol Genet* **24**, 299-313 (2015).

26. K. M. Loh *et al.*, Mapping the Pairwise Choices Leading from Pluripotency to Human Bone, Heart, and Other Mesoderm Cell Types. *Cell* **166**, 451-467 (2016).

27. K. Umeda *et al.*, Human chondrogenic paraxial mesoderm, directed specification and prospective isolation from pluripotent stem cells. *Sci Rep* **2**, 455 (2012).

28. R. A. Oldershaw *et al.*, Directed differentiation of human embryonic stem cells toward

chondrocytes. *Nat Biotechnol* **28**, 1187-1194 (2010).

29. B. O. Diekman *et al.*, Cartilage tissue engineering using differentiated and purified induced pluripotent stem cells. *Proc Natl Acad Sci U S A* **109**, 19172-19177 (2012).

30. S. S. Adkar *et al.*, Step-Wise Chondrogenesis of Human Induced Pluripotent Stem Cells and Purification Via a Reporter Allele Generated by CRISPR-Cas9 Genome Editing. *Stem Cells* **37**, 65-76 (2019).

31. J. Lim *et al.*, BMP-Smad4 signaling is required for precartilaginous mesenchymal condensation independent of Sox9 in the mouse. *Dev Biol* **400**, 132-138 (2015).

32. A. S. Patil, R. B. Sable, R. M. Kothari, An update on transforming growth factor-beta (TGF-beta): sources, types, functions and clinical applicability for cartilage/bone healing. *J Cell Physiol* **226**, 3094-3103 (2011).

33. Q. O. Tang *et al.*, TGF-beta3: A potential biological therapy for enhancing chondrogenesis. *Expert Opin Biol Ther* **9**, 689-701 (2009).

34. A. M. Craft *et al.*, Generation of articular chondrocytes from human pluripotent stem cells. *Nat Biotechnol* **33**, 638-645 (2015).

35. A. Yamashita *et al.*, Generation of scaffoldless hyaline cartilaginous tissue from human iPSCs. *Stem Cell Reports* **4**, 404-418 (2015).

36. B. Johnstone, T. M. Hering, A. I. Caplan, V. M. Goldberg, J. U. Yoo, In vitro chondrogenesis of bone marrow-derived mesenchymal progenitor cells. *Exp Cell Res* **238**, 265-272 (1998).

37. A. Dicks *et al.*, Prospective isolation of chondroprogenitors from human iPSCs based on cell surface markers identified using a CRISPR-Cas9-generated reporter. *Stem Cell Res Ther* **11**, 66 (2020).

38. C. L. Wu *et al.*, Single cell transcriptomic analysis of human pluripotent stem cell chondrogenesis. *Nat Commun* **12**, 362 (2021).

39. A. Yamashita *et al.*, Considerations in hiPSC-derived cartilage for articular cartilage repair. *Inflamm Regen* **38**, 17 (2018).

40. C. Murphy, A. Mobasheri, Z. Tancos, J. Kobolak, A. Dinnyes, The Potency of Induced Pluripotent Stem Cells in Cartilage Regeneration and Osteoarthritis Treatment. *Adv Exp Med Biol* **1079**, 55-68 (2018).

41. Y. Krishnan, A. J. Grodzinsky, Cartilage diseases. *Matrix Biol* **71-72**, 51-69 (2018).

42. K. Musunuru, Genome editing of human pluripotent stem cells to generate human cellular disease models. *Dis Model Mech* **6**, 896-904 (2013).

43. S. Yumlu *et al.*, Gene editing and clonal isolation of human induced pluripotent stem cells using CRISPR/Cas9. *Methods* **121-122**, 29-44 (2017).

44. C. J. O'Conor, N. Case, F. Guilak, Mechanical regulation of chondrogenesis. *Stem Cell Res Ther* **4**, 61 (2013).

45. J. M. Brunger, A. Zutshi, V. P. Willard, C. A. Gersbach, F. Guilak, Genome Engineering of Stem Cells for Autonomously Regulated, Closed-Loop Delivery of Biologic Drugs. *Stem Cell Reports* **8**, 1202-1213 (2017).

46. L. Pferdehirt, A. K. Ross, J. M. Brunger, F. Guilak, A Synthetic Gene Circuit for Self-Regulating Delivery of Biologic Drugs in Engineered Tissues. *Tissue Eng Part A* **25**, 809-820 (2019).

47. R. J. Nims *et al.*, A synthetic mechanogenetic gene circuit for autonomous drug delivery in engineered tissues. *Sci Adv* **7**, (2021).

48. F. Guilak *et al.*, Designer Stem Cells: Genome Engineering and the Next Generation of Cell-Based Therapies. *J Orthop Res* **37**, 1287-1293 (2019).

49. R. Tang *et al.*, Differentiation of human induced pluripotent stem cells into nucleus pulposus-like cells. *Stem Cell Res Ther* **9**, 61 (2018).

50. S. Thirion, F. Berenbaum, Culture and phenotyping of chondrocytes in primary culture. *Methods Mol Med* **100**, 1-14 (2004).

51. D. Nasrabadi, S. Rezaeiani, M. B. Eslaminejad, A. Shabani, Improved Protocol for Chondrogenic Differentiation of Bone Marrow Derived Mesenchymal Stem Cells -Effect of PTHrP and FGF-2 on TGFbeta1/BMP2-Induced Chondrocytes Hypertrophy. *Stem Cell Rev Rep* **14**, 755-766 (2018).

52. B. T. Estes, B. O. Diekman, J. M. Gimble, F. Guilak, Isolation of adipose-derived stem cells and their induction to a chondrogenic phenotype. *Nat Protoc* **5**, 1294-1311 (2010).

53. A. I. Caplan, Mesenchymal Stem Cells: Time to Change the Name! *Stem Cells Transl Med* **6**, 1445-1451 (2017).

54. Y. K. Yang, C. R. Ogando, C. Wang See, T. Y. Chang, G. A. Barabino, Changes in phenotype and differentiation potential of human mesenchymal stem cells aging in vitro. *Stem Cell Res Ther* **9**, 131 (2018).

55. K. Drela, L. Stanaszek, A. Nowakowski, Z. Kuczynska, B. Lukomska, Experimental Strategies of Mesenchymal Stem Cell Propagation: Adverse Events and Potential Risk of Functional Changes. *Stem Cells Int* **2019**, 7012692 (2019).

56. K. Takahashi *et al.*, Induction of pluripotent stem cells from adult human fibroblasts by defined factors. *Cell* **131**, 861-872 (2007).

57. H. Nejadnik *et al.*, Improved approach for chondrogenic differentiation of human induced pluripotent stem cells. *Stem Cell Rev Rep* **11**, 242-253 (2015).

58. J. Lee *et al.*, Early induction of a prechondrogenic population allows efficient generation of stable chondrocytes from human induced pluripotent stem cells. *FASEB J* **29**, 3399-3410 (2015).

59. W. M. Suchorska, E. Augustyniak, M. Richter, T. Trzeciak, Comparison of Four Protocols to Generate Chondrocyte-Like Cells from Human Induced Pluripotent Stem Cells (hiPSCs). *Stem Cell Rev Rep* **13**, 299-308 (2017).

60. Q. Lian *et al.*, Functional mesenchymal stem cells derived from human induced pluripotent stem cells attenuate limb ischemia in mice. *Circulation* **121**, 1113-1123 (2010).

61. M. Xu, G. Shaw, M. Murphy, F. Barry, Induced Pluripotent Stem Cell-Derived Mesenchymal Stromal Cells Are Functionally and Genetically Different From Bone Marrow-Derived Mesenchymal Stromal Cells. *Stem Cells* **37**, 754-765 (2019).

62. I. P. Chen *et al.*, Induced pluripotent stem cell reprogramming by integration-free Sendai virus vectors from peripheral blood of patients with craniometaphyseal dysplasia. *Cell Reprogram* **15**, 503-513 (2013).

63. A. R. Crowe, W. Yue, Semi-quantitative Determination of Protein Expression using Immunohistochemistry Staining and Analysis: An Integrated Protocol. *Bio Protoc* **9**, (2019).

64. T. Nolan, R. E. Hands, S. A. Bustin, Quantification of mRNA using real-time RT-PCR. *Nat Protoc* **1**, 1559-1582 (2006).

Chapter 5

Skeletal Dysplasia-causing TRPV4 Mutations Suppress the Hypertrophic Differentiation of Human iPSC-derived Chondrocytes

5.1 Abstract

Mutations in the TRPV4 ion channel can lead to a range of skeletal dysplasias. However, the mechanisms by which TRPV4 mutations lead to distinct disease severity remain unknown. Here, we use CRISPR-Cas9-edited human induced pluripotent stem cells (hiPSCs) harboring either the mild V620I or lethal T89I mutations to elucidate the differential effects on channel function and chondrogenic differentiation. We found that hiPSC-derived chondrocytes with the V620I mutation exhibited increased basal currents through TRPV4. However, both mutations showed more rapid calcium signaling with a reduced overall magnitude in response to TRPV4 agonist GSK1016790A compared to wildtype. There were no differences in overall cartilaginous matrix production, but the V620I mutation resulted in reduced mechanical properties of cartilage matrix later in chondrogenesis. mRNA sequencing revealed that both mutations upregulated several anterior HOX genes and downregulated antioxidant genes CAT and GSTA1 throughout chondrogenesis. BMP4 treatment upregulated several essential hypertrophic genes in WT chondrocytes; however, this hypertrophic maturation response was inhibited in mutant

chondrocytes. These results indicate that the TRPV4 mutations alter BMP signaling in chondrocytes and prevent proper chondrocyte hypertrophy, as a potential mechanism for dysfunctional skeletal development. Our findings provide potential therapeutic targets for developing treatments for TRPV4-mediated skeletal dysplasias.

5.2 Introduction

Skeletal dysplasias comprise a heterogeneous group of over 450 bone and cartilage diseases with an overall birth incidence of 1 in 5000 (*1-5*). In the specific cases of moderate autosomal-dominant brachyolmia and severe metatropic dysplasia, among other dysplasias, arthropathies, and neuropathies, the disease is caused by mutations in transient receptor potential vanilloid 4 (TRPV4), a non-selective cation channel (*6, 7*). For example, a V620I substitution (exon 12, G858A) in TRPV4 is responsible for moderate brachyolmia, which exhibits short stature, scoliosis, and delayed development of deformed bones (*6, 8, 9*). These features, albeit more severe, are also present in metatropic dysplasia. Metatropic dysplasia can be caused by a TRPV4 T89I substitution (exon 2, C366T) and leads to joint contractures, disproportionate measurements, and, in severe cases, death due to small chest size and cardiopulmonary compromise (*6, 9, 10*). Both V620I and T89I TRPV4 mutations are considered gain-of-function variants (*11, 12*). Given the essential role of TRPV4 during chondrogenesis (*13*) and cartilage homeostasis (*14*), it is hypothesized that TRPV4 mutations may affect the cartilaginous phase of endochondral ossification during skeletal development.

Endochondral ossification is a process by which bone tissue is created from a cartilage template (*2, 10, 15, 16*). During this process, chondrocytes transition from maintaining the homeostasis of cartilage, regulated by transcription factor SRY-box containing gene 9 (*SOX9*) (*16-19*), to hypertrophy. Hypertrophy is driven by runt related transcription factor 2 (*RUNX2*)

and bone morphogenic protein (BMP) signaling (*16, 18, 19*) and leads to chondrocyte apoptosis

or differentiation into osteoblasts to form bone (*16, 18, 19*). However, how TRPV4 and its

signaling cascades regulate endochondral ossification remains to be determined.

The activation of TRPV4 increases *SOX9* expression (*13*) and prevents chondrocyte

hypertrophy and endochondral ossification (*18, 20-23*). One study found that overexpressing

wildtype *Trpv4* in mouse embryos increased intracellular calcium (Ca^{2+}) concentration and

delayed bone mineralization (*24*), a potential link between intracellular Ca^{2+}, such as with gain-

of-function TRPV4 mutations, and delayed endochondral ossification. Our previous study also

observed increased expression of follistatin (*FST),* a potent BMP inhibitor, and delayed

hypertrophy in porcine chondrocytes overexpressing human V620I- and T89I-TRPV4 (*12, 25*).

While previous studies have greatly increased our knowledge of the influence of TRPV4

mutations on chondrogenesis and hypertrophy, most of them often involved animal models (*12,

24*) or cells (*2, 8, 10, 11*) (*12*) overexpressing mutant TRPV4. Therefore, these approaches may

not completely recapitulate the effect of TRPV4 mutations on human chondrogenesis.

Human induced pluripotent stem cells (hiPSCs), which are derived from adult somatic

cells (*26*), offer a system for modeling human disease to study the effect of mutations throughout

differentiation (*27, 28*). In fact, two studies have used patient-derived hiPSCs with TRPV4

mutations to study lethal and non-lethal metatropic dysplasia-causing variants I604M (*29*) and

L619F (*30*), respectively. However, patient samples are often challenging to procure due to the

rarity of skeletal dysplasias. In this regard, CRISPR-Cas9 technology allows the creation of

hiPSC lines harboring various mutations along with isogenic controls (i.e., wildtype; WT).

The goal of this study was to elucidate the detailed molecular mechanisms underlying

how two TRPV4 gain-of-function mutations lead to strikingly distinct severities of skeletal

dysplasias (i.e., moderate brachyolmia vs. lethal metatropic dysplasia). To achieve this goal, we used CRISPR-Cas9 gene-edited hiPSC lines bearing either the V620I or T89I TRPV4 mutation, and their isogenic WT control, to delineate the effects of TRPV4 mutations on chondrogenesis and hypertrophy using RNA sequencing and transcriptomic analysis. We further examined the effects of the mutations on channel function and matrix production and properties. We hypothesized the V620I and T89I TRPV4 mutations would enhance chondrogenesis with differing degrees of altered hypertrophy. This study will improve our understanding of the role of TRPV4 in chondrocyte homeostasis and maturation and lay the foundation for treatment and prevention of TRPV4-mediated dysplasias.

5.3 Methods

5.3.1 hiPSC culture

The BJFF.6 (BJFF) human iPSC line (Washington University Genome Engineering and iPSC Center (GEiC), St. Louis, MO), was used in this study as the isogenic-wildtype control. CRISPR-Cas9 gene editing was used to create the V620I and T89I mutations in the BJFF cell line as described previously (*31*). The hiPSCs were maintained on vitronectin (VTN-N; cat. num. A14700; Thermo Fisher Scientific, Waltham, MA)-coated plates in Essential 8 Flex medium (E8; cat. num. A2858501; Gibco, Thermo Fisher Scientific, Waltham, MA). Medium was changed daily until cells were passaged at 80-90% confluency (medium supplemented with Y-27632 [cat. num. 72304; STEMCELL Technologies, Vancouver, Canada] for 24 hours) or induced into mesodermal differentiation at 30-40% confluency.

5.3.2 Mesodermal differentiation

The hiPSCs were differentiated through the mesodermal pathway as previously described (*31-33*). In brief, cells were fed daily with different cocktails of growth factors and small molecules

for twelve days in mesodermal differentiation medium and driven through the anterior primitive streak (1 day; 30 ng/ml Activin [cat. num. 338-AC; R&D Systems, Minneapolis, MN], 20 ng/ml FGF2 [cat. num. 233-FB-025/CF; R&D Systems, Minneapolis, MN], 4 µM CHIR99021 [cat. num. 04-0004-02; Reprocell, Beltsville, MD]), paraxial mesoderm (1 day; 20 ng/ml FGF2, 3 µM CHIR99021, 2 µM SB505124 [cat. num. 3263; Tocris Bioscience, Bristol, UK], 4 µM dorsomorphin [DM; cat. num. 04-0024; Reprocell, Beltsville, MD]), early somite (1 day; 2 µM SB505124, 4 µM dorsomorphin, 500 nM PD173074 [cat. num. 3044; Tocris Bioscience, Bristol, UK], 1 µM Wnt-C59 [cat. num. C7641-2s; Cellagen Technologies, San Diego, CA]), and sclerotome (3 days; 1 µM Wnt-C59, 2 µM purmorphamine [cat. num. 04-0009; Reprocell, Beltsville, MD]) into chondroprogenitor cells (6 days; 20 ng/ml BMP4 [cat. num. 314-BP-010CF; R&D Systems, Minneapolis, MN]). Mesodermal differentiation medium had a base of Iscove's Modified Dulbecco's Medium, glutaMAX (IMDM; cat. num. 31980097; Gibco, Thermo Fisher Scientific, Waltham, MA) and Ham's F-12 nutrient mix, glutaMAX (F12; cat. num. 31765092; Gibco, Thermo Fisher Scientific, Waltham, MA) in equal parts supplemented with 1% penicillin-streptomycin (P/S; cat. num. 15140122; Gibco, Thermo Fisher Scientific, Waltham, MA), 1% Insulin-Transferrin-Selenium (ITS+; cat. num. 41400045; Gibco, Thermo Fisher Scientific, Waltham, MA), 1% chemically defined concentrated lipids (cat. num. 11905031; Thermo Fisher Scientific, Waltham, MA), and 450 µM 1-thioglycerol (cat. num. M6145; Millipore Sigma, St. Louis, MO). The chondroprogenitor cells were then disassociated for chondrogenic differentiation.

5.3.3 Chondrogenic differentiation with 3D pellet culture

Cells were differentiated into chondrocytes using a high-density, suspension pellet culture (*31-33*). In summary, cells were resuspended in chondrogenic medium: Dulbecco's Modified Eagle

189

Medium/F12, glutaMAX (DMEM/F12; cat. num. 10565042; Gibco, Thermo Fisher Scientific, Waltham, MA), 1% P/S, 1% ITS+, 1% Modified Eagle Medium (MEM) with nonessential amino acids (NEAA; cat. num. 11140050; Gibco, Thermo Fisher Scientific, Waltham, MA), 0.1% dexamethasone (Dex; cat. num. D4902; Millipore Sigma, St. Louis, MO), and 0.1% 2-Mercaptoethnol (2-ME; cat. num. 21985023; Gibco, Thermo Fisher Scientific, Waltham, MA) supplemented with 0.1% L-ascorbic acid (ascorbate; cat. num. A8960; Millipore Sigma, St. Louis, MO), 0.1% L-proline (proline; cat. num. P5607; Millipore Sigma, St. Louis, MO), 10 ng/ml human transforming growth factor-β3 (TGFβ3; cat. num. 243-B3-010/CF; R&D Systems, Minneapolis, MN), 1 μM Wnt-C59, and 1 μM ML329 (cat. num. 22481; Cayman Chemical, Ann Arbor, MI) at 5×10^5 cells/mL. One mL of the cell solution was added to a 15 mL-conical tube (cat. num. 430790; Corning, Corning, NY) and centrifuged to form the spherical pellets. Pellets were fed every 3-4 days with complete chondrogenic medium until the desired time point. Several timepoints of the chondrogenic pellets were used to study chondrocyte maturation (7, 14, 28, and 42 days), mechanical properties (28 and 42 days), hypertrophy (28 days) or, after digestion to single cell day-28 chondrocytes, on Ca^{2+} signaling in response to pharmacological activation of TRPV4.

5.3.4 BMP4 treatment to promote hypertrophic differentiation

Some day-28 pellets were also further differentiated for an additional 4 weeks to examine the effects of the mutations on chondrocyte hypertrophy. Pellets were cultured with complete chondrogenic medium with either TGFβ3 (10 ng/mL) alone, BMP4 (50 ng/mL) alone, or a combination of TGFβ3 (10 ng/mL) and BMP4 (50 ng/mL).

5.3.5 Dissociation of chondrogenic pellets to obtain single cell hiPSC-derived chondrocytes

To isolated hiPSC-derived chondrocytes, day-28 chondrogenic pellets were rinsed and placed in

an equal volume (1 pellet per 1 mL) of digestion medium (0.4% w/v type II collagenase [cat. num. LS00417; Worthington Biochemical, Lakewood, NJ] in DMEM/F12 with 10% fetal bovine serum [FBS; cat. num. S11550; Atlanta Biologicals, R&D Systems, Minneapolis, MN]). The tubes were placed on an orbital shaker at 37ºC and vortexed every 20 minutes for approximately 2 hours. Once the tissue was digested and could no longer be seen by the naked eye, the digestion medium was neutralized in DMEM/F12 medium containing 10% FBS. These cells were used for patch clamping and confocal experiments.

5.3.6 TRPV4 agonists and antagonists

Solutions were prepared immediately before experiments and held at room temperature. GSK1016790A (GSK101; cat. num. G0798; Sigma Aldrich, St. Louis, MO) and/or GSK205 (cat. num. AOB1612 1263130-79-5; AOBIOUS, Gloucester, MA), in addition to DMSO for a vehicle control, were added to assay buffer (Hanks' Balanced Salt Solution [HBSS; cat. num. 14025076; Gibco, Thermo Fisher Scientific, Waltham, MA] with 2% HEPES [cat. num. 15630130; Gibco, Thermo Fisher Scientific, Waltham, MA]) at 2x the desired concentration (20 nM GSK101, 40 µM GSK205). Solutions were made at 2x the desired concentration because they would be mixed at an equal volume of assay buffer after capturing a baseline fluorescence in Ca^{2+} signaling experiments.

5.3.7 Patch clamping

Isolated chondrocytes were kept on ice and used for patching within 36 hours. Patch-clamp experiments were carried out at RT under two conditions. Single-channel measurements were made in excised inside-out membrane patches in a symmetric potassium chloride (KCl) solution (148mM KCl, 1mM K_2EDTA, 1mM EGTA, 10mM HEPES, pH 7.4). Channel activation was achieved by bath perfusion with the same buffer solution containing 10 nM GSK101. Blocking

was performed using the same buffer solution supplied with both 10 nM GSK101 and 20 µM GSK205. Recordings were made at -30mV membrane. Whole-cell currents were recorded using an external sodium chloride (NaCl) solution (150 mM NaCl, 5 mM KCl, 1 mM EGTA, 10 mM Glucose, 10 mM HEPES, and 10 µM free Ca^{2+}) and KCl pipette solution as used for single-channel recordings. Inhibition of basal currents was performed by pre-incubation of the cells in external solution supplied with 20 µM GSK205 for 20 min before patching; the drug was also present in the bath at the same concentration during the experiment. Data were acquired at 3 kHz, low-pass filtered at 1 kHz with Axopatch 1D patch-clamp amplifier and digitized with Digidata 1320 digitizer (Molecular Devices, San Jose, CA). Data analysis was performed using the pClamp software suite (Molecular Devices, San Jose, CA). Pipettes with 2.0-4.0 MOhm resistance in symmetric 150 mM KCl buffer were pulled from Kimble Chase 2502 soda lime glass with a Sutter P-86 puller (Sutter Instruments, Novato, CA).

5.3.8 Confocal imaging of Ca^{2+} signaling

hiPSC-derived chondrocytes from digested pellets were plated in DMEM medium containing 10% FBS at 2.1 x 10^4 cells/cm^2 in 35 mm-dishes for 6-8 hours to allow the cells to adhere without dedifferentiating. Cells were then rinsed and stained for 30 min with Fluo-4 AM (cat. num. F14201; Thermo Fisher Scientific, Waltham, MA), Fura Red AM ((cat. num. F3021; Thermo Fisher Scientific, Waltham, MA), and sulfinpyrazone (cat. num. S9509-5G; Sigma Aldrich, St. Louis, MO) with 20 mM GSK205 or 1000x DMSO (vehicle control). The dye solution was replaced with assay buffer before imaging cells on a confocal microscope (LSM 880; Zeiss, Oberkochen, Germany) at baseline for the first 100 frames (approximately 6 min). Then, an equal volume of a 2x solution of GSK101 or GSK101 and GSK205 was added, and imaging continued for an additional 300 frames (approximately 20 min). Fiji software (ImageJ,

version 2.1.0) was used to locate cells and quantify the ratiometric fluorescence intensity ($Intensity_{fluo-4}$/$Intensity_{fura\ red}$). In brief, .czi files were imported into Fiji and the channels were split. After applying the median filter, the image calculator divided the green channel by the red. A Z-projection was performed based on the maximum fluorescence of the red channel (to ensure that all cells were identified even in groups were there was no increase in Ca^{2+} signaling). A threshold and watershed binary were then applied, and measurements were set for a cell size of 100-infinity. Outlines were projected, and the mean fluorescence of each cell was measured over time. The average fluorescence was plotted for all the cells in the group over time. Area under the curve and time of response were calculated to quantify differences between groups. Cells were classified as responders if they had a fluorescence greater than the baseline mean plus 3 times the standard deviation in at least a quarter of the frames. Time of response was the time of the first frame in which the cell responded for at least 2 consecutive frames. The fluorescence was measured for all the cells in the frame of view as technical replicates for 2 experimental replicates.

5.3.9 AFM measurement of neocartilage mechanical properties

Day-28 and day-42 hiPSC-derived pellets were rinsed in PBS and snap frozen in optimal cutting temperature (OCT; cat. num. 4583; Sakura Finetek, Torrance, CA) medium and stored at -80 ºC. Pellets were cryosectioned using cryofilm (type 2C(10); Section-Lab, Hiroshima, Japan) in multiple different regions of the pellet (i.e., zones). The 10 µm cryosection with cryofilm was fixed on a microscope slide using chitosan and stored at 4 ºC overnight. The next day, cryosections were mechanically loaded using an atomic force microscopy (AFM, MFP-3D Bio, Asylum Research, Goleta, CA) as previously described (*34*). Briefly, the samples were tested in PBS at 37 ºC to maintain hydration and mimic physiologic conditions, respectively. The sections

were mechanically probed using a silicon cantilever with a spherical tip (5μm diameter, k~7.83 N/m, Novascan Technologies, Ames, IA). An area of 10 μm^2 with 0.5 μm intervals (400 indentations) was loaded to 300 nN with the loading rate of 10 μm/sec. Multiple locations from different sites of each zone and pellet were loaded as replicates. The curves obtained from AFM were imported into a custom written MATLAB code to determine the mechanical properties of the pellets. Using contact point extrapolation, the contact point between the cantilever's tip and the tissue was detected, and the elastic modulus was calculated using a modified Hertz model (*34-38*).

5.3.10 Histology

Chondrogenic pellets at days 7, 14, 28, 42, and 56 (with and without BMP4) were fixed and dehydrated in sequential steps of increasing ethanol and xylene solutions until embedded in paraffin wax. Wax blocks were cut into 8 μm sections on microscope slides for histological and immunohistochemical analysis. Slides were rehydrated in ethanol and water and the nuclei were stained with Harris hematoxylin and sGAGs with Safranin-O. Antigen retrieval was performed on rehydrated slides followed by blocking, the addition of primary and secondary antibodies, and AEC development to label collagen proteins (COL1A1, COL2A1, COL6A1, and COL10A1) and Vector Hematoxylin QS counterstain.

5.3.11 Biochemical analysis

Chondrogenic pellets at days 7, 14, 28, and 42 were washed with PBS and digested in papain overnight at 65ºC. sGAG and dsDNA content were measured using the dimethylmethylene blue (DMMB) and PicoGreen assays (Quant-iT™ PicoGreen™ dsDNA Assay Kit; cat. num. P7589; Thermo Fisher Scientific, Waltham, MA) respectively. sGAG content was normalized to dsDNA. Three to four independent experiments were performed with 3-4 technical replicates per

group.

5.3.12 Western blot

Day-56 pellets treated with TGFβ3, TGFβ3+BMP4, or BMP4 were digested to single cells, as described above, and lysed in RIPA buffer (cat. num. 9806S; Cell Signaling Technology, Danvers, MA) with protease inhibitor (cat. num. 87786; Thermo Fisher Scientific, Waltham, MA). Protein concentration was then measured using the BCA Assay (Pierce). Twenty micrograms of proteins for each well were separated on 10% sodium dodecyl sulfate-polyacrylamide gel electrophoresis gel with pre-stained molecular weight markers (cat. num. 161-0374; Bio-Rad, Hercules, CA) and transferred to a polyvinylidene fluoride (PVDF) membrane. The PVDF membrane blot was cut through the line at 50 kD. Two blots were incubated overnight at 4 °C with the primary antibodies: anti-COL10A1 (1:500; cat. num. PA5-97603; Thermo Fisher Scientific, Waltham, MA) and anti-GAPDH (1:30000; cat. num. 60004-1-Ig; Proteintech, Rosemont, IL), as the loading control. TidyBlot-Reagent-HRP (1:1000; cat. num. 147711; Bio-RAD, Hercules, CA) and horse anti-mouse IgG secondary antibody (1:3000; cat. num. 7076; Cell Signaling, Danvers, MA) were then used respectively. Immunoblots were imaged and analyzed using the iBright FL1000 Imaging System (Thermo Fisher Scientific, Waltham, MA).

5.3.13 RNA isolation

Chondrogenic pellets at days 7, 14, 28, 42, and 56 were washed with PBS, lysed, snap frozen, and homogenized. RNA was isolated using the Total RNA Purification Plus Kit (cat. num. 48400; Norgen Biotek, Thorold, Canada) and used immediately for either RT-qPCR or RNA-seq.

5.3.14 Gene expression with RT-qPCR

Isolated RNA was reverse transcribed into cDNA. The cDNA was used to run real-time, quantitative PCR using Fast SYBR green. Gene expression was analyzed using the $\Delta\Delta C_T$ method with hiPSC as the reference time point and *TBP* as the housekeeping gene (*39*). Three to four independent experiments were performed with 3-4 technical replicates per group. Primers can be found in the Table 5.1.

Table 5.1 Primers for RT-qPCR.

Gene	Forward Primer (3')	Reverse Primer (5')
ACAN	CACTTCTGAGTTCGTGGAGG	ACTGGACTCAAAAAGCTGGG
COL1A1	TGTTCAGCTTTGTGGACCTC	TTCTGTACGCAGGTGATTGG
COL2A1	GGCAATAGCAGGTTCACGTA	CTCGATAACAGTCTTGCCCC
COL10A1	CATAAAAGGCCCACTACCCAAC	ACCTTGCTCTCCTCTTACTGC
FST	TGTGCCCTGACAGTAAGTCG	GTCTTCCGAAATGGAGTTGC
S100B	AGGGAGGGAGACAAGCACAA	ACTCGTGGCAGGCAGTAGTA
SOX9	CGTCAACGGCTCCAGCAAGAACAA	GCCGCTTCTCGCTCTCGTTCAGAAGT
TRPV4	AGAACTTGGGCATCATCAACGAG	GTTCGAGTTCTTGTTCAGTTCCAC
TBP	AACCACGGCACTGATTTTCA	ACAGCTCCCCACCATATTCT

5.3.15 Genome-wide mRNA sequencing

Isolated RNA was treated with DNase (cat. num. 25720; Norgen Biotek, Thorold, Canada) and cleaned (cat. num. 43200; Norgen Biotek, Thorold, Canada) according to manufacturer instructions prior to submitting to the Genome Technology Access Center at Washington University in St. Louis (GTAC). Libraries were prepared according to manufacturer's protocol. Samples were indexed, pooled, and sequenced at a depth of 30 million reads per sample on an Illumina NovaSeq 6000. Basecalls and demultiplexing were performed with Illumina's bcl2fastq

software and a custom python demultiplexing program with a maximum of one mismatch in the indexing read. RNA-seq reads were then aligned to the Ensembl release 76 primary assembly with STAR version 2.5.1a (*40*). Gene counts were derived from the number of uniquely aligned unambiguous reads by Subread:featureCount version 1.4.6-p5 (*41*). Isoform expression of known Ensembl transcripts were estimated with Salmon version 0.8.2 (*42*). Sequencing performance was assessed for the total number of aligned reads, total number of uniquely aligned reads, and features detected. The ribosomal fraction, known junction saturation, and read distribution over known gene models were quantified with RSeQC version 2.6.2 (*43*).

5.3.16 Transcriptomic analysis of sequencing datasets

R and the DESeq2 package were used to read un-normalized gene counts, and genes were removed if they had counts lower than 200 (*44*). Regularized-logarithm transformed data of the samples were visualized with the *Pheatmap* package (*45*) function on the calculated Euclidean distances between samples or with the *ggplot2* package (*46*) to create a principle component analysis (PCA). The transformed data was also used to determine the top 5000 most variable genes across the samples. The replicates, from DESeq data, for each group were averaged together, and the up- and down-regulated differentially expressed genes (DEGs) were determined. The total number of DEGs was plotted using GraphPad Prism. At day 28, the V620I and T89I lines were compared to WT. At day 56, TGFβ3-treated V620I and T89I were compared to TGFβ3-treated WT, and BMP4-treated groups were compared to their respective TGFβ3-treated group of the same line (e.g., BMP4-treated WT vs. TGFβ3-treated WT). Genes were considered differentially expressed if adjusted p value (p_{adj}) < 0.1 and $\log_2$(fold change) ≥ 1 or ≤ -1. The intersecting and unique DEGs were determined and plotted with the *intersect* and *setdiff,* and *venn.diagram* (*VennDiagram* package (*47*)) functions. The fold changes of common

chondrogenic, hypertrophic, growth factor, Ca^{2+} signaling, and off-target genes, in the top 5000 most variable genes, were plotted using the *pheatmap* function. The top 25 most up-regulated and down-regulated for each group, based on $\log_2$(fold change), and the $\log_2$(fold change) of that gene for the other group(s) were also plotted with the *pheatmap*. Gene lists (e.g., intersected genes, genes upregulated with BMP4 treatment) were entered into g:profiler to determine associated Gene Ontology (GO) Biological Processes, Molecular Functions, Cellular Components, KEGG pathways, Reactome pathways, and Human Phenotype (HP) Ontologies (*48*). The negative $\log_{10}$ of the adjusted p value for each term was plotted with GraphPad Prism or using a function to scale circle diameter to the p value in Illustrator.

The gap statistic method determined the ideal number of clusters resulting from BMP4 treatment was either 1 or 9. We then performed k-means clustering with 9 clusters and plotted the gene expression trends for each gene within the cluster with the average expression trend overlaying for each cell line of the largest cluster using the *tidyverse* package (*49*). The genes in each cluster, with the normalized counts for each group, are listed in Table S5.1. The largest cluster was plotted using the Cytoscape String app's protein interaction to create a protein-protein network (*50, 51*). Using the average log fold change with BMP4 treatment across lines, the network was propagated using the Diffusion app, and functional enrichment with EnrichmentMap was performed on the network (*52*). We then created a network connecting the genes to their associated genes with black lines and to their associated Gene Ontology processes using grey lines. We colored the gene circles with three colors representing the log fold change of that gene in each line. The white arrows were added to the color scale legend to indicate maximum log fold change for each line.

5.3.17 Statistical analysis

Data were graphed and analyzed using GraphPad Prism (Version 9.1.0). Outliers were removed

from the data using the ROUT method (Q = 1%), and the data were tested for normality with the

Shapiro-Wilk test ($\alpha = 0.05$). For RT-qPCR, normally distributed data were analyzed within

each time point using a Brown-Forsythe and Welch one-way ANOVA with multiple

comparisons (mean of each column, cell line, with every other column). A Kruskal-Wallis test

was used if data was not normally distributed. For biochemical analysis, mechanical properties,

and area under the curve, and time of response, data were analyzed using an ordinary two-way

ANOVA, comparing each cell with all other cells, with Tukey's post-hoc test. Area under the

curve was quantified for plots over time considering a baseline of Y=0, ignoring peaks less than

10% of the distance from minimum to maximum Y, and all peaks going over the baseline.

5.4 Results

5.4.1 Mutant TRPV4 has altered response to chemical agonist GSK101

We first assessed TRPV4 channel function and alterations in Ca^{2+} signaling due to the V620I and

T89I mutations in day-28 hiPSC-derived chondrocytes using electrophysiology and fluorescence

imaging. Using whole-cell patch clamping, we measured the basal membrane current of the

hiPSC-derived chondrocytes from the mutated and WT lines. V620I-TRPV4 had the highest

basal currents at both 70 and -70 mV (70/-70 mV pA/pF – WT: 18.52/5.93 vs. V602I:

77.79/55.33 vs. T89I: 40.97/50.13; Figure 5.1A). However, when TRPV4 was inhibited with

GSK205 (*53*), TRPV4-specfic chemical antagonist, the three lines had similar, decreased

currents (70/-70 mV – WT: 18.72/14.36 pA/pF vs. V620I: 13.55/9.15 pA/pF vs. T89I:

29.27/13.8 pA/pF; Figure 5.1A). To capture the specific current through TRPV4, we took the

difference of the basal current (no GSK205) and the average TRPV-inhibited current (with

GSK205). TRPV4 inhibition caused a significant change in current in V620I at both 70 and -70 mV (70 mV – V620I: Δ64.28 vs. WT: Δ -0.19, p=0.0379 and T89I: Δ11.67, p<0.0001; -70 mV – V620I: Δ46.13 vs. WT: Δ -8.47, p<0.0001 and T89I: Δ36.33, p=0.0057; Figure 5.1B). Interestingly, T89I-TRPV4 was not significantly different from WT despite also causing a gain-of-function in recombinant channels (*11*).

Next, we activated WT and mutant TRPV4 with chemical agonist GSK1016790A (GSK101) (*54*) and found that the mutations decreased the cellular response to the agonist, resulting in reduced Ca^{2+} signaling. These results were supported using two methods: inside-out excised patches and confocal imaging of Ca^{2+} signaling (Figure 5.1C-D). The representative traces of inside-out patches showed increased current through the patch with the addition of GSK101 and the attenuation by GSK205 (Figure 5.1C). GSK205 continued to block the channel and prevented another increase in current despite the addition of GSK101. Though the unitary currents were indistinguishable (8 pA at -30mV) among WT and mutants, in excised inside-out patches WT typically produced higher GSK101-induced currents than the mutants (WT: 290 pA vs. V620I: 87.1 pA and T89I: 62.3 pA at -30mV), potentially indicative of more channels per patch (Figure 5.1C). In the confocal imaging experiments, a ratiometric fluorescence indicated Ca^{2+} signaling of the hiPSC-derived chondrocytes in response to either 10 nM GSK101 or a cocktail of 10 nM GSK101 and 20 µM GSK205. WT cells had significantly higher fluorescence, and therefore Ca^{2+} signaling, in response to GSK101 according to the plots and their area under the curve (AUC; WT: 1470 vs. V620I: 1114 and T89I: 1044; p<0.0001; Figure 5.1D-E). The presence of GSK205 attenuated this response for all three lines, confirming the Ca^{2+} influx was due to the TRPV4 ion channel (WT: 366 vs. V620I: 460 vs T89I: 358). We also evaluated the response time of the cells to GSK101 and GSK101+GSK205. We considered a cell to be

responding if more than a quarter of its frames, after stimuli, had a fluorescence higher than the mean baseline plus 3 times the standard deviation. The mutants responded faster to GSK101 than the WT (WT: 46.2 sec vs. V620I: 12 sec, p=0.0048 and T89: 10.8 sec, p=0.0097; Figure 5.1F). Interestingly, the addition of GSK205 did not significantly slow the response of WT, but it did slow the response of the mutants, with the severe mutation slower than the moderate (WT: 35.4 sec vs. V620I: 234 sec and T89: 366 sec; p<0.0001; Figure 5.1F).
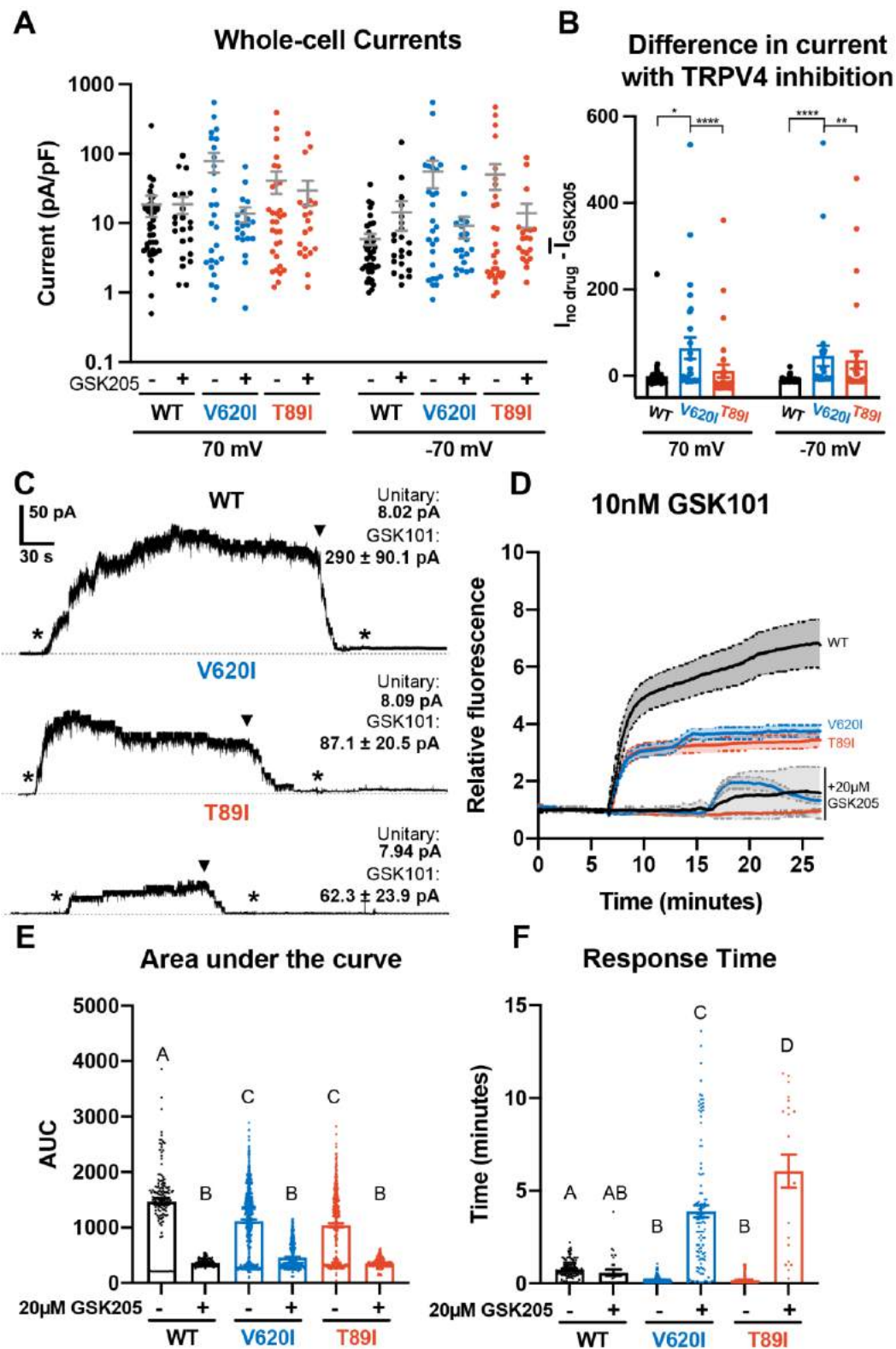
Figure 5.1 Differences in TRPV4 electrophysiological properties of WT and mutant hiPSC-derived chondrocytes. (**A**) Whole-cell currents were higher, on average, in mutant hiPSC-derived

chondrocytes than WT at 70 and -70 mV. TRPV4 inhibition with 20 µM GSK205 reduced mutant currents to similar levels as WT. Mean ± SEM. n=20-40 cells. (**B**) The difference between the current through TRPV4 without GSK205 from the average current through inhibited channels was significantly higher in V620I. There was no difference between no drugs and GSK205 in WT. Mean ± SEM. n=20-40 cells. Kruskal-Wallis test with multiple comparisons comparing cell lines at 70 mV and -70 mV. *$p<0.05$, **$p<0.01$, ****$p<0.001$. (**C**) Inside-out excised patches of WT had a higher current in response to 10 nM GSK101 (indicated by *) than mutants. The addition of 10 nM GSK101 + 20 µM GSK205 (indicated by ▼) decreased the current and continued to block the channel when GSK101 alone was re-introduced (*). Representative plots with average unitary current and current in response to GSK101. Mean ± SEM. n=5, 9, and 8 for WT, V620I, and T89I, respectively. (**D**) Mutant TRPV4 decreased the channels' sensitivity to activation with GSK101 as shown with confocal imaging of ratiometric fluorescence indicating Ca^{2+} signaling. GSK205 attenuated GSK101-mediated signaling. Mean ± 95% CI. N = 3 experiments with a total of 158-819 cells per line. (**E**) Quantification of the area under the curve of (**D**). Mean ± SEM. n=158-819 cells from N=3 experiments. Ordinary two-way ANOVA with Tukey's post-hoc test. Interaction, cell line, and treatment $p<0.0001$. (**F**) Time of initial response of each responding cell (≥25% of frames for that cell are responding) measured from the addition of stimulus. Mutant TRPV4 responded faster to GSK101, but the response was significantly slowed by GSK205. Responding frames were considered to have a fluorescence greater than the mean plus three times the standard deviation. Mean ± SEM. Ordinary two-way ANOVA with Tukey's post-hoc test. Interaction, cell line, and treatment $p<0.0001$.

5.4.2 Chondrogenic differentiation of WT and mutant hiPSC lines

To confirm if the hiPSCs with dysplasia-causing mutations would undergo proper

chondrogenesis, we differentiated CRISPR-Cas9-edited hiPSCs with mutant *TRPV4* alongside an

isogenic wildtype (WT) using our previously published protocol (*31, 33*). After 12 days of

monolayer mesodermal differentiation, the cells underwent 42 days of chondrogenic

differentiation, and pellets were collected at days 7, 14, 28, and 42. At day 28, the three lines had

similar chondrogenic matrix as shown with Safranin-O staining for sulfated glycosaminoglycans

(sGAGs) and collagen type 2 alpha chain 1 (COL2A1) labeling with immunohistochemistry

(IHC; Figure 5.2A-B). All three lines had little to no labeling of fibrocartilage marker COL1A1

and hypertrophic cartilage marker COL10A1 with IHC (Figure 5.2C-D). To quantitatively

confirm the matrix production throughout chondrogenesis, we performed biochemical assays to

measure sGAG production and normalize it to double-stranded DNA content. As expected,

differences in matrix production were significant between time points (p<0.0001; Figure 5.2E). The sGAG/DNA ratio increased in WT by 8-fold and in V620I and T89I by 5- to 5.5-fold from day 14 to 28 (p<0.0001). V620I pellets also increased in matrix content by 150% from day 28 to 42 (p=0.0163) with all three lines reaching an sGAG/DNA ratio of approximately 30. However, there were no differences in sGAG/DNA ratios among the three cell lines at any time point (cell line: p=0.1206; interaction: p=0.7426).

Atomic force microscopy (AFM) was then used to measure the mechanical properties of the hiPSC-derived cartilaginous matrix deposited by the WT and two TRPV4 mutated cell lines. The elastic modulus ranged from 14 to 20 kPa, consistent with mouse iPSC-derived cartilage (*55*). At day 28, the three lines had similar properties (WT: 14.4 kPa vs. V620I: 15.9 kPa vs. T89I: 14.8 kPa); however, at day 42, V620I had a significantly decreased elastic modulus (V620I: 10.32 kPa vs. WT: 20.0 kPa, p=0.0004 and T89I: 17.5 kPa, p=0.0328; Figure 5.2F). These experiments indicated that all three lines could properly differentiate into chondrocytes and had similar cartilaginous matrix production by day 28. Therefore, we used the day 28 time point for further studies.
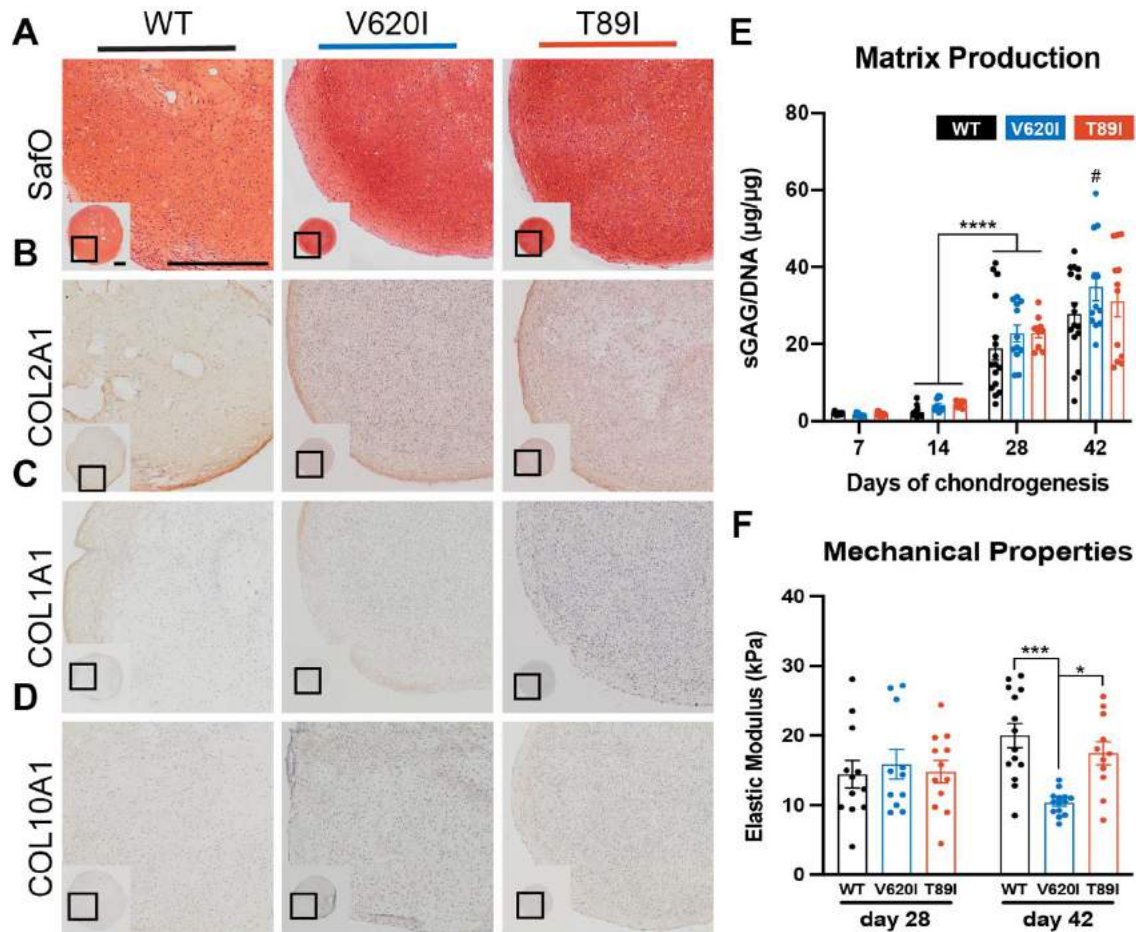
Figure 5.2 Mutant TRPV4 had little effect on chondrogenic matrix production. (**A-D**) WT, V620I, and T89I day-28 pellets exhibit similar matrix production shown by staining for sGAGs with Safranin-O and hematoxylin (**A**) and labeling with IHC for COL2A1 (**B**), COL1A1 (**C**), and COL10A1 (**D**). Scale bar = 500 µm. (**E**) The sGAG/DNA ratio increased in all three lines from day 14 to 28 of chondrogenesis. There were no differences between lines at each time point. Mean ± SEM. n = 11-16 from 3-4 different experiments. ****$p<0.0001$ Statistical significance determined by an ordinary two-way ANOVA with Tukey's post-hoc test. (**F**) There were no differences in the elastic modulus of the matrix at day 28. Day-42 V620I had a significantly lower elastic modulus than WT and T89I. Mean ± SEM. n=11-14 from 3 experiments. *$p<0.05$, ***$p<0.001$ Statistical significance determined by an ordinary two-way ANOVA with Tukey's post-hoc test.

5.4.3 TRPV4 mutations altered chondrogenic gene expression in hiPSC-derived chondrocytes

RT-qPCR analysis throughout differentiation shows that mutants had higher *ACAN* expression compared to WT at day 28; however, expression decreased at day 42 in T89I (day-42 fold changes; V620I: 5933 vs. WT: 2687, p=0.0016 and T89I: 2631, p=0.0058; Figure 5.3A).

205

COL2A1 expression was similar among the three lines at day 28 but significantly lower in T89I at day 42 (day-42 fold changes; T89I: 2798 vs. WT: 9209, p=0.0144 and V620I: 7177, p=0.0007; Figure 5.3B). Throughout chondrogenesis, V620I significantly increased expression of chondrogenic transcription factor *SOX9* (day-42 fold changes; V620I: 195.3 vs. WT: 44.29, p<0.0001 and T89I: 32.19, p=0.0003; Figure 5.3C) and *TRPV4* (day-42 fold changes; V620I: 168.5 vs. WT: 48.82, p<0.0001 and T89I: 44.72, p<0.0001; Figure 5.3D). On the other hand, T89I significantly increased expression of pro-inflammatory, calcium binding protein *S100B* (*56*) throughout chondrogenesis (day-42 fold changes; T89I: 1363 vs. WT: 362.0, p=0.0018 and V620I: 507.8, p=0.0439; Figure 5.3E). T89I also had significantly higher expression of fibrocartilage marker *COL1A1* at days 7, 14, and 28 than the other two lines, and both mutations had increased expression at day 42 compared to WT (day-42 fold changes; WT: 32.47 vs. V620I: 76.42, p=0.01.58 and T89I: 74.23, p=0.0132; Figure 5.3F). In contrast, hypertrophic marker *COL10A1* was significantly higher in the WT line than the mutants at days 28 and 42 (day-42 fold changes; WT: 615.7 vs. V620I: 71.00, p=0.0001 and T89I: 83.07, p=0.0015; Figure 5.3G). Surprisingly, there was not a significant increase in follistatin (*FST*) expression in mutants at later time points (day-42 fold changes; WT: 0.5342 vs. V620I: 0.6808, p=0.6882 and T89I: 0.3158, p>0.9999; Figure 5.3H).
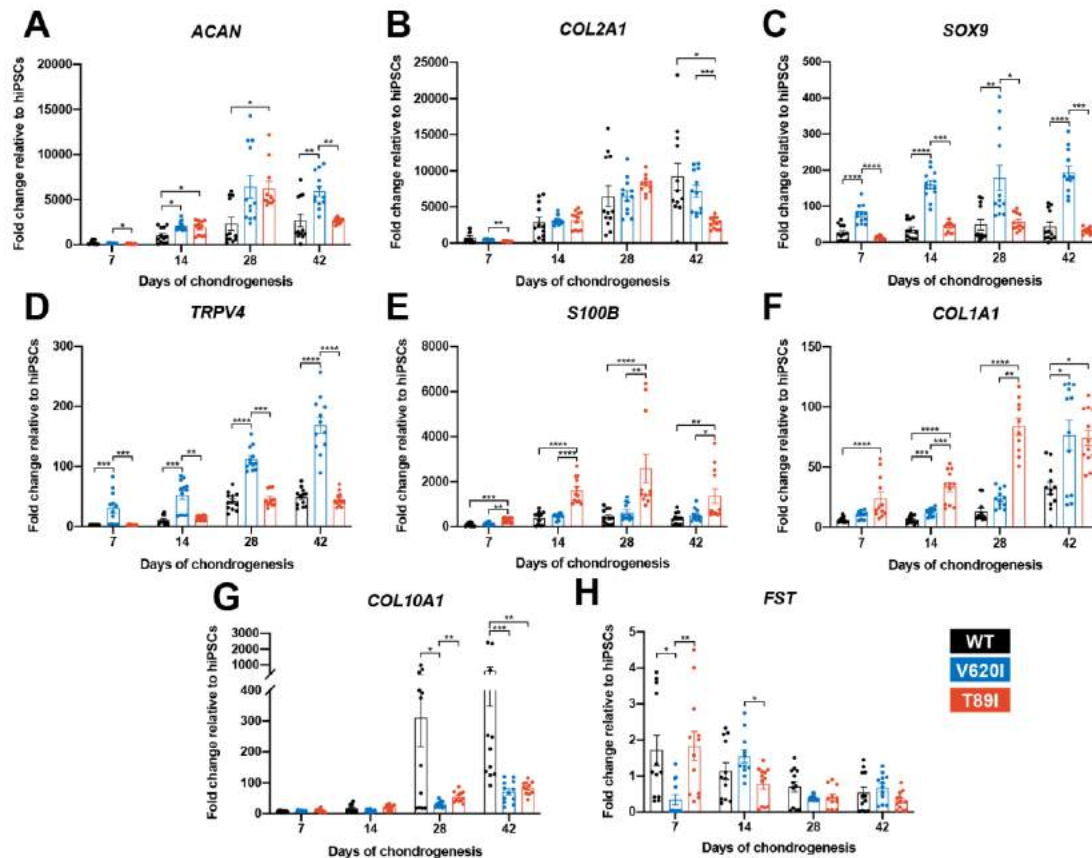
Figure 5.3 V620I and T89I had differing effects on gene expression during chondrogenic differentiation. (**A**) T89I and V620I had increased *ACAN* gene expression at day 28 and 42, respectively, compared to WT. (**B**) Day-42 T89I chondrocytes had decreased expression of *COL2A1*. (**C-D**) V620I increased expression of *SOX9* (C) and *TRPV4* (D) throughout chondrogenesis. (**E-F**) T89I increased expression of *S100B* (E) and *COL1A1* (F) throughout chondrogenesis. (**G**) Both mutations decreased *COL10A1* gene expression at day 28 and 42, compared to WT. (**H**) There were no differences in *FST* expression at later time points day 28 and 42. Mean ± SEM. n=10-12. *p<0.05, **p<0.01, ***p<0.001, ****p<0.0001 Significance determined by one-way ANOVA with Tukey's post-hoc test for each time point.

To obtain comprehensive transcriptomic profiles of WT and TRPV4 mutated cell lines, we performed bulk RNA sequencing of day-28 chondrogenic pellets. We compared V620I and T89I gene expression to WT and plotted the log$_2$ fold change in heatmaps (Figure 5.4A-B). While many chondrogenic and hypertrophic genes had similar levels of expression between the lines, the mutants had increased expression of cartilage ECM genes cartilage oligomeric matrix protein (*COMP*), collage type 6 alpha chains 1 and 3 (*COL6A1, COL6A3*), growth differentiation

factor 5 (*GDF5*), high-temperature requirement A serine peptidase 1 *(HTRA1),* and secreted

protein acidic and cysteine rich (*SPARC)* (Figure 5.4A). In contrast, the mutants had decreased

expression of hypertrophic markers *COL10A1,* secreted phosphoprotein 1 *(SPP1),* and alkaline

phosphatase, biomineralization associated (*ALPL)* in addition to *SST* (Figure 5.4B). The

mutations up-regulated expression levels of bone morphogenic protein 6 (*BMP6*), transforming

growth factor 3 (*TGFB3)*, nuclear factor of activated T-Cells C2 (*NFATC2*), Twist family BHLH

transcription factor 1 (*TWIST1*), ADAM metallopeptidase with thrombospondin type 1 motif 4

(*ADAMTS4*), and *Wnt3A* (Figure 5.4B). The mutations also downregulated osteoblastogenesis

transcription factors *SOX2* and *SOX11* and previously identified genes governing off-target

differentiation during hiPSC chondrogenesis including nestin (*NES),* orthodenticle homeobox 2

(*OTX2), Wnt7A,* and *Wnt7B* (Figure 5.4B)*.* Interestingly, *BMP4* was downregulated to a greater

extent in V620I than T89I when compared to WT.

5.4.4 V620I and T89I mutants demonstrate similar gene expression profiles

First, to evaluate the similarities and differences in transcriptomic profiles between the hiPSC-

derived chondrocytes with and without the TRPV4 mutations, we computed the Euclidean

distance between day-28 samples of each cell line. The WT samples clustered away from the

mutants, and the V620I samples were the most variable. (Figure 5.4C). In terms of total

differentially expressed genes (DEGs) compared to WT, V620I had 8% fewer DEGs than T89I

(2459 vs. 2671; Figure 5.4D). Mutants had only about half of the number of up-regulated genes

compared to down-regulated genes (V620I: 884 vs. 1575, T89I: 978 vs. 1693; Figure 5.4D). The

majority of the down-regulated DEGs were shared between the two mutants when compared to

WT, comprising 76% and 71% of V620I's and T89I's total down-regulated DEGs, respectively

(Figure 5.4E). We plotted the top 25 most down-regulated DEGs for each line in a heatmap.

These included antioxidant catalase (*CAT*), anti-inflammatory nucleotide-binding and leucine-rich repeat receptor family pyrin domain containing 2 (*NLRP2),* and kruppel like factor 8 *(KLF8)* (Figure 5.4F)*.* Interestingly, many of the down-regulated DEGs, both unique and shared between V620I and T89I, were associated with Gene Ontology (GO) terms related to nervous system development, including many potassium channel genes (i.e., *KCN* family; Figure 5.4G).

In contrast, 686 up-regulated DEGs were shared by both mutants, while 22% of V620I's and 30% of T89I's up-regulated DEGs were unique to each mutation (198 vs. 292; Figure 5.4H). A heatmap of the top 25 up-regulated DEGs showed that several homeobox (HOX) genes were highly expressed in chondrocytes with the TRPV4 mutations (Figure 5.4I). These included *HOXA2* to *HOXA7, HOXA-AS2, HOXB2* to *HOXB4,* and *HOXB-AS1,* which are associated with morphogenesis and anterior patterning (*57*). Furthermore, the shared, up-regulated DEGs between two mutants are associated with extracellular matrix production and organization and growth factor binding in GO term analysis, while V620I genes were associated with type I interferon (Figure 5.4J). These data highlight an early morphogenic genetic profile in hiPSC-derived chondrocytes with the V620I and T89I mutations.

5.4.5 The severe T89I mutation inhibits chondrocyte hypertrophy more than moderate V620I mutation

Following an additional 4 weeks of chondrogenic culture, we performed RNA sequencing to investigate how the differences between the WT and the two mutants change with further differentiation. Using Euclidean distances, we compared the WT, V620I, and T89I hiPSC-derived chondrocytes at both day 28 and 56 (Figure 5.4K). WT clustered together at both day 28 and 56; however, the mutants clustered by time point. Again, there were more down-regulated genes than up-regulated at day 56 (Figure 5.4L). T89I had the most DEGs, and the number increased from day 28 to 56. In contrast, V620I's DEGs decreased at day 56. 74% of V620I up-

regulated DEGs, but only 24% of T89I DEGs, were shared between the two lines (424 total

genes; Figure 5.4M). These intersecting, up-regulated genes were associated with the biological

processes of skeletal development, morphogenesis, and patterning due to the up-regulation of

many *HOX* genes (Figure S5.1A). Most of the top up- and down-regulated genes were consistent

between day 28 and 56 (Figure S5.1A-B), including both anterior and posterior *HOX* genes (i.e.,

HOXA1 to *HOXA7, HOXB2* to *HOXB4, HOXB6* to *HOXB8, HOXC4, HOXD8, HOXA-AS2-3,*

and *HOXB-AS1-2*)(*57*). Although V620I and T89I TRPV4 mutants continued to share the up-

regulated *HOX* genes, which may be responsible for dysfunctional chondrogenic hypertrophy

compared to WT cells, our results also indicate that these two mutated lines started to

demonstrate divergent transcriptomic profiles in later chondrogenesis.
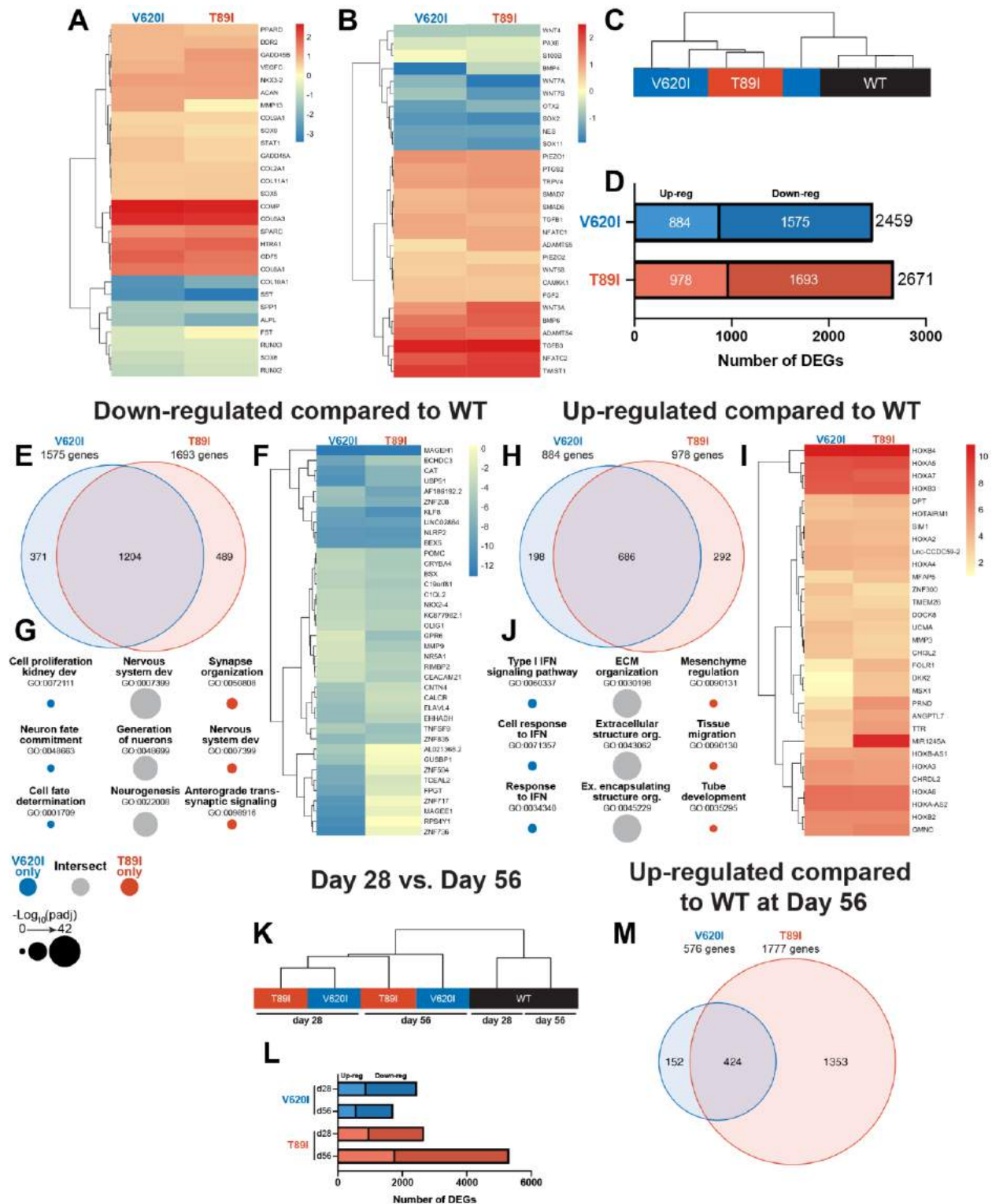
Figure 5.4 Dynamic changes in transcriptomic profiles of V620I and T89I mutants during chondrogenesis. (**A-B**) Heatmaps comparing the $\log_2$ fold change of common chondrogenic and hypertrophic genes (**A**) and growth factor and signaling genes (**B**) in day-28 V620I and T89I

chondrocytes compared to WT. (**C**) Clustering of the samples using Euclidean distances reveals that V620I and T89I hiPSC-derived chondrocytes are more similar to each other than WT. (**D**) The number of up- and down-regulated DEGs in V620I and T89I day-28 chondrocytes compared to WT. (**E-G**) Analysis of the down-regulated genes compared to WT. (**E**) A Venn diagram reveals the number of similar and different down-regulated DEGs between V620I and T89I, where most genes are shared. (**F**) A heatmap showing the $\log_2$ fold change, compared to WT, of the top 25 down-regulated genes for each line. (**G**) The top 3 GO Terms (biological process) associated with the DEGs unique to V620I, shared between V620I and T89I, and unique to T89I. (**H-J**) Analysis of the up-regulated genes compared to WT. (**H**) A Venn diagram reveals the number of similar and different up-regulated DEGs between V620I and T89I, where most genes are shared. (**I**) A heatmap showing the $\log_2$ fold change, compared to WT, of the top 25 up-regulated genes for each line. (**J**) The top 3 GO Terms (biological process) associated with the DEGs unique to V620I, shared between V620I and T89I, and unique to T89I. (**K**) Clustering of the day-28 and day-56 samples using Euclidean distances reveals that the WT chondrocytes, at both day 28 and 56, cluster together while mutants cluster by time point. (**L**) The number of up-regulated and down-regulated DEGs for V620I and T89I compared to WT at day 28 and day 56. (**M**) A Venn diagram reveals the number of similar and different up-regulated DEGs between V620I and T89I, with T89I becoming more unique at day 56.

5.4.6 TRPV4 mutations exhibit dysregulated BMP4-induced chondrocyte hypertrophy

To evaluate how TRPV4 mutations may affect hypertrophy, BMP4 was added to the

chondrogenic medium with and without TGFβ3 to stimulate hypertrophic differentiation starting

at day 28 of chondrogenic pellet culture (*58*). At day 56, Safranin-O staining indicated the

BMP4-treated WT had developed a more hypertrophic phenotype compared to TGFβ3- and

TGFβ3+BMP4-treated pellets with enlarged chondrocytes (cell diameter; WT-BMP4: 27.6 µm

vs. WT-TGFβ3: 11.8 µm, V620I-BMP4: 12.5 µm, and T89I-BMP4: 11.3 µm; p<0.0001; Figure

5.5A-B). This phenotype was not present in any of the groups from the V620I and T89I lines.

Western blot further confirmed this with an increase in hypertrophic cartilage protein COL10A1

secretion in the WT-BMP4 group (Figure 5.5C), consistent with the day-28 gene expression data

(Figure 5.3G, 5.4A). RNA sequencing and PCA revealed that the WT line was more sensitive to

BMP4, as indicated by the arrows (Figure 5.5D). Given that the BMP4-treated WT

chondrocytes had the most apparent hypertrophic phenotype, later analyses were performed

comparing the BMP4- and TGFβ3-treated chondrocytes for simplification.
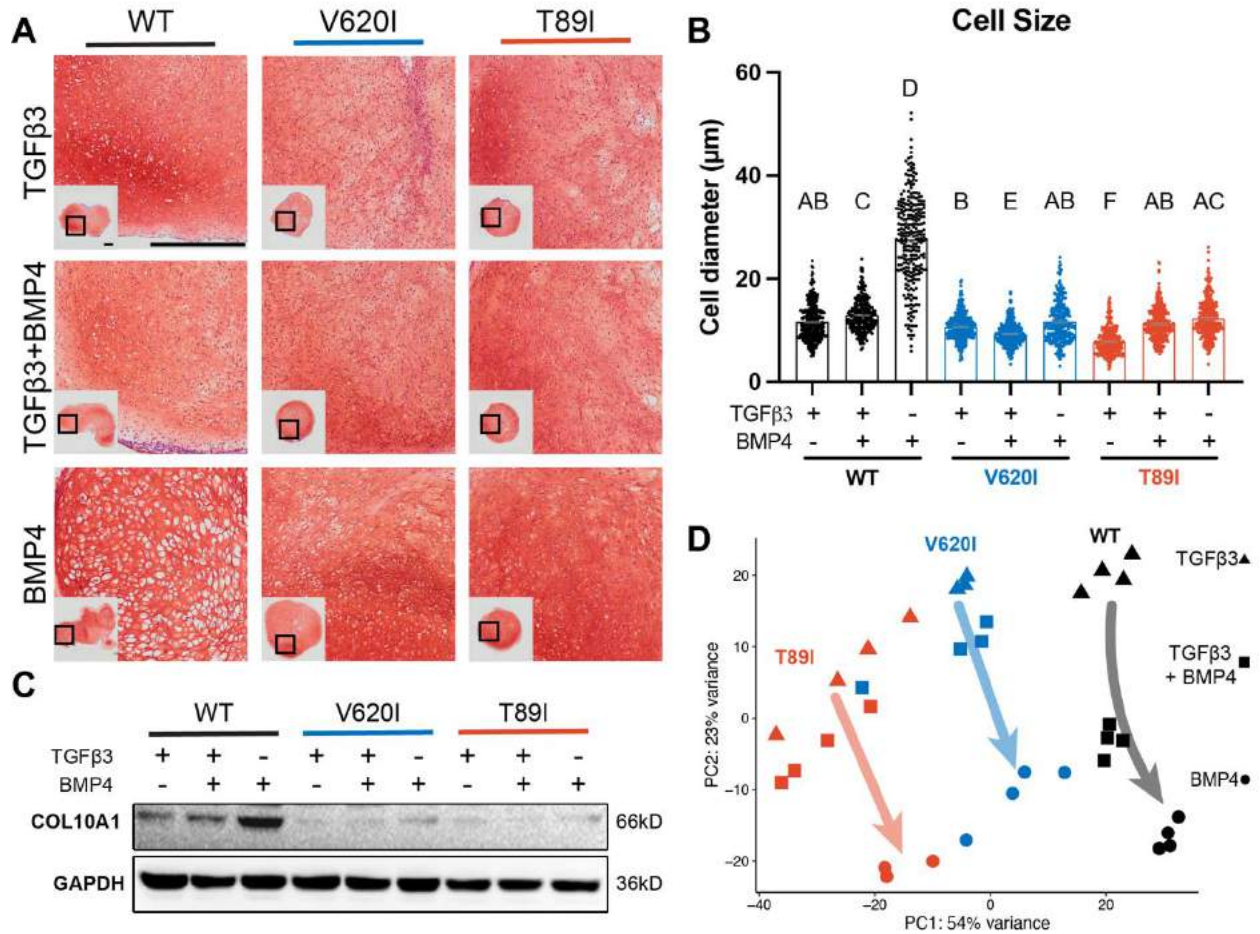
Figure 5.5 WT chondrocytes are more sensitive to BMP4 treatment. (**A**) WT chondrocytes treated with BMP4 developed a hypertrophic phenotype with enlarged lacunae, which was not present in the mutant cell lines or other conditions, as shown by Safranin-O and hematoxylin staining. Scale bar = 500 µm. (**B**) Cell diameter was significantly increased in the WT with BMP4 treatment compared to all other groups indicating a hypertrophic phenotype. Mean ± SEM. n = 249-304 cells from 2 pellets. Different letters indicate statistical significance (p<0.05) between groups as determined by Kruskal-Wallis test with multiple comparisons since data was not normally distributed. (**C**) Western blot shows that WT had increased production COL10A1 in response to BMP4 treatment. (**D**) PCA of bulk RNA-seq reveals an increased sensitivity to BMP4 (and TGFβ3+BMP4) treatment in WT hiPSC-derived chondrocytes compared to V620I and T89I.

Hierarchical K-means clustering of gene expression profiles of BMP4- and TGFβ3-treated chondrocytes resulted in 9 unique clusters, as determined using the gap statistics method (Figure 5.6A). Most of the clusters, including the largest (i.e., cluster 1), showed up-regulation of gene expression with BMP4 treatment, while clusters 4, 5, and 9 showed down regulation. The

gene expression per group for each cluster is listed in Table S5.1. Overall, WT responded to BMP4 treatment with the largest number of DEGs, over 2500, with only 22% of them shared among all three lines (Figure 5.6B). Although cluster 1 shows an overall increase in gene expression with BMP4 treatment, WT had a larger increase in expression than the mutants (Figure 5.6C). In fact, some of the genes that were up-regulated with BMP4 treatment in WT may have no change or down-regulation in mutants (cluster 1, Figure 5.6A).

As cluster 1 represents the primary response to BMP4 treatment and may highlight how the TRPV4 mutations inhibit chondrocyte hypertrophy, we constructed a gene network of this cluster (Figure 5.6D). The log fold change of each gene per cell line is represented by a color scale, which is consistent with WT having overall higher expression of the genes (as indicated by the white arrows in the legend; Figure 5.6D). With GO term analysis, the cluster 1 gene network is highly associated with ossification, biomineral tissue development, skeletal system development, tissue development, and osteoblast differentiation (Figure 5.6D). Alkaline phosphatase, biomineralization associated (*ALPL*), amelogenin X-linked (*AMELX*), fibroblast growth factor receptor 3 (*FGFR3*), interferon induced transmembrane protein 5 (*IFITM5*), Indian hedgehog (*IHH*), parathyroid hormone 1 receptor (*PTH1R*), and noggin (*NOG*) were connected to at least 4 of the top 5 GO terms. Of those, *ALPL, AMELX,* and *IFITM5* showed much higher expression in WT than the mutants alongside antioxidant glutathione S-transferase alpha 1 (*GSTA1*) and bone ECM proteins integrin binding sialoprotein (*IBSP*) and matrix extracellular phosphoglycoprotein (*MEPE*). Lack of expression of these key genes may be responsible for the inhibited hypertrophy in TRPV4 V620I- and T89I-mutated chondrocytes.

We next investigated and plotted the top 25 up-regulated genes for each line with BMP4 treatment (compared to their respective TGFβ3 control) (Figure 5.6E). 88% of these genes were

also present in cluster 1. The key genes *ALPL, AMELX, IFITM5, GSTAI, IBSP*, and *MEPE* had

distinctly higher expression in WT than mutants, in agreement with the network analysis. Both

mutants showed higher expression than WT of ankyrin repeat and SOCS box containing 10

(*ASB10),* GTPase, IMAP family member 6 (*GIMAP6),* and adhesion G protein-coupled receptor

D1 (*ADGRD1*) when compared to their corresponding TGFβ3 control group. GO term analysis

was further performed on all BMP4 up-regulated DEGs for each line (Figure 5.6F). WT was

highly associated with skeletal system development, ossification, endochondral ossification, and

extracellular structure organization, followed by V620I mutants, while T89I showed little to no

association with these concepts.

A

Clusters:

B Total DEGs

C Cluster 1

D Cluster 1

E Top up-regulated DEGs

F Gene Ontology and Biological Pathways
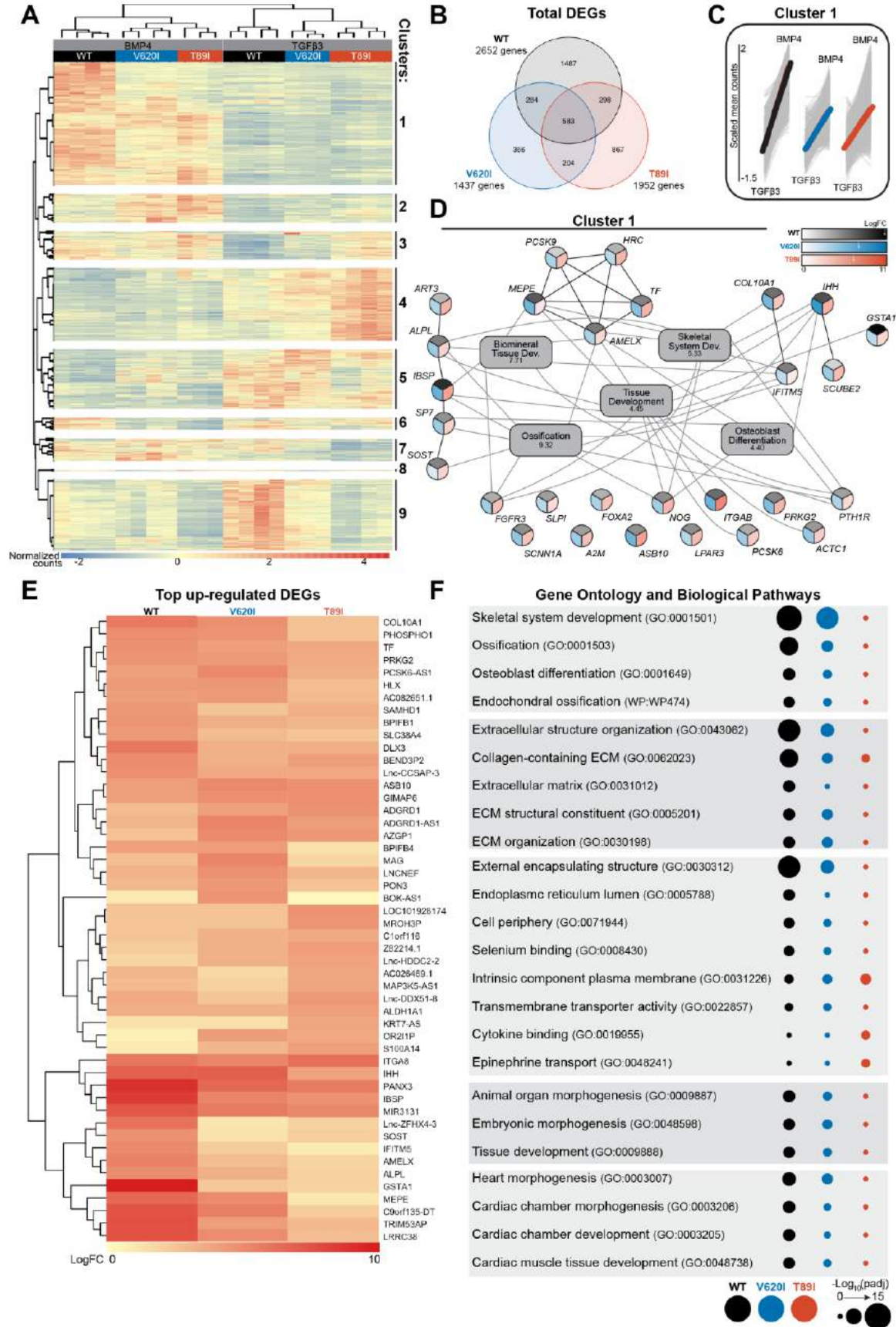
Figure 5.6 V620I and T89I had an inhibited hypertrophic response to BMP4 treatment. (**A**) There are 9 clusters of genes based on expression and hierarchical k-means clustering of the samples. (**B**) Venn diagram shows similar and distinct DEGs in response to BMP4 treatment in all three lines. (**C**) Cluster 1 represented increasing in expression from TGFβ3-treatment to BMP4-treatment (left to right on x-axis). Y-axis scale (-1.5 to 2) represents the scaled mean counts. (**D**) A protein-protein interaction network with functional enrichment analysis of cluster 1 reveals the top regulating genes and their associated concepts. Connections between protein-coding genes and GO processes are based on the average log fold change between cell lines. Coloring of the protein-coding gene circles is divided into three to represent the log fold change for each cell line as shown in the legend. The white arrows in the legend indicates the location of the maximum log fold change for each respective cell line. The grey boxes represent the top 5 GO terms (biological process) identified for the network with the $\log_{10}$(false discovery rate) underneath the term. (**E**) A heatmap of the top 25 up-regulated genes, and their $\log_2$ fold change, in each line compared to their respective TGFβ3 controls. (**F**) The top GO terms and biological pathways associated with the up-regulated DEGs with BMP4 treatment. Symbol color represents the cell line, and size represents the $-\text{Log}_{10}(p_{adj})$.

5.5 Discussion

To elucidate the detailed molecular mechanisms underlying the distinct severity of skeletal dysplasias caused by two TRPV4 mutations (brachyolmia-causing V620I vs. metatropic dysplasia-causing T89I), we used CRISPR-Cas9 gene editing to generate hiPSC-derived chondrocytes bearing these two mutations. We observed that day-28 chondrocytes exhibited differences in channel function and gene expression between the mutants and WT control. Differences in transcriptomic profiles between V620I and T89I and from WT became more apparent with maturation following 4 additional weeks of culture with TGFβ3 or hypertrophic differentiation with BMP4 treatment. Of note, WT was significantly more sensitive to BMP4-induced hypertrophy. At the transcriptomic level, TRPV4 mutations inhibited chondrocyte hypertrophy, particularly with the T89I mutation, whereas V620I exhibited a milder phenotype, consistent with the clinical presentation of these two conditions. Our results suggest that skeletal dysplasias may be, at least in part, resulting from improper chondrocyte hypertrophy downstream of altered TRPV4 function. Furthermore, with our genome-wide RNA sequencing analysis, we also identified several putative genes that may be responsible for these dysregulated pathways in

human chondrocytes bearing V620I or T89I TRPV4 mutations.

Our findings are generally consistent with previous non-human models of V620I and T89I mutations. Two other models that have studied the V620I and T89I mutations include *X. laevis* oocytes injected with rat TRPV4 cRNA (*11*) or primary porcine chondrocytes transfected with human mutant TRPV4 (*12*). Both reports and our current study investigated the baseline currents of the mutant TRPV4 compared to WT. Here, we used patch clamping and observed high basal currents in V620I with a significant decrease when TRPV4 was inhibited. However, this characteristic was trending, but not significant, in T89I, despite both V620I and T89I being reported as gain-of-function mutations (*8, 10*). Both the *X. laevis* oocyte and porcine chondrocyte models confirmed high basal currents through V620I-TRPV4 (*11, 12*). Interestingly, *X. laevis* oocytes, but not the humanized porcine chondrocytes, showed an increase in basal Ca^{2+} signaling through T89I (*11, 12*). Furthermore, our results were consistent with a summary of TRPV4 channelopathies reporting an increase in conductivity in V620I but no change in T89I (*6*). The conflicting basal current results could be due to the species of the TRPV4, but this was not the case regarding channel activation. As mentioned, the hiPSC-derived chondrocytes with V620I and T89I TRPV4 had reduced currents and Ca^{2+} signaling in response to chemical agonist GSK101. However, our previous study showed the porcine chondrocytes with mutant human TRPV4 had increased peak Ca^{2+} signaling in response to hypotonic changes (*12*). This discrepancy could be due to the mode of activation of TRPV4 (i.e., osmotic vs. chemical agonist). In contrast, the oocytes with mutant rat TRPV4 had lower currents in response to both hypotonic and chemical (GSK101) TRPV4 activation compared to WT-TRPV4, consistent with our findings. It can be speculated that there is decreased sensitivity to the antagonist because the mutated hiPSC-derived chondrocytes are compensating for the increased basal activity by

reducing the number of TRPV4 channels, or other ion channels and signaling transducers as shown with the RNAseq data and associated GO terms. The increased basal currents and decreased channel sensitivity to TRPV4 agonist GSK101 with mutated TRPV4 is also likely due to an increased open probability of TRPV4 making the channels less likely to open due to an agonist (*11*). The obvious differences in both resting and activated states confirm functional differences with TRPV4 mutations that may ultimately lead to changes downstream of the channel, which alter joint development and result in skeletal dysplasias.

It was hypothesized, in the porcine chondrocyte study, that the increased Ca^{2+} signaling due to the V620I and T89I TRPV4 mutations increased *FST* expression that inhibited BMP signaling and hypertrophy (*12, 25*). Surprisingly, we found no differences in *FST* expression in mutant hiPSC-derived chondrocytes compared to WT. However, our previous study used non-human cells, which could alter the effects of the human TRPV4 mutations and downstream gene expression. Another previous hypothesis made was that the altered TRPV4 signaling increased *SOX9* expression, a known regulator of resting and proliferating chondrocytes upregulated by TRPV4 activation (*13*), thus decreasing hypertrophy (*8*). *SOX9*-knockin mice exhibit a dwarfism phenotype (*20*), and *SOX9* overexpression inhibits hypertrophy and endochondral ossification (*22, 23*), likely via parathyroid hormone-related protein (PTHrP) (*18, 20*). However, PTHrP was not strongly regulated in our data set. Furthermore, our RT-qPCR revealed that only V602I significantly upregulated *SOX9*, and the RNAseq data showed that *SOX9* had a smaller fold change compared to other chondrogenic genes, such as *GDF5, COL6A1, COL6A3,* and *COMP*. In fact, these genes, which were upregulated in V620I- and T89I-hiPSC-derived chondrocytes, have a pro-chondrogenic but anti-hypertrophic phenotype (*59-61*). Therefore, these results suggest additional and alternative pathways to *FST* and *SOX9* that are responsible for the V620I

and T89I skeletal dysplasias.

Our results are also generally consistent with previous reports on the effects of other TRPV4 mutations such as lethal and non-lethal metatropic dysplasia-causing I604M (*29*) and L619F (*30*). The data also reveal potential differences in the effects of these varying TRPV4 mutations on cell electrophysiology or differentiation. For example, we saw an increase in *SOX9* expression in V620I, while no change in T89I. Gain-of-function mutation L619F also increased *SOX9* expression (*30*), while I604M, which has been reported to not alter conductivity like T89I (*6*), decreased *SOX9* (*29*). I604M also decreased *COL2A1*, *COL10A1*, and *RUNX2* expression consistent with our T89I results (*29*). Intriguingly, the L619F mutation was reported to increase Ca^{2+} signaling with activation via a TRPV4 agonist (*30*). However, we observed that V620I and T89I had significantly reduced Ca^{2+} signaling compared to WT in response to chemical agonist GSK101, as confirmed by both confocal imaging and patch clamping. These results highlight that TRPV4 mutations have heterogeneous effects on downstream signaling pathways and thus lead to diverse disease phenotypes, despite similar classification of these mutations as "gain-of-function." It is also important to note that in previous studies, chondrogenic differentiation of iPSCs (*29*) or dental pulp cells (*30*) were performed in short-term micromass culture, and not long-term pellet culture as in our study, potentially leading to different levels of chondrogenesis and maturation of the cells.

Our transcriptomic analysis showed significant changes in various *HOX* family genes due to TRPV4 mutations, suggesting a potential role of these genes in maintaining the immature, chondrogenic phenotype in the mutated lines. At both day 28 and 56, the top 25 up-regulated genes in the V620I and T89I lines included genes from the anterior *HOX* family (*57, 62*). The high expression of anterior *HOX* genes indicates that the mutants are maintaining the

chondrocytes in an early developmental stage with axial patterning. At day 28 and 56, *HOXA2*, *HOXA3*, and *HOXA4* were in the top upregulated genes, with *HOXA4* having the largest fold change. Interestingly, gain-of-function mutations or overexpression of *HOXA2, HOXA3*, and *HOXA4* impair chondrogenesis, limit skeletal development, decrease endochondral ossification regulators, and delay mineralization in animal models (*57, 63-67*). *HOXA5* was also highly upregulated at both day 28 and 56, and mutations in this gene showed disordered patterning of limb bud development (*68*). Finally, the rib and spine phenotypes associated with brachyolmia and metatropic dysplasia could be contributed to the altered expression of *HOXA4* to *HOXA7* as it has been shown that these genes are associated with rib and spine patterning, and alterations in expression have led to defects (*69, 70*). The only up-regulated posterior *HOX* genes were *HOXC8* and *HOXD8* at day 56 (*57, 62*). The absence of posterior *HOX9, HOX11,* and *HOX13*, which are associated with limb development and hypertrophic *RUNX2/3* expression (*68, 71*), may be at least partially responsible for the improper development in skeletal dysplasias. Interestingly, many links have been identified between *HOX* genes and TGFβ3-family signaling, specifically through SMAD proteins, both within skeletal development and other processes (e.g., murine lung development) (*67, 72, 73*).

In fact, TRPV4 and TGF-β signaling have recently been shown to interact, with effects specific to the order in which they occur (*14, 74, 75*). Consistent with previous finding with hiPSCs housing the I604M TRPV4 mutations (*29*), the altered TRPV4 activity in our hiPSC-derived chondrocytes could be altering their response to the TGFβ3 and BMP4 treatments. Furthermore, the V620I and T89I mutations increased expression of *HTRA1,* which has been shown to bind to and alter the response to members of the TGFβ family (*76*). Furthermore, *TGFβ3* and *TWIST,* which is downstream of TGFβ3-signaling, were both upregulated in TRPV4-

mutated hiPSC-derived chondrocytes. It has been reported that *TGFB3* expression and signaling prevent osteoblastogenesis of mesenchymal stem cells (*18, 21*), while *TWIST* inhibits hypertrophy regulators *RUNX2* and *FGFR2* (*77, 78*). Therefore, another mechanism of hypertrophic dysregulation with these mutations could be altered response to TGFβ family signaling.

Furthermore, significantly lower expression of *ALPL, AMELX, IFITM5, GSTA1, IBSP*, and *MEPE* in mutated chondrocytes compared to WT suggest that mutated cells had altered response to BMP4-induced hypertrophy. Indeed, mutations in *ALPL* have been shown to lead to hypophosphatasia with deformed long bones (*79*), while mutations in *IFITM5* lead to osteogenic imperfecta (*80*). Our results indicate a connection between these genes and delayed endochondral ossification in chondrocytes bearing V620I and T89I mutations; however, how the expression levels of these genes are associated with TRPV4 function and mutations still warrants further investigation.

Another gene increased in BMP4-treated WT, but less in mutants, was *GSTA1,* which produces the antioxidant glutathione (*81, 82*). The TRPV4-mutated chondrocytes also had significant downregulation of catalase (*CAT*), another antioxidizing gene (*82*). Interestingly, BMP4 treatment of T89I-mutated chondrocytes was able to significantly increase *CAT* expression, potentially indicating an association between antioxidant expression and maturation. One study observed that chondrocyte maturation is associated with decreasing catalase (*83*). However, many others report that reactive oxygen species (ROS; e.g., H_2O_2), which can be removed by *CAT* and *GSTA1*, prevent endochondral ossification, potentially via inhibition of the hedgehog pathways (*82, 84, 85*). Interestingly, *IHH* also had the lowest expression level in our T89I mutant chondrocytes. These findings suggest that decreased expression of *CAT* and *GSTA1*

in TRPV4 mutants may also be involved in dysregulating endochondral ossification in these cells.

The decrease in mechanical properties with increased basal current of the V620I mutant was unexpected since TRPV4 activation was previously shown to increase matrix production and properties (*14*). Furthermore, genes uniquely upregulated in V620I were associated with interferon type I (IFNβ). IFNβ has been reported to decrease inflammatory markers and matrix degradation (*86-89*), despite the decrease in moduli observed in the day-42 V620I chondrogenic pellets. Interestingly, a study comparing bone marrow-derived MSCs from healthy and systemic lupus erythematous patients found that IFNβ inhibited osteogenesis via suppression of *RUNX2* and other osteogenic genes (*90*). Highlighting a potential, unique regulator of the delayed hypertrophy in V620I leading to brachyolmia. In contrast, T89I became more unique at later time points of chondrogenesis and was not associated with many of the same biological processes as WT and V620I, especially those regarding endochondral ossification, when treated with BMP4. This, in conjunction with the high number of unique DEGs, represents a potential inhibition of hypertrophy, particularly in response to BMP4 treatment, with the T89I mutation leading to severe metatropic dysplasia.

Here, we present multiple putative genes and pathways that could be involved in delaying, and potentially inhibiting, chondrocyte hypertrophy in V620I- and T89I-TRPV4 mutants. It should be noted, however, that this study has some potential limitations. It is well-recognized that Wnt/β-catenin signaling plays an important role in chondrocyte hypertrophy (*78, 91, 92*). However, we may be preventing some hypertrophy since our chondrogenic protocol uses a pan-Wnt inhibitor to prevent off-target differentiation and promote a homogenous chondrocyte population (*33*). Nevertheless, our WT chondrocytes, but not TRPV4 mutants, exhibited

hypertrophic differentiation with BMP4 treatment, suggesting that DEGs/pathways detected in our sequencing analysis are still robust. Since this study focuses on TRPV4 gain-of-function mutations, future studies could fully or partially inhibit TRPV4 signaling to determine if that would increase similarity between the mutant and WT lines at various stages of chondrogenic and hypertrophic differentiation. Additionally, this study only activated TRPV4 using the pharmacological activator GSK101. Other future experiments could activate the channel osmotically or with mechanical loading to investigate additional differences in TRPV4 function leading to skeletal dysplasias during development.

5.6 Supplemental Figures and Tables
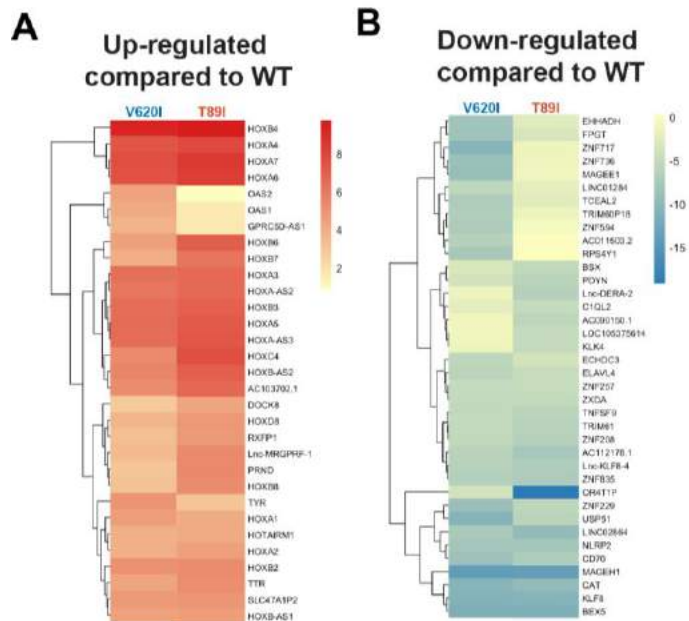
Figure S5.1 Top DEGs of V620I and T89I chondrocytes compared to WT remain from day 28 to day 56. (**A**) The top 25 up-regulated genes, and their $\log_2$ fold change, for day-56 TGFβ3-treated V620I and T89I chondrocytes compared WT. (**B**) The top 25 down-regulated genes, and their $\log_2$ fold change, for day-56 TGFβ3-treated V620I and T89I chondrocytes compared WT.

Table S5.1 Clustering of BMP4 treatment. The top 10 genes of each cluster with normalized gene counts for each group. The top upregulated genes were determined for the group with the highest expression in that cluster: 1 – WT BMP4, 2 – T89I BMP4, 3 – T89I BMP4, 4 – T89I

TGFβ3, 5 – WT TGFβ3, 6 – WT TGFβ3, 7 – V620I BMP4, 8 – T89I BMP4, and 9 – WT TGFβ3. Related to Figure 5.6A.

Ensembl Gene ID	Symbol	WT TGFβ3	WT BMP4	V620I TGFβ3	V620I BMP4	T89I TGFβ3	T89I BMP4
Cluster 1							
ENSG00000136630	*HLX*	-0.4407717	2.0402195	-0.5407056	-0.3272783	-0.535553	-0.4414497
ENSG00000134215	*VAV3*	-0.4322642	2.0374974	-0.5033759	-0.389187	-0.4886749	-0.4664525
ENSG00000154143	*PANX3*	-0.4953438	2.03064846	-0.4974411	-0.3205407	-0.4982932	-0.4578532
ENSG00000162551	*ALPL*	-0.4919204	2.03056528	-0.5327131	-0.2125114	-0.5488725	-0.5036349
ENSG00000103056	*SMPD3*	-0.1974815	2.02602223	-0.5671042	-0.2903093	-0.6396414	-0.6310159
ENSG00000176842	*IRX5*	-0.465913	2.02293985	-0.5606691	-0.2921023	-0.5380299	-0.4085238
ENSG00000170962	*PDGFD*	-0.1915284	2.01873261	-0.659709	-0.4009481	-0.6770205	-0.3392717
ENSG00000153446	*C16orf89*	-0.4773729	2.01744291	-0.5845101	-0.2737777	-0.5435154	-0.3791925
ENSG00000163501	*IHH*	-0.5298648	2.01702244	-0.5431994	-0.2002987	-0.5405259	-0.4519113
ENSG00000101280	*ANGPT4*	-0.5302453	2.01695715	-0.5428197	-0.1350517	-0.603895	-0.4542005
Cluster 2							
ENSG00000134061	*CD180*	-0.4622938	-0.5288295	-0.3577376	-0.3482325	-0.1581304	2.35438578
ENSG00000230815		-0.4489383	-0.8685342	0.18583502	-0.1584488	-0.2552786	2.12243149
ENSG00000267529		-0.444944	-0.8809379	-0.4730726	0.3989153	-0.1495932	1.90848578
ENSG00000250250	*CTD-2350J17.1*	0.24000783	-0.9939455	-0.1426133	-0.1043512	-0.3913171	1.80875466
ENSG00000129422	*MTUS1*	-0.4016571	0.49891994	-0.654169	0.56752143	-1.3036937	1.50604821
ENSG00000231104		0.29347029	-1.0471918	0.46399309	0.15234796	-0.817868	1.42832896
ENSG00000261997		-0.3339501	-0.7616808	-0.1494389	0.64731428	-0.4849139	1.39374618
ENSG00000148680	*HTR7*	0.36576125	-0.0299804	-0.5503075	0.4317182	-1.371105	1.35511546
ENSG00000232903	*LINC01166*	0.37813758	0.11002898	-0.8602688	0.50836176	-1.3454177	1.32545463
ENSG00000243175	*RPSAP36*	0.13741559	-0.890453	-0.0641273	0.59088704	-0.7695273	1.30636422
Cluster 3							
ENSG00000162078	*ZG16B*	-0.8551802	-0.1800379	-0.930196	0.12377608	0.12377608	1.98041735

ENSG00000116455	WDR77	-1.2364286	-0.3366992	-0.5494202	0.15785895	0.34689005	1.97392514
ENSG00000170006	TMEM154	-1.2573605	-0.0147801	-0.5923283	0.10134896	0.15941346	1.94083253
ENSG00000136943	CTSV	-0.8907691	-0.6416754	-0.7378985	0.30115571	0.41522664	1.82598136
ENSG00000171428	NAT1	-0.9289641	-0.097933	-0.8605664	0.29193349	0.12777919	1.67014557
ENSG00000169504	CLIC4	-1.4859539	0.13092627	-0.3119891	0.22835859	0.11867718	1.65597823
ENSG00000153029	MR1	-1.4531496	-0.1979707	-0.5965094	0.31339853	0.56036661	1.63298287
ENSG00000155918	RAET1L	-0.6734798	-1.1691676	-0.4812131	0.34493311	0.64234574	1.62170451
ENSG00000114450	GNB4	-1.3812791	0.4524834	-0.3327172	0.18743492	-0.2225245	1.61789756
ENSG00000203392		-0.880589	-0.5792242	-0.9690578	0.62794695	0.35569132	1.60395769

Cluster 4

ENSG00000142661	MYOM3	-0.1800364	-0.5676659	-0.3980397	-0.6631954	2.02449127	-0.420085
ENSG00000265190	ANXA8	-0.4662521	-0.6012199	-0.2862952	-0.5472328	2.01715398	-0.2503038
ENSG00000188015	S100A3	-0.4862037	-0.7025085	-0.2076937	-0.4734799	2.01614534	-0.2642439
ENSG00000164764	SBSPON	-0.6366146	-0.4165159	-0.5056698	-0.4938291	2.01153508	-0.1137641
ENSG00000065325	GLP2R	-0.4285246	-0.7675511	-0.1872943	-0.5589194	2.00985763	-0.1525224
ENSG00000196154	S100A4	-0.3852601	-0.5834099	0.04349122	-0.6381075	2.0018262	-0.5702228
ENSG00000007171	NOS2	-0.3798747	-0.5060131	-0.2511371	-0.4794094	2.00161854	-0.5972914
ENSG00000174946	GPR171	-0.2568739	-0.6297553	-0.0524796	-0.6711866	2.00113036	-0.5386065
ENSG00000214688	C10orf105	-0.4068724	-0.7431708	-0.1763876	-0.3974435	1.99436058	-0.4194443
ENSG00000177283	FZD8	-0.396451	-0.7014113	-0.0357477	-0.6369388	1.98680373	-0.3002558

Cluster 5

ENSG00000244953		1.93036295	-0.4874654	-0.1516559	-0.4744663	-0.42247	-0.5762924
ENSG00000125869	LAMP5	1.9113851	-0.3544688	-0.2506172	-0.5999363	-0.2128529	-0.7415522
ENSG00000259881	LOC101927793	1.88877557	-0.4321825	0.15904637	-0.4519634	-0.4255889	-0.9311006
ENSG00000263155	MYZAP	1.84143074	-0.751481	-0.3599587	-0.5963496	-0.0644702	-0.2122145
ENSG00000141750	STAC2	1.75760823	-0.8245062	-0.3863292	-0.6367161	0.24311552	-0.3330061
ENSG00000101938	CHRDL1	1.72579926	-0.1375551	-0.2522428	-0.8218159	0.09439777	-0.8955253

ENSG00000120057	SFRP5	1.70244888	-0.2222804	0.03070915	-0.944713	0.20955956	-1.0240626
ENSG00000139292	LGR5	1.65667334	-0.5917232	0.15125745	-0.8029446	0.11975952	-0.6602775
ENSG00000270228		1.64512369	-0.0663858	-0.3402273	-0.0663858	-0.1804865	-1.4355934
ENSG00000106327	TFR2	1.64094873	-0.7710817	0.04517224	-0.4726389	0.42422017	-1.1404366

Cluster 6

ENSG00000185742	C11orf87	1.54928318	0.52412284	-0.068401	-0.5339555	-0.6750326	-1.0841562
ENSG00000122254	HS3ST2	1.54484352	0.69539965	-0.1085645	-0.4269226	-0.8670489	-1.1531311
ENSG00000125804	FAM182A	1.49677851	0.46950232	0.61491584	-0.6562798	-0.9517976	-1.0925204
ENSG00000184828	ZBTB7C	1.48468335	0.81548377	-0.2924263	-0.6119857	-0.6213616	-1.1300001
ENSG00000239268		1.47666919	0.59588969	0.12571513	-0.7540006	-0.5880567	-1.0997172
ENSG00000129151	BBOX1	1.41603923	0.14942686	-0.1857581	-0.6965929	0.00922931	-0.9850453
ENSG00000187135	VSTM2B	1.37532225	0.98960864	-0.5246744	-0.5675315	-0.6103885	-1.0580068
ENSG00000133636	NTS	1.34744728	0.67247136	-0.4800385	-0.4433051	-0.4708552	-0.9943059
ENSG00000184492	FOXD4L1	1.33955469	0.06928731	-0.3541351	-0.9151699	0.51388089	-0.9892688
ENSG00000243319	FGF14-IT1	1.31866392	0.56172241	0.18599419	-0.3268611	-1.273038	-0.5599772

Cluster 7

ENSG00000183644	HOATZ	-0.8453249	-0.4201194	-0.3940103	1.73947729	-0.10681	-0.0956204
ENSG00000154342	Wnt3A	-1.0716829	-0.5651792	-0.01912	1.72421754	-0.2873257	0.28574702
ENSG00000138356	AOX1	-0.7979798	-0.4018139	-0.6671427	1.7178925	-0.6232867	0.80739331
ENSG00000141448	GATA6	-1.0975583	-0.402573	0.21816165	1.71356796	-0.3802979	0.00432003
ENSG00000189001	SBSN	-1.1766072	-0.414439	0.04404355	1.69481709	0.06058673	-0.263187
ENSG00000152669	CCNO	-1.0056734	-0.2531982	-0.0784151	1.67736047	-0.4030122	0.05777953
ENSG00000120949	TNFRSF8	-0.8457057	-0.525458	-0.5571943	1.67473023	-0.5462308	0.88074675
ENSG00000256673		-0.7951926	-0.4642983	-0.5650053	1.66493452	-0.6800989	0.9312124
ENSG00000212993	POU5F1B	-0.8110902	-0.48146	-0.3129823	1.6501491	-0.3276325	0.27302709
ENSG00000115363	EVA1A	-1.3417184	-0.2438053	-0.5302174	1.60919416	0.35505632	0.02524845

Cluster 8

ENSG00000154080	CHST9	0.79674683	-0.3558075	-0.6039268	-0.8960673	-0.4158364	1.76521261
ENSG00000109193	SULT1E1	-0.2211121	0.92346818	-1.0657016	-0.7472498	-0.3088017	1.5372955
ENSG00000268089	GABRQ	1.05785547	0.0056823	-0.5794371	-0.4526902	-1.1845235	1.34433826
ENSG00000129159	KCNC1	1.14171692	-0.402278	-0.2372079	-0.0078783	-1.3714752	1.09042729
ENSG00000162645	GBP2	1.23597668	-0.4515684	0.04491227	-0.5396142	-1.060552	1.042765
ENSG00000164093	PITX2	-0.1260545	1.24124219	-1.0665402	-1.0719021	0.1184503	0.85089238
ENSG00000129824	RPS4Y1	0.35003319	0.82149811	-1.3769648	-1.3832455	0.60788477	0.8487374
ENSG00000175084	DES	1.28288386	-0.2443785	-1.1495016	-1.0843542	0.30456241	0.80455019

Cluster 9

ENSG00000171722	SPATA46	1.97614501	-0.3838787	0.08643424	-0.5006111	-0.6071928	-0.732384
ENSG00000087250	MT3	1.97175135	-0.2804736	-0.0235548	-0.5370286	-0.5806975	-0.7411808
ENSG00000146360	GPR6	1.96269185	-0.2126427	0.00307151	-0.5245186	-0.6531674	-0.7662224
ENSG00000257126		1.94280226	-0.1402269	-0.232513	-0.57529	-0.5621063	-0.6543924
ENSG00000115155	OTOF	1.936001	-0.0992158	-0.3563582	-0.3942778	-0.6555677	-0.6928948
ENSG00000100078	PLA2G3	1.93320458	-0.2334559	0.10590057	-0.4635004	-0.6641775	-0.8686616
ENSG00000144119	C1QL2	1.93116843	-0.3228628	-0.1106777	-0.4724358	-0.6324442	-0.5605564
ENSG00000186960	LINC01551	1.92885289	-0.2396521	-0.1617074	-0.512869	-0.5768657	-0.6375806
ENSG00000105509	HAS1	1.92860762	0.15041891	-0.5956422	-0.5807668	-0.4880813	-0.7512624
ENSG00000127329	PTPRB	1.92160498	0.00830095	-0.3770758	-0.5227041	-0.6449196	-0.6393005

5.7 Conclusion

In summary, our study found that dysregulated skeletal development in the V620I- and T89I-TRPV4 dysplasias is likely due, at least in part, to delayed and inhibited chondrocyte hypertrophy. The gain-of-function mutations may lead to increased *HOX* gene expression, altered TGFβ signaling, decreased hypertrophic and biomineralization gene expression (e.g., *ALPL, AMELX, IFITM5, IBSP*, and *MEPE*), and genes regulating hedgehog pathways and ROS accumulation (e.g., *GSTA1, CAT*). These findings lay a foundation for the development of

therapeutics for these diseases and give insights into the regulation of endochondral ossification

via TRPV4.

5.8 References

1. A. Superti-Furga, S. Unger, Nosology and classification of genetic skeletal disorders: 2006 revision. *Am J Med Genet A* 143A, 1-18 (2007).

2. D. Krakow, D. L. Rimoin, The skeletal dysplasias. *Genet. Med.* 12, 327-341 (2010).

3. A.-V. Ngo, M. Thapa, J. Otjen, S. Kamps, Skeletal Dysplasias: Radiologic Approach with Common and Notable Entities. *Seminars in Musculoskeletal Radiology* 22, 066-080 (2018).

4. S. F. Nemec *et al.*, The importance of conventional radiography in the mutational analysis of skeletal dysplasias (the TRPV4 mutational family). *Pediatr. Radiol.* 42, 15-23 (2012).

5. I. M. Orioli, E. E. Castilla, J. G. Barbosa-Neto, The birth prevalence rates for the skeletal dysplasias. *J. Med. Genet.* 23, 328-332 (1986).

6. S. Sun, in *Mutagenesis,* Kang, Ed. (InTech, 2012).

7. E. Andreucci *et al.*, TRPV4 related skeletal dysplasias: a phenotypic spectrum highlighted byclinical, radiographic, and molecular studies in 21 new families. *Orphanet J. Rare Dis.* 6, 37 (2011).

8. M. J. Rock *et al.*, Gain-of-function mutations in TRPV4 cause autosomal dominant brachyolmia. *Nat. Genet.* 40, 999-1003 (2008).

9. S. S. Kang, S. H. Shin, C.-K. Auh, J. Chun, Human skeletal dysplasia caused by a constitutive activated transient receptor potential vanilloid 4 (TRPV4) cation channel mutation. *Exp. Mol. Med.* 44, 707 (2012).

10. N. Camacho *et al.*, Dominant TRPV4 mutations in nonlethal and lethal metatropic dysplasia. *Am J Med Genet A* 152A, 1169-1177 (2010).

11. S. Loukin, Z. Su, C. Kung, Increased basal activity is a key determinant in the severity of human skeletal dysplasia caused by TRPV4 mutations. *PLoS One* 6, e19533 (2011).

12. H. A. Leddy *et al.*, Follistatin in chondrocytes: the link between TRPV4 channelopathies and skeletal malformations. *FASEB J.* 28, 2525-2537 (2014).

13. S. Muramatsu *et al.*, Functional gene screening system identified TRPV4 as a regulator of chondrogenic differentiation. *J. Biol. Chem.* 282, 32158-32167 (2007).

14. C. J. O'Conor, H. A. Leddy, H. C. Benefield, W. B. Liedtke, F. Guilak, TRPV4-mediated mechanotransduction regulates the metabolic response of chondrocytes to dynamic loading. *Proc. Natl. Acad. Sci. U. S. A.* 111, 1316-1321 (2014).

15. D. L. Rimoin *et al.*, The Skeletal Dysplasias: Clinical Molecular Correlations. *Ann. N. Y. Acad. Sci.* 1117, 302-309 (2007).

16. G. Breeland, M. A. Sinkler, R. G. Menezes, *Embryology, Bone Ossification*. (Treasure Island (FL): StatPearls Publishing, SttatPearls (Internet), 2021).

17. A. J. Sophia Fox, A. Bedi, S. A. Rodeo, The basic science of articular cartilage: structure, composition, and function. *Sports Health* 1, 461-468 (2009).

18. R. Nishimura *et al.*, Regulation of endochondral ossification by transcription factors. *Front Biosci (Landmark Ed)* 17, 2657-2666 (2012).

19. C. Prein, F. Beier, ECM signaling in cartilage development and endochondral ossification. *Curr. Top. Dev. Biol.* 133, 25-47 (2019).

20. K. Amano *et al.*, Sox9 Family Members Negatively Regulate Maturation and Calcification of Chondrocytes through Up-Regulation of Parathyroid Hormone–related Protein. *Mol. Biol. Cell* 20, 4541-4551 (2009).

21. R. Nishimura, K. Hata, T. Matsubara, M. Wakabayashi, T. Yoneda, Regulation of bone and cartilage development by network between BMP signalling and transcription factors. *J. Biochem.* 151, 247-254 (2012).

22. T. Hattori *et al.*, SOX9 is a major negative regulator of cartilage vascularization, bone marrow formation and endochondral ossification. *Development* 137, 901-911 (2010).

23. J. C. Lui *et al.*, Persistent Sox9 expression in hypertrophic chondrocytes suppresses transdifferentiation into osteoblasts. *Bone* 125, 169-177 (2019).

24. M. M. Weinstein, S. W. Tompson, Y. Chen, B. Lee, D. H. Cohn, Mice expressing mutant Trpv4 recapitulate the human TRPV4 disorders. *J Bone Miner Res* 29, 1815-1822 (2014).

25. H. A. Leddy, A. L. McNulty, F. Guilak, W. Liedtke, Unraveling the mechanism by which TRPV4 mutations cause skeletal dysplasias. *Rare Dis* 2, e962971 (2014).

26. K. Takahashi *et al.*, Induction of Pluripotent Stem Cells from Adult Human Fibroblasts by Defined Factors. *Cell* 131, 861-872 (2007).

27. S. S. Adkar *et al.*, Genome Engineering for Personalized Arthritis Therapeutics. *Trends Mol. Med.* 23, 917-931 (2017).

28. M.-S. Lee *et al.*, Comparative evaluation of isogenic mesodermal and ectomesodermal chondrocytes from human iPSCs for cartilage regeneration. *Science Advances* 7, eabf0907 (2021).

29. B. Saitta *et al.*, Patient-derived skeletal dysplasia induced pluripotent stem cells display abnormal chondrogenic marker expression and regulation by BMP2 and TGFbeta1. *Stem Cells Dev.* 23, 1464-1478 (2014).

30. K. Nonaka *et al.*, Novel gain-of-function mutation of TRPV4 associated with accelerated chondrogenic differentiation of dental pulp stem cells derived from a patient with metatropic dysplasia. *Biochem Biophys Rep* 19, 100648 (2019).

31. S. S. Adkar *et al.*, Step-Wise Chondrogenesis of Human Induced Pluripotent Stem Cells and Purification Via a Reporter Allele Generated by CRISPR-Cas9 Genome Editing. *Stem Cells* 37, 65-76 (2019).

32. A. Dicks *et al.*, Prospective isolation of chondroprogenitors from human iPSCs based on cell surface markers identified using a CRISPR-Cas9-generated reporter. *Stem Cell. Res. Ther.* 11, 66 (2020).

33. C. L. Wu *et al.*, Single cell transcriptomic analysis of human pluripotent stem cell

chondrogenesis. *Nat Commun* 12, 362 (2021).

34. L. Votava, A. G. Schwartz, N. S. Harasymowicz, C. L. Wu, F. Guilak, Effects of dietary fatty acid content on humeral cartilage and bone structure in a mouse model of diet-induced obesity. *J. Orthop. Res.* 37, 779-788 (2019).

35. R. E. Wilusz, S. Zauscher, F. Guilak, Micromechanical mapping of early osteoarthritic changes in the pericellular matrix of human articular cartilage. *Osteoarthritis Cartilage* 21, 1895-1903 (2013).

36. E. M. Darling, R. E. Wilusz, M. P. Bolognesi, S. Zauscher, F. Guilak, Spatial mapping of the biomechanical properties of the pericellular matrix of articular cartilage measured in situ via atomic force microscopy. *Biophys. J.* 98, 2848-2856 (2010).

37. E. M. Darling, S. Zauscher, F. Guilak, Viscoelastic properties of zonal articular chondrocytes measured by atomic force microscopy. *Osteoarthritis Cartilage* 14, 571-579 (2006).

38. N. A. Zelenski *et al.*, Type VI Collagen Regulates Pericellular Matrix Properties, Chondrocyte Swelling, and Mechanotransduction in Mouse Articular Cartilage. *Arthritis Rheumatol* 67, 1286-1294 (2015).

39. K. J. Livak, T. D. Schmittgen, Analysis of relative gene expression data using real-time quantitative PCR and the 2(-Delta Delta C(T)) Method. *Methods* 25, 402-408 (2001).

40. A. Dobin *et al.*, STAR: ultrafast universal RNA-seq aligner. *Bioinformatics* 29, 15-21 (2013).

41. Y. Liao, G. K. Smyth, W. Shi, featureCounts: an efficient general purpose program for assigning sequence reads to genomic features. *Bioinformatics* 30, 923-930 (2014).

42. R. Patro, G. Duggal, M. I. Love, R. A. Irizarry, C. Kingsford, Salmon provides fast and bias-aware quantification of transcript expression. *Nat. Methods* 14, 417-419 (2017).

43. L. Wang, S. Wang, W. Li, RSeQC: quality control of RNA-seq experiments. *Bioinformatics* 28, 2184-2185 (2012).

44. M. I. Love, W. Huber, S. Anders, Moderated estimation of fold change and dispersion for RNA-seq data with DESeq2. *Genome Biol.* 15, 550 (2014).

45. R. Kolde. (2015).

46. H. Wickham, *ggplot2: Elegant Graphics for Data Analysis*. Use R! (Springer-Verlag New York, ed. 1, 2009).

47. H. Chen, P. C. Boutros, VennDiagram: a package for the generation of highly-customizable Venn and Euler diagrams in R. *BMC Bioinformatics* 12, 35 (2011).

48. U. Raudvere *et al.*, g:Profiler: a web server for functional enrichment analysis and conversions of gene lists (2019 update). *Nucleic Acids Res.* 47, W191-W198 (2019).

49. N. Altman, M. Krzywinski, Clusterinig. *Nat. Methods* 14, 545-546 (2017).

50. N. T. Doncheva, J. H. Morris, J. Gorodkin, L. J. Jensen, Cytoscape StringApp: Network Analysis and Visualization of Proteomics Data. *J. Proteome Res.* 18, 623-632 (2019).

51. P. Shannon, Cytoscape: A Software Environment for Integrated Models of Biomolecular Interaction Networks. *Genome Res.* 13, 2498-2504 (2003).

52. D. Merico, R. Isserlin, O. Stueker, A. Emili, G. D. Bader, Enrichment Map: A Network-Based Method for Gene-Set Enrichment Visualization and Interpretation. *PLoS One* 5, e13984 (2010).

53. P. Kanju *et al.*, Small molecule dual-inhibitors of TRPV4 and TRPA1 for attenuation of inflammation and pain. *Sci. Rep.* 6, 26894 (2016).

54. M. Jin *et al.*, Determinants of TRPV4 activity following selective activation by small molecule agonist GSK1016790A. *PLoS One* 6, e16713 (2011).

55. B. O. Diekman *et al.*, Cartilage tissue engineering using differentiated and purified induced pluripotent stem cells. *Proc. Natl. Acad. Sci. U. S. A.* 109, 19172-19177 (2012).

56. R. R. Yammani, S100 proteins in cartilage: role in arthritis. *Biochim Biophys Acta* 1822, 600-606 (2012).

57. A. Seifert, Role of Hox genes in stem cell differentiation. *World J. Stem Cells* 7, 583 (2015).

58. A. M. Craft *et al.*, Generation of articular chondrocytes from human pluripotent stem cells. *Nat. Biotechnol.* 33, 638-645 (2015).

59. W. C. Chu *et al.*, Distribution of pericellular matrix molecules in the temporomandibular joint and their chondroprotective effects against inflammation. *International Journal of Oral Science* 9, 43-52 (2017).

60. M. M. J. Caron *et al.*, Aggrecan and COMP Improve Periosteal Chondrogenesis by Delaying Chondrocyte Hypertrophic Maturation. *Frontiers in Bioengineering and Biotechnology* 8, (2020).

61. J. T. Hecht, E. H. Sage, Retention of the Matricellular Protein SPARC in the Endoplasmic Reticulum of Chondrocytes from Patients with Pseudoachondroplasia. *J. Histochem. Cytochem.* 54, 269-274 (2006).

62. T. Iimura, O. Pourquié, Hox genes in time and space during vertebrate body formation. *Development, Growth & Differentiation* 49, 265-275 (2007).

63. P. M. Deprez, M. G. Nichane, B. G. Lengele, R. Rezsohazy, C. Nyssen-Behets, Molecular study of a Hoxa2 gain-of-function in chondrogenesis: a model of idiopathic proportionate short stature. *Int. J. Mol. Sci.* 14, 20386-20398 (2013).

64. L. Massip *et al.*, Expression of Hoxa2 in cells entering chondrogenesis impairs overall cartilage development. *Differentiation* 75, 256-267 (2007).

65. B. Kanzler, S. J. Kuschert, Y. H. Liu, M. Mallo, Hoxa-2 restricts the chondrogenic domain and inhibits bone formation during development of the branchial area. *Development* 125, 2587-2597 (1998).

66. S. Creuzet, G. Couly, C. Vincent, N. M. Le Douarin, Negative effect of Hox gene expression on the development of the neural crest-derived facial skeleton. *Development* 129, 4301-4313 (2002).

67. X. Li, BMP Signaling and Skeletogenesis. *Ann. N. Y. Acad. Sci.* 1068, 26-40 (2006).

68. K. M. Pineault, D. M. Wellik, Hox Genes and Limb Musculoskeletal Development. *Current Osteoporosis Reports* 12, 420-427 (2014).

69. F. Chen, J. Greer, M. R. Capecchi, Analysis of Hoxa7/Hoxb7 mutants suggests periodicity in the generation of the different sets of vertebrae. *Mech. Dev.* 77, 49-57 (1998).

70. D. M. Wellik. (Elsevier, 2009), pp. 257-278.

71. F. Qu, I. C. Palte, P. M. Gontarz, B. Zhang, F. Guilak, Transcriptomic analysis of bone and fibrous tissue morphogenesis during digit tip regeneration in the adult mouse. *The FASEB Journal* 34, 9740-9754 (2020).

72. X. Li, X. Cao, BMP signaling and HOX transcription factors in limb development. *Front. Biosci.* 8, s805-812 (2003).

73. M. V. Volpe *et al.*, Regulatory Interactions between Androgens, Hoxb5, and TGFβSignaling in Murine Lung Development. *BioMed Research International* 2013, 1-12 (2013).

74. S. Woods *et al.*, Regulation of TGFβ Signalling by TRPV4 in Chondrocytes. *Cells* 10, 726 (2021).

75. R. J. Nims *et al.*, A synthetic mechanogenetic gene circuit for autonomous drug delivery in engineered tissues. *Science Advances* 7, eabd9858 (2021).

76. I. Polur, P. L. Lee, J. M. Servais, L. Xu, Y. Li, Role of HTRA1, a serine protease, in the progression of articular cartilage degeneration. *Histol. Histopathol.* 25, 599-608 (2010).

77. H. Miraoui, P. J. Marie, Pivotal role of Twist in skeletal biology and pathology. *Gene* 468, 1-7 (2010).

78. T. Michigami, Current understanding on the molecular basis of chondrogenesis. *Clin Pediatr Endocrinol* 23, 1-8 (2014).

79. A. Taillandier *et al.*, Molecular diagnosis of hypophosphatasia and differential diagnosis by targeted Next Generation Sequencing. *Mol Genet Metab* 116, 215-220 (2015).

80. N. Hanagata, IFITM5 mutations and osteogenesis imperfecta. *Journal of Bone and Mineral Metabolism* 34, 123-131 (2016).

81. J. D. Hayes, J. U. Flanagan, I. R. Jowsey, GLUTATHIONE TRANSFERASES. *Annual Review of Pharmacology and Toxicology* 45, 51-88 (2005).

82. C.-T. Chen, Y.-R. V. Shih, T. K. Kuo, O. K. Lee, Y.-H. Wei, Coordinated Changes of Mitochondrial Biogenesis and Antioxidant Enzymes During Osteogenic Differentiation of Human Mesenchymal Stem Cells. *Stem Cells* 26, 960-968 (2008).

83. K. Morita *et al.*, Reactive oxygen species induce chondrocyte hypertrophy in endochondral ossification. *J. Exp. Med.* 204, 1613-1623 (2007).

84. E. Fragonas *et al.*, Sensitivity of chondrocytes of growing cartilage to reactive oxygen species. *Biochimica et Biophysica Acta (BBA) - General Subjects* 1425, 103-111 (1998).

85. F. Atashi, A. Modarressi, M. S. Pepper, The Role of Reactive Oxygen Species in Mesenchymal Stem Cell Adipogenic and Osteogenic Differentiation: A Review. *Stem Cells Dev.* 24, 1150-1163 (2015).

86. J. van Holten *et al.*, Treatment with recombinant interferon-beta reduces inflammation and slows cartilage destruction in the collagen-induced arthritis model of rheumatoid arthritis. *Arthritis Res. Ther.* 6, R239-249 (2004).

87. R. Zhao *et al.*, Exogenous IFN-beta regulates the RANKL-c-Fos-IFN-beta signaling pathway in the collagen antibody-induced arthritis model. *J. Transl. Med.* 12, 330 (2014).

88. G. Palmer *et al.*, Interferon beta stimulates interleukin 1 receptor antagonist production in human articular chondrocytes and synovial fibroblasts. *Ann. Rheum. Dis.* 63, 43-49 (2004).

89. X. Hu, H. H. Ho, O. Lou, C. Hidaka, L. B. Ivashkiv, Homeostatic role of interferons conferred by inhibition of IL-1-mediated inflammation and tissue destruction. *J. Immunol.* 175, 131-138 (2005).

90. L. Gao, J. Liesveld, J. Anolik, A. McDavid, R. J. Looney, IFNβ signaling inhibits osteogenesis in human SLE bone marrow. *LUPUS* 29, 1040-1049 (2020).

91. X. Huang, L. Zhong, J. Hendriks, J. N. Post, M. Karperien, The Effects of the Wnt-Signaling Modulators BIO and PKF118-310 on the Chondrogenic Differentiation of Human Mesenchymal Stem Cells. *Int. J. Mol. Sci.* 19, (2018).

92. W. Hou *et al.*, Cation Channel Transient Receptor Potential Vanilloid 4 Mediates Topography-Induced Osteoblastic Differentiation of Bone Marrow Stem Cells. *ACS Biomaterials Science & Engineering* 5, 6520-6529 (2019).

Chapter 6

Skeletal Dysplasia-causing TRPV4 Mutations Increase Mechanosensitivity of Human iPSC-derived Chondrocytes

6.1 Abstract

Transient receptor potential vanilloid 4 (TRPV4) is a mechanically sensitive ion channel highly expressed in chondrocytes. Mutations in TRPV4 prevent proper skeletal development and cause skeletal dysplasias, such as V620I and T89I that lead to brachyolmia and metatropic dysplasia, respectively. However, how these mutations alter mechanotransduction and inhibit chondrocyte hypertrophy and endochondral ossification has yet to be elucidated. Therefore, we chondrogenically differentiated human induced pluripotent stem cells (hiPSCs) harboring the moderate V620I and severe T89I TRPV4 mutations. We cultured the derived chondrocytes in an agarose hydrogel prior to compressive loading of 10% strain at 1 Hz for 3 hours. Using mRNA sequencing and bioinformatic analyses, we assessed the transcriptomic response of chondrocytes 0, 3, 12, and 24 hours after loading. hiPSC-derived chondrocytes synthesized cartilaginous matrix in agarose hydrogels. We observed an increased mechanosensitivity of mutant TRPV4 with higher fold changes and more differentially expressed genes compared to the wildtype control. From the transcriptomic data, we propose that TRPV4 mutations V620I and T89I increase cell cycle regulating genes (e.g., *E2F1, TP53, NFKB1*) resulting in continued proliferation of chondrocytes and inhibition of hypertrophy, ultimately leading to the dysfunctional developmental phenotype in skeletal dysplasias.

6.2 Introduction

Articular cartilage lines the ends of long bones and provides a nearly frictionless surface for joint movements (*1*). Interestingly, not only does cartilage withstand millions of cycles of loading, but loading maintains the homeostasis of the tissue (*2, 3*). Chondrocytes, the primary residing cell type, synthesize and degrade extracellular matrix (ECM) proteins, including glycosaminoglycans (GAGs) and type II collagen (COL2A1), in response to physiologic loading (*1, 4*). Chondrocyte mechanotransduction occurs as compressive, shear, hydrostatic pressure, and osmotic forces are filtered through the pericellular matrix surrounding the chondrocyte to mechanosensors, such as integrins, primary cillium, and ion channels (*5, 6*). The signal is then converted into downstream pathways (e.g., Indian hedgehog, Wnt, TGFβ, MAPK-ERK) and results in transcriptomic changes (*5*). One mechanosensor of particular interest is ion channel transient receptor potential vanilloid 4 (TRPV4).

TRPV4 is a non-selective cation channel activated by, but not limited to, heat, acidity, chemical agonists (e.g., 4α-phorbol 12,13-didecanoate, ruthenium red, GSK1016790A), osmolarity, and mechanical loading (*7, 8*). The channel is expressed throughout the body with high expression in chondrocytes (*7*). In fact, TRPV4 is essential to the development and homeostasis of cartilage. TRPV4 activation increased expression of chondrogenic transcription factor SRY-box transcription factor 9 (*SOX9*) promoting chondrogenesis in ATDC5 cells (*9*) and increased matrix production and Young's modulus in primary porcine chondrocytes (*4*). However, knockout of TRPV4 in murine adipose-derived stem cells decreased chondrogenic potential (*10*). To better understand the downstream effects of TRPV4 activation on chondrocytes, our recent study identified the shared transcriptome between TRPV4 activation via loading and chemical agonist GSK1016790A (GSK101; *11*). The primary porcine chondrocytes

had increased gene expression associated with rheumatoid arthritis, TGFβ signaling, and PPAR signaling (*11*). These results highlight the essential function of mechanical loading on cartilage development and homeostasis, particularly via TRPV4 and its downstream signaling cascades.

In fact, mutations in TRPV4 have been shown to cause skeletal dysplasias, diseases of improper skeletal development (*12, 13*). For example, the V620I substitution causes moderate autosomal dominant brachyolmia, and the T89I substitution causes severe, neonatally lethal metatropic dysplasia. Both mutations lead to a disproportionate skeletal phenotype with scoliosis and deformed long bones (*14, 15*). Previous studies, including ours, showed increased basal membrane currents with V620I and T89I TRPV4 (*16-18*). However, there have been conflicting results as to whether the mutant channel has increased or decreased sensitivity to activation via chemical agonist GSK101 and hypotonic solutions (*16-18*). Using human induced pluripotent stem cells (hiPSC)-derived chondrocytes, we found that V620I and T89I mutations decrease channel sensitivity to GSK101 and delay and inhibit chondrocyte hypertrophy (*18*). However, how the mutations alter the response to mechanical, compressive loading, has not been elucidated. Here, we investigate the transient, transcriptomic response of hiPSC-derived chondrocytes to physiologic, cyclic loading and the differences in the response due to dysplasia-causing gain-of-function mutations. These results will provide insights into TRPV4 mechanotransduction, hiPSC-derived tissue-engineered cartilage optimization, and skeletal dysplasia treatments.

6.3 Methods

6.3.1 hiPSC culture

BJFF.6 (BJFF; Washington University Genome Engineering and iPSC Center (GEiC)) was the isogenic, wildtype control hiPSC line used in this study. V620I and T89I substitutions were

added to BJFF using CRISPR-Cas9 to create the two mutated hiPSC lines as previously

described (*19*). The hiPSCs were cultured on vitronectin (VTN-N; Fisher Scientific, A14700)-

coated plates and fed Essential 8 Flex medium (E8; Gibco, A2858501) daily. For expansion,

cells were passaged at 80-90% confluency using ReLeSR (STEMCELL Technologies, 05872)

and cultured with rock inhibitor Y-27632 (STEMCELL Technologies, 72304) for 24 hours. For

mesodermal differentiation, cells were induced at 30-40% confluency.

6.3.2 Mesodermal differentiation

The hiPSCs were differentiated along the mesodermal lineage to chondroprogenitors in

monolayer for 12 days as previously described (*19-21*). In brief, the cells were fed daily with

mesodermal differentiation medium: Iscove's Modified Dulbecco's Medium, glutaMAX

(IMDM; Gibco, 31980097) and Ham's F-12 nutrient mix, glutaMAX (F12; Gibco, 31765092) in

equal parts supplemented with 1% penicillin-streptomycin (P/S; Gibco, 15140122), 1% Insulin-

Transferrin-Selenium (ITS+; Gibco, 41400045), 1% chemically defined concentrated lipids

(Thermo Fisher Scientific, 11905031), and 450 µM 1-thioglycerol (Millipore Sigma, M6145).

Various combinations of growth factors and small molecules were used each day for specified

differentiation: day 1, anterior primitive streak, 30 ng/ml Activin (R&D Systems, 338-AC), 20

ng/ml FGF2 (R&D Systems, 233-FB-025/CF), 4 µM CHIR99021 (Reprocell, 04-0004-02); day

2, paraxial mesoderm, 20 ng/ml FGF2, 3 µM CHIR99021, 2 µM SB505124 (Tocris Bioscience,

3263), 4 µM dorsomorphin (DM; Reprocell, 04-0024); day 3, early somite, 2 µM SB505124, 4

µM dorsomorphin, 500 nM PD173074 (Tocris Bioscience, 3044), 1 µM Wnt-C59 (Cellagen

Technologies, C7641-2s); days 4-6, sclerotome, 1 µM Wnt-C59, 2 µM purmorphamine

(Reprocell, 04-0009); and days 7-12, chondroprogenitor cells, 20 ng/ml BMP4 (R&D Systems,

314-BP-010CF)). The chondroprogenitor cells were then disassociated with TrypLE™ Select

Enzyme (1X), no phenol red (Gibco, 12563029) for chondrogenic differentiation.

6.3.3 Chondrogenic differentiation

Chondroprogenitor cells were chondrogenically differentiated for 28 days in a high-density, 3D

pellet culture as previously described (*19-21*). Chondroprogenitor cells were resuspended at 5 x

10^5 cells/mL in chondrogenic medium: Dulbecco's Modified Eagle Medium/F12, glutaMAX

(DMEM/F12; Gibco, 10565042), 1% P/S, 1% ITS+, 1% Modified Eagle Medium (MEM) with

nonessential amino acids (NEAA; Gibco, 11140050), 0.1% dexamethasone (Dex; Millipore

Sigma, D4902), and 0.1% 2-Mercaptoethnol (2-ME; Gibco, 21985023) supplemented with 0.1%

L-ascorbic acid (ascorbate; Millipore Sigma, A8960), 0.1% L-proline (proline; Millipore Sigma,

P5607), 10 ng/ml human transforming growth factor beta 3 (TGFβ3; R&D Systems, 243-B3-

010/CF), 1 µM Wnt-C59, and 1 µM ML329 (Cayman Chemical, 22481). Pellets were formed by

centrifuging 1 mL of the cell solution in a 15-mL conical tube and fed every 3-4 days.

6.3.4 Digestion of chondrogenic pellets to obtain hiPSC-derived chondrocytes

A 0.4% w/v type II collagenase (Worthington Biochemical, LS00417) digestion solution was

created in DMEM/F12 with 10% fetal bovine serum (FBS; Atlanta Biologicals, S11550). Day-28

chondrogenic pellets were then rinsed and digested in an equal volume of digestion solution (1

mL per pellet) on an orbital shaker at 37 °C. Digestion solution with pellets was vortexed every

20 minutes until tissue was no longer visible and was neutralized with an equal volume of

DMEM/F12 with 10% FBS.

6.3.5 Casting of hiPSC-derived chondrocytes in agarose

A 4% (w/v) agarose (low gelling temperature Type VII-A; Sigma, A0701) solution was made in

PBS and autoclaved. hiPSC-derived chondrocytes were resuspended in chondrogenic medium at

6×10^7 cells/mL and mixed with an equal volume of 60 °C agarose. The 3×10^7 cells per 1 mL of

2% agarose solution was cast in a mold for 10 min at room temperature before creating disks with a 3 mm diameter biopsy punch. Agarose constructs were fed every 3-4 days with chondrogenic medium for 2 weeks to allow for matrix production.

6.3.6 Inhibition of TRPV4 during culture

Some agarose constructs were continued in culture for an addition 2 weeks. The chondrogenic medium was supplemented with 20 µM GSK205 (cat. num. AOB1612 1263130-79-5; AOBIOUS, Gloucester, MA) or an equal volume of DMSO for 1 hour per day, 5 days per week for 2 weeks.

6.3.7 Analysis of elastic modulus

Agarose constructs were transferred to PBS and stored at 4 ℃ for mechanical testing. Using the ELF 3220 (ELectroForce with WinTest Software, EnduraTEC Systems Corporation), a 2 g tare was applied to the constructs before undergoing a stress relaxation test with a 10% displacement at a rate of 1 µm/s for 20 min to calculate the elastic modulus of the constructs.

6.3.8 Histology

Agarose constructs were fixed and dehydrated in sequential steps of increasing ethanol and xylene solutions until embedded in paraffin wax. Wax blocks were cut into 8 µm sections on microscope slides, and slides were rehydrated in ethanol and water. Nuclei were stained with Harris hematoxylin and sGAGs with Safranin-O. Antigen retrieval was performed on rehydrated slides followed by blocking, the addition of primary and secondary antibodies, and AEC development to label type II collagen proteins and Vector Hematoxylin QS counterstain.

6.3.9 Biochemical analysis

Agarose were rinsed in PBS and digested in a papain solution at 65 ℃ overnight. Sulfated glycosaminoglycan (sGAG) content was measured using a dimethylmethylene blue (DMMB)

solution. Double-stranded DNA (dsDNA) was measured using the PicoGreen assay (Quant-iT™ PicoGreen™ dsDNA Assay Kit, P7589). sGAG content was normalized to dsDNA.

6.3.10 Sinusoidal compressive loading

After 2 weeks, agarose constructs were switched to chondrogenic medium without TGFβ3. Constructs were sinusoidally loaded with a 10% peak-to-peak strain at 1 Hz for 3 hours at 37 ℃ alongside a free swelling control. The loading was performed with a custom-made bioreactor (*4, 11*). The loaded agarose constructs were incubated until harvested in chondrogenic medium without TGFβ3. Agarose constructs were rinsed and snap frozen 0, 3 (2 samples), 12, or 24 hours after loading completed. The free-swelling constructs were harvested at 0 hours, immediately after loading. Constructs were stored at -80 ℃ until RNA isolation.

6.3.11 RNA isolation

Samples were thawed on ice, lysed, and homogenized. RNA was isolated using the Quiagen Total RNA Purification Plus Kit (Norgen Biotek, 48400) according to manufacturer instructions and immediately submitted for mRNA sequencing with the Genome Technology Access Center at Washington University in St. Louis (GTAC).

6.3.12 Genome-wide mRNA sequencing

Libraries were prepared according to manufacturer's protocol. Samples were indexed, pooled, and sequenced at a depth of 30 million reads per sample on an Illumina NovaSeq 6000. Basecalls and demultiplexing were performed with Illumina's bcl2fastq software and a custom python demultiplexing program with a maximum of one mismatch in the indexing read. RNA-seq reads were then aligned to the Ensembl release 76 primary assembly with STAR version 2.5.1a (*22*). Gene counts were derived from the number of uniquely aligned unambiguous reads by Subread:featureCount version 1.4.6-p5 (*23*). Isoform expression of known Ensembl transcripts

were estimated with Salmon version 0.8.2 (*24*). Sequencing performance was assessed for the total number of aligned reads, total number of uniquely aligned reads, and features detected. The ribosomal fraction, known junction saturation, and read distribution over known gene models were quantified with RSeQC version 2.6.2 (*25*).

6.3.13 Transcriptomic analysis of sequencing datasets

Working in RStudio, we used the DESeq package to read un-normalized gene counts and remove the genes if they had counts lower than 200 (*26*). Regularized-logarithm transformed data of the samples were visualized with the *ggplot2* package (*27*) to create a principal component analysis (PCA). The two 3-hour replicates clustered together confirming reproducibility and were then averaged together. The up-regulated differentially expressed genes (DEGs) were determined at each time point compared to the free swelling control for each line and the total number were plotted using GraphPad Prism. Genes were considered differentially expressed if adjusted p value (p_{adj}) < 0.1 and $\log_2$(fold change) ≥ 1 or ≤ -1. The intersecting and unique DEGs between time points for each cell lines and between cell lines at each time point were determined and plotted with the *intersect* and *setdiff,* and *venn.diagram* functions (*VennDiagram* package (*28*)). The fold change of top 25 genes in the intersection of the two mutants, but not WT, for each time point were determined and the 0 and 3 hour gene lists and 12 and 24 hour gene lists were visualized with the *Pheatmap* package (*29*). The fold changes at each time point of cAMP/Ca^{2+} transcription factors and TRPV4-responsive genes (*11*) were plotted using GraphPad Prism and significance was indicated based on p values. The upregulated genes at 0, 3, 12, and 24 hours were ordered based on $\log_2$(fold change) and analyzed with g:Profiler (*30*) and Transcriptional Regulatory Relationships Unraveled by Sentence-based Text Mining (TRRUST) (*31*). gProfiler identified KEGG and reactome pathways associated with the ordered gene set. Then, we plotted

the negative $\log_{10}$ of the adjusted p value for each term using a function to scale circle diameter

to the p value in Illustrator. TRRUST identified associated transcription factors with the gene set,

and we plotted the $\log_{10}$(p value) of association for each transcription factor for either V620I or

T89I vs. WT on a scatter plot using GraphPad Prism. The transcription factors with the strongest

association to one line compared to the other on the graph were highlighted in that cell line's

color and labeled. If the transcription factor was strongly associated with both lines, it was

labeled in grey. We also performed k-means clustering with 4 clusters and plotted the gene

expression trends (scaled mean counts) for each gene within the cluster with the average

expression trend overlaying for each cell line of the largest cluster using the *tidyverse* package

(*32*). Cluster 1 represented increased expression at 12 and 24 hours, and cluster 2 and 3

represented increased expression at 0 and 3 hours. The top 20 up-regulated genes from cluster 1

or clusters 2 and 3 for each cell line were determined. The $\log_2$(fold change) of that gene for each

group was plotted with *pheatmap*.

6.3.14 Statistical analysis

Replicates were graphed and analyzed using GraphPad Prism (Version 9.1.0). Outliers were

removed from the data using the ROUT method ($Q = 1\%$), and the data were tested for normality

with the Shapiro-Wilk test ($\alpha = 0.05$). A Kruskal-Wallis test was used if data was not normally

distributed. For biochemical analysis and mechanical properties, data were analyzed using an

ordinary two-way ANOVA, comparing each cell with all other cells, with Tukey's post-hoc

multiple comparison test.

6.4 Results

6.4.1 hiPSC-derived chondrocytes secrete a cartilaginous matrix in agarose

hiPSC chondrogenesis occurs in a 3D, spherical pellet culture; however, compressive loading of

a sphere results in an uneven distribution of stress throughout the tissue. Therefore, we digested

the day-28 chondrogenic pellets to obtain hiPSC-derived chondrocytes at a single-cell level that

were then cast in 2% agarose, cylindrical constructs and cultured for 2 weeks. This culture

system has been used extensively for mechanical loading studies with primary chondrocytes (*4,

11*). Like primary chondrocytes, the hiPSC-derived chondrocytes secreted cartilaginous matrix

(Figure 6.1A-C). Safranin-O staining of sGAGs showed the chondrocytes began secreting matrix

directly around the cell, which was more distributed throughout the agarose in mutant lines

(Figure 6.1A). All lines also showed COL2A1 labeling, which appeared more localized around

the cell in WT (Figure 6.1B). The ratio of sGAG to dsDNA, as determined by biochemical

analysis, was not significantly different between lines, but T89I trended higher (T89I: 45.4 µg/µg

vs. WT: 22.2 µg/µg, p=0.4248 and V620I: 24.3 µg/µg, p=0.4720; Figure 6.1C).
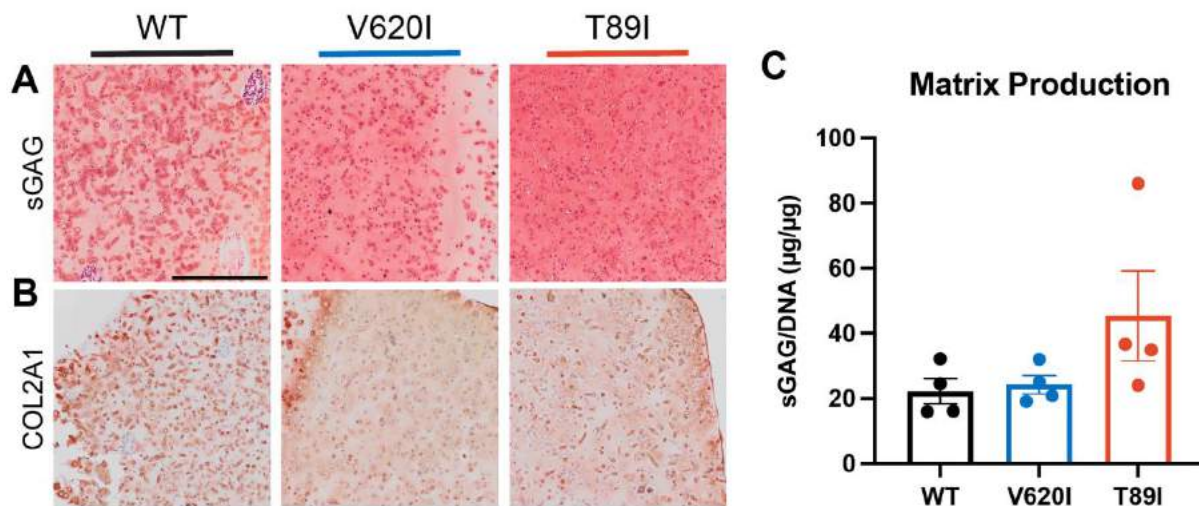
Figure 6.1 hiPSC-derived chondrocytes secrete cartilaginous matrix in agarose after 2 weeks of culture. (**A-B**) Day-28 hiPSC-derived chondrocytes seeded in agarose and cultured in chondrogenic medium for 14 days secrete matrix rich in sGAGs as shown by Safranin-O staining (**A**) and COL2A1 as labeled by IHC (**B**). Scale bar = 500 µm. (**C**) The three lines have similar sGAG/DNA ratios between 20-40 µg/µg. Mean ± SEM. n-4. No significance after ordinary one-way ANOVA.

Next, we investigated whether TRPV4 signaling was responsible for the matrix

production within the agarose since severe mutation T89I appeared to increase sGAG secretion. We continued to culture the agarose for an additional 2 weeks with and without TRPV4-specific antagonist GSK205. The differences between lines with localization of Safranin-O staining were no longer present at 4 weeks; however, WT had showed somewhat increased labeling for COL2A1 (Figure 6.2A-B). Treatment with GSK205 appeared to slightly decrease sGAG staining with no effect on COL2A1 labeling (Figure 6.2C-D). When quantified, TRPV4 inhibition trended toward decreasing sGAG/DNA in T89I (veh vs. GSK205 (μg/μg) – WT: 57.7 vs. 52.5; V620I: 52.3 vs. 59.9; T89I: 55.8 vs. 37.4; ns). The additional two weeks of culture did however increase the sGAG/DNA ratio for all lines from an average of 20 to 50 μg/μg. We also observed a trend of higher elastic moduli in mutants compared to WT, which was slightly attenuated by GSK205 in T89I (veh vs. GSK205 (kPa) – WT: 98.8 vs. 83.9; V620I: 134.1 vs. 116.6; T89I: 140.8 vs. 70.4; ns).
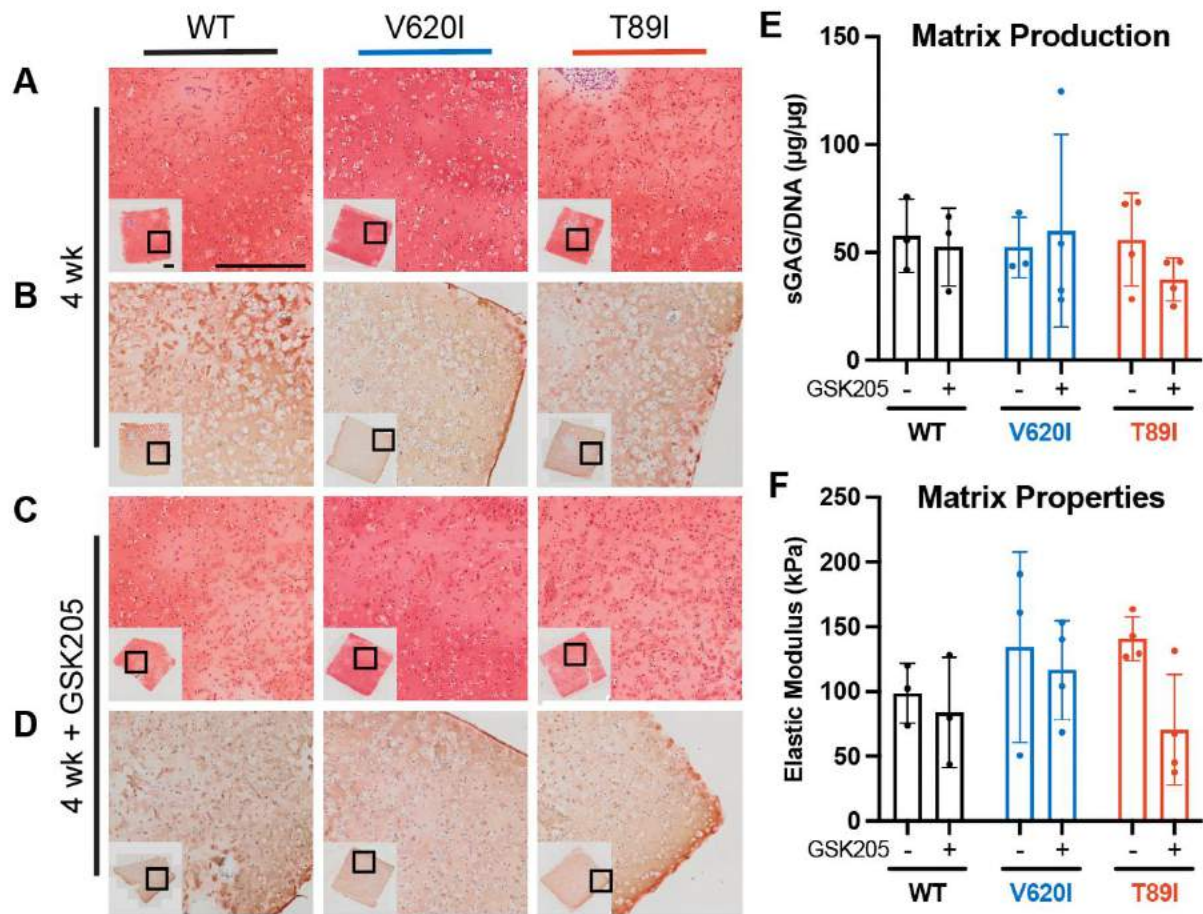
Figure 6.2 TRPV4 inhibition during hiPSC-derived chondrocyte agarose culture. (**A-B**) WT, V620I, and T89I had similar matrix production after 4 weeks in culture as shown by Safranin-O staining of sGAG (**A**) and IHC labeling of COL2A1 (**B**). (**C-D**) TRPV4 inhibition with GSK205 did not have a major effect on Safranin-O staining of sGAG (**C**) or IHC labeling of COL2A1 (**D**). Scale bar = 500 µm. (**E**) Quantification of the matrix production showed all three lines, with and without GSK205, had an sGAG/DNA ratio of approximately 50 µg/µg. Mean ± SEM. n=3-4. No significance with an ordinary two-way ANOVA. (**F**) V620I and T89I have slightly higher elastic moduli (approximately 150 kPa) compared to WT (approximately 100 kPa), which trended lower with GSK205 treatment. Mean ± SEM. n=3-4. No significance with an ordinary two-way ANOVA.

6.4.2 Mutant chondrocytes are more responsive to loading

WT, V620I, and T89I 2-week agarose constructs were loaded with 10% strain at 1 Hz for 3

hours alongside a free swelling control (Figure 6.3A). The constructs were collected for mRNA

sequencing 0, 3, 12, and 24 hours after loading completed (Figure 6.3A). Principal component

analysis (PCA) shows that the 3 cell lines followed a similar trajectory over time post-loading;

however, WT samples were more similar to each other at each time point than mutants (Figure 6.3B). This was further confirmed when comparing the number of upregulated DEGs at each time point; in fact, T89I has more than double the number of upregulated DEGs than WT (WT: 887 vs. V620I: 1672 vs. T89I: 2379; Figure 6.3C). We then compared the DEGs at each time point within each line (Figure 6.3D). Interestingly, WT showed an increase in DEGs over time with the largest response at 24 hours (0hr: 92 vs. 3hr: 237 vs. 12hr: 233 vs. 24 hr: 325; Figure 6.3D). However, V620I showed the largest response at 3 and 12 hours, with fewer DEGs than WT at 24 hours (0hr: 157 vs. 3hr: 549 vs. 12hr: 676 vs. 24 hr: 290; Figure 6.3D). T89I had a larger response at 0 hours than WT did at 24 hours, which continued to increase through 3, 12, and 24 hours (0hr: 464 vs. 3hr: 656 vs. 12hr: 567 vs. 24 hr: 692; Figure 6.3D). For all lines, many DEGs were unique to the time point, but the largest intersections were between 0 and 3 hours or 12 and 24 hours (Figure 6.3D). V620I also showed significant overlap between 3 and 12 hours (Figure 6.3D).
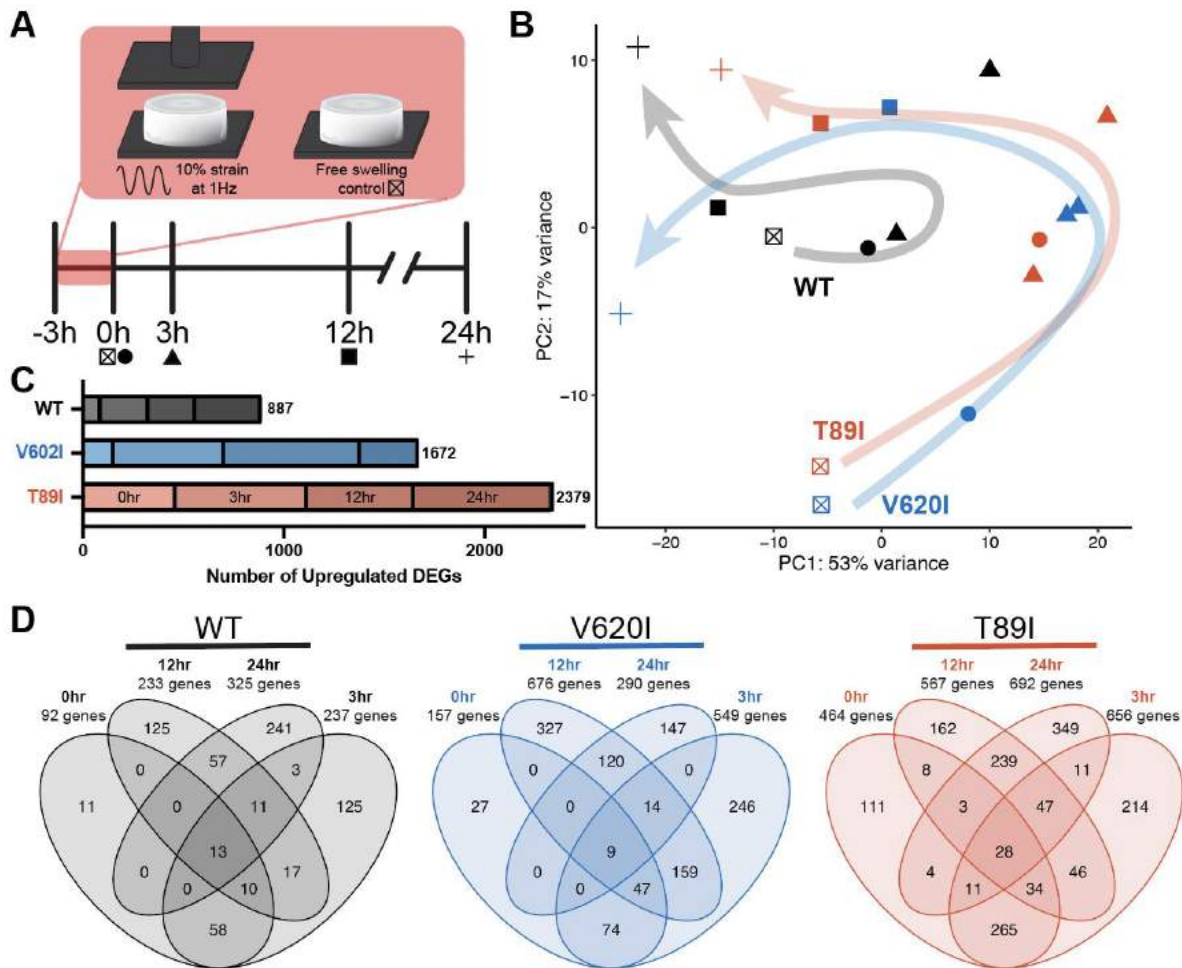
Figure 6.3 Mechanical loading response of hiPSC-derived chondrocyte agarose. (**A**) The loading regimen and sample collection timeline. Agarose constructs were loaded with 10% compressive strain at 1 Hz for 3 hours alongside a free swelling control. Loaded constructs were harvested 0, 3, 12, and 24 hours after loading. (**B**) PCA comparing the free swelling and 0, 3, 12, and 24 hour-post-loading samples for WT, V620I, and T89I. Arrows indicate the trajectory over time for each cell line. Two samples at 3 hours to show reproducibility. (**C**) The number of up-regulated differentially expressed genes at each time point after loading compared to respective lines' free swelling control. T89I had more than twice the number of up-regulated DEGs in WT. (**D**) Venn diagrams comparing the up-regulated DEGs at each time point for each cell line. Genes were typically unique to each time point; however, 0 and 3 hours and 12 and 24 hours showed the most similarity.

We compared expression over time of each of the three lines for cyclic adenosine monophosphate (cAMP) and Ca^{2+} responsive transcription factors and other TRPV4-responsive target genes as previously identified in porcine chondrocytes (*11*) (Figure 6.4A-I). There was

immediate upregulation after loading, with higher expression in the severe T89I line, of transcription factors jun proto-oncogene, AP-1 transcription factor subunit (*JUN*: 0 hr, T89I vs. WT p<0.0001, T89I vs. V620I p<0.0001) and early growth response 1 and 2 (*EGR1*: 0 hr, T89I vs. WT p <0.0001, T89I vs. V620I p=0.0043; *EGR2*: 0 hr, T89I vs. WT p < 0.0001; Figure 6.4A-C). Nuclear receptor subfamily 4 group A member 2 (*NR4A2*) showed upregulation at 0 hours in T89I (T89I vs. WT p<0.0001) but 3 hours in WT (WT vs. V620I p=0.0004, WT vs. T89I p=0.0003; Figure 6.4D). Bone morphogenic proteins 2 and 6 (*BMP2* and *BMP6*) had peak expression at 3 hours post loading, with slightly higher expression in mutants (3 hr *BMP2*, T89I vs. WT p=0.0009; Figure 6.4E-F). However, WT had higher *BMP2* expression at 24 hours (WT vs. V620I p<0.0001). Fos proto-oncogene, AP-1 transcription factor subunit (*FOS*) was upregulated immediately after loading but had much lower expression in T89I (3 hr, T89I vs. WT p=0.0019; Figure 6.4G). Nuclear receptor subfamily 4 group A member 3 (*NR4A3*; also known as *NOR-1;* 3 hr, WT vs. V620I p=0.0018, WT vs. T89I p<0.0001) and CAMP responsive element binding protein 1 (*CREB1*; ns) both had higher expression in WT compared to mutants and were upregulated short- and long-term, respectively (Figure 6.4H-I).

Given that the TRPV4 mutants and WT showed similar trends, with varying expression levels, we next investigated how similar the DEGs were between lines at each time point. The majority of WT's DEGs were shared with at least one mutant at each time point other than 12 hours with 74%, 81%, 36%, and 57% of the WT DEGs shared with both V620I and T89I at 0, 3, 12, and 24 hours, respectively (Figure 6.4J). V620I also shared the majority of the DEGs with the other two lines and shared 43%, 41%, 44%, 24% of its total DEGs with T89I alone at 0, 3, 12, and 24 hours, respectively (Figure 6.4J). However, T89I was the most unique of the 3 lines with 68%, 35%, 32%, and 54% of the total DEGs being unique to T89I at 0, 3, 12, and 24 hours,

respectively (Figure 6.4J). These data indicate that the TRPV4 mutations were more sensitive to loading with an increase in the number of upregulated genes as opposed to an altered response to loading by changing the upregulated genes.

To investigate the overall expression pattern of the loading response and the expression levels of the shared DEGS, we used hierarchical k means clustering. The loading response resulted in 4 clusters (Figure 6.4K-O). The largest cluster (i.e., cluster 1) represented a long-term response with genes that are upregulated at 12 and 24 hours post loading (Figure 6.4K-L). WT had the highest mean counts by 24 hours; however, it also had the highest counts in the free swelling control (Figure 6.4K-L). Cluster 2 and 3 represented the short-term response (Figure 6.4K, M-N). Genes in cluster 2 had an increase in expression 3 hours after loading and had highest expression in T89I chondrocytes (Figure 6.4K, M). Genes in cluster 3 had increased expression at 0 and 3 hours in V602I and T89I and decreased expression at 12 and 24 hours in all lines (Figure 6.4K, N). Finally, cluster 4 represented genes downregulated by loading with the highest expression in WT (Figure 6.4K, O).
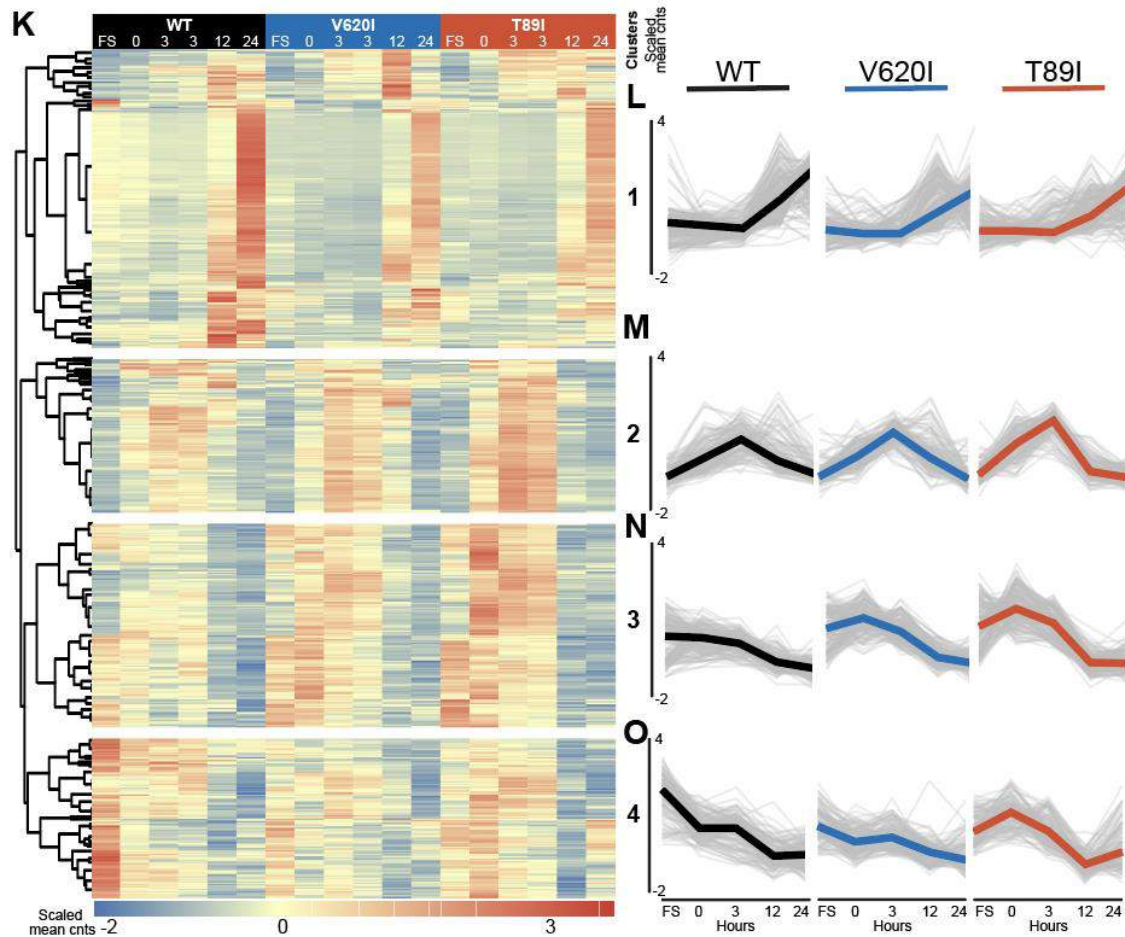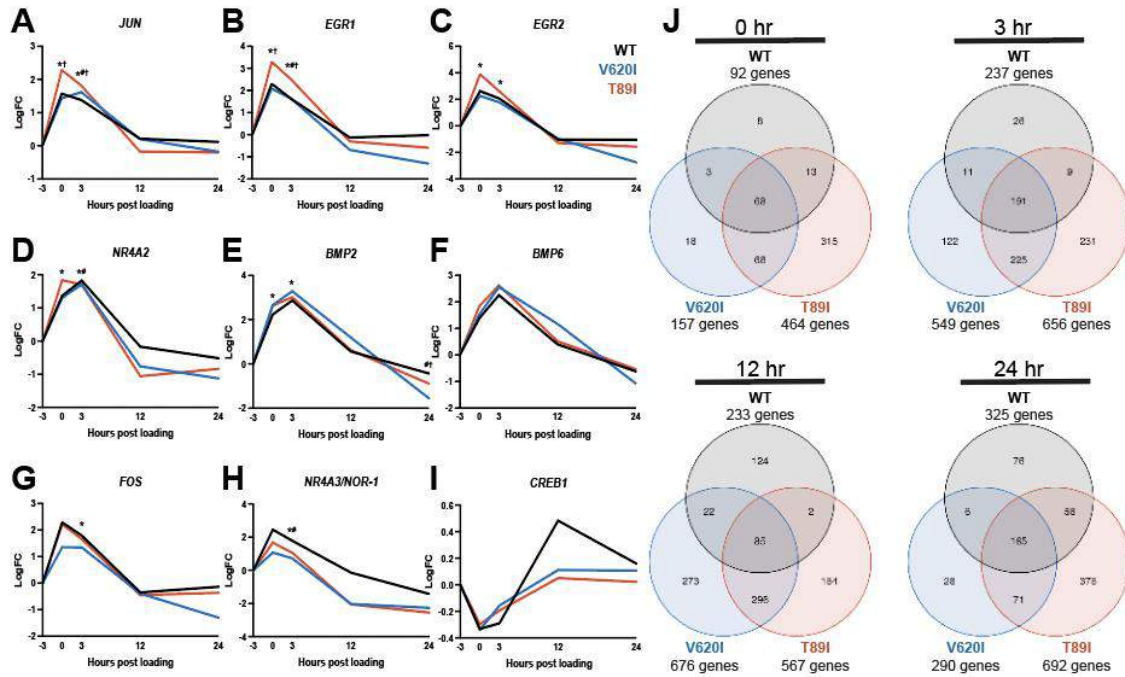
Figure 6.4 TRPV4 mutants had an altered and increased response to loading. (**A-I**) CAMP, Ca^{2+} responsive, and TRPV4 target genes *JUN* (**A**), *EGR1* (**B**), *EGR2* (**C**), *NR4A2* (**D**), *BMP2* (**E**), *BMP6* (**F**), *FOS* (**G**), *NR4A2/NOR-1* (**H**), *CREB1* (**I**) show altered response profiles between WT, V620I, and T89I. *$p<0.01$ for T89I vs. WT; †$p<0.01$ for T89I vs. V620I; #$p<0.01$ for V620I vs. WT. (**J**) Venn diagrams comparing cell lines at each time point indicate TRPV4 mutations upregulate many of the same as and additional genes compared to WT. (**K**) Hierarchical clustering of the DEGs into 4 clusters. (**L-O**) The scaled mean count profile of each line within the long-term upregulation cluster (**L**), 3-hour upregulation cluster (**M**), 0-hour upregulation cluster (**N**), and the downregulation cluster (**O**).

6.4.3 Proliferative genes are upregulated long-term after loading

We investigated cluster 1 to understand the long-term response to loading (i.e., 12 and 24 hours post-loading). Using the genes in cluster 1, we identified the top 20 upregulated genes for each line at 12- and 24-hours post-loading and plotted the LogFC in a heatmap (Figure 6.5A). Despite the mean count trends, mutants typically had higher LogFC of the top DEGs compared to WT, likely because WT had higher expression of these genes in the free swelling control. There were a few genes with the highest expression in V620I; these included cell adhesion genes integrin subunit alpha 5 (*ITGA5*) and CXADR like membrane protein (*CLMP*), cell proliferation regulator ALK and LTK ligand 2 (*ALKAL2*), and ECM remodeling protein matrix metallopeptidase 10 (*MMP10*). WT had high expression, despite little to no expression in mutants, of a few genes such as SRY-box transcription factor 12 (*SOX12*) and vascular endothelial growth factor B (*VEGFB*). However, most of the genes showed increasing expression from WT to the severe T89I mutant line. For example, many histone genes (e.g., *H1-2* through *5*, *H2BC14*, *H4C1*) had high expression at 24 hours for all lines but was highest for T89I. These genes also started increasing in expression at 12 hours in V620I and T89I but not in WT. Some helicase genes (e.g., *MCM2, MCM5, MCM6, MCM10*) had high expression at 12 hours, which slightly decreased at 24 hours, and was stronger in the mutants than WT.

Since many of the top up-regulated DEGs from cluster 1 were shared among the three cell lines, albeit higher expression in mutants, we next investigated genes that were uniquely

upregulated long-term in the mutants but not WT. We plotted the LogFC of top 25 upregulated DEGs unique to V620I and T89I at 12 and 24 hours in a heatmap (Figure 6.5B). Similar to the top genes in cluster 1, many of the long-term DEGs in mutants also showed increased expression in WT, although not significant. We observed that for many genes, there was increased expression at more time points in T89I compared to V620I and WT. An increase in expression and time of expression was associated with an increase in disease severity in many genes, including Ca^{2+} binding proteins *S100A3* and *S100A4,* anti-synthetic insulin growth factor binding protein 3 (*IGFBP3*), metalloproteases tolloid like 1 (*TLL1*) and pappalysin 1 (*PAPPA*), and inflammatory interleukin 17 receptor C (*IL17RC*). Additionally, we observed that common biological processes and pathways associated with the mutant-specific DEGs were associated with cell cycle, mitosis, proliferation, and DNA elongation and replication, such as proliferative histone *H1-2* and transcription factor *E2F1* and mini-chromosome maintenance protein *MCM3*.

To determine the transcription factors that are driving the response to loading at 12 and 24 hours, particularly those driving the differing responses between lines, we determined the transcription factors associated with the upregulated genes at each time point using TRRUST (Figure 6.5C-D). *E2F1* and *E2F4* were both strongly associated with V620I and T89I, but not WT, at 12 hours; however, at 24 hours, they became associated with all three lines (Figure 6.5C-D). *TP53* had a similar pattern but remained stronger in the mutants despite an increase in association in WT at 24 hours. All three are tumor suppressors and play a role in cell cycle control. Interestingly, the association of transcription factors between mutants and WT is more correlated at 24 hours (V620I vs. WT r^2=0.8081, T89I vs. WT r^2=0.8118) than 12 hours (V620I vs. WT r^2=0.1822, T89I vs. WT r^2=0.0999), indicating the differences in response due to mutant TRPV4 is occurring earlier.

To better understand what pathways the upregulated genes were associated with, we used g:Profiler to identify top KEGG and REAC pathways. V620I and T89I had higher association with many DNA replication and stress and cell cycle processes compare to WT, both at 12 and 24 hours (Figure 6.5E-F). The upregulation of many histone genes resulted in an association with DNA damage disorders such as systemic lupus erythematosus and alcoholism. Interestingly, lupus was only associated with T89I at 12 hours (Figure 6.5E); however, at 24 hours, it was more strongly associated with WT and V620I (Figure 6.5F).

255

Figure 6.5 Long-term response to loading. (**A**) Top 20 up-regulated long-term genes from cluster 1. Most of the genes show higher, and earlier, expression in mutants than WT. (**B**) The top 25 genes upregulated in V620I and T89I, but not WT, at 12 and 24 hours. (**C-D**) Associated transcription factors with the upregulated DEGs at 12 hours (**C**) and 24 hours (**D**). Log_{10}(p value of association) based on TRRUST data base plotted for V620I vs. WT and T89I vs. WT. Colored transcription factors indicate a stronger association with one line or the other. Linear fit indicates how correlated the mutant's associated transcription factors are to WT's. (**E-F**) The top associated KEGG and REAC pathways to the upregulated DEGs at 12 hours (**E**) and 24 hours (**F**) for each line. Circle color represents the cell line, and circle size represents the $-log_{10}(p_{adj})$.

6.4.4 Loading upregulates ECM-related proteins, particularly with mutant TRPV4

Next, we investigated clusters 2 and 3 to understand the short-term response (i.e., 0 and 3 hours

post loading). We plotted a heatmap with the LogFC of the top 20 upregulated genes in clusters 2

and 3 for each line 0- and 3-hours post-loading (Figure 6.6A). Most genes showed increased

expression at both 0 and 3 hours with higher expression at 3 hours. Interestingly, many of these

genes also showed high expression at 12 hours but only in the V620I line. Interleukin 1 receptor

like 1 (*IL1RL1*) was upregulated at 0, 3, and 12 hours for all lines but had the highest expression

in V620I. In fact, most genes had higher expression in mutants than WT. Some of the top

upregulated genes included actin filament protector xin actin binding repeat containing 1

(*XIRP1*), integrin signaling and actin linker FERM domain containing kindlin 1 (*FERMT1*),

tyrosine phosphorylation-dependent regulator CUB domain containing protein 1 (*CDCP1*),

TGFβ family member inhibin subunit beta A (*INHBA*), mechanoresponsive FOS family member

FosB proto-oncogene, AP-1 transcription factor subunit (*FOSB*), mechanoresponsive

transcription factors early growth response 1 and 2 (*EGR1* and *EGR2*), negative regulator of the

MAPK family dual specificity phosphatase 2 (*DUSP2*), heparin binding epidermal growth factor

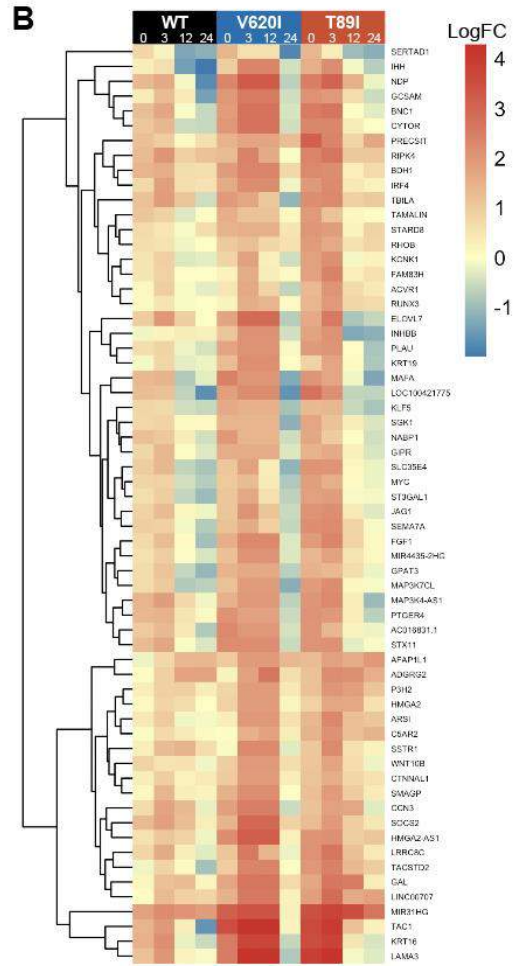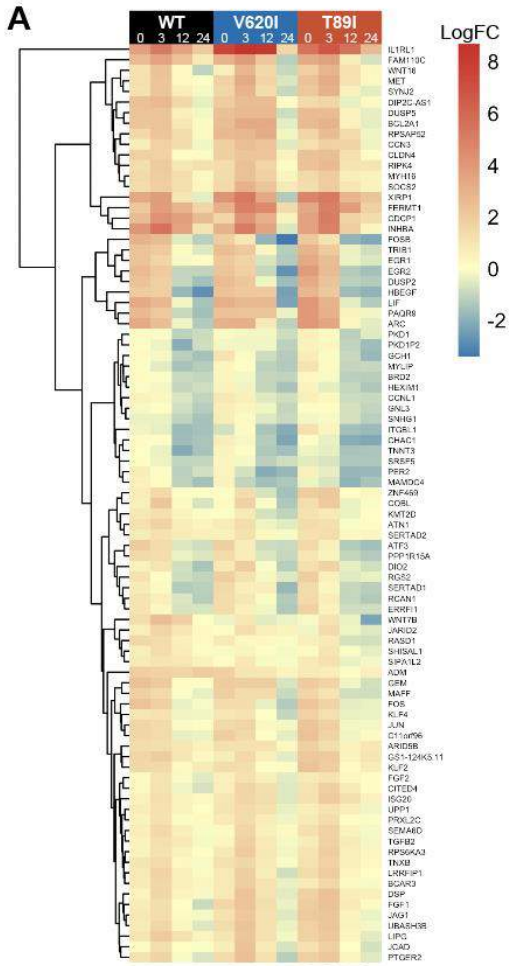like growth factor (*HBEGF*)*,* and interleukin 6 family cytokine *LIF*.

Furthermore, we explored the DEGs unique to V620I and T89I at 0 and 3 hours. The top

25 mutant-specific, short-term DEGs and their LogFC were plotted in a heatmap (Figure 6.6B).

As expected, there was a slight, non-significant upregulation of many genes in WT as well. There was also more sustained upregulation of a few genes in T89I compared to V620I. Short-term genes were typically upregulated at either 0 and 3 hours or at 3 and 12 hours. However, interestingly, some genes showed upregulation and 0 and 3 for T89I but 3 and 12 for V620I, showing a faster response of the severely mutated TRPV4. Nuclear factor kappa B (NFκB) regulator long non-coding RNA *MIR31HG*, BMP/SMAD-regulated keratin 16 (*KRT16*), and mechanical signal transducer laminin subunit alpha 3 (*LAMA3*) were among the top mutant-specific genes. Proliferation was a common theme for both short- and long-term with upregulation of cell cycle progression oncogene *MYC* and chondrocyte proliferation gene high mobility group AT-hook 2 (*HMGA2*) at 0 and 3 hours and 3 and 12 hours, respectively. The short-term, mutant-specific genes also showed association with IL4/IL13 signaling, cell migration and mobility, integrins, ligands, and ECM (e.g., upregulation of collagen chain assembly gene prolyl 3-hydroxylase 2 [*P3H2*] at 3 and 12 hours). Despite the dysregulated endochondral ossification associated with brachyolmia and metatropic dysplasia, many hypertrophy-associated genes were upregulated with loading in V620I and T89I, including RUNX Family Transcription Factor 3 (*RUNX3*), Indian hedgehog (*IHH*), and fibroblast growth factor 1 (*FGF1*), which is found in growth plate cartilage.

We then looked at the transcription factors associated with upregulated genes at 0 and 3 hours for each line using TRRUST. Both 0 and 3 hours showed less correlation between the mutants and WT than at 24 hours; however, the 3 lines were more similar at 3 hours (0 hr: V620I vs. WT r^2=0.4638, T89I vs. WT r^2=0.4948; 3 hr: V620I vs. WT r^2=0.4908, T89I vs. WT r^2=0.5639; Figure 6.5C, 6.6C-D). Pro-inflammatory nuclear factor kappa B subunit 1 (*NFKB1*) was strongly associated with the two mutant lines at 0 hours and became more associated with

WT at 3 hours, especially compared to T89I. T89I was highly associated with transcription factor *SP1* at both 0 and 3 hours while V620I was associated with *SP1* at 3 hours. Enhancer of zeste homolog 2 (*EZH2*), an epigenetic regulator of development and differentiation, was associated with T89I and V620I, but not WT, at 0 and 3 hours, respectively. V620I and T89I also showed unique association compared to WT with TGFβ family signaling antagonist SMAD family member 7 (*SMAD7*) and NFκB inhibitor zinc finger protein 382 (*ZNF382*), respectively, at 3 hours. WT, however, had a stronger association with cytokine and chemokine transcription factor ETS proto-oncogene 1 (*ETS1*) than both mutations at 0 hours. *MEF2D* was also unique to WT's upregulated genes at 3 hours.

Again, we assessed the top associated KEGG and REAC pathways with the upregulated genes in each line at 0 and 3 hours (Figure 6.6E-F). The three lines shared a similar association with nerve growth factor (NGF)-stimulated transcription at 0 hours, which was slightly decreased at 3 hours in the mutant lines. At 0 hours, WT showed an association with inflammatory pathways such as interleukin 17 (IL-17) and tumor necrosis factor (TNF) signaling and cytokine-cytokine receptors unlike the mutations. In contrast, T89I uniquely had a strong association with ECM organization and receptors, collagen formation, and proteoglycan synthesis at 0 and 3 hours.
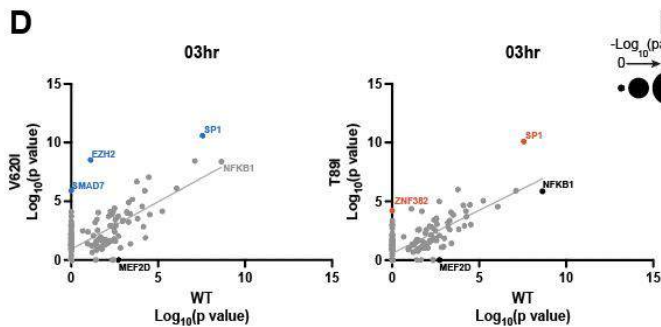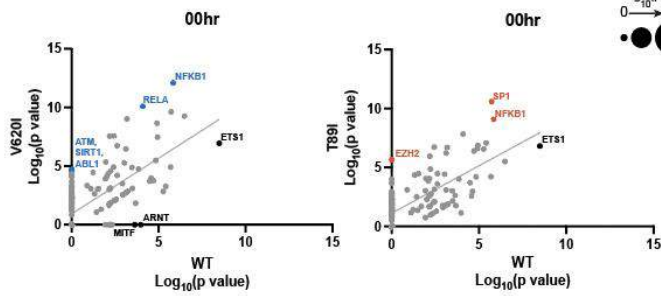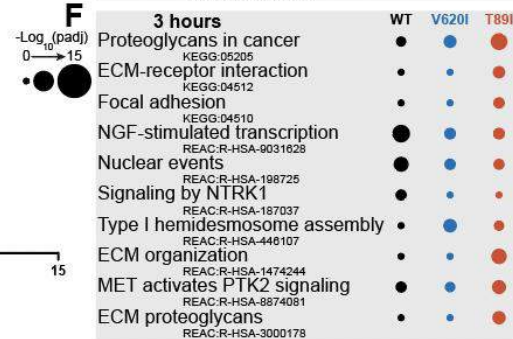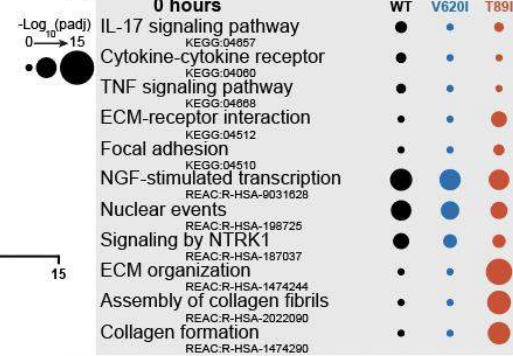
Figure 6.6 Short-term response to loading. (**A**) Top 20 up-regulated genes short-term from clusters 2 and 3. There is a similar expression profile between the three cell lines with slightly higher expression in mutants than WT. (**B**) The top 25 genes upregulated in V620I and T89I, but not WT, at 0 and 3 hours. (**C-D**) Associated transcription factors with the upregulated DEGs at 0 hours (**C**) and 3 hours (**D**). Log_{10}(p value of association) based on TRRUST data base plotted for V620I vs. WT and T89I vs. WT. Colored transcription factors indicate a stronger association with one line or the other. Linear fit indicates how correlated the mutant's associated transcription factors are to WT's. (**E-F**) The top associated KEGG and REAC pathways to the upregulated DEGs at 0 hours (**E**) and 3 hours (**F**) for each line. Circle color represents the cell line, and circle size represents the $-log_{10}(p_{adj})$.

6.5 Discussion

To investigate how skeletal dysplasia-causing mutations alter TRPV4 mechanotransduction, we used CRISPR-Cas9-edited hiPSCs harboring the moderate V620I and severe, neonatally lethal T89I mutations. hiPSC-derived chondrocytes produced matrix rich in sGAGs and COL2A1 after 2 weeks of culture in agarose, and the constructs were then mechanically loaded to physiologically mimic TRPV4 activation during development. V620I and T89I increased TRPV4 mechanosensitivity and resulted in increased upregulation both in fold change and number of differentially expressed genes (vs. free swelling controls) compared to WT. When we evaluated the associated transcription factors and pathways with the up-regulated genes, mutant-specific genes were associated with ECM, inflammation, and cell mobility at 0 and 3 hours post-loading and proliferation and cell cycle at 12 and 24 hours post-loading. The mutant associated transcription factors were the most different from WT 12 hours post loading; however, the three lines became more similar at 24 hours. Our results indicate that gain-of-function mutations V620I and T89I are hypersensitive to mechanical stimulus. The increased transcriptomic profiles and downstream signaling likely lead to dysfunctional skeletal development resulting in moderate brachyolmia and severe metatropic dysplasia.

To the best of our knowledge, this is the first study to mechanically load hiPSC-derived chondrocytes and investigate mechanotransduction of mutant TRPV4. After 4 weeks in culture,

WT hiPSC-derived chondrocyte-ridden agarose constructs achieved an elastic modulus of 100 kPa. These values are lower than what has been reported for adult cartilage tissue and tissue-engineered cartilage with fibrous scaffold systems (compressive Young's modulus = 240-850 kPa; aggregate modulus = 100-2000 kPa; Poisson's ratio = 0.06-0.3) (*33*). However, the modulus is greater than free-swelling primary porcine chondrocytes in agarose for 6 weeks, which had a Young's modulus of approximately 65 kPa (*4*), and hiPSC-derived chondrocytes in a collagen type I scaffold, which had an average aggregate modulus of 85 kPa (Young's modulus = 62.4-83.4 kPa, assuming Poisson's ratio is consistent with reported values of primary cartilage (*33*)) (*34*). The increase in modulus from 100 kPa to 150 kPa with mutant hiPSC-derived chondrocytes, despite it not being significant, is indicative of increased TRPV4 activation. Not only did GSK205 inhibition of TRPV4 slightly decrease the mechanical properties, but TRPV4 activation via mechanical, osmotic, and chemical stimuli has been shown to increase mechanical properties of cartilage (*4, 35*).

The increased activation of mutant TRPV4 was further supported in this study with the increase in upregulated DEGs and fold change of DEGs in response to cyclical, compressive loading. Interestingly, there is conflicting evidence of the role of the gain-of-function V620I and T89I mutations on channel activity. Studies using *Xenopus* oocytes, porcine chondrocytes, and hiPSC-derived chondrocytes previously found both increases and decreases in basal, chemically activated, and osmotically activated V620I-TRPV4 and T89I-TRPV4 compared to WT (*16-18*). While it is well known that TRPV4 is activated by mechanical and osmotic loading and chemical agonists, among other stimuli, the mechanisms of action are not well understood. Therefore, TRPV4 may be activated and respond differently to various agonists. Additionally, the mutation may alter sensitivity to these agonists differently. In fact, the effects of mutations on TRPV4

mechanotransduction in chondrocytes has not been studied before despite studies in primary and derived (e.g., hiPSC, dental pulp mesenchymal cells) chondrogenic, osteogenic, and neurogenic cell types and model systems (e.g., oocytes) (*16, 17, 36-40*).

Histology from patients with brachyolmia and metatropic dysplasia show fewer hypertrophic chondrocytes with cartilage islands within immature, woven bone, likely due to dysfunctional endochondral ossification (*12, 15, 41*). Additionally, our previous study showed that V620I and T89I inhibited BMP4-induced hypertrophy of hiPSC-derived chondrocytes (*18*). In contrast, osteoblasts derived from dental pulp mesenchymal stem cells harboring metatropic dysplasia-causing TRPV4 mutation L619F showed increased calcification and expression of osteogenic genes runt-related transcription factor 2 (*RUNX2*), osteocalcin (*OCN*), and nuclear factor of activated T cells 1 (*NFATC1*) (*38*). Therefore, it was hypothesized that ectopic ossification occurs after direct osteoblastic differentiation of mesenchymal cells (*15, 38*), indicative of dysfunction in the chondrocyte, hypertrophy, endochondral ossification pathway. This was again highlighted in our results with both pro- and anti-hypertrophic gene expression in response to loading in mutant chondrocytes compared to WT. For example, mutants had lower expression compared to WT of skeletal development regulator *SOX12* (*42*) 12 and 24 hours post loading. In contrast, growth plate protein *FGF1* (*43*) and endochondral ossification regulators *IHH* and *RUNX3* (*44*) were upregulated at 0 and 3 hours post loading. Despite the conflicting expression of hypertrophy-associated genes, we observed an increase in expression of genes associated with inflammation, cell mobility, and proliferation in V620I and T89I chondrocytes, which may be responsible for the dysregulated skeletal development.

Given that proliferation inhibits chondrocyte maturation (*45*), the increased expression and association with proliferative genes, such as *E2F1*, *TP53, SP1*, and *MYC* in mutants could be

preventing chondrocyte hypertrophy. There was a unique upregulation of *E2F1* in mutants at 12 and 24 hours, particularly in T89I. Additionally, association between the transcription factor and the upregulated genes occurred earlier (i.e., 12 hours vs. 24 hours) in mutants compared to WT. Beyond *E2F1's* role in increasing proliferation, overexpression of the gene has been found to suppress endochondral ossification with reduced chondrocyte maturation, collagen type X expression and secretion, hypertrophic zones, and organization of the growth plate (*46, 47*). We also saw a similar association between upregulated genes and *TP53* with the association occurring in mutants at 12 and 24 hours but only a small association with WT at 24 hours. Interestingly, unlike *E2F1*, *TP53* was not a top upregulated gene; however, it is associated with many processes and genes involved in proliferation and endochondral ossification. *TP53* is regulated by cell cycle checkpoint kinase *ATM,* which was uniquely associated with V620I DEGs compared to WT immediately after loading. Signaling from and overexpression of p53, the protein encoded by *TP53*, has been shown to inhibit chondrocyte and osteoblast differentiation (*48-51*). In fact, an increase in *TP53* expression in MSCs promoted adipogenic but inhibited osteogenic differentiation (*52*). This anti-osteogenic effect was rescued by FGF2-induced *TWIST2* expression (*52*), which is also uniquely associated with WT at 24 hours.

Furthermore, members of the p53 family have been found to promote *SMAD7* expression (*53*). Upregulated genes in V620I at 3 hours showed high association with *SMAD7,* which inhibits TGFβ and activin signaling, and T89I had the highest expression of the transcription factor. While *SMAD7* is required to mediate cell stress in the growth plate (*54*), overexpression inhibited chondrocyte hypertrophy (*55*). Interestingly, absence of *SMAD7* increased HIF1α levels (*54*), and *HIF1A* was strongly and uniquely associated with WT DEGs at 24 hours, opposite of the association with *SMAD7* at 3 hours. *MYC*, an oncogene, had increased expression

263

in and association with mutants compared to WT short- and long-term, respectively. *MYC* has been found to be present in proliferating, but not hypertrophic, chondrocytes (*56, 57*). *SP1*, a proliferative gene with decreased expression in hypertrophic chondrocytes (*51, 58*), also had increased association with mutants compared to WT at 0 and 3 hours. Despite *SP1's* role in proliferation, a member of its family, *KLF10*, inhibited chondrocyte proliferation through downregulation of *INHBB* (*59*). We did observe increased, unique expression of *INHBB* in mutants. These results are indicative of a proliferative effect of the TRPV4 mutations, which ultimately prevents proper hypertrophy.

We also observed increased association with and expression of *NFKB1* in the mutant lines in response to loading. The increase in *NFKB1* with GOF TRPV4 mutations is consistent with our previous study that used a NF-κB circuit stimulated by TRPV4 activation for drug delivery (*11*). Interestingly, the pro-inflammatory gene has been shown to promote both proliferation and apoptosis, including regulation of *TP53* (*60-62*). Furthermore, *RELA*, which is bound with *NFKB1* to form the most common NF-κB complex, prevents chondrocyte apoptosis, is active in early stage chondrogenesis, and increases degradative *ADAMTS5* expression (*63, 64*). Additionally, a study found NF-κB to inhibit osteogenic gene transcription and transcription factor binding (*65*). Despite the increase in inflammatory NF-κB signaling cascades in TRPV4 mutants in response to loading, other studies have found TRPV4 activation to have an anti-inflammatory effect. In fact, TRPV4 activation attenuated loading-induced *ADAMTS4* and *IL-1R* expression or IL-1β-induced degradation (*66, 67*). Therefore, TRPV4 activation, particularly in response to compressive loading, likely has both pro- and anti-inflammatory components due to differences in the activation of inflammatory signaling cascades.

This study provides novel insights into hiPSC-derived chondrocyte mechanotransduction

on a transcriptomic level in addition to how this signaling is altered by dysplasia-causing TRPV4 mutations V620I and T89I. However, it must be noted that this study has a few limitations. First, we had limited sample size due to the complexity of the experiment and the number of groups. The three-hour time point had two replicates that confirmed consistent results between samples. Also, the potential pathways responsible for the altered mechanotransduction that leads to the dysfunctional skeletal development have not been validated. In future experiments, we will repeat the loading. We will increase the sample size and inhibit TRPV4 and specific pathways (e.g., *E2F1,* p53, NF-κB/cMYC) to investigate gene expression. We will also analyze proliferation with an EdU assay as another output to validate the proposed pathways.

6.6 Conclusion

The results of the current and future experiments will offer better understandings of hiPSC-derived tissue-engineered cartilage and the role of mechanical loading and TRPV4 mechanotransduction on the tissue. Furthermore, this work will provide therapeutic targets for brachyolmia and metatropic dysplasia.

6.7 References

1. A. J. Sophia Fox, A. Bedi, S. A. Rodeo, The Basic Science of Articular Cartilage: Structure, Composition, and Function. *Sports Health: A Multidisciplinary Approach* 1, 461-468 (2009).

2. F. Guilak, Biomechanical factors in osteoarthritis. *Best Practice & Research Clinical Rheumatology* 25, 815-823 (2011).

3. J. Sanchez-Adams, H. A. Leddy, A. L. McNulty, C. J. O'Conor, F. Guilak, The Mechanobiology of Articular Cartilage: Bearing the Burden of Osteoarthritis. *Current Rheumatology Reports* 16, (2014).

4. C. J. O'Conor, H. A. Leddy, H. C. Benefield, W. B. Liedtke, F. Guilak, TRPV4-mediated mechanotransduction regulates the metabolic response of chondrocytes to dynamic loading. *Proc Natl Acad Sci U S A* 111, 1316-1321 (2014).

5. Z. Zhao *et al.*, Mechanotransduction pathways in the regulation of cartilage chondrocyte homoeostasis. *Journal of Cellular and Molecular Medicine* 24, 5408-5419 (2020).

6. F. Guilak, R. J. Nims, A. Dicks, C. L. Wu, I. Meulenbelt, Osteoarthritis as a disease of the cartilage pericellular matrix. *Matrix Biol* 71-72, 40-50 (2018).

7. W. Everaerts, B. Nilius, G. Owsianik, The vanilloid transient receptor potential channel TRPV4: From structure to disease. *Progress in Biophysics and Molecular Biology* 103, 2-17 (2010).

8. M. Jin *et al.*, Determinants of TRPV4 Activity following Selective Activation by Small Molecule Agonist GSK1016790A. *PLoS ONE* 6, e16713 (2011).

9. S. Muramatsu *et al.*, Functional Gene Screening System Identified TRPV4 as a Regulator of Chondrogenic Differentiation. *Journal of Biological Chemistry* 282, 32158-32167 (2007).

10. C. J. O'Conor, T. M. Griffin, W. Liedtke, F. Guilak, Increased susceptibility ofTrpv4-deficient mice to obesity and obesity-induced osteoarthritis with very high-fat diet. *Annals of the Rheumatic Diseases* 72, 300-304 (2013).

11. R. J. Nims *et al.*, A synthetic mechanogenetic gene circuit for autonomous drug delivery in engineered tissues. *Science Advances* 7, eabd9858 (2021).

12. D. Krakow, D. L. Rimoin, The skeletal dysplasias. *Genetics in Medicine* 12, 327-341 (2010).

13. S. Sun, in *Mutagenesis,* Kang, Ed. (InTech, 2012).

14. M. J. Rock *et al.*, Gain-of-function mutations in TRPV4 cause autosomal dominant brachyolmia. *Nat Genet* 40, 999-1003 (2008).

15. N. Camacho *et al.*, Dominant TRPV4 mutations in nonlethal and lethal metatropic dysplasia. *Am J Med Genet A* 152A, 1169-1177 (2010).

16. H. A. Leddy *et al.*, Follistatin in chondrocytes: the link between TRPV4 channelopathies and skeletal malformations. *FASEB J* 28, 2525-2537 (2014).

17. S. Loukin, Z. Su, C. Kung, Increased basal activity is a key determinant in the severity of human skeletal dysplasia caused by TRPV4 mutations. *PLoS One* 6, e19533 (2011).

18. A. R. Dicks *et al.*, Skeletal dysplasia-causing TRPV4 mutations suppress the hypertrophic differentiation of human iPSC-derived chondrocytes. *bioRxiv*, 2021.2006.2015.448562 (2021).

19. S. S. Adkar *et al.*, Step-Wise Chondrogenesis of Human Induced Pluripotent Stem Cells and Purification Via a Reporter Allele Generated by CRISPR-Cas9 Genome Editing. *Stem Cells* 37, 65-76 (2019).

20. A. Dicks *et al.*, Prospective isolation of chondroprogenitors from human iPSCs based on cell surface markers identified using a CRISPR-Cas9-generated reporter. *Stem Cell Res Ther* 11, 66 (2020).

21. C. L. Wu *et al.*, Single cell transcriptomic analysis of human pluripotent stem cell chondrogenesis. *Nat Commun* 12, 362 (2021).

22. A. Dobin *et al.*, STAR: ultrafast universal RNA-seq aligner. *Bioinformatics* 29, 15-21 (2013).

23. Y. Liao, G. K. Smyth, W. Shi, featureCounts: an efficient general purpose program for assigning sequence reads to genomic features. *Bioinformatics* 30, 923-930 (2014).

24. R. Patro, G. Duggal, M. I. Love, R. A. Irizarry, C. Kingsford, Salmon provides fast and bias-

aware quantification of transcript expression. *Nat Methods* 14, 417-419 (2017).

25. L. Wang, S. Wang, W. Li, RSeQC: quality control of RNA-seq experiments. *Bioinformatics* 28, 2184-2185 (2012).

26. M. I. Love, W. Huber, S. Anders, Moderated estimation of fold change and dispersion for RNA-seq data with DESeq2. *Genome Biol* 15, 550 (2014).

27. H. Wickham, *ggplot2: Elegant Graphics for Data Analysis*. Use R! (Springer-Verlag New York, ed. 1, 2009).

28. H. Chen, P. C. Boutros, VennDiagram: a package for the generation of highly-customizable Venn and Euler diagrams in R. *BMC Bioinformatics* 12, 35 (2011).

29. R. Kolde. (2015).

30. U. Raudvere *et al.*, g:Profiler: a web server for functional enrichment analysis and conversions of gene lists (2019 update). *Nucleic Acids Res* 47, W191-W198 (2019).

31. H. Han *et al.*, TRRUST v2: an expanded reference database of human and mouse transcriptional regulatory interactions. *Nucleic Acids Res* 46, D380-D386 (2018).

32. N. Altman, M. Krzywinski, Clusterinig. *Nature Methods* 14, 545-546 (2017).

33. C. J. Little, N. K. Bawolin, X. Chen, Mechanical properties of natural cartilage and tissue-engineered constructs. *Tissue Eng Part B Rev* 17, 213-227 (2011).

34. J. M. Middendorf *et al.*, Multiscale mechanics of tissue-engineered cartilage grown from human chondrocytes and human-induced pluripotent stem cells. *Journal of Orthopaedic Research* 38, 1965-1973 (2020).

35. J. K. Lee, C. A. Gegg, J. C. Hu, P. H. Kass, K. A. Athanasiou, Promoting increased mechanical properties of tissue engineered neocartilage via the application of hyperosmolarity and 4alpha-phorbol 12,13-didecanoate (4alphaPDD). *J Biomech* 47, 3712-3718 (2014).

36. K. Nonaka *et al.*, Novel gain-of-function mutation of TRPV4 associated with accelerated chondrogenic differentiation of dental pulp stem cells derived from a patient with metatropic dysplasia. *Biochem Biophys Rep* 19, 100648 (2019).

37. B. Saitta *et al.*, Patient-derived skeletal dysplasia induced pluripotent stem cells display abnormal chondrogenic marker expression and regulation by BMP2 and TGFbeta1. *Stem Cells Dev* 23, 1464-1478 (2014).

38. X. Han *et al.*, Accelerated osteoblastic differentiation in patient-derived dental pulp stem cells carrying a gain-of-function mutation of TRPV4 associated with metatropic dysplasia. *Biochem Biophys Res Commun* 523, 841-846 (2020).

39. R. Das, C. Goswami, TRPV4 expresses in bone cell lineages and TRPV4-R616Q mutant causing Brachyolmia in human reveals "loss-of-interaction" with cholesterol. *Biochem Biophys Res Commun* 517, 566-574 (2019).

40. X. Sun *et al.*, Impaired neurite development and mitochondrial dysfunction associated with calcium accumulation in dopaminergic neurons differentiated from the dental pulp stem cells of a patient with metatropic dysplasia. *Biochem Biophys Rep* 26, 100968 (2021).

41. D. L. Rimoin *et al.*, The Skeletal Dysplasias: Clinical Molecular Correlations. *Annals of the New York Academy of Sciences* 1117, 302-309 (2007).

42. P. Bhattaram *et al.*, SOXC proteins amplify canonical Wnt signaling to secure nonchondrocytic fates in skeletogenesis. *Journal of Cell Biology* 207, 657-671 (2014).

43. P. Krejci, D. Krakow, P. B. Mekikian, W. R. Wilcox, Fibroblast Growth Factors 1, 2, 17, and 19 Are the Predominant FGF Ligands Expressed in Human Fetal Growth Plate Cartilage. *Pediatric Research* 61, 267-272 (2007).

44. C. Prein, F. Beier. (Elsevier, 2019), pp. 25-47.

45. A. Shimazu *et al.*, Syndecan-3 and the control of chondrocyte proliferation during endochondral ossification. *Exp Cell Res* 229, 126-136 (1996).

46. B. Scheijen, M. Bronk, T. van der Meer, R. Bernards, Constitutive E2F1 overexpression delays endochondral bone formation by inhibiting chondrocyte differentiation. *Mol Cell Biol* 23, 3656-3668 (2003).

47. T. Yanagino, K. Yuasa, M. Nagahama, Y. Matsuda, A. Tsuji, Transcriptional regulation of fibrillin-2 gene by E2F family members in chondrocyte differentiation. *Journal of Cellular Biochemistry* 106, 580-588 (2009).

48. J. Wu *et al.*, EFTUD2 gene deficiency disrupts osteoblast maturation and inhibits chondrocyte differentiation via activation of the p53 signaling pathway. *Human Genomics* 13, (2019).

49. N. Artigas *et al.*, p53 inhibits SP7/Osterix activity in the transcriptional program of osteoblast differentiation. *Cell Death & Differentiation* 24, 2022-2031 (2017).

50. X. Wang *et al.*, p53 functions as a negative regulator of osteoblastogenesis, osteoblast-dependent osteoclastogenesis, and bone remodeling. *Journal of Cell Biology* 172, 115-125 (2006).

51. F. Oliver *et al.*, Transcription factors TP53 and SP1 and the osteogenic differentiation of dental stem cells. *Differentiation* 83, 10-16 (2012).

52. S. V. Boregowda *et al.*, Basal p53 expression is indispensable for mesenchymal stem cell integrity. *Cell Death & Differentiation* 25, 679-692 (2018).

53. L. De Rosa *et al.*, p63 Suppresses Non-epidermal Lineage Markers in a Bone Morphogenetic Protein-dependent Manner via Repression of Smad7. *Journal of Biological Chemistry* 284, 30574-30582 (2009).

54. K. D. Estrada *et al.*, Smad7 regulates terminal maturation of chondrocytes in the growth plate. *Developmental Biology* 382, 375-384 (2013).

55. T. Iwai, J. Murai, H. Yoshikawa, N. Tsumaki, Smad7 Inhibits Chondrocyte Differentiation at Multiple Steps during Endochondral Bone Formation and Down-regulates p38 MAPK Pathways. *Journal of Biological Chemistry* 283, 27154-27164 (2008).

56. M. Iwamoto *et al.*, Expression and role of c-myc in chondrocytes undergoing endochondral ossification. *J Biol Chem* 268, 9645-9652 (1993).

57. O. Ishida, Y. Tanaka, I. Morimoto, M. Takigawa, S. Eto, Chondrocytes Are Regulated by Cellular Adhesion Through CD44 and Hyaluronic Acid Pathway. *Journal of Bone and*

Mineral Research 12, 1657-1663 (1997).

58. C. Magee, M. Nurminskaya, L. Faverman, P. Galera, T. F. Linsenmayer, SP3/SP1 Transcription Activity Regulates Specific Expression of CollagenType X in HypertrophicChondrocytes. *Journal of Biological Chemistry* 280, 25331-25338 (2005).

59. L. Zheng, H. Lu, H. Li, X. Xu, D. Wang, KLF10 is upregulated in osteoarthritis and inhibits chondrocyte proliferation and migration by upregulating Acvr1 and suppressing inhbb expression. *Acta Histochem* 122, 151528 (2020).

60. S. Tilborghs *et al.*, The role of Nuclear Factor-kappa B signaling in human cervical cancer. *Crit Rev Oncol Hematol* 120, 141-150 (2017).

61. L. Zhang *et al.*, Effects of the NF-κB/p53 signaling pathway on intervertebral disc nucleus pulposus degeneration. *Molecular Medicine Reports* 22, 1821-1830 (2020).

62. R. K. Wang, X. M. Shao, J. P. Yang, H. L. Yan, Y. Shao, MicroRNA-145 inhibits proliferation and promotes apoptosis of HepG2 cells by targeting ROCK1 through the ROCK1/NF-kappaB signaling pathway. *Eur Rev Med Pharmacol Sci* 23, 2777-2785 (2019).

63. H. Kobayashi *et al.*, Biphasic regulation of chondrocytes by Rela through induction of anti-apoptotic and catabolic target genes. *Nat Commun* 7, 13336 (2016).

64. S. Itoh *et al.*, GSK-3alpha and GSK-3beta proteins are involved in early stages of chondrocyte differentiation with functional redundancy through RelA protein phosphorylation. *J Biol Chem* 287, 29227-29236 (2012).

65. R. S. Tarapore *et al.*, NF-κB Has a Direct Role in Inhibiting Bmp- and Wnt-Induced Matrix Protein Expression. *Journal of Bone and Mineral Research* 31, 52-64 (2016).

66. Y. Takeda *et al.*, Compressive mechanical stress enhances susceptibility to interleukin-1 by increasing interleukin-1 receptor expression in 3D-cultured ATDC5 cells. *BMC Musculoskeletal Disorders* 22, (2021).

67. S. Fu *et al.*, Activation of TRPV4 by mechanical, osmotic or pharmaceutical stimulation is anti-inflammatory blocking IL-1beta mediated articular cartilage matrix destruction. *Osteoarthritis Cartilage* 29, 89-99 (2021).

Chapter 7

Conclusions and Future Directions

Human induced pluripotent stems cells (hiPSCs) offer great potential in the field of cartilage tissue engineering. Beyond their extensive proliferation and differentiation capacity, hiPSCs are derived from adult somatic cells that can be harvested from a patient with minimal donor site morbidity. Here, we addressed the heterogeneity and off-target differentiation challenges associated with hiPSC chondrogenesis using a chemically defined, serum-free medium in Chapters 2-4. This improved, novel protocol creates possibilities for personalized medicine, disease modeling, and regenerative therapies.

In Chapters 5 and 6, we used the hiPSC chondrogenesis protocol for *in vitro* disease modeling. Using CRISPR-Cas9 gene editing technology, we created hiPSC lines harboring the V620I or T89I TRPV4 mutations, which cause mild brachyolmia and severe, neonatally lethal metatropic dysplasia. We differentiated the hiPSCs through chondrogenesis and into hypertrophy and tested TRPV4 activation in the hiPSC-derived chondrocytes to investigate how these mutations lead to skeletal dysplasias. We used mRNA sequencing and transcriptomic analysis to identify many key genes whose expression is altered by the mutations during chondrogenesis, hypertrophy, and loading. We found that the mutations suppressed hypertrophic differentiation, likely preventing proper endochondral ossification and long bone development. Furthermore, the mutations increased sensitivity of TRPV4 to loading with an increase in gene expression, especially of proliferative genes.

These key genes can be investigated in future studies as potential therapeutic strategies. For example, inhibition of genes upregulated in the mutants, such as *HOX* genes, could promote

chondrocyte maturation. Additionally, the BMP/TGFβ signaling pathway could be modulated to allow for chondrocyte hypertrophy. Mutant hiPSC-derived chondrocytes appeared to be more prolific than wildtype; therefore, inhibition of these proliferation pathways may restore proper mechanotransduction. In fact, we are preparing an experiment to inhibit TRPV4 signaling and other pathways identified during loading. We will investigate if this inhibition decreases proliferation and increases similarity between mutants and WT. Furthermore, it would be interesting to continue the differentiation of TRPV4-mutant chondrocytes through osteogenesis to determine additional therapeutic targets. TRPV4 is a well-known signal regulator in both bone and cartilage. Apart from skeletal dysplasia therapeutic development, these findings may also be applicable for optimizing tissue engineering, particularly from hiPSCs. In fact, the proliferative and anti-hypertrophic properties of mutant hiPSC-derived chondrocytes are ideal for cartilage tissue engineering.

Other genetic mutations can also be studied using this protocol. For example, a mutation in collagen type VI alpha chain 3 (COL6A3) has been found to increase predisposition to osteoarthritis. Therefore, we created a mutant hiPSC line, and an isogenic control, to differentiate into chondrocytes and study how this mutation leads to disease. Since COL6A3 is a primary component of the pericellular matrix, a biochemical and biomechanical filter for chondrocytes, we hypothesize that the mutation alters PCM properties rendering the chondrocyte more susceptible to injurious loading and pro-inflammatory cytokines. Our lab and collaborators are currently using these hiPSC-derived chondrocytes in an inflammatory and loading model to investigate transcriptomic and epigenetic changes and differences in mutant chondrocytes.

The large volume of chondrocytes produced in a single round of differentiation is ideal for high throughput drug screening. hiPSCs can be made from a patient suffering from a cartilage

271

disease, such as degenerative arthritis. The resulting hiPSC-derived chondrocytes can then be used for drug screening to identify the therapeutic the patient will best respond to. Ideally, in the future, the hiPSC-derived cartilage will not only be applicable *in vitro* but also *in vivo*. For that to happen, there remains many obstacles. hiPSC-derived cartilage addresses the issue of immune rejection since it can be derived from the patient's own cells. However, the mechanical properties are an order of magnitude lower than native cartilage. Moreover, due to their pluripotency, hiPSCs and hiPSC-derived cells are tumorigenic; therefore, this must be preventable prior to human implantation.

In summary, we believe the work in this thesis has made a significant contribution to the fields of tissue engineering and orthopedics. We have developed a novel hiPSC chondrogenesis protocol that addresses many current issues. We demonstrated one of the many uses for the protocol, disease modeling, to elucidate underlying mechanisms of skeletal dysplasias caused by mutations in ion channel TRPV4. We hope that the findings of these studies will be applied to the development of skeletal dysplasia therapeutics and continued *in vitro* disease modeling, drug screening, and tissue engineering for many other cartilage diseases.

Curriculum Vitae

Amanda Dicks

adicks@wustl.edu

(330) 692-0277

Professional Profile

- Biomedical Engineering PhD candidate at Washington University in St. Louis using human induced pluripotent stem cells, molecular and cellular biology techniques, including RNA sequencing, and mechanical bioreactors to study skeletal dysplasia-causing mutations in cartilage
- Project manager for a student-run nonprofit consulting group in St. Louis
- Editor-in-Chief of a trainee-run scientific communication network at Washington University
- Incoming Strategy Insights and Planning Associate at ZS Associates

Education

Washington University in Saint Louis   St. Louis, MO
Biomedical Engineering, *Doctor of Philosophy Candidate, NIH T32 Fellow*   *Aug 2021*

Indiana Institute of Technology (Indiana Tech)   Fort Wayne, IN
Biomedical Engineering, *Bachelor of Science, Summa Cum Laude*   *May 2016*

Johns Hopkins University   Coursera
Certificate, *Clinical Trial Design*   *2020*

Scientific Research Experience

Department of Orthopedic Surgery, Center of Regenerative Medicine, Musculoskeletal Research Center, and Shriners Hospital for Children
Washington University School of Medicine, *St Louis, MO*   *Aug 2016 – present*

- Study skeletal dysplasia and osteoarthritis-causing mutations to understand cartilage development, homeostasis, and function in an effort to identify therapeutic targets
- Lead a team, organize collaboration, schedule experiments, and mentor junior graduate students
- Publish peer-reviewed articles in academic journals, most notably Nature Communications
- Presented work at 6 international and institutional conferences and received a poster award
- *Skills*: project management, experimental design, data analysis, cell culture, human iPSC differentiation, RNA sequencing, histology, immunohistochemistry, RT-qPCR, biochemical analysis, mechanical loading & testing, Microsoft Office Suite, RStudio, Adobe Illustrator, GraphPad Prism

Department of Biomedical Engineering, *Undergraduate Researcher*
Indiana Tech*, Fort Wayne, IN*   *Aug 2014 – May 2016*

- Led a team in the R&D of a total revision knee arthroplasty system and individually developed a tracheostomy tube system making modifications and improvements compared to current systems on the market
- Developed a design history file (DHF) and mock FDA 510(k) submission including all regulatory documentation
- Presented work and won a presentation award at national honor society conference

Life Science and Healthcare Professional Experience

The BALSA Group, *Project Manager, Consultant*

St. Louis, MO   *July 2019 – present*

- Manage projects and workstreams from client engagement kickoff to delivery by supervising and assigning weekly tasks for three junior team members to meet external stakeholder needs
- Synthesize quantitative and qualitative results and assembles strategic recommendations via written communications and visual and verbal presentations at client meetings
- Performed comprehensive primary and secondary market research and competitor analysis for emerging and mid-size pharmaceutical and medical device companies as a consultant
- Promoted to project manager after three projects due to high performance consultant track record and strong understanding of client business needs – awarded Project Manager of the Year 2020

InPrint – A Scientific Editing Network, *Editor-in-Chief, Associate Editor-in-Chief, Secretary, Editor, Designer*

Washington University School of Medicine, *St. Louis, MO*   *Feb 2019 – present*

- Provide organizational, conceptual, structural, and grammatical advice, constructive criticism, and edits for abstracts, manuscripts, grants, and other types of scientific writing
- Design vector graphic figures and supervise junior designers to visually communicate research studies for clients
- Develop content for and present workshops and instruct scientists on effective science communication including data visualization
- Lead a team of 50+ editors and designers, implement new external services and internal programming, initiate new collaborations and events, review applications, and conduct interviews as Editor-in-Chief
- Launched the annual Scientific Communication Workshop Series with approximately 100 attendees per workshop
- Facilitated the commencement of the Presentation Consulting Service
- Processed submissions, communicated with clients, reviewed applications, conducted interviews, and initiated collaborations and events with other departments and groups at the university as Associate Editor-in-Chief
- Organized meetings, booked locations, scheduled events, and recorded meetings and membership as Secretary

Engineering Product Development, *Intern*

K2M (Acquired by Stryker), *Leesburg, VA*   *May 2015 – Aug 2015*

- Collaborated with R&D engineers to 3D design a new implant system satisfying customer requirements
- Restructured and revised FDA regulatory submission support material such as traceability matrices, risk forms, and clinical evaluation reports

State Tested Nurses Aid, Masternick Memorial Health Care

Windsor House*, New Middletown, OH*   *July 2013; May 2014 – Aug 2014; Dec 2014 – Jan 2015*

- Assisted residents in activities of daily living while monitoring and documenting vitals, inputs, and outputs
- Collaborated with, mentored, and trained co-workers to provide optimal care
- Observed healthcare in long-term facilities to understand needs of patients and health providers

Publications

Dicks AR, Maksaev GI, Harissa Z, Savadipour A, Tang R, Steward N, Liedtke W, Nichols CG, Wu CL[*], Guilak F[*]. Skeletal dysplasia-causing TRPV4 mutations suppress the hypertrophic differentiation of human iPSC-derived chondrocytes. *bioRxiv* (2021). doi: 10.1101/2021.06.15.448562. *eLife* (submitted).

Dicks AR, Steward N, Guilak F[*], Wu CL.[*] Chondrogenic differentiation of human induced pluripotent stem cells. *Methods in Molecular Biology: Cartilage Tissue Engineering* (submitted).

Dicks AR[*], Harissa Z[*], Kim Y, Steward N, Liedtke W, Wu CL, Guilak F. Skeletal dysplasa-causing TRPV4 mutations increase mechanosensitivity of human iPSC-derived chondrocytes. (in preparation).

Dicks A[*], Wu CL[*], Steward N, Adkar SS, Gersbach CA, Guilak F. Prospective isolation of chondroprogenitors from human iPSCs based on cell surface markers identified using a CRISPR-Cas9-generated reporter. *Stem Cell Research & Therapy* (2020).

Wu CL[*], **Dicks A**[*], Steward N, Tang R, Katz DB, Choi YR, Guilak F. Single cell transcriptomic analysis of human pluripotent stem cell chondrogenesis. *Nature Communications* (2021).

Dicks A, Bhatia H, Clemens A, Locke M, Mueller E, Murphy D, Pomper N, Robinson A, Schoch K. Improving scientific communication with service, education, and career development. *Nature Biotechnology* (submitted).

Rodríguez Ruiz A, **Dicks A**, Tuerlings M, Schepers K, van Pel M, Nelissen RGHH, Freund C, Mummery C, Orlova V, Guilak F, Meulenbelt I, Ramos YFM. Cartilage from human induced pluripotent stem cells: comparison with neo-cartilage from chondrocytes and bone marrow mesenchymal stromal cells. *Cell and Tissue Research* (2021).

Rai MF, Wu CL, Capellini TD, Guilak F, **Dicks AR,** Muthuirulan P, Grandi F, Bhutani N, Westendorf JJ. Single Cell Omics for musculoskeletal Research. *Current Osteoporosis Reports* (2021).

Harasymowicz NS, **Dicks A,** Wu CL, Guilak F. Physiologic and pathologic effects of dietary free fatty acids on cells of the joint. *Ann. N.Y. Acad. Sci Marrow* (2019).

Guilak F, Nims R, **Dicks A,** Wu CL, Meulenbelt I. Osteoarthritis as a disease of the cartilage pericellular matrix. *Matrix Biology* (2018).

Adkar SS, Wu CL, Willard VP, **Dicks A,** Ettyreddy A, Steward N, Bhutani N, Gersbach CA, Guilak F. Highly efficient chondrogenic differentiation of human iPSCs and purification via a reporter allele generated by CRISPR-Cas9 genome editing. *Stem Cells* (2018).

*authors contributed equally

Posters and Presentations

Dicks A, Wu CL, Harissa Z, Steward N, Guilak F. Differentiation and disease modeling using human iPSC-derived chondrocytes. Human Pluripotent Stem Cell Differentiation Work-in-Progress. Washington University School of Medicine, St. Louis, MO. March 2021. *Virtual presentation.*

Dicks A, Wu CL, Harissa Z, Steward N, Liedtke W, Guilak F. Skeletal dysplasia-causing mutations in the ion channel TRPV4 alter human iPSC chondrogenic differentiation and calcium signaling. Orthopedic Research Society Annual Meeting, Virtual. February 2021. *Podium presentation.*

Dicks A, Schoch K, Robinson A. Data Visualization: how to effectively communicate science through easily digestible data visuals. *Presentation and interactive workshop.*
- Washington University School of Medicine Pediatric Fellowship. St. Louis, MO. January 2020.
- Publication Writing Course, Engineering Communication Center. St. Louis, MO. February 2020, October 2020, February 2021.
- Probability & Statistics Course, Engineering Communication Center. St. Louis, MO. February 2020.
- Technical Writing, Engineering Communication Center. St. Louis, MO. February 2021.
- Mechanical Engineering Lab, School of Engineering. St. Louis, MO. April 2021.
- Scientific Communication Workshop Series, Washington University School of Medicine. St. Louis, MO. June 2021.

Dicks A, Schoch K, Cimpean M, Clemens A, Locke M, Pomper N. How to write a strong qualifying exam document. Washington University Division of Biological and Biomedical Sciences. St. Louis, MO. March 2020. *Virtual presentation.*

Schoch K, Alspach E, **Dicks A**, Locke M. How to write an abstract: conference vs. manuscript. Pediatric Fellowship. November 2019, October 2020. *Presentation and interactive workshop.*

Dicks A, Mack M, Robinson A. Using Adobe Illustrator for Scientific Schema Design. Washington University School of Medicine. September 2019. *Presentation and interactive workshop.*

Wu CL, **Dicks A**, Steward N, Tang R, Katz DB, Choi YR, Guilak F. Single Cell Transcriptomic Analysis of Human Pluripotent Stem Cell Chondrogenesis. Orthopedic Research Society Annual Meeting, Phoenix, AZ. February 2020. *Presentation.* Orthoregeneration Award.

Dicks A, Wu CL, Harissa Z, Steward N, Guilak F. Mechanotransduction of hiPSC-derived Chondrocytes. Washington University Biomedical Engineering Annual Retreat. September 2019. *Presentation.*

Dicks A, Wu CL, Steward N, Adkar S, Willard V, Gersbach CA, Guilak F. Prospective Isolation of Chondroprogenitors from Human iPSCs Based on a Collagen II Reporter Allele Generated by CRISPR-Cas9 Genome Editing.
- Orthopedic Research Society Annual Meeting, Austin, TX. February 2019. *Moderated ePoster and poster.*
- Musculoskeletal Winter Symposium, Washington University, St. Louis, MO. February 2019. *Poster.*
- Center of Regenerative Medicine Symposium, Washington University, St. Louis, MO. March 2019. *Poster.*

Wu CL, **Dicks A,** Steward N, Guilak F. Dissecting molecular and cellular heterogeneity in human iPSC chondrogenesis using single-cell RNA sequencing. Orthopedic Research Society Annual Meeting, Austin, TX. February 2019. *Poster.*

Dicks A, Wu CL, Nims R, Steward N, Guilak F. Role of TRPV4 Mechanotransduction in Diabetes-associated Osteoarthritis. Interdisciplinary Training in Mechanobiology from nm to cm Retreat, Washington University, St. Louis, MO. June 2018. *Poster.*

Dicks A, Wu CL, Steward N, Adkar S, Willard V, Guilak F. Highly Efficient Stepwise Differentiation of human iPSCs into Chondrocytes.
• Center of Investigation of Membrane Excitability Diseases Research Day, Washington University, St. Louis, Mo. June 2018. *Poster.*
• Musculoskeletal Winter Symposium, Washington University, St. Louis, MO. February 2018. *Poster.* Poster presenter award.

Wu CL, **Dicks A,** Steward N, Adkar S, Willard V, Guilak F. Highly Efficient Stepwise Differentiation of Human iPSCs into Chondrocytes. Orthopedic Research Society Annual Meeting, New Orleans, LA. March 2018. *Poster and presentation.* New investigator recognition award.

Adkar SS, Willard VP, Wu CL, **Dicks A,** Ettyreddy A, Steward N, Bhutani N, Gersbach CA, Guilak F. Purification of hiPSC-derived chondrocyte-like cells using a CRISPR-Cas9-generated collagen II reporter enhances chondrogenesis and cartilaginous matrix production. Orthopedic Research Society Annual Meeting, New Orleans, LA. March 2018. *Presentation.*

Dicks A, Phlipot J. Developing the Next-generation Tracheostomy Tube: Design, Modeling, and Analysis. Alpha Chi National College Honor Society Convention, Alexandria, VA. April 2016. *Presentation.* Computer science and engineering presentation award.

Dicks A, Phlipot J. Developing the Next-generation Tracheostomy Tube: Research to Design. Annual Northeast Bioengineering Conference, Binghamton University, NY. April 2016. *Poster.*

Teaching, Mentorship, and Volunteering

Intermediate Biomechanics, *Assistant to the Instructor*	Aug 2018 – Dec 2018
Young Scientists Program, *Continuing Mentor for High Schoolers*	Oct 2016 – Apr 2020
Young Scientists Program, *Summer Focus Tutor for High Schoolers*	June 2019 – Aug 2019
Moving and Shaking: An Intro to Engineering for Middle Schoolers, *Teaching Assistant*	Oct 2017 – Nov 2017
Engineering and Science Summer Camp for High Schoolers, *Counselor, Organizer*	June 2016
Build and Learn Summer Day Camp for Middle Schoolers, *Counselor, Organizer*	June 2016
Office of Student Success, *Peer Tutor*	Aug 2013 – May 2016
Bard Life Sciences Cadaver Lab, *Technician*	Aug 2014 – June 2016
Student Support Services, *Peer Tutor*	Aug 201 – May 2016
Anatomy & Physiology Cadaver Lab, *Teaching Assistant*	Aug 2014 – May 2016
BME 3600 Medical Device Design, *Course Preparation*	May 2016 – July 2016
Indiana Tech Residential Life, *Resident Assistant*	Aug 2014 – May 2016

Professional Societies

International Society of Stem Cell Research
Orthopedic Research Society
Biomedical Engineering Society

Honors and Awards

Project Manager of the Year, *The BALSA Group*	2020
T32: Imaging, Modeling and Engineering of Diabetic Tissues, *Fellow*	Jan 2018 – Dec 2019
T32: Mechanobiology from nm to cm, *Affiliate Fellow*	Sept 2017 – Aug 2018
Professional Development Workshop, *NSF Science and Technology Centers*	Aug 2018
Poster Presenter Travel Award, *Musculoskeletal Winter Symposium*	Feb 2018
Most Outstanding Graduate, *College of Engineering & Biomedical Engineering*	May 2016
Floyd Tesmer and Strayer University Prize in Computer Science and Engineering, *Alpha Chi National Honor Society Convention*	April 2016
Alpha Chi, *National Honor Society*	March 2015 – present
Alpha Eta Mu Beta, *National Biomedical Engineering Honor Society*	Aug 2015 – present
Who's Who Among Students in American Colleges and Universities	2015, 2016
Peer Tutor of the Year	2016
Student Ambassador of the Year	2014, 2016